ივანე ჯავახიშვილის სახელობის თბილისის სახელმწიფო უნივერსიტეტი
ზუსტ და საბუნებისმეტყველო მეცნიერებათა ფაკულტეტი

დოქტორანტურის საგანმანათლებლო პროგრამა ფიზიკა

არჩილ დურგლიშვილი

არომატის შემცვლელი ნეიტრალური დენებით მიმდინარე ტოპ-კვარკის იშვიათი დაშლების ძიება და ადრონული ტაილ-კალორიმეტრის მახასიათებლების ოპტიმიზაცია ATLAS ექსპერიმენტში

ფიზიკის დოქტორის აკადემიური ხარისხის
მოსაპოვებლად წარმოდგენილი დისერტაცია

სამეცნიერო ხელმძღვანელები:
თამარ ჯობავა
ფიზ-მათ. მეცნ. დოქტორი
თსუ მაღალი ენერგიების ფიზიკის ინსტიტუტი

ანა მარია ჰენრიქეს კორეია
ფიზიკის დოქტორი
ნაწილაკების ფიზიკის ევროპული ლაბორატორია, ცერნი

თბილისი
2020 წელი

Ivane Javakhishvili Tbilisi State University
Faculty of Exact and Natural Sciences

Doctoral Program: Physics

Archil Durglishvili

Search for Flavour-Changing Neutral Current Top-Quark Decays and Optimization of the Hadronic Tile Calorimeter Performance at the ATLAS Experiment

The thesis work is performed to obtain a PhD academic degree in Physics

Scientific Supervisors:
Dr. Tamar Djobava
High Energy Physics Institute of Tbilisi State University

Dr. Ana Maria Henriques Correia
European Laboratory for Particle Physics, CERN

Tbilisi
2020 Year

აბსტრაქტი

დისერტაციის მთავარ თემას წარმოადგენს დიდი ადრონული კოლაიდერის ATLAS ექსპერიმენტზე დაგროვებულ პროტონ-პროტონული დაჯახებების მონაცემებში ახალი ფიზიკი სიგნალის ძიება. ახალი ფიზიკის სიგნალად განხილული იქნა ტოპ-კვარკის არომატის შემცვლელი ნეიტრალური დენებით (აშნდ) მიმდინარე დაშლის პტოცესები $t \to qZ$ ($q = u, c$), რისი ძიებაც ჩატარდა ტოპ-კვარკ-ტოპ-ანტიკვარკ წყვილური დაბადების შემთხვევებში, როდესაც ერთი ტოპ-კვარკი იშლება $t \to qZ$ აშნდ არხით, ხოლო მეორე - სტანდარტული მოდელის მიხედვით დომინანტური $t \to bW$ არხით. გამოყენებული იქნა 2012 წელის $\sqrt{s} = 8$ ტევ-ზე მიღებული 20.3 ფბ$^{-1}$ ინტეგრალური ნათების მქონე და 2015-2016 წლების $\sqrt{s} = 13$ ტევ-ზე მიღებული 36.1 ფბ$^{-1}$ ინტეგრალური ნათების მქონე მონაცემები. ახალი ფიზიკის არანაირი ცხადი ნიშანი არ იქნა დამზერილი. საბოლოოდ, 95% საიმედოობის დონის მქონე ზედა ზღვარი დადებული იქნა $t \to qZ$ დაშლების ფარდობით ალბათობებზე: BR$(t \to uZ) < 1.7 \times 10^{-4}$ და BR$(t \to cZ) < 2.4 \times 10^{-4}$, რაც წარმოადგენს დისერტაციის დასრულების დღემდე ყველაზე ძლიერ ექსპერიმენტულ ლიმიტებს. შესწავლილი იქნა მაღალი ნათების ფაზაში დიდი ადრონულ კოლაიდერზე, $\sqrt{s} = 14$ ტევ და 3000 ფბ$^{-1}$ ინტეგრალური ნათებით, $t \to qZ$ დაშლების მიმართ ATLAS ექსპერიმენტის მგრძნობიაროზა. მოსალოდნელია $\sqrt{s} = 13$ ტევ მონაცემებით მიღებული შედეგების ოთხჯერ უფრო მეტად გაუმჯობესება. ასევე წარმოდგენილია ATLAS დეტექტორის მახასიათებლების ოპტიმიზაციის მიზნით ჩატარებული კვლევებიც. კერძოდ, ATLAS დეტექტორის ადრონული ტაილ-კალორიმეტრის გრანულაციის გაუმჯობესება მაღალი ნათების მქონე დიდი ადრონული კოლაიდერის კონტექსტში და ელექტრონების ენერგიის ყალიბრების გაუმჯობესება ATLAS ელექტრო-მაგნიტური კალორიმეტრის "ღრეჩოს" არეში ($1.4 < |\eta| < 1.6$).

Abstract

The main topic of the thesis is the search for new physics signal in the LHC proton–proton collisions data collected by the ATLAS experiment. A flavour-changing neutral-current (FCNC) top-quark decays $t \to qZ$ ($q = u, c$) are searched as a new physics signal using the top-quark–top-antiquark pair production events, with one top quark decaying through the $t \to qZ$ FCNC channel, and the other through the dominant Standard Model mode $t \to bW$. The search is performed in the data collected in 2012 at a center of mass energy of $\sqrt{s} = 8$ TeV and in 2015-2016 at $\sqrt{s} = 13$ TeV, corresponding to an integrated luminosity of 20.3 fb^{-1} and 36.1 fb^{-1}, respectively. No evidence of a new physics signal is found. The 95% CL limits on the $t \to qZ$ branching ratio are set at BR$(t \to uZ) < 1.7 \times 10^{-4}$ and BR$(t \to cZ) < 2.4 \times 10^{-4}$, constituting the most stringent experimental limits to date of finishing of the dissertation work. The sensitivity of the ATLAS experiment in the search for $t \to qZ$ FCNC decays is studied in the context of the high luminosity phase of the Large Hadron Collider with a center-of-mass energy of 14 TeV and an integrated luminosity of 3000 fb^{-1}. An improvement by a factor of four is expected over the current results with $\sqrt{s} = 13$ TeV data. The branching ratio limits that are obtained are at the level of 4 to 5 $\times 10^{-5}$ depending on the considered scenarios for the systematic uncertainties. The ATLAS detector performance studies are also performed and described in the thesis, which are important in the search for new physics. Namely, the high granularity upgrade of the ATLAS Hadronic Tile Calorimeter in the context of high luminosity LHC upgrade, and the electron energy calibration improvements for the ATLAS EM calorimeter crack region ($1.4 < |\eta| < 1.6$) are investigated.

Acknowledgements

There are a lot of people I would like to thank, but certainly the first is Dr. Tamar Djobava, my supervisor in the work devoted to the search for new physics. Without her, I would not have opportunity to do the work in this exciting topic. She was excellent supervisor, even more than supervisor, providing me continuous support, motivation and guidance that were invaluable during the course of this work and in my personal development.

I would like to thank Dr. Ana Maria Henriques Correia, my supervisor in the work related to the ATLAS Hadronic Tile Calorimeter. Her support, advice and guidance played an important role in my formation as a physicist able to deal with new challenges. Thanks to her for giving me opportunity to stay at CERN for a long periods and make relations and to work with many experts in several fields, which acquired me many important skills and knowledge.

I would also like to thank Dr. Irakli Minashvili not only as Tbilisi ATLAS team leader but also as friend. I appreciate that he was always ready to help me whenever and whatever I needed during my stays at CERN.

Thanks to Prof. Gela Devidze who was always ready and able to shed the light to the spots that I had in my knowledge of theoretical physics.

I would also like to thank Dr. Maia Mosidze for the discussions that were always productive and encouraging.

This PhD studies would not have been possible without support from ATLAS *Top Working* group, *TileCal*, *E/gamma* and *Jet/Etmiss* groups. I am very grateful to members of these groups for their support, discussions and feedback.

Thanks to all Tbilisi ATLAS team members from the HEPI TSU and to all HEPI TSU staff for having welcomed me, care, sharing their knowledge and experience, and for the productive work together.

The dissertation works were supported by: SRNSFG through the grant projects #13/03, #31/44, #DI/20/6-200/14, #FR_184, #DI_18-293; ISTC grant project #G-2098; the scholarship of the Project #48/04 of SRNSFG and Ref. 93 562 VolkswagenStiftung foundations "Regional Doctoral Program in Theoretical and Experimental Particle Physics".

Contents

Introduction

The Standard Model (SM) is the most successful theory by now in describing elementary particles and their interactions. It has so far well explained almost all experimental results and precisely predicted a wide variety of phenomena. However, there are some critical points that arise both from theoretical considerations and experimental results that does not fit in the SM and may indicate a presence of new physics beyond the Standard Model. One way to search for new physics is through the study of top-quark, which is the heaviest elementary particle predicted by the Standard Model. Its large mass, close to electroweak symmetry breaking scale, makes it a good probe of new physics. The top quark was discovered in 1995 by the CDF and D0 experiments at the Tevatron collider and since that it is heavily studied by several collaborations. In this thesis, a search for flavour-changing neutral-current (FCNC) processes in top-quark decays is presented, which is performed with the proton-proton collisions data collected by the ATLAS experiment at the Large Hadron Collider (LHC). The FCNC processes in top-quark decays are highly suppressed in the Standard Model, nonetheless they can be highly enhanced by several beyond-SM scenarios. Therefore, any significant signal of top-quark FCNC decays will indicate the existence of new physics. In the doctorate work, the top-quark FCNC decay into a Z boson and a q-quark ($q = u, c$) is considered.

The two more works developed in different topics are presented in this thesis. First, the study of high granularity upgrade of the ATLAS Hadronic Tile Calorimeter is described, which emphasis possible improvements in the jet performance that is important in the search for exotic W' and Z' bosons. Second, the electron energy calibration improvements for the ATLAS EM calorimeter crack region ($1.4 < |\eta| < 1.6$) is presented.

The thesis is organized as follows. Chapter 1 gives a brief introduction to the Standard Model, focusing on the top-quark properties. Several SM extensions are emphasised in which some top-quark FCNC decays might be enhanced and results of experimental searches for $t \to qZ$ FCNC decays are discussed. In Chapter 2, an overview of the LHC accelerator complex and the ATLAS detector is provided. More detailed description of the ATLAS hadronic Tile Calorimeter (TileCal) system is presented in Chapter 3, where a granularity upgrade is considered and a possible improvements in the jet performance are investigated. In Chapter 4, the use of the TileCal E4 scintillators in the electron energy calibration is investigated. The results of this study is a part of the journal publication [1]. Chapter 5 and Chapter 6 are devoted to the search for FCNC top-quark decays $t \to qZ$ in top-quark–top-antiquark pair production events with $\sqrt{s} = 8$ TeV and $\sqrt{s} = 13$ TeV proton-proton collisions data, respectively. In the analysis with $\sqrt{s} = 8$ TeV data, the trilepton ($t\bar{t} \to bWqZ \to j\ell\nu j\ell\ell$) and dilepton

($t\bar{t} \to bWqZ \to jjjj\ell\ell$) topologies are considered. The analysis in trilepton topology is published in Ref. [2]. The search for $t \to qZ$ FCNC with $\sqrt{s} = 13$ TeV data is performed only in trilepton topology and the analysis is published in Ref. [3]. The final chapter, Chapter 7, presents the future prospects for $t \to qZ$ FCNC searches in the context of the High-Luminosity LHC upgrade for a center-of-mass energy of 14 TeV and a luminosity of 3000 fb^{-1}. This study is released by the ATLAS Collaboration as a public document [4].

Chapter 1.

Theoretical overview

1.1. The Standard Model of particle physics

The Standard Model (SM) is a renormalizable quantum field theory [5–8] that describes the fundamental constituents of matter and their interactions through the strong, weak, and electromagnetic forces. In the SM, Lagrangians describing the evolution and interactions of the particles remain invariant under local transformations of a symmetry group $SU(3) \times SU(2) \times U(1)$, where $SU(3)$ describes the strong force, while $SU(2) \times U(1)$ corresponds to the unification of the weak and the electromagnetic forces.

1.1.1. Elementary particles

In the SM, the elementary particles are described as excitations of quantum fields in (3+1)-dimensional spacetime. There are two types of particles, *fermions* and *bosons*. Fermions have half-integer spin with antisymmetric wave functions under identical particle exchange, while *bosons* have integer spin with symmetric wave functions under the exchange of two identical particles.

The matter is constituted of 12 fundamental *fermions* with spin $\frac{1}{2}$ and their anti-particles, with identical mass and opposite quantum numbers. The fundamental *fermions* are divided in two subgroups: *quarks*, participating in the strong interaction, and *leptons*, not interacting via strong force. *Leptons* only interact through the electromagnetic and the weak forces, with corresponding quantum numbers that are the electric charge and the weak isospin, respectively. *Quarks* have an additional quantum number, "color", allowing them to interact through the strong force. *Leptons* can be observed as isolated particles, while *quarks* are always bound together in order to form colorless particles with integer charge, a phenomenon known as "confinement" [9]. Thus, quarks are isolated in composite particles, called *hadrons*.

Fermions are organized in three generations depending on the particles masses. The first generation particles are the lightest and the most stable while the second and the third generations are heavier and less stable. Each generation contains an "up-type" quark (with an electric

charge of $+\frac{2}{3}$), a "down-type" quark (with an electric charge of $-\frac{1}{3}$), a charged lepton (with an electric charge of -1), and a neutral lepton, called a neutrino.

The interactions between elementary matter particles are described by gauge *bosons* (with spin 1), force mediator particles. The mediator of the electromagnetic interaction is the photon (γ). The weak force is mediated by $W^{\pm}$ and Z^0 bosons while the strong force is carried by gluons (g).

The last fundamental particle in the SM is the Higgs boson (H), which is a neutral scalar particle (with spin 0) introduced in the theory through the mass generation mechanism. The field of the Higgs boson causes other elementary particles to acquire masses. This particle was recently discovered by the ATLAS and CMS Collaborations [10, 11].

1.1.2. Fundamental interactions

The interactions between elementary particles can be described in terms of the four fundamental interactions: strong, electromagnetic, weak and gravitational. The SM, only describes the strong, electromagnetic and weak interactions. The gravitational interaction is weak by far compared to other three interactions and can be neglected in the description of the interactions between elementary particles.

The strong interaction

The quantum field theory describing the strong interaction is named as Quantum Chromodynamics (QCD), which is the theory of $SU(3)_C$ *color* symmetry gauge group [12]. In this theory, each flavor of quark contains a triplet of fields, while the gluon contains an octet of fields. Each of these fields corresponds to a "color" state. Therefore, quarks have a color of *red*, *green* or *blue* and antiquarks have a color of *antired*, *antigreen* or *antiblue*. The gauge transformation of $SU(3)_C$ group yields eight linear independent gluon fields G^{α}_{μ} ($\alpha \in \{1, 2, 3, ..., 8\}$) carrying a combination of two colors (one of *red*, *green* or *blue* and one of *antired*, *antigreen* or *antiblue*), which allow gluon-gluon interactions. Therefore, QCD is known as a non-Abelian gauge theory. The coupling constant of the strong interaction, α_s, depends on the scale of the momentum transfer Q. At high momentum transfer, or at short distances, the strength of the strong interaction becomes small, therefore QCD has a perturbative regime, allowing quarks and gluons to behave as asymptotically free particles [13]. The virtual particles participating in the interaction can yield infinities through loops in the Feynman diagrams in the calculation of the physical quantities. Reparameterizing of the bare parameters into physical parameters compensate virtual-particle loop effects and absorbs the divergences. This procedure is known as renormalization [14] and introduces the (unphysical) renormalization scale μ_R. Therefore, in the framework of pertubative QCD, predictions for observables are expressed in terms of the renormalized coupling $\alpha_s(\mu_R^2)$, a function of an renormalization scale μ_R. The value of the renormalization scale is not defined in QCD. Most commonly it is chosen as the scale of

the momentum transfer Q in a given process, then $\alpha_s(\mu_R^2 = Q^2)$ is indicative of the effective strength of the strong interaction in that process. In the leading-order approximation, it can be expressed as:

$$\alpha_s(\mu_R^2) = \frac{12\pi}{(33 - 2n_f)ln\left(\frac{\mu_R^2}{\Lambda_{\rm QCD}^2}\right)}, \tag{1.1}$$

where n_f is the number of quark flavors that can be produced at the energy Q^2 and $\Lambda_{\rm QCD}$ is the energy scale at which the perturbative QCD coupling diverges ($\Lambda_{\rm QCD} \approx 200$ MeV). Equation 1.1 shows that the strength of the strong interaction increases as $\mu_R^2 \to 0$, or at large distances, and reaching the point of diverging. This property is responsible to the phenomenon that quarks and gluons can not appear as free particles, known as "confinement" [9].

The electroweak interactions

The electroweak (EW) theory unifying the electromagnetic and weak interactions was produced by Glashow [5], Salam [6] and Weinberg [8]. The underlying symmetry group of this theory is $SU(2)_L \times U(1)_Y$. The three components of the weak *isospin* ($\boldsymbol{T}$) and weak *hypercharge* (Y) are generators of $SU(2)_L$ and $U(1)_Y$ groups, respectively. The weak *isospin* differentiates between *left-handed* ($T = \frac{1}{2}$) and *right-handed* ($T = 0$) chirality state fermions, while the weak *hypercharge* is related to the electric charge Q (in units of the elementary charge) and the third component T_3 of weak *isospin* by equation:

$$Q = T_3 + \frac{Y}{2}. \tag{1.2}$$

The quantum fields in the $SU(2)_L$ group theory are written in terms of two components (a weak isospin doublets), while $SU(1)_Y$ group fields are with one component (a weak isospin singlets). The subscript L means that the weak isospin doublets are composed only of *left-handed* chirality state fermions, and *right-handed* chirality state anti-fermions. The *right-handed* fermions and *left-handed* anti-fermions are grouped in weak isospin singlets and therefore are not affected by the $SU(2)_L$ local gauge transformation. There are no *right-handed* neutrinos in the EW theory. The generators of the $SU(2)_L \times U(1)_Y$ gauge symmetry group introduces W_μ^k ($k = 1, 2, 3$) (associated to $SU(2)_L$) and B_μ (associated to $SU(1)_Y$) boson fields, implying existence of positive and negative weak charged-currents as well as weak neutral-current and electromagnetic interactions. The weak interactions are known to violate parity, so that the weak charged-current interaction couples only to *left-handed* chirality state fermions and *right-handed* chirality state anti-fermions. The physical electroweak bosons mediating the weak charged-current interactions are W^+ and W^- bosons, with gauge fields written as a linear

combination of W_μ^1 and W_μ^2 boson fields:

$$W_\mu^\pm = \frac{1}{\sqrt{2}}(W_\mu^1 \mp iW_\mu^2). \tag{1.3}$$

The weak neutral-current and electromagnetic interactions are carried by neutral bosons, the Z boson and the photon, respectively. Experimentally, it is shown that the physical Z boson couples to both *left-handed* (weak isospin dublets) and *right-handed* (weak isospin singlets) chirality state fermions (although not equally), so that the W_μ^3 boson field can not be directly associated to the Z boson. Similarly, B_μ field can not be directly associated to the photon since it interacts in the same way with both components of *left-handed* chirality state fermions, which include neutrinos, while the photon does not couple with them. Therefore, Z boson field Z_μ and photon field A_μ are written as a mixing of W_μ^3 and B_μ fields:

$$\begin{pmatrix} A_\mu \\ Z_\mu \end{pmatrix} = \begin{pmatrix} \cos\theta_W & \sin\theta_W \\ -\sin\theta_W & \cos\theta_W \end{pmatrix} \begin{pmatrix} B_\mu \\ W_\mu^3 \end{pmatrix}, \tag{1.4}$$

where θ_W is the weak-mixing angle, also known as Weinberg angle, defined from the gauge coupling constants g and g' of $SU(2)_L$ and $U(1)_Y$ groups, respectively:

$$\theta_W = \tan^{-1}(g'/g) \tag{1.5}$$

The electric charge e is the photon coupling strength, which is related to the gauge coupling constants as:

$$e = g \cdot \sin\theta_W = g' \cdot \cos\theta_W. \tag{1.6}$$

The gauge coupling constant g represents the coupling strength of the weak charged-current interactions, while the weak neutral-current interactions have different couplings for *vector* and *axial-vector* interactions and are given as:

$$g_V^f = T_3^f - 2Q^f \sin^2\theta_W, \tag{1.7}$$

$$g_A^f = T_3^f, \tag{1.8}$$

where the index f is the fermion type meaning that the weak neutral-current couplings depend on the fermion type.

1.1.3. Spontaneous symmetry breaking

All gauge bosons in unbroken $SU(2)_L \times U(1)_Y$ symmetry group theory are massless. Also fermions are not allowed to have mass terms in the Lagrangian, since such type of terms would

break the $SU(2)_L$ gauge invariance. In contradiction, observation is that fermions, W and Z bosons have masses, which indicates existence of the mechanism that spontaneously breaks the $SU(2)_L \times U(1)_Y$ group local gauge symmetry and gives masses to particles participating in weak interactions. In order to generate the *spontaneous symmetry breaking*, the *Brout–Englert–Higgs mechanism* [15–18] is introduced. This mechanism consists of a isospin doublet of complex scalar fields ϕ, also known as Higgs field:

$$\phi = \frac{1}{\sqrt{2}} \begin{pmatrix} \phi_1 + i\phi_2 \\ \phi_3 + i\phi_4 \end{pmatrix} \tag{1.9}$$

with the corresponding potential that depends on two parameters, μ^2 and λ:

$$V(\phi) = \mu^2 \phi^\dagger \phi + \lambda (\phi^\dagger \phi)^2. \tag{1.10}$$

The λ must be positive since its negative value leads to a infinite minimum which is unphysical. If $\mu^2 > 0$, then the potential $V(\phi)$ has a minimum at 0 and in that case the $SU(2)_L \times U(1)_Y$ group symmetry is kept, therefore particles would be still massless. If $\mu^2 < 0$, then the potential $V(\phi)$ has a minimum when

$$\phi^\dagger \phi = \frac{1}{2}(\phi_1^2 + \phi_2^2 + \phi_3^2 + \phi_4^2) = -\frac{\mu^2}{2\lambda} \equiv \frac{\nu^2}{2}, \tag{1.11}$$

which means that the ground state of the Higgs field is not at zero, moreover it is not unique. The choice of the ground state *spontaneously breaks* the $SU(2)_L \times U(1)_Y$ group symmetry. The canonical choice is the option where $\phi_1 = \phi_2 = \phi_4 = 0$ and $\phi_3 = \nu$, therefore the ground state is defined as:

$$\phi_0 = \frac{1}{\sqrt{2}} \begin{pmatrix} 0 \\ \nu \end{pmatrix}, \tag{1.12}$$

while expansion around the ground state can be written as:

$$\phi(x) = \frac{1}{\sqrt{2}} \begin{pmatrix} 0 \\ \nu + H(x) \end{pmatrix}, \tag{1.13}$$

where the $H(x)$ is a real scalar field. The ϕ_0 remains invariant under the local transformation of the $U(1)_{\text{EM}}$ gauge group with the generator

$$Q = T^3 + \frac{Y}{2}, \tag{1.14}$$

meaning that the photon does not acquire the mass. The spontaneous breaking of the $SU(2)_L \times U(1)_Y$ group symmetry generates masses for the corresponding real gauge bosons ($W^\pm$ and Z bosons) via the interaction with the Higgs field. The excitation of the Higgs field represents the neutral scalar boson known as Higgs boson, H, with the mass expression of $m_H = \nu\sqrt{2\lambda}$, where

ν is the vacuum expectation value of the Higgs field related to the Fermi coupling constant G_F:

$$\nu = \sqrt{\frac{1}{\sqrt{2}G_F}} \approx 246 \text{ GeV}. \tag{1.15}$$

The value of the Higgs boson mass is not predicted by theory due to the unknown constant λ. The masses of $W^{\pm}$ and Z bosons are given by $m_W = \frac{1}{2}\nu g$ and $m_Z = \frac{1}{2}\sqrt{g^2 - g'^2}$, respectively.

1.1.4. Quark mixing and CKM matrix

The fermions acquire masses through the *Yukawa interactions* that couple left- and right-handed chirality state fermions to the Higgs field. Mass terms for neutrinos are omitted since there are no right-handed chirality state neutrinos in the SM. In order to generate masses for other fermions, they need to be changed from flavour states to mass states using unitary matrices V:

$$u'_{L,R} = V^u_{L,R} u_{L,R},\ d'_{L,R} = V^d_{L,R} d_{L,R},\ l'_{L,R} = V^l_{L,R} l_{L,R}, \tag{1.16}$$

where u, d and l represent gauge fields of up-type quarks, down-type quarks and leptons, respectively. The left-handed quarks are transformed by different matrices ($V^u_L \neq V^d_L$), consequently the $SU(2)$ left-handed quark doublets are constructed as:

$$\begin{pmatrix} u \\ d'' \end{pmatrix}_L, \begin{pmatrix} c \\ s'' \end{pmatrix}_L, \begin{pmatrix} t \\ b'' \end{pmatrix}_L, \tag{1.17}$$

where

$$\begin{pmatrix} d'' \\ s'' \\ b'' \end{pmatrix} = V_{\text{CKM}} \begin{pmatrix} d \\ s \\ b \end{pmatrix},\ V_{\text{CKM}} \equiv V^{u\dagger}_L V^d_L = \begin{pmatrix} V_{ud} & V_{us} & V_{ub} \\ V_{cd} & V_{cs} & V_{cb} \\ V_{td} & V_{ts} & V_{tb} \end{pmatrix}. \tag{1.18}$$

The V_{CKM} is the a unitary matrix called *Cabibo-Kobayashi-Maskawa* (CKM) matrix [19, 20]. As a result, the coupling of weak charged currents to quarks is changed allowing a quark from one doublet to decay into a quark from another doublet via weak charged current. This behaviour is know as *quark mixing*. The probability of the up-type quark i, from one doublet, to decay into the down-type quark j, in the same or other doublet, is given by the amplitude $|V_{ij}|^2$ of the CKM matrix elements. Those are determined experimentally and the diagonal elements found being close to unity [21]. Due to the unitarity condition $(V^{u,d}_{L,R})^\dagger (V^{u,d}_{L,R}) = 1$, these transformations does not affect the weak neutral current interactions, therefore the flavour-changing neutral currents (FCNCs) are forbidden at tree level. In higher order terms we can have FCNCs with the help of the $W^{\pm}$ boson in the loop. The amplitudes of FCNC processes in the up-type (down-type) quarks are proportional to $\sum_k V_{ik} V^*_{jk}$ ($\sum_k V^*_{ki} V_{kj}$) with $i, j = u, c, t$ (d, s, b) and $k = d, s, b$

(u, c, t). Since the CKM matrix is unitary matrix, this kind of terms are off-diagonal elements of the unit matrix, which are zeros. However, since the propagators of quarks participating in the loop depend on their masses, that are different, we can have non-zero terms like the following:

$$\frac{1}{M_W^2} \sum_k V_{ik} V_{jk}^* m_k^2, \tag{1.19}$$

where M_W is the W boson mass, while m_k is the quark mass. Since the off-diagonal elements of the CKM matrix are close to zero, amplitudes of FCNC processes are suppressed. In addition, the FCNC transitions in the up-type quarks are suppressed by $M_W \gg m_k$ $(k = d, s, b)$. This is known as *Glashow–Iliopoulos–Maiani* (GIM) mechanism [22].

1.2. Beyond the Standard Model

The SM has been tested in multiple experiments and proven that it is a successful model in describing experimental observations. The SM predicted several particles and all of those are already discovered. Nevertheless it is an incomplete theory since it leaves many critical questions unanswered.

In the SM neutrinos are massless particles, but several experiments have confirmed the opposite [23–26]. The SM does not provide any candidate for the dark matter that is measured to be $\sim 26.8\%$ of the total mass-energy of the known universe [27]. There is no consistent way to incorporate gravity in the SM. Another issue is the "hierarchy problem" that can be expressed as the quadratically divergent quantum corrections in the Higgs mass calculation, which would make the Higgs mass huge contrary to the observed low mass value. Only solution to have the low Higgs mass is to cancel this divergency by assuming the bare Higgs mass comparable to the new physics scale Λ, which is taken far above the electroweak scale. This is known as *fine-tuning* that is considered unnatural.

These and some other unresolved problems motivate the theoretical developments Beyond the Standard Model (BSM). Over the years, several BSM extensions have been proposed to address one or several shortcomings of the SM. Examples of such extensions are the quark-singlet model (QS) [28], the two-Higgs-doublet model with (FC 2HDM) or without (2HDM) flavour conservation [29], the Minimal Supersymmetric Standard Model (MSSM) [30], the MSSM with R-parity violation (RPV SUSY) [31], models with warped extra dimensions (RS) [32], or extended mirror fermion models (EMF) [33]. All these models affects the calculations for the flavour-changing neutral currents in the top-quark sector, therefore search for the SM inconsistency in the top-quark FCNC decays is motivated to test the BSM models experimentally.

1.3. The top-quark

The top quark is set apart from all other known fundamental particles by its large mass. Being the only particle with its Yukawa coupling close to unity also raises the question whether it plays a special role in the process of mass generation. It was discovered in 1995 by the CDF [34] and D0 [35] collaborations in proton-antiproton ($p\bar{p}$) collisions with centre-of-mass energy of 1.8 TeV at Fermilab's Tevatron collider. For the top quark mass the first world combination of the Tevatron and LHC experiments results reads m_{top} = 173.34± 0.36 (stat.) ± 0.67 (syst.) GeV [36] marking the most massive fundamental particle known to date. The latest direct mass measurements are summarised in Figure 1.1. The consequent lifetime of the top quark in the Standard Model (SM) of $\approx 0.5 \times 10^{-24}$ s [21] is extremely short and it decays before hadronization almost exclusively to bW. This makes top quark the only quark that does not form bound states and a good object to test the SM of particle physics.

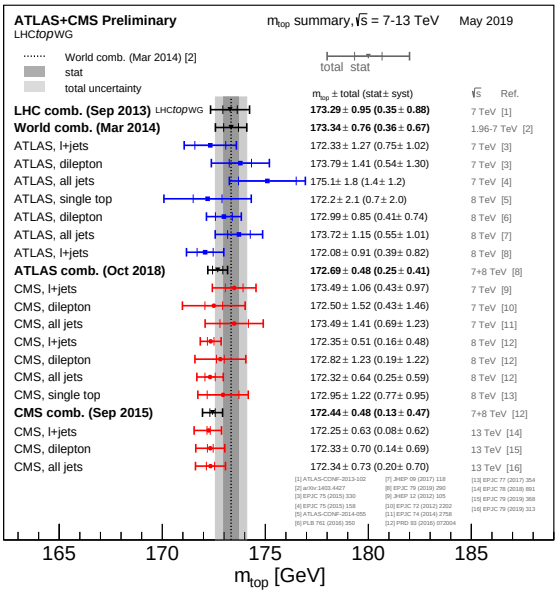

Figure 1.1.: Summary of the ATLAS and CMS direct m_{top} measurements. The results are compared with the LHC and Tevatron+LHC m_{top} combinations. Taken from [37].

1.3.1. Top-quark production

In hadron colliders, top quarks are mainly produced via the strong interaction in top-quark–antitop-quark ($t\bar{t}$) pairs and via the electroweak interaction in single top quarks.

At the leading order (LO) in QCD, the top quark pairs are produced via quark-antiquark annihilation and gluon-gluon fusion. The corresponding Feynman diagrams are shown in Figure 1.2. At the Large Hadron Collider (LHC) with the centre-of-mass energies of a few TeV, the $t\bar{t}$ production cross section is expected to be dominated from gluon-gluon fusion, with a fraction of $\sim 87\%$, with the remainder from quark-antiquark annihilation [38]. The predicted

$t\bar{t}$ cross section in pp collisions at a centre-of-mass energy of $\sqrt{s} = 8$ TeV and $\sqrt{s} = 13$ TeV are $\sigma_{t\bar{t}} = 253^{+13}_{-15}$ pb and $\sigma_{t\bar{t}} = 832^{+46}_{-51}$ pb, respectively. The values are calculated with the Top++2.0 program to next-to-next-to-leading order (NNLO) in perturbative QCD, including soft-gluon resummation to next-to-next-to-leading-log (NNLL) order (see Ref. [39] and references therein), and assuming $m_{top} = 172.5$ GeV. The uncertainty in the theoretical cross-section comes from independent variations of the factorisation and renormalisation scales and variations in the PDF and α_S, following the PDF4LHC prescription with the MSTW 2008 NNLO, CT10 NNLO and NNPDF2.3 5f FFN PDF sets (see Ref. [40] and references therein, and Refs. [41–43]). The summary of LHC and Tevatron measurements compared to the NNLO QCD+NNLL calculations of top quark pair production as a function of centre-of-mass energy is presented on Figure 1.3.

Electroweak single top-quark production has several mechanisms leading to a lower cross sections: production of a top quark and bottom quark through the s-channel decay of a virtual W boson; production of a top quark and a light quark through the t-channel exchange of a virtual W boson; Wt-channel associated production of a top quark and an on-shell W boson. The corresponding leading-order Feynman diagrams are shown in Figure 1.4. The ATLAS and CMS measurements of the single top production cross-sections in various channels as a function of the center of mass energy is summarized in Figure 1.5.

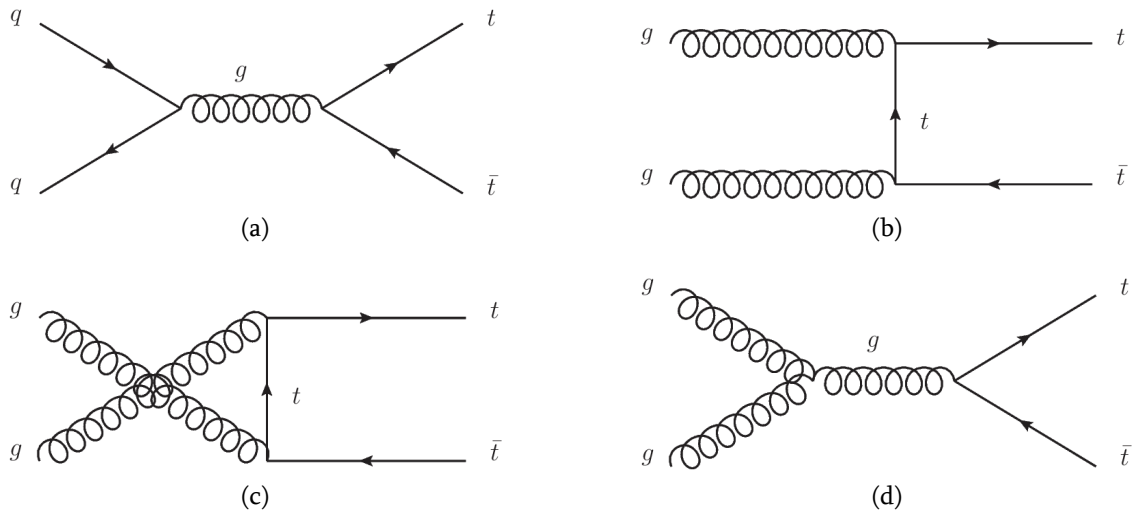

Figure 1.2.: The LO Feynman diagrams of the top quark pair production.

1.3.2. Top-quark FCNC decays

According to the SM, the top-quark flavour-changing neutral current (FCNC) decays are forbidden at tree level. They can occur at one-loop level but are strongly suppressed by the GIM mechanism, as mentioned in Section 1.1.4. The top-quark FCNC decays include transition into u- or c-quark via emission of a Z boson, Higgs boson, a photon or a gluon. In this dissertation

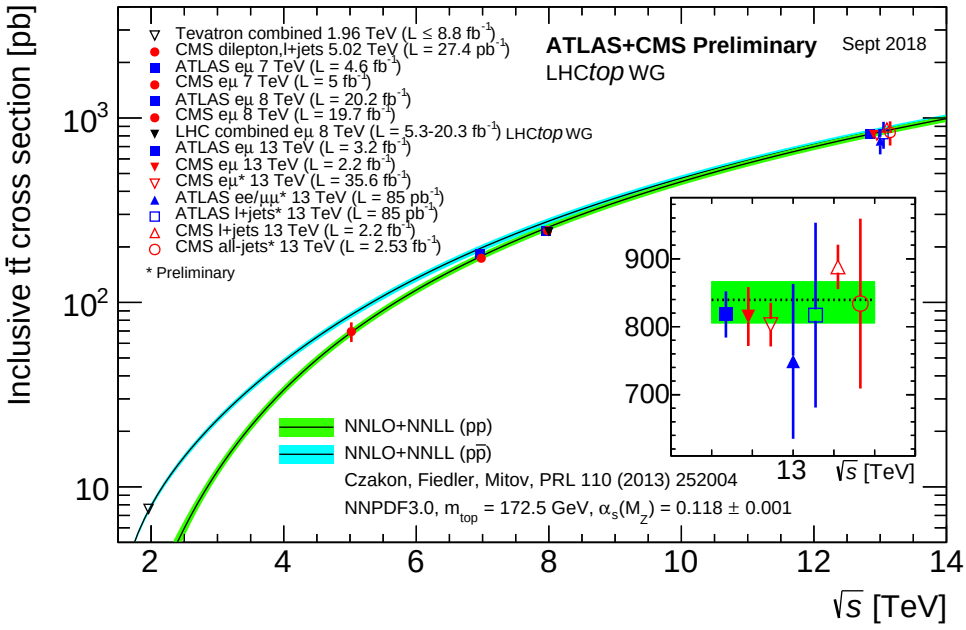

Figure 1.3.: Summary of LHC and Tevatron measurements of the top-pair production cross-section as a function of the centre-of-mass energy compared to the NNLO QCD calculation complemented with NNLL resummation (top++2.0). The theory band represents uncertainties due to renormalisation and factorisation scale, parton density functions and the strong coupling. The measurements and the theory calculation are quoted at m_{top}=172.5 GeV. Measurements made at the same centre-of-mass energy are slightly offset for clarity. Taken from [44].

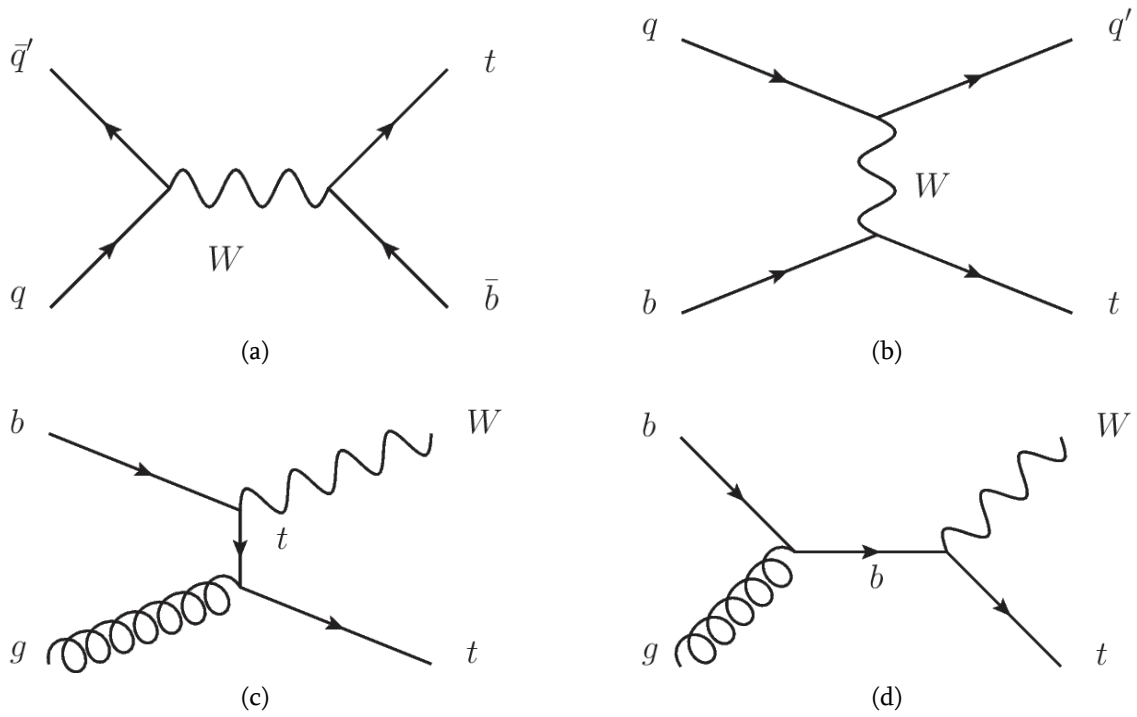

Figure 1.4.: The LO Feynman diagrams of the single top-quark production, (a) s-channel, (b) t-channel, (c) and (d) Wt-channel.

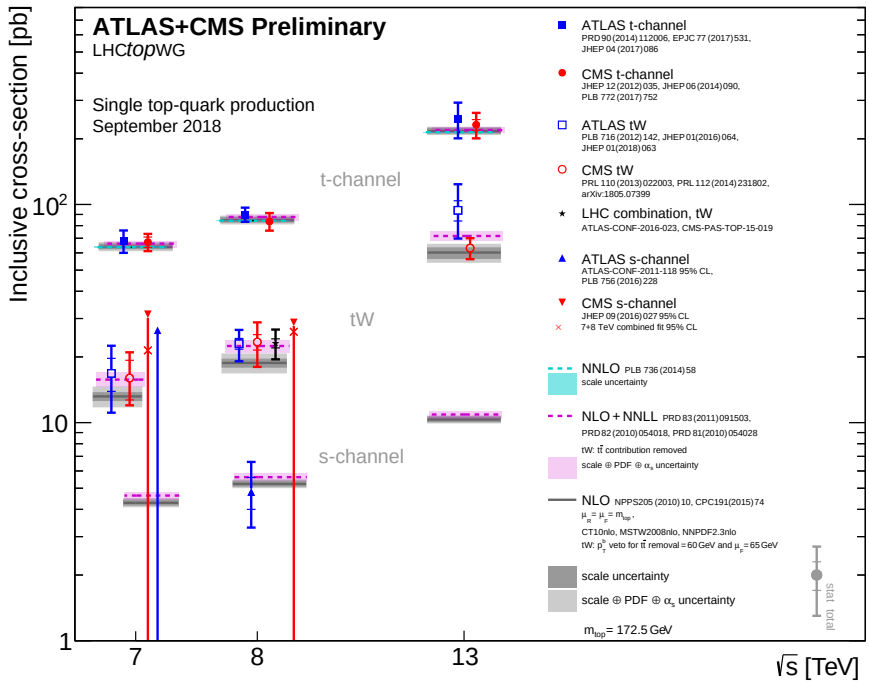

Figure 1.5.: Summary of ATLAS and CMS measurements of the single top production cross-sections in various channels as a function of the center of mass energy. The measurements are compared to theoretical calculations based on: NLO QCD, NLO QCD complemented with NNLL resummation and NNLO QCD (t-channel only). Taken from [45].

work only FCNC $t \to qZ$ ($q = u, c$) decay is considered. The corresponding one-loop level Feynman diagram in the SM is presented in Figure 1.6. The SM prediction for the branching ratios (BRs) of FCNC $t \to qZ$ processes are lower than 10^{-13} [46], which are much smaller than the BR of the dominant decay mode ($t \to bW$) and well below to the experimental sensitivities, as can be seen in the Table 1.2. This essentially guarantees that any measurable BR of FCNC $t \to qZ$ decay would be a clear sign of new physics.

There are several BSM extensions, as mentioned in Section 1.2, where FCNC $t \to qZ$ decays are enhanced leading to potentially measurable BRs by the current experiments. Therefore, experiments can test these BSM extensions by searching of FCNC $t \to qZ$ decays. Even if FCNC BRs are not measured, parameters space of models can be constrained or a model eventually excluded. Table 1.1 provides the maximum values for the branching ratios BR($t \to qZ$) predicted by BSM models mentioned in Section 1.2 and compares them to the value predicted by the SM. Reference [47] gives a comprehensive review of the various extensions of the SM that have been proposed.

Experimental limits on the FCNC branching ratio BR($t \to qZ$) were established by experiments at the Large Electron–Positron collider [48–52], HERA [53], the Tevatron [54, 55], and the Large Hadron Collider (LHC) [56–59]. Before publishing of the latest results obtained in this dissertation work, the most stringent limits were BR($t \to uZ$)$< 2.2 \times 10^{-4}$ and BR($t \to cZ$)$< 4.9 \times 10^{-4}$ at 95% confidence level (CL), both set by the CMS Collaboration [58] using data collected at $\sqrt{s} = 8$ TeV. The ATLAS results obtained at $\sqrt{s} = 7$ TeV are available in [56]. Present experimental 95% CL upper limits on the branching ratio of the FCNC $t \to qZ$ decays are summarized in Table 1.2, excluding results by the ATLAS that are part of this thesis.

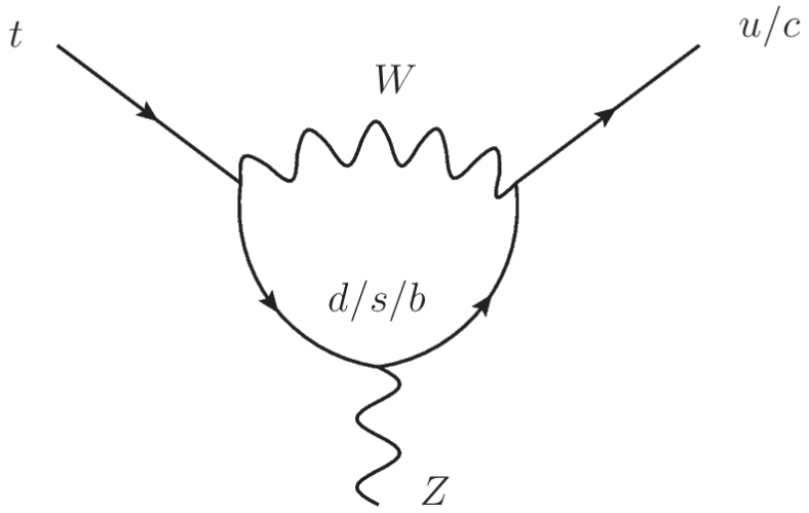

Figure 1.6.: The FCNC $t \to qZ$ ($q = u, c$) decay Feynman diagram in the SM.

Table 1.1.: Maximum allowed FCNC $t \to qZ$ $(q = u, c)$ branching ratios predicted by several models [28–33, 46, 47].

Model:	SM	QS	2HDM	FC 2HDM	MSSM	RPV SUSY	RS	EMF
BR($t \to qZ$):	10^{-14}	10^{-4}	10^{-6}	10^{-10}	10^{-7}	10^{-6}	10^{-5}	10^{-6}

$\sqrt{s}$ (TeV)	Experiment	BR($t \to qZ$) (%)
1.96	CDF	3.7
1.96	D0	3.2
up to 0.208	LEP	7.8
0.315	HERA	30 (tuZ)
7	ATLAS	0.73 ($q = u$)
8	CMS	0.022 ($q = u$)
13	CMS	0.045 ($q = c$)

Table 1.2.: Present experimental 95% CL upper limits on the branching ratio of the FCNC $t \to qZ$ decays. The ATLAS results that are part of this thesis are not presented.

Effective Lagrangian

The scale of new physics (Λ) in the top-quark flavour-changing neutral currents is assumed to be large ($\Lambda \gtrsim 1$ TeV), however it can be revealed in the energies of current experiments through small deviations from the SM. Effects of the new physics on the observables in the low energy processes can be parametrized in a BSM model-independent way using the Effective-Field-Theory (EFT) approach [60]. In this approach, an effective Lagrangian is constructed by operators expansion of the SM Lagrangian density. The new physics effects are included by at least of dimension-five operators that are based on SM fields and are suppressed by inverse of powers of the new physics scale Λ. At dimension-five, only operator is allowed by gauge invariance that gives rise to a Majorana mass for neutrinos. Due to the tiny neutrino masses, the new physics is constrained at very high energy scale of the order of 10^{15} GeV. Therefore, effects from this operator in the low energy processes would be completely negligible and therefore it is not considered in the effective Lagrangian. Since the expected deviations from the SM are small, only the first order of the expansion, i. e. only the dimension-six operators are of relevance at the current experiments. Thus, the effective Lagrangian can be written as:

$$\mathcal{L}_{eff} = \mathcal{L}_{SM} + \sum_i \frac{C_i}{\Lambda^2} O_i + H.c., \tag{1.20}$$

where $\mathcal{L}_{SM}$ denotes the SM Lagrangian of dimension-four, O_i represents gauge invariant dimension six operators and the dimensionless coefficients C_i indicate the strength of the corresponding effective operator O_i. More than 80 dimension-six operators exists, but not all of

them are independent and only a few of them (about 15) have a significant effect on the top quark [60, 61].

For the FCNC signal events generation in the analysis with $\sqrt{s} = 8$ TeV data, the leading order Lagrangian is used with the dimension-six operators written in terms of anomalous couplings [61]. The most general Ztu vertex term that arises from dimension-six operators can be parametrized as:

$$\mathcal{L}_{Ztu} = -\frac{g}{2c_W}\bar{u}\gamma^{\mu}(X_{ut}^{L}P_L + X_{ut}^{R}P_R)tZ_{\mu} - \frac{g}{2c_W}\bar{u}\frac{i\sigma^{\mu\nu}q_{\nu}}{M_Z}(\kappa_{ut}^{L}P_L + \kappa_{ut}^{R}P_R)tZ_{\mu} + H.c., \quad (1.21)$$

where γ^{μ} are the gamma matrices, $\sigma^{\mu\nu}$ are the Pauli matrices, g is the electroweak coupling, c_W is the cosine of the weak mixing angle, u and t are the quark spinors, Z_{μ} is the Z boson field, P_L (P_R) is the left-handed (right-handed) projection operator, M_Z is the Z boson mass and $q_{\nu} = p_t^{\nu} - p_u^{\nu}$ is the outgoing boson momentum, while X_{ut}^{L}, X_{ut}^{R} and $\kappa_{ut}^{L}, \kappa_{ut}^{R}$ are the anomalous vector and tensor couplings, respectively. The coupling choice in the FCNC signal generation does not have a significant effect on the kinematics of the event [62]. The Ztc vertex can be parametrized analogously.

Later, the TopFCNC[1] model became available, which does calculations at NLO in QCD and use directly dimension-six effective operators instead of anomalous couplings [63, 64]. This model is used to generate the signal events in the analysis with $\sqrt{s} = 13$ TeV data and in the High Luminosity LHC upgrade study. However, the NLO QCD corrections are not that significant in the top-quark FCNC decay processes (approximately 10%) [64].

[1] https://feynrules.irmp.ucl.ac.be/wiki/TopFCNC

Chapter 2.

Experimental setup

2.1. Large Hadron Collider

The Large Hadron Collider (LHC) [65] is a two-ring-superconducting-hadron accelerator and collider installed in the existing 26.7 km tunnel constructed for the Large Electron-Positron Collider [66] (1989) at CERN. The LHC tunnel lies on the plan with 1.4% inclination and 45-170 m below the surface of the French and Swiss countryside. It is designed to collide protons at a center of mass energy of up to $\sqrt{s} = 14$ TeV. The LHC is the last ring in a complex chain of particle accelerators presented in Figure 2.1. The proton source is a hydrogen gas. The electric field is applied to strip hydrogen atoms of their electrons to yield protons. The proton beams undergo several acceleration steps before reaching the desired energy. At first step, they are accelerated up to 50 MeV in the linear accelerator LINAC2. Then the beam is injected into the Proton Synchrotron Booster (PSB), where the energy is increased up to 1.4 GeV, followed by the Proton Synchrotron (PS) accelerating up to 25 GeV. Protons are then sent to the Super Proton Synchrotron (SPS) where they are accelerated to 450 GeV. Finally, two counter-rotating proton beams are entered into the LHC beam pipes and accelerated to their maximum energies before collision happens. The CERN accelerator complex is also used to accelerate lead ions to the similar energies as protons.

The LHC has eight straight sections and eight arcs. Each straight section is approximately 528 m long. The particle beams collide at four interaction points located in the straight sections, where four main-experiment detectors are built: ATLAS (A Toroidal LHC ApparatuS) [67], CMS (Compact Muon Solenoid) [68], ALICE (A Large Ion Collider Experiment) [69] and LHCb (A Large Hadron Collider beauty Experiment) [70]. The two high luminosity experiment detectors, ATLAS and CMS, are located at diametrically opposite straight sections Point 1 and Point 5, respectively. The ALICE is located at Point 2, while the LHCb – at Point 8.

The LHC curved sections consist of 1232 dipole magnets to deflect proton bunches keeping them in the orbit and then straight sections are composed by 392 quadrupole magnets to focus the beam. Furthermore to correct the beam trajectory higher order magnetic multipoles are also used. These are superconducting magnets made of Niobium-Titanium that operate at an

average temperature of 1.9 K achieved using super-fluid Helium. The dipole magnets produce a peak dipole field of 8.33 T limiting the beam energy to 7 TeV.

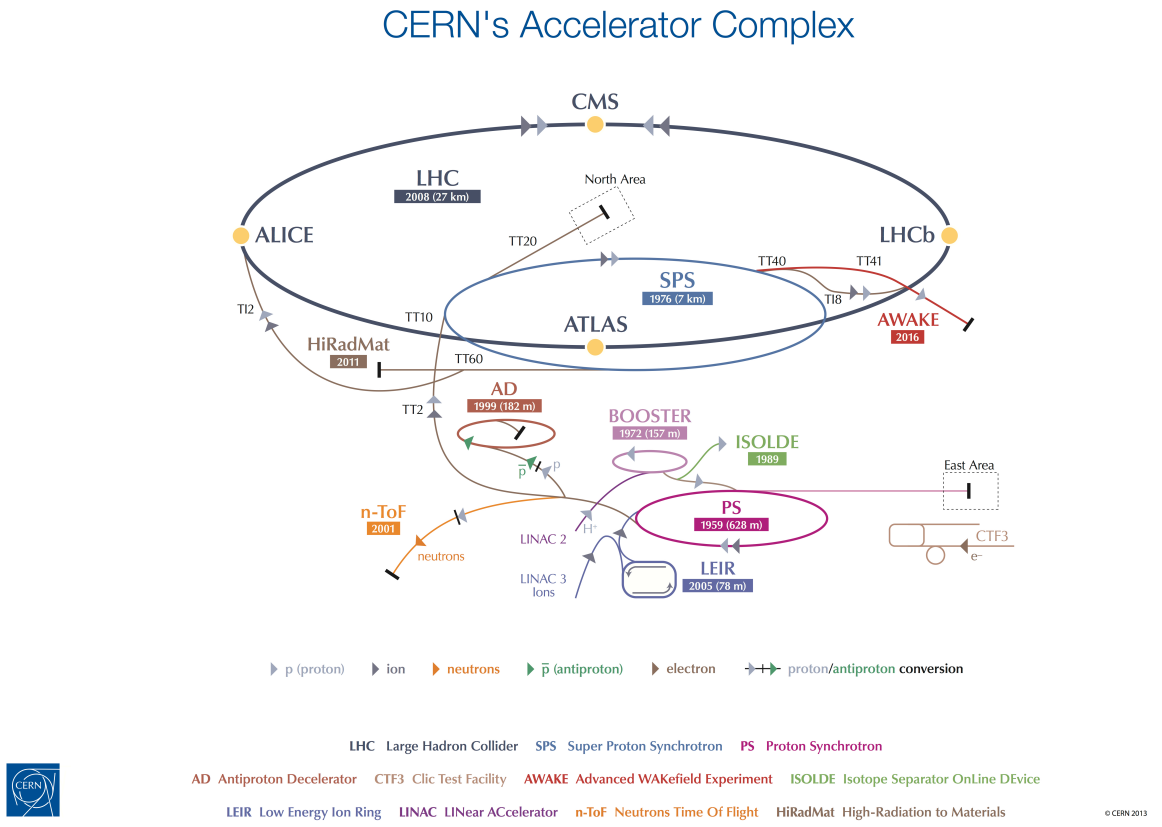

Figure 2.1.: Schematic view of the CERN particle accelerator complex. Figure is taken from [71].

2.1.1. Luminosity and pile-up

Beside the beam energy, the *instantaneous luminosity* ($\mathcal{L}$) is the most important parameter of the particle accelerator. It relates the event rate (R) of the physics process under study to the cross-section (σ) of that process:

$$R \equiv \frac{dN}{dt} = \sigma\mathcal{L}. \tag{2.1}$$

In general, the instantaneous luminosity of the ring collider is defined as:

$$\mathcal{L} = \frac{N_1 N_2 n_b f_r}{A}, \tag{2.2}$$

where N_1 and N_2 are the number of particles in each of two colliding bunches, n_b is the number of bunches that cross at the interaction point, f_r is the collider revolution frequency and A is the effective beam overlap cross section which depends on several beam parameters [65]. The

designed value for the instantaneous luminosity for the LHC is 1.0×10^{34} cm^{-2} s^{-1}. It is not constant during the active time of the accelerator but decreases with time due to the degradation of the emittance[1] of the circulating beams. The maximum instantaneous luminosity delivered to ATLAS by LHC during the stable beams for pp collisions as a function of time in 2012, 2015 and 2016 is presented in Figure 2.2. Integrating the instantaneous luminosity over a period of the accelerator active time gives the *integrated luminosity* (L), which is used to describe the number of events (N) of a certain process produced in collisions over that period:

$$N = \sigma \int \mathcal{L} dt = \sigma L. \tag{2.3}$$

In order to deliver a high integrated luminosity it is necessary to have the high frequency of collisions and the high density of bunches, which rise the probability to have multiple inelastic pp interactions in the same bunch collision. This event is referred to as *pile-up*. The multiple pp collisions in pile-up events are originated mainly from *minimum-bias*[2] interactions that are the most frequent interactions in the LHC bunch crossings. Pile-up events increase the number of hits in the detector therefore complicates identification of pp interaction vertices, reconstruction of tracks and deteriorates energy resolution of reconstructed physics objects (leptons, jets, etc.). The pile-up activity is characterized using the mean number of interactions per bunch crossing (μ) defined as:

$$\mu = \frac{\sigma_{inel} \mathcal{L}}{n_b f_r}, \tag{2.4}$$

where σ_{inel} is the inelastic pp interaction cross section which is taken to be 73 mb (80 mb) for 8 TeV (13 TeV) centre-of-mass energy. The mean number of interactions per bunch crossing in 2012, 2015 and 2016 is summarized in Figure 2.3. It amounts to $\langle \mu \rangle = 20.7$ in 2012, $\langle \mu \rangle = 13.7$ and $\langle \mu \rangle = 24.9$ in 2015 and 2016, respectively.

In Table 2.1 the LHC luminosity and other performance related parameters in 2012-2016 are summarized and compared to the designed values.

2.2. The ATLAS detector

The ATLAS [67] is one of the two largest multi-purpose particle physics detectors installed at the LHC. It is a set of cylindric sub-detectors, which covers almost the full solid angle[3] around

[1] Phase space volume of the colliding particle bunches.

[2] The long distance interactions in which protons behave as elementary particles and have low transferred momentum.

[3] ATLAS uses a right-handed coordinate system with its origin at the nominal interaction point in the centre of the detector and the z-axis along the beam pipe. The x-axis points from the interaction point to the centre of the LHC ring, and the y-axis points upward. Cylindrical coordinates (r, ϕ) are used in the transverse plane, ϕ being the azimuthal angle around the beam pipe. The pseudorapidity is defined in terms of the polar angle θ as $\eta = -\ln \tan(\theta/2)$. The ΔR distance is defined as $\Delta R = \sqrt{(\Delta\eta)^2 + (\Delta\phi)^2}$.

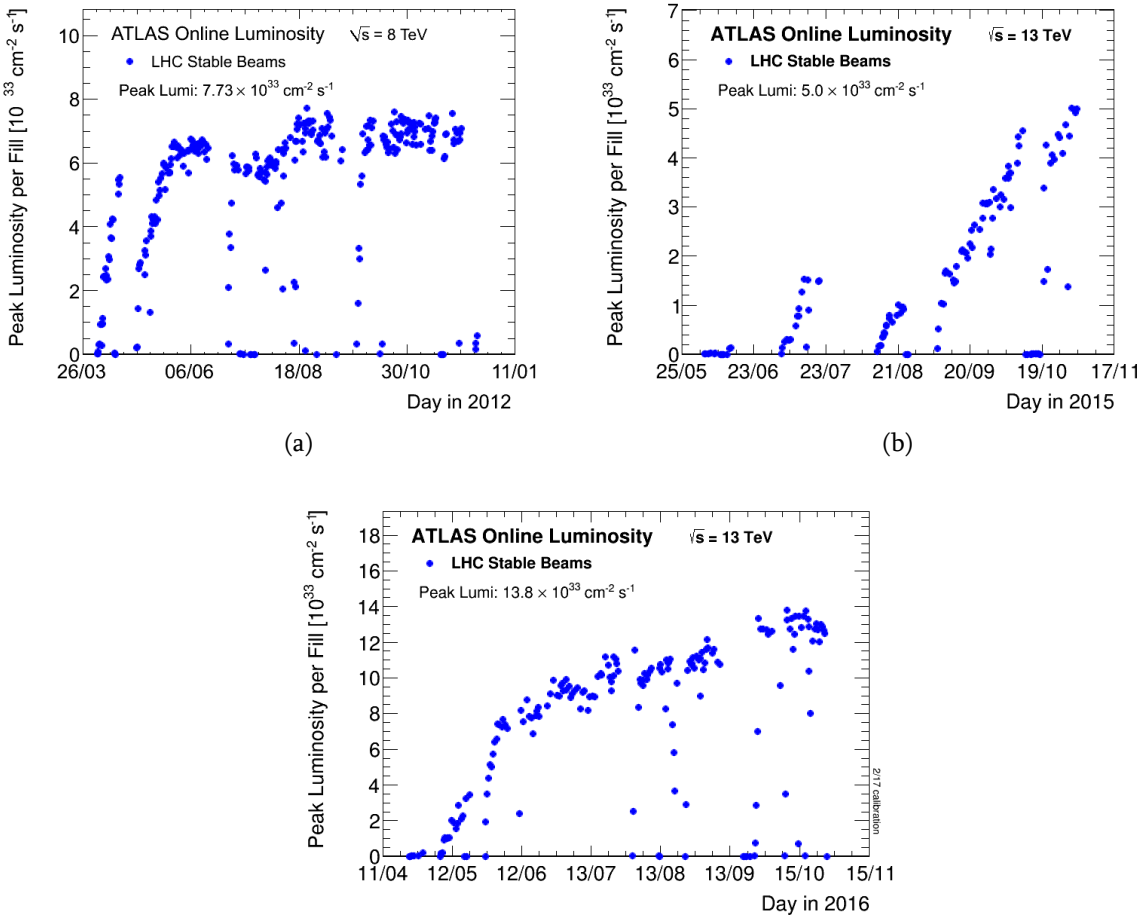

Figure 2.2.: The peak instantaneous luminosity delivered to ATLAS during stable beams for pp collisions is shown as a function of time in a) 2012, b) 2015 and c) 2016. Figures are taken from [72] and [73].

Machine parameter	Design	2012	2015	2016
Beam energy (TeV)	7.0	4.0	6.5	6.5
Protons/bunch (average at start of collisions) (10^{11} p)	1.15	1.5	1.0	1.1
Max. number of bunches	2808	1380	2244	2200
Bunch spacing (ns)	25	50	25	25
Max. peak luminosity (10^{34} cm^{-2} s^{-1})	1.0	0.77	0.47	1.45
Total integrated luminosity, average over ATLAS and CMS (fb^{-1})		22.8	4.2	39.3

Table 2.1.: Overview of the parameters for the LHC performance during the operation in 2012-2016 and comparing the design values [74].

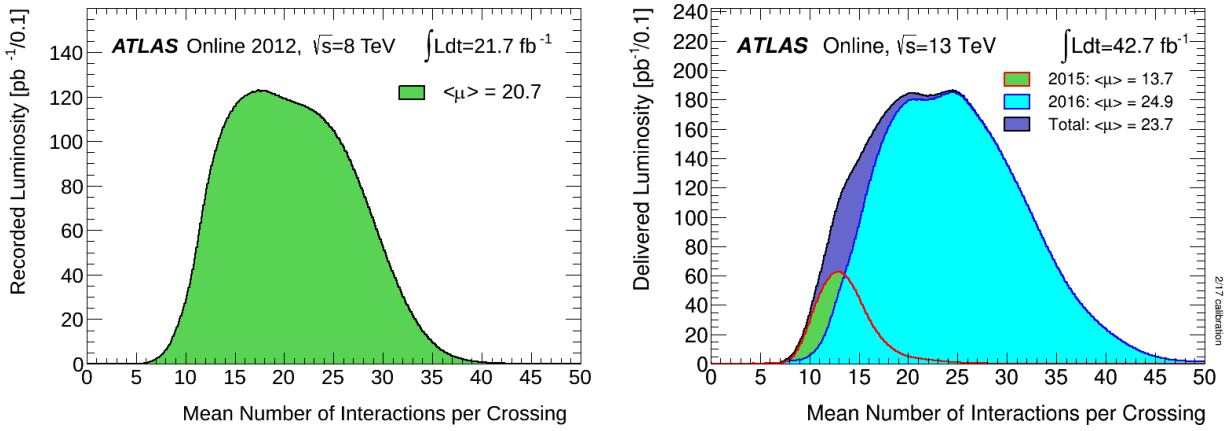

(a) (b)

Figure 2.3.: The luminosity-weighted distribution of the mean number of interactions per crossing for the a) 2012 pp collision data at 8 TeV centre-of-mass energy and b) 2015 and 2016 pp collision data at 13 TeV centre-of-mass energy. Figures are taken from [72] and [73].

the interaction point and has a forward-backward symmetry. The basic detector shape is completed by two end-caps in the bases of the cylinder. The sub-detectors of the end-caps are disc shaped, centered in the beam pipe. A schematic representation of the ATLAS detector can be seen in Figure 2.4. The ATLAS is composed of an inner tracking system close to the interaction point and immersed in a 2 T axial magnetic field produced by a thin superconducting solenoid. A lead/liquid-argon (LAr) electromagnetic calorimeter, a steel/scintillator-tile hadronic calorimeter, copper/LAr hadronic endcap calorimeters, copper/LAr and tungsten/LAr forward calorimeters, and a muon spectrometer with three superconducting magnets, each one with eight toroid coils, complete the detector. A new innermost silicon pixel layer was added to the inner detector after Run 1 [75, 76]. The combination of all these systems provides charged-particle momentum measurements, together with efficient and precise lepton and photon identification in the pseudorapidity range $|\eta| < 2.5$. Energy deposits over the full coverage of the calorimeters, $|\eta| < 4.9$, are used to reconstruct jets and missing transverse momentum. A two-level trigger system is used to select interesting events [77]. The first level is implemented with custom hardware and uses a subset of detector information to reduce the event rate. It is followed by a software-based trigger level to reduce the event rate to approximately 1 kHz.

The main performance goals of the ATLAS detector are summarized in Table 2.2.

The studies presented in this thesis use the pp collision data collected by the ATLAS experiment in 2012 at a center of mass energy of $\sqrt{s} = 8$ TeV and in 2015-2016 at $\sqrt{s} = 13$ TeV. In 2012, the integrated luminosity recorded by the ATLAS is 21.3 fb^{-1}, while 3.9 fb^{-1} and 35.6 fb^{-1} in 2015 and 2016, respectively. Figure 2.5 presents the cumulative integrated luminosity delivered to and recorded by the ATLAS detector in these years. The total integrated luminosity recorded by the ATLAS differs from the amount delivered by the LHC because of data-taking inefficiencies. Also, only a part of recorded luminosity is usable for physics analy-

sis. The recorded events are checked offline by each subdetector groups and experts to certify that performance of a detector was conform to expectations. Only events fulfilling all physics requirements are stored in the so-called Good Run List (GRL) and are useful for the physics analysis. The GRLs, giving a total integrated luminosity of 20.3 fb^{-1} for 2012 data at $\sqrt{s} = 8$ TeV and 36.1 fb^{-1} for 2015-2016 data at $\sqrt{s} = 13$ TeV, are used in analyses presented in this thesis.

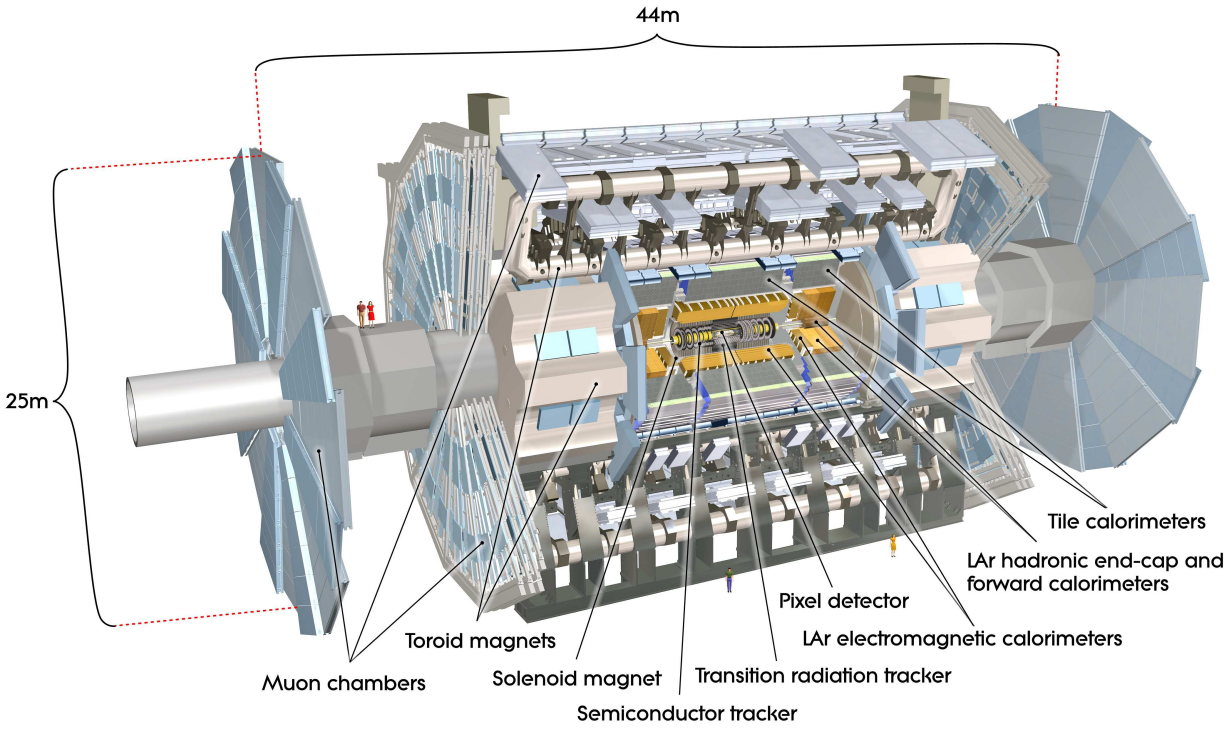

Figure 2.4.: Cut-away view of the ATLAS detector showing the different subdetectors and the magnet systems. The dimensions of the detector are 25 m in height and 44 m in length. The overall weight of the detector is approximately 7000 tonnes. Figure is taken from [67].

Detector component	Required resolution	η coverage	
		Measurement	Trigger
Tracking	$\sigma_{p_T}/p_T = 0.05\%\ p_T \oplus 1\%$	± 2.5	
EM calorimetry	$\sigma_E/E = 10\%/\sqrt{E} \oplus 0.7\%$	± 3.2	± 2.5
Hadronic calorimetry (jets)			
barrel and end-cap	$\sigma_E/E = 50\%/\sqrt{E} \oplus 3\%$	± 3.2	± 3.2
forward	$\sigma_E/E = 100\%/\sqrt{E} \oplus 10\%$	$3.1 < \lvert\eta\rvert < 4.9$	$3.1 < \lvert\eta\rvert < 4.9$
Muon spectrometer	$\sigma_{p_T}/p_T = 10\%$ at $p_T = 1$ TeV	± 2.7	± 2.4

Table 2.2.: General performance goals of the ATLAS detector. Note that, for high-p_T muons, the muon-spectrometer performance is independent of the inner-detector system. The units for E and p_T are GeV. Taken from [67].

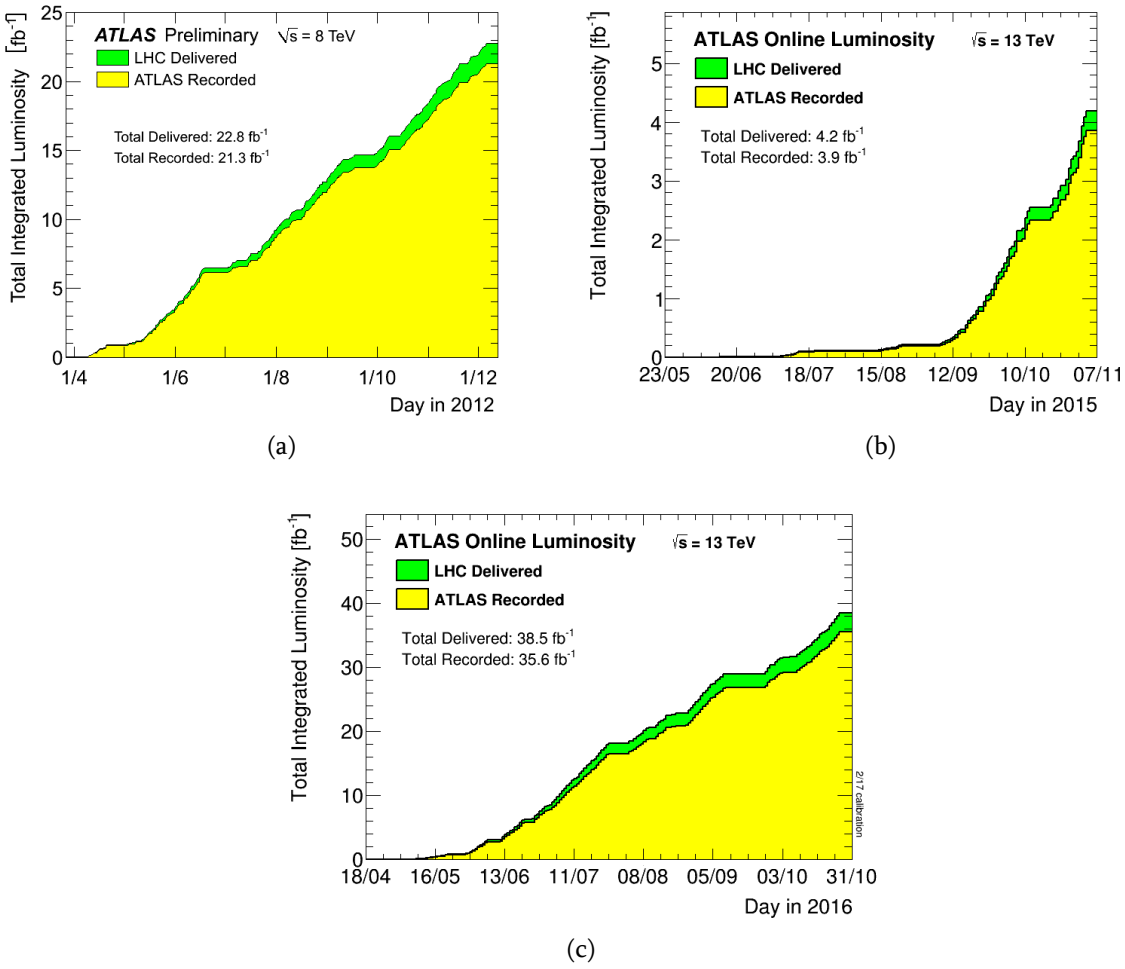

Figure 2.5.: Integrated luminosity versus time delivered by the LHC (green), recorded by ATLAS (yellow), during stable beam conditions for pp collisions at $\sqrt{s} = 8$ TeV in 2012 (a) and at $\sqrt{s} = 13$ TeV in 2015 (b) and 2016 (c). Figures are taken from [72] and [73].

Chapter 3.

Study of high granularity geometry of the ATLAS hadronic Tile Calorimeter

In this chapter, the study of high granularity upgrade of the ATLAS Hadronic Tile Calorimeter is described. The study is done in the context of the ATLAS Phase-II upgrade for the High Luminosity LHC (HL-LHC) [78, 79], which is expected to begin operations in the second half of 2026, to achieve an ultimate luminosity of 7.5×10^{34} cm^{-2} s^{-1}. The study is mostly focused on the jets originating from the hadronic decays of the massive particles such as top-quark or W/Z bosons with a significant Lorentz boost. The source of these particles can be new heavy vector bosons, with a wide-common names W' and Z', that are predicted by several BSM models (see e.g. [80–83]). The decay products of boosted massive particles are highly collimated, therefore the entire hadronic decay may be captured inside a single jet. The mass of such jets is one of the most powerful tools for distinguishing massive particle decays from the continuum multijet background. Therefore, a good reconstruction of the jet mass is critical in the search for new heavy resonances like W' and Z' bosons.

The effect of collimated decay products in hadronic W boson decays is illustrated in Figure 3.1. It shows the angular distance between the light quark and anti-quark from a $t \to bW$ decay as a function of the p_{T} of the W boson [84]. The figure illustrates how the separation between two quarks for $p_{\mathrm{T}}^{W} > 600$ GeV becomes comparable with a granularity of first layer of the ATLAS Hadronic Tile Calorimeter ($\Delta\eta \times \Delta\phi = 0.1 \times 0.1$). This makes it difficult to use the Tile Calorimeter to gain information on substructure of such boosted W-jets, where each subjet originates from a quark from the W decays.

In this study, the impact of the Tile Calorimeter granularity increase on the reconstruction of the jet mass and other jet properties variables is investigated. The Monte Carlo simulated events with a high-mass new physics particles (W' and Z' bosons) and Standard Model events with high-p_{T} jets in the final-state are used.

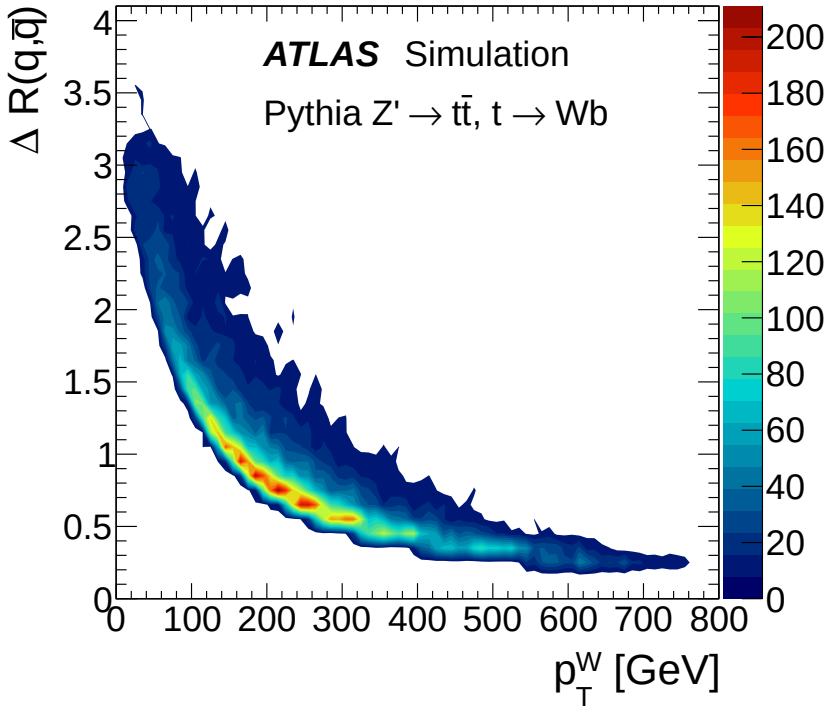

Figure 3.1.: The angular distance between the light quark and anti-quark from $t \to bW$ decays as a function of the p_{T} of the W boson. The distribution is at the generator level and do not include effects due to initial and final-state radiation, or the underlying event. Figure is taken from [84].

3.1. ATLAS hadronic Tile Calorimeter

The Tile Calorimeter [85] (TileCal) is the central section of the hadronic calorimeter of the ATLAS detector. The TileCal captures approximately 30% of jet energy and plays an important role in the reconstruction of hadrons, jets, hadronic decays of tau-leptons and missing transverse energy with a jet energy resolution $\sigma/E \sim 50\%/\sqrt{E} \oplus 3\%$. It covers the $|\eta| < 1.7$ region of the detector and is composed of one barrel and two extended barrels. It surrounds the Liquid Argon (LAr) barrel electromagnetic and endcap hadronic calorimeters, as illustrated in Figure 3.2. Azimuthally, the barrel and extended barrels are divided into 64 module each covering the azimuthal ϕ angle of $2\pi/64 \approx 0.1$. Each module is made of alternating layers of iron plates as the absorber and scintillating tiles as the active material. The scintillating tiles are placed radially and staggered in depth, as illustrated in Figure 3.3. Two sides of scintillating tiles are read out by wavelength shifting (WLS) fibres into two separate photomultipliers (PMTs). The PMTs are located in the outer radius iron structure that also houses the front-end electronics. Each module is longitudinally segmented in three layers: A, BC and D (A,B,D) with 1.5, 4.1 and 1.8 (1.5, 2.6, 3.3) interaction lengths thick, respectively, in the barrel (extended barrels). In each layer, the readout cells are built by grouping fibres into PMTs resulting a granularity of $\Delta\eta \times \Delta\phi = 0.1 \times 0.1$ ($\Delta\eta \times \Delta\phi = 0.2 \times 0.1$ in the last layer), as illustrated in Figure 3.4. In addition to the regular cells, gap/crack scintillators (so-called "E-cells") have been installed in front of the TileCal extended barrels and LAr electromagnetic end-cap calorimeters, to correct the energy lost in the inactive material that fills the gap/crack region.

3.2. Tile Calorimeter granularity upgrade setup

The Phase-II upgrade of the Tile Calorimeter includes full redesign of the front-end and back-end electronics [87]. The detector and optics are kept untouched from the current setup. In the dissertation work presented in this chapter, an additional granularity upgrade of the TileCal is considered by means of a modifications to readout of the TileCal cells, leaving aside questions of the technical implementation of this proposal. The technical details of the readout splitting implementation can be found in the TileCal Phase-II Initial Design Report [88].

The TileCal cell readout can be split to increase the effective granularity without modifying the detector and optics of the current setup. The splitting of the cell readout can only be achieved in η, since the increase of the readout granularity in ϕ is technically not feasible due to the fixed modularization of the TileCal barrel and extended barrels in the ϕ direction. Furthermore, at limited extra cost for the bandwidth, it is also possible to split the cells in the second TileCal layer, BC-layer, into the B and C layers, to increase the depth granularity.

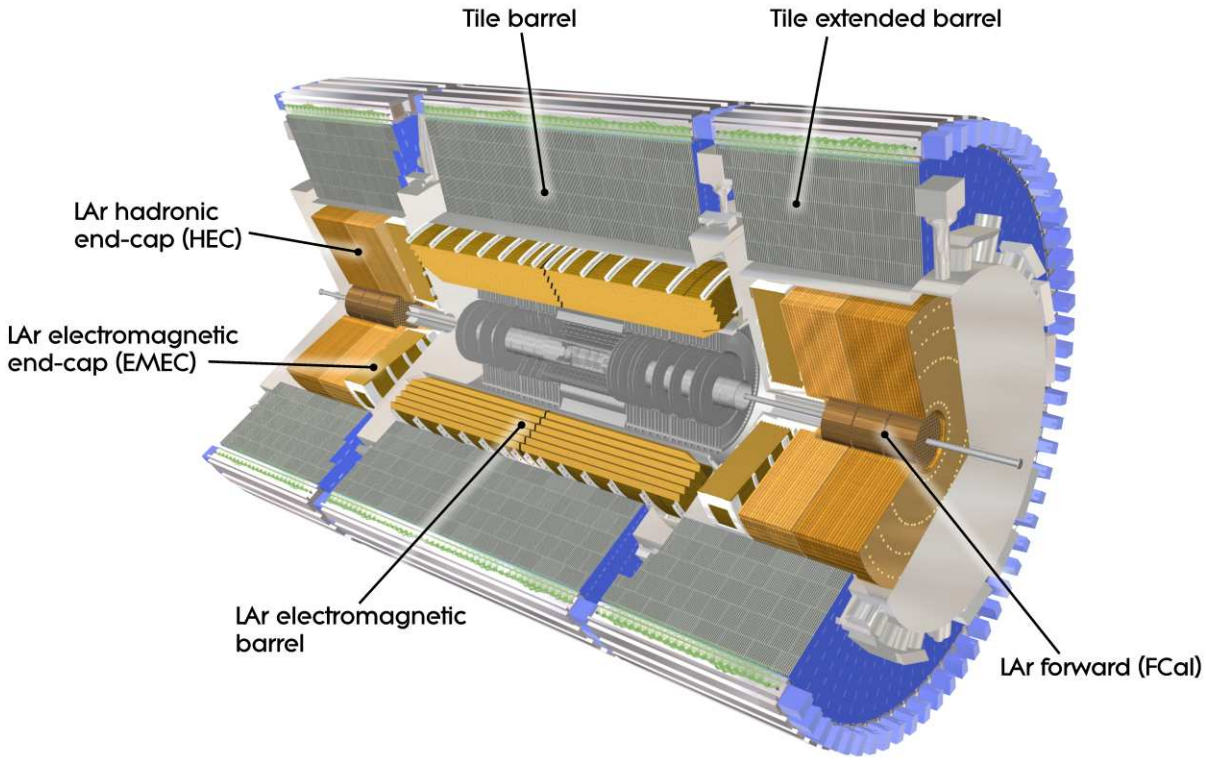

Figure 3.2.: A cut-away drawing of the ATLAS inner detector and calorimeters. Tile Calorimeter consists of one barrel and two extended barrel sections and surrounds the LAr barrel electromagnetic and endcap hadronic calorimeters. Figure is taken from [86].

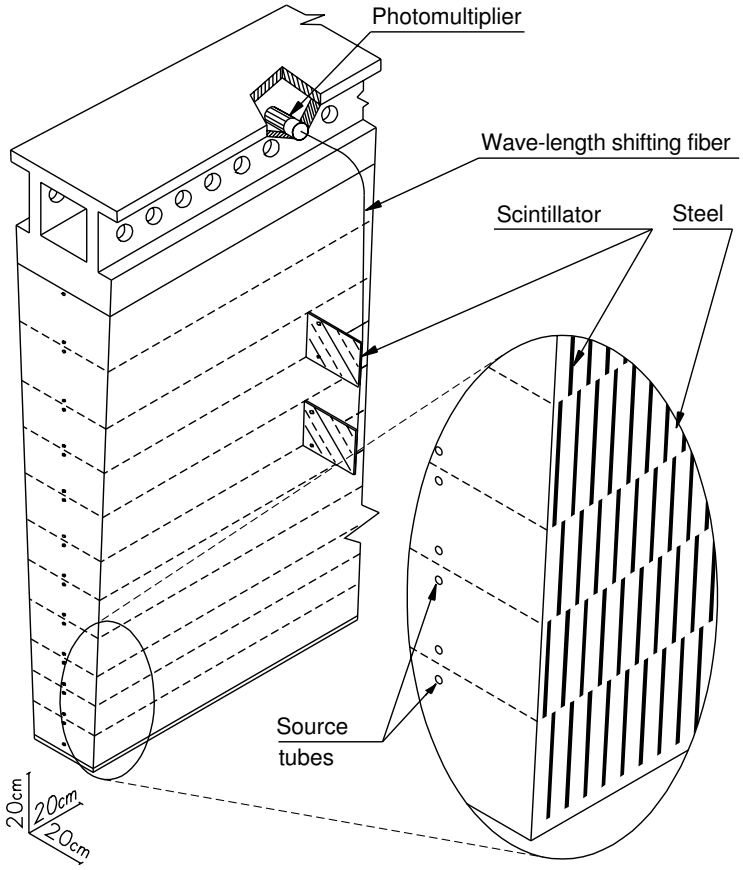

Figure 3.3.: Schematic showing how the mechanical assembly and the the optical readout of the tile calorimeter are integrated together. The various components of the optical readout, namely the tiles, the fibres and the photomultipliers, are shown. Figure is taken from [86].

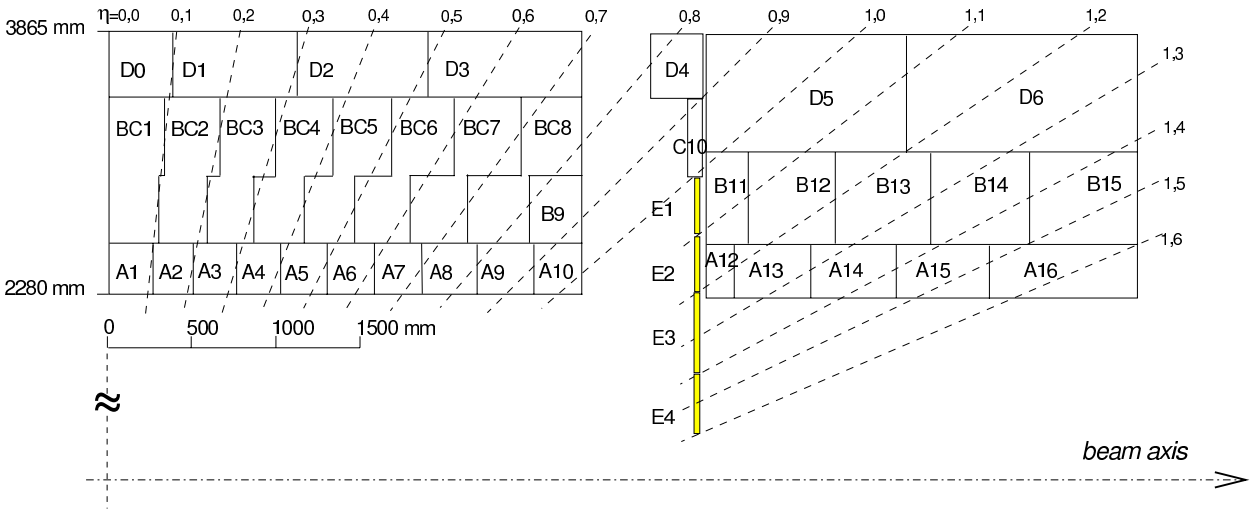

Figure 3.4.: Schematic showing the TileCal cell and scintillator structure, including the so-called "E-cells" (E1-E4) which are highlighted in yellow. Figure is taken from [86].

3.2.1. Simulation setup

Monte Carlo (MC) simulations provide the means to investigate the possible modification to the TileCal readout, that may lead to performance improvements in the reconstruction of high-p_{T} objects (jets, missing transverse energy and single particles). New ATHENA [89] simulation packages were designed for a modified TileCal geometry. This geometry has separate readouts for the B and C layers, and cells of the A-layer (except for the A12 cell) were divided into 4 independent cells in η (i.e. $\Delta\eta \times \Delta\phi = 0.025 \times 0.1$).

The Optimal Filtering [90, 91] (OF) algorithm is used to reconstruct the energy deposits in the TileCal cells, minimizing the contribution of the total noise, that is composed of the electronics and pileup noise contributions. The OF is based on a weighted sum of the digital samples, where the weights are computed for a particular total noise environment. The reconstruction of physics objects, such as jets and τ candidates uses the TileCal cells with energies greater than a certain threshold of the total noise. In the new geometry with increased granularity, the total noise can be different compared to the nominal scenario. The electronics noise constants are assumed to be the same as for the nominal geometry, while the pileup noise constants were calculated for the case of new geometry.

In the modified TileCal geometry, the reduced size of the A-layer cells should increase the number of reconstructed jet constituents, that are the topological clusters[1] (topo-cluster). This should lead to a better inference of the jet properties. According to the ATLAS topo-cluster formation algorithm [92], the location of cells providing the local maxima to split the cluster, is restricted to cells in the electromagnetic (EM) sampling layers, where calorimeters have very good spatial resolution. Since the segmentation of the A-layer in the new simulation setup with modified TileCal geometry is enhanced, the A-layer cells are also allowed to split a topo-cluster. A dedicated study of the jet performance in the nominal detector geometry with a modified splitting scheme was performed. The summary of this study is presented in Appendix A. The results of these investigations suggest that the jet reconstruction performance benefits from both the increased TileCal cell granularity and the modification of the topo-cluster splitting procedure.

3.3. Simulated samples

Samples of Monte Carlo simulated events are used for studying the high granularity TileCal performance. The Standard Model QCD multijets production and production of new physics W' and Z' bosons with the mass of 5 TeV provide a copious source of simulated jets, boosted W and Z-bosons, top quarks. These samples are simulated using Pythia 8 [93] with NNPDF23LO [43] PDF set and A14 [94] set of tuned parameters. The QCD-multijet sample is generated requiring the leading jet transverse momentum between 400 and 2500 GeV. All samples are generated

[1] The collection of topologically connected calorimeter cells that pass certain cell signal selection criteria. More details in Ref. [92]

at a center-of-mass energy of 14 TeV. The response of the detector to particles is modelled using the full HL-LHC upgraded ATLAS detector simulation [89, 95, 96] based on Geant4 [95]. Samples are produced with both, nominal and upgrade geometry of the ATLAS hadronic Tile Calorimeter. All simulated events are overlaid with additional pp interactions occurring in the same and neighbouring bunch crossings, that are simulated by the Pythia 8.186 soft QCD processes using the A2 set of tuned parameters [97] and the MSTW2008LO [98] PDF set. Assuming the mean number of interactions per bunch crossing $\mu = 200$.

3.4. Jet performance with the Tile Calorimeter granularity upgrade

The considered scenario of the Tile Calorimeter granularity upgrade is expected to improve the angular resolution in η of the reconstructed small-radius jets originating from a single particle as well as reconstruction of the substructure of the large radius jets originating from the hadronic decay of a massive particle.

3.4.1. Angular resolution of small-radius jets

The small-radius jets are reconstructed using the standard anti-k_t jet clustering algorithm [99] with distance parameter $R = 0.4$. The input to this algorithm are topo-clusters at the EM-scale. Jet four-momenta are computed by summing over the topo-clusters that constitute each jet, treating the energy of each cluster as a four-momentum with zero mass. No further calibration is applied. The QCD dijet events are used produced with Pythia 8. Jet angular resolution in η is studied by matching particle-level jets to reconstruction-level jets in the simulation. Only two highest p_{T} particle-level jets in the event are selected and matched to the closest in ΔR reconstruction-level jets. The angular resolution in η is obtained from a Gaussian fit to the distribution of the difference $\eta_{\text{reco}} - \eta_{\text{true}}$ of reconstruction-level and particle-level jet η. Fits are performed in a range of ± 1.5 standard deviations from the mean value. Figure 3.5 presents the comparison of the jet angular resolution in η as a function of particle-level jet (truth jet) p_{T} in the central region, $|\eta| < 0.8$, with the nominal and upgrade TileCal geometry. The higher granularity geometry of the TileCal provide about 20% better jet angular resolution in η in the full p_{T} range.

The jet angular distribution is often used in the searches of new phenomena, e.g. see the Ref. [100]. These searches would have a significant benefit from the TileCal granularity upgrade.

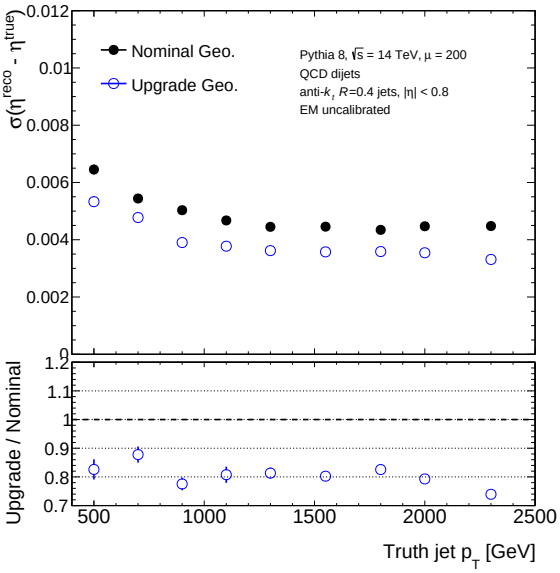

Figure 3.5.: Comparison of the small-radius jet angular resolution in η as a function particle-level jet p_{T} in the $|\eta| < 0.8$ region with the nominal (closed black circles) and upgrade (open blue circles) TileCal geometry.

3.4.2. Large-radius jet substructure performance

The high centre-of-mass energy of pp collisions at the LHC enables a production of heavy particles with a significant Lorentz boost. The decay products of these particles are highly collimated and can be reconstructed as a single jet in the case of the fully hadronic decays. High mass resonances W' and Z' decaying into W, Z bosons and $t\bar{t}$ could be such cases.

Large-radius jets are formed using FastJet [101] implementation of the anti-k_t jet algorithm with the distance parameter R = 1.0. Input for this algorithm are topo-clusters calibrated to the hadronic scale using the local cell signal weighting (LCW) method [92]. In order to reduce the impact from additional pp interactions in the event and from the underlying event, jets are trimmed [102] by re-clustering the constituents of the jet into subjets using the k_t algorithm with the distance parameter $R_{\mathrm{sub}} = 0.2$ and removing any of these subjets with the transverse momentum less than 5% of the original jet p_{T}. No further calibration is applied. They are matched to the particle-level jets within the cone of $\Delta R < 0.6$. In the simulated events of $W' \to WZ \to q\bar{q}q\bar{q}$ ($Z' \to t\bar{t} \to$ full hadronic) the large-radius jets are identified as W/Z-jets (top-jets) if there is a truth W/Z-boson (top quark) associated to their untrimmed jet area using the ghost association method [103].

The jet substructure variables are a set of jet properties that are designed to discover hard substructure within jets in order to distinguish massive boosted objects from gluons or light quarks. The jet substructure variables considered in this work are defined below:

- **Jet mass**

  The calorimeter-based jet mass (m^{calo}) is given by the difference between the squared sums

of the energy E_i and momentum $\vec{p}_i$ ($|\vec{p}_i| = E_i$) of the constituents:

$$m^{\text{calo}} = \sqrt{\left(\sum_i E_i\right)^2 - \left(\sum_i \vec{p}_i\right)^2} \tag{3.1}$$

- **N-subjettiness**

  The "N-subjettiness" [104, 105] jet shape variables describe to what degree the substructure of a given jet J is compatible with being composed of N or fewer subjets. The 0-, 1- and 2-subjettiness are defined as:

$$\tau_0 = \sum_{i \in J} p_{\text{T}i} \Delta R\,, \tag{3.2a}$$

$$\tau_1 = \frac{1}{\tau_0} \sum_{i \in J} p_{\text{T}i} \Delta R_{a_1,i}\,, \tag{3.2b}$$

$$\tau_2 = \frac{1}{\tau_0} \sum_{i \in J} p_{\text{T}i} \min(\Delta R_{a_1,i}, \Delta R_{a_2,i}) \tag{3.2c}$$

  where the distance ΔR denotes the distance between the constituent i and the jet axis. The calculation of τ_N requires the definition of N axes, such that the distance between each constituent and any of these axes is $R_{aN,i}$. The ratios of the N-subjettiness functions can be used to generate the dimensionless variables:

$$\tau_{21} = \frac{\tau_2}{\tau_1}, \tag{3.3a}$$

$$\tau_{32} = \frac{\tau_3}{\tau_2}. \tag{3.3b}$$

  The ratio τ_{21} is particularly useful in identifying two-body structures within jets, while τ_{32} in identifying three-body structures.

- **Energy correlation ratios**

  The 1-point, 2-point and 3-point energy correlation functions for a jet J are given by:

$$E_{\text{CF}1} = \sum_{i \in J} p_{\text{T}i}\,, \tag{3.4a}$$

$$E_{\text{CF}2} = \sum_{i<j \in J} p_{\text{T}i} p_{\text{T}j} \Delta R_{ij}\,, \tag{3.4b}$$

$$E_{CF3}(\beta) = \sum_{i<j<k\in J} p_{Ti}p_{Tj}p_{Tk}\Delta R_{ij}\Delta R_{ik}\Delta R_{jk}\,. \tag{3.4c}$$

For the energy correlation functions we define the dimensionless observables, that can be used to determine if the jet J has 2 or 3 sub-jets:

$$e_2 = \frac{E_{CF2}}{(E_{CF1})^2}\,, \tag{3.5a}$$

$$e_3 = \frac{E_{CF3}}{(E_{CF1})^3}\,. \tag{3.5b}$$

These ratios of the energy correlation functions are used in the definitions of the dimensionless variable D_2 [106], that can be useful for identifying two-body structures within jets:

$$D_2 = \frac{e_3}{(e_2)^3}. \tag{3.6}$$

QCD jet mass performance

In the ATLAS, simulated QCD dijet events are used to derive the calibration for the large-radius jet energy and mass scales [107]. The Tile Calorimeter granularity upgrade is not expected to change the jet energy and mass scales since the granularity increase does not change the amount of jet energy measured in the TileCal. Therefore, calibration factors for the jet energy and mass scales would not be significantly different in different TileCal geometries. Therefore, difference between nominal and upgrade TileCal geometry in the fractional jet mass resolution would be similar for uncalibrated and calibrated jets. In this study only uncalibrated jets are used.

The calorimeter-based jet mass scale is defined as the average of jet mass response $R = m^{\text{calo}}/m^{\text{truth}}$, where m^{truth} is the particle-level jet (truth jet) mass. The fractional resolution of the calorimeter-based jet mass is defined as the half of the 68% interquantile range divided by the median of the jet mass response distribution. It is an outlier insensitive measure of the resolution.

The calorimeter-based jet mass scale for the large-radius QCD jets in the very central region, $|\eta| < 0.4$, and in the $0.4 < |\eta| < 0.8$ region as a function of the particle-level jet mass is presented in Figures 3.6 and 3.7, respectively. As expected, performance is similar for both TileCal geometries. The average jet mass response and fractional jet mass resolution as a function of the particle-level jet p_{T} is shown in Figures 3.8 and 3.9. The jet mass response is very similar for both geometries, but an improvement of 10–20% in the jet mass fractional resolution is clearly visible.

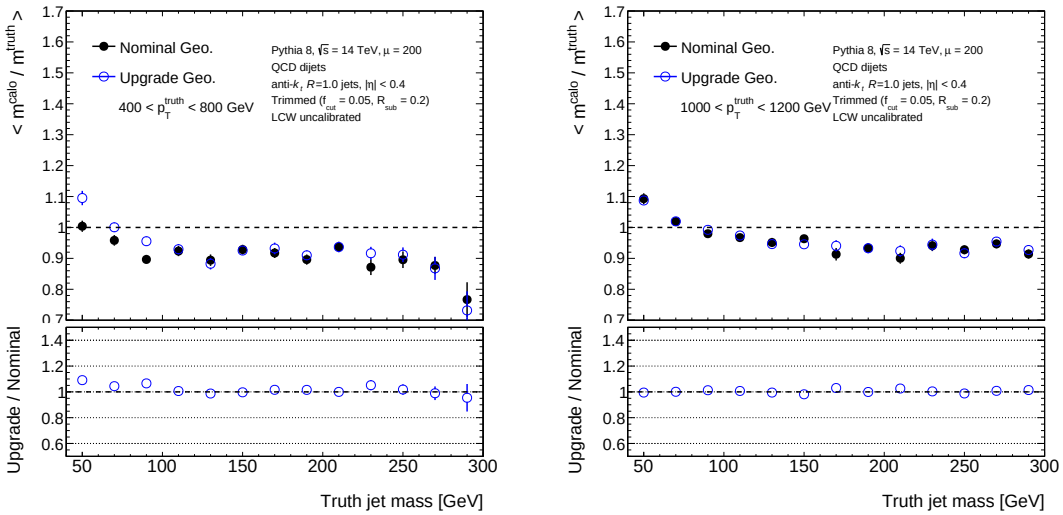

(a)

(b)

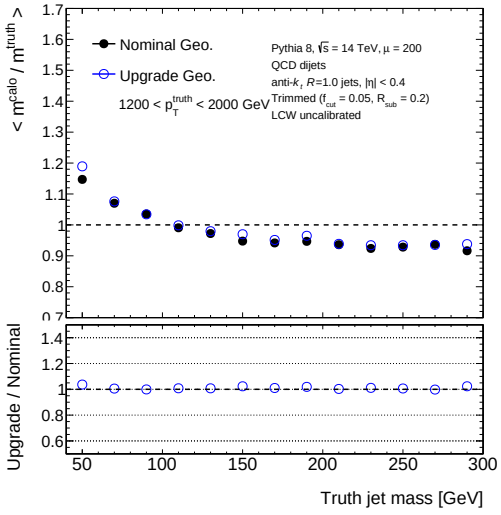

(c)

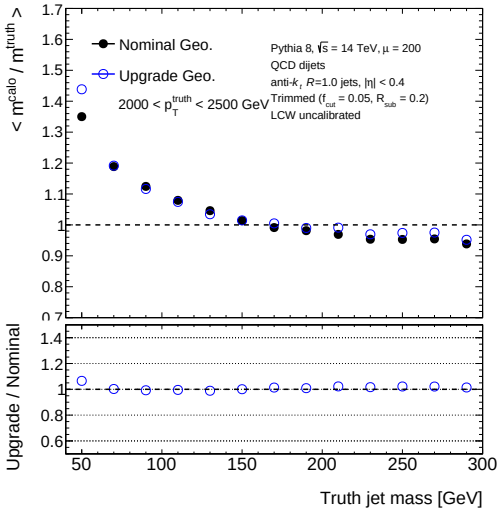

(d)

Figure 3.6.: The calorimeter-based jet mass scale as a function of the truth jet mass for the QCD dijets in the nominal (black closed circles) and upgrade (blue open circles) TileCal geometry. Results are for the truth jet p_{T} ranges of a) [400,800] GeV, b) [1000, 1200] GeV, c) [1200, 2000] GeV and d) [2000, 2500] GeV in the $|\eta| < 0.4$ region.

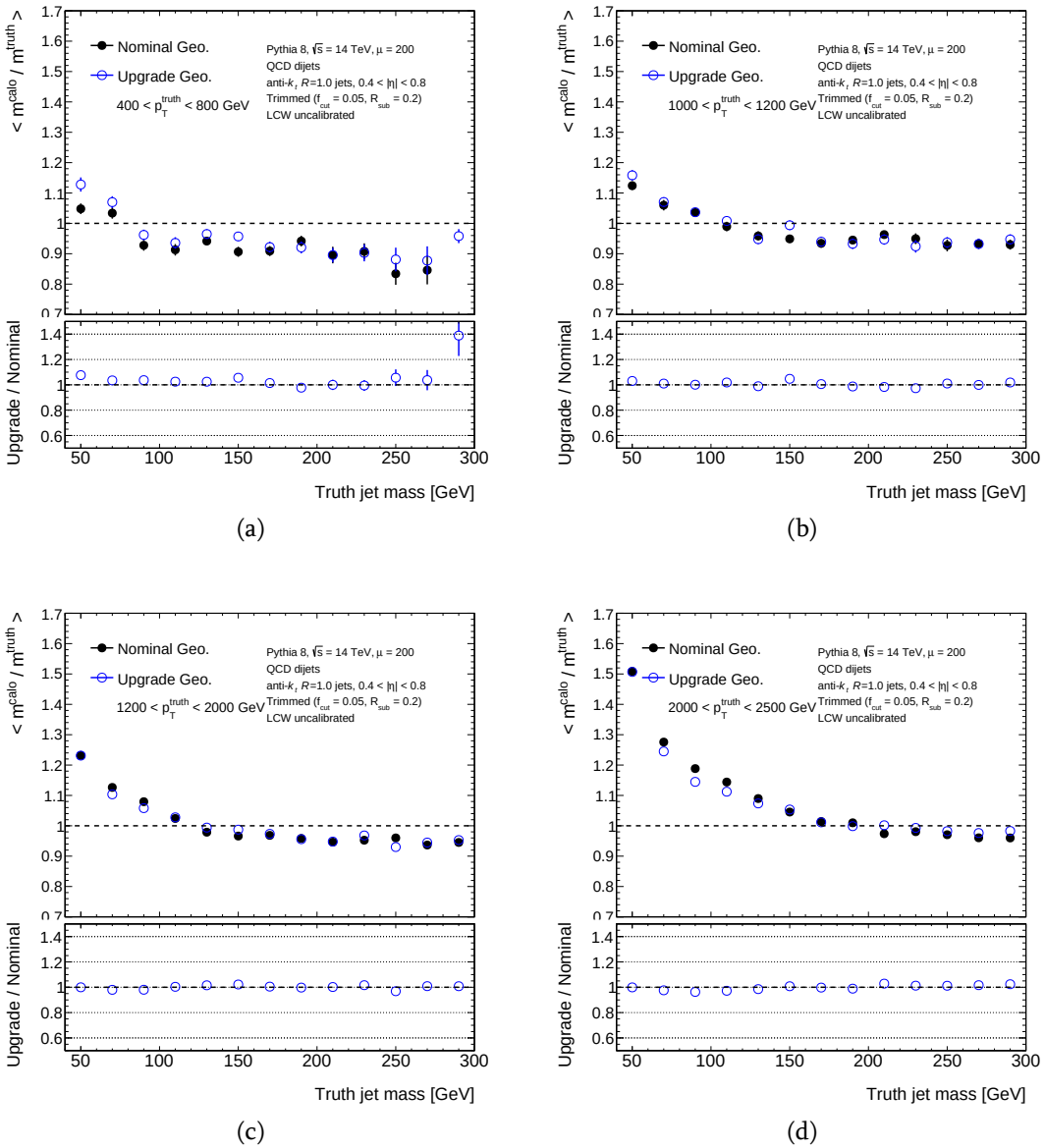

Figure 3.7.: The calorimeter-based jet mass scale as a function of the truth jet mass for the QCD dijets in the nominal (black closed circles) and upgrade (blue open circles) TileCal geometry. Results are for the truth jet p_{T} ranges of a) [400,800] GeV, b) [1000, 1200] GeV, c) [1200, 2000] GeV and d) [2000, 2500] GeV in the $0.4 < |\eta| < 0.8$ region.

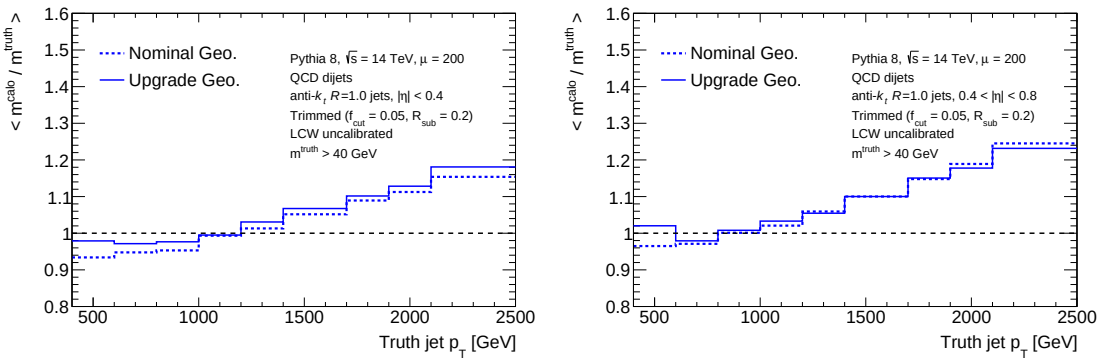

(a) (b)

Figure 3.8.: The calorimeter-based jet mass scale as a function of the truth jet transverse momentum for the QCD dijets in the nominal (dashed line) and upgrade (solid line) geometry. Results are obtained in the a) $|\eta| < 0.4$ and b) $0.4 < |\eta| < 0.8$ regions.

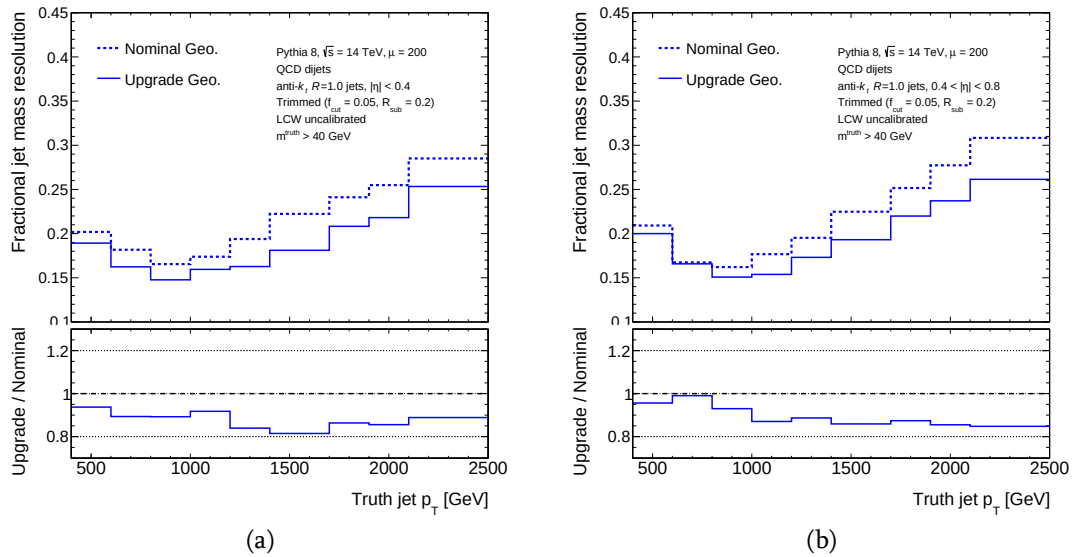

(a) (b)

Figure 3.9.: The fractional calorimeter-based jet mass resolution as a function of the truth jet transverse momentum for the QCD dijets in the nominal (dashed line) and upgrade (solid line) geometry. Results are obtained in the a) $|\eta| < 0.4$ and b) $0.4 < |\eta| < 0.8$ regions. The half of the 68% interquantile range divided by the median of the jet mass response is used as an outlier insensitive measure of the resolution.

W/Z-jet and top-jet performance

Simulated samples of W' ($\rightarrow WZ \rightarrow q\bar{q}q\bar{q}$) and Z' ($\rightarrow t\bar{t} \rightarrow$ full hadronic) bosons are used to study the W/Z-jet and top-jet performance in the high granularity TileCal geometry.

The W/Z-jets and top-jets have 2 and 3 subjets, respectively, therefore the high number of reconstructed large-radius jet constituents is important to determine the jet substructure and have a good inference about its properties. The distribution of the number of jet constituents in bins of particle-level jet p_{T} for W/Z-jets and top-jets is presented in Figures 3.10 and 3.11, respectively. This distribution gets broader and is shifted towards higher number of constituents in the increased TileCal granularity setup. The average number of jet constituents dependence on the particle-level jet p_{T} for W/Z-jets and top-jets is shown in Figures 3.12. It decreases with increasing p_{T} in both geometries. Nevertheless, one resolves 30–50% more jet constituents in the increased TileCal granularity setup.

The calorimeter-based jet mass response distribution of large-radius W/Z-jets and top-jets in bins of particle-level jet p_{T} is presented in Figures 3.13 and 3.14 for both TileCal geometries. The jet mass scale as function of particle-level jet p_{T} is similar for both geometry options, while the fractional jet mass resolution is around 20% better for the TileCal with increased granularity, as shown in Figures 3.15 and 3.16.

The distributions of some of the substructure variables for W/Z-jets and top-jets in both TileCal geometries are shown in Figure 3.17. Since this variables are used to discriminate between QCD-jets and jets from boosted hadronically decaying heavy particles, the comparison of ROC curves for nominal and higher-granularity TileCal geometries are presented in Figure 3.18. Clearly, the high TileCal granularity setup provides much better discrimination compared to the nominal geometry.

3.5. Conclusions and perspectives

The Phase-II upgrade of the Tile Calorimeter includes full redesign of front-end and back-end electronics, leaving the detector and optics intact. However, the signals from individual scintillating tiles are grouped in the readout to form the TileCal cells, leaving a technical possibility to increase the effective granularity of the detector without modifying significantly the mechanics and optics of the current setup. The increase of the granularity as a function of the azimuthal angle is not possible, due to the fixed partitioning of the TileCal in 64 identical modules in the ϕ direction. Nevertheless, re-grouping of the read-out of individual tiles in each TileCal sampling can provide an increased cell granularity in the η-direction.

In this study, developed in the dissertation work, the jet reconstruction performance improvements with the possible modification of TileCal readout is investigated. The study is done using full Monte Carlo simulations of the ATLAS detector using events with high-p_{T} jets. The considered modification of the TileCal readout includes separate readouts for the B and C layers,

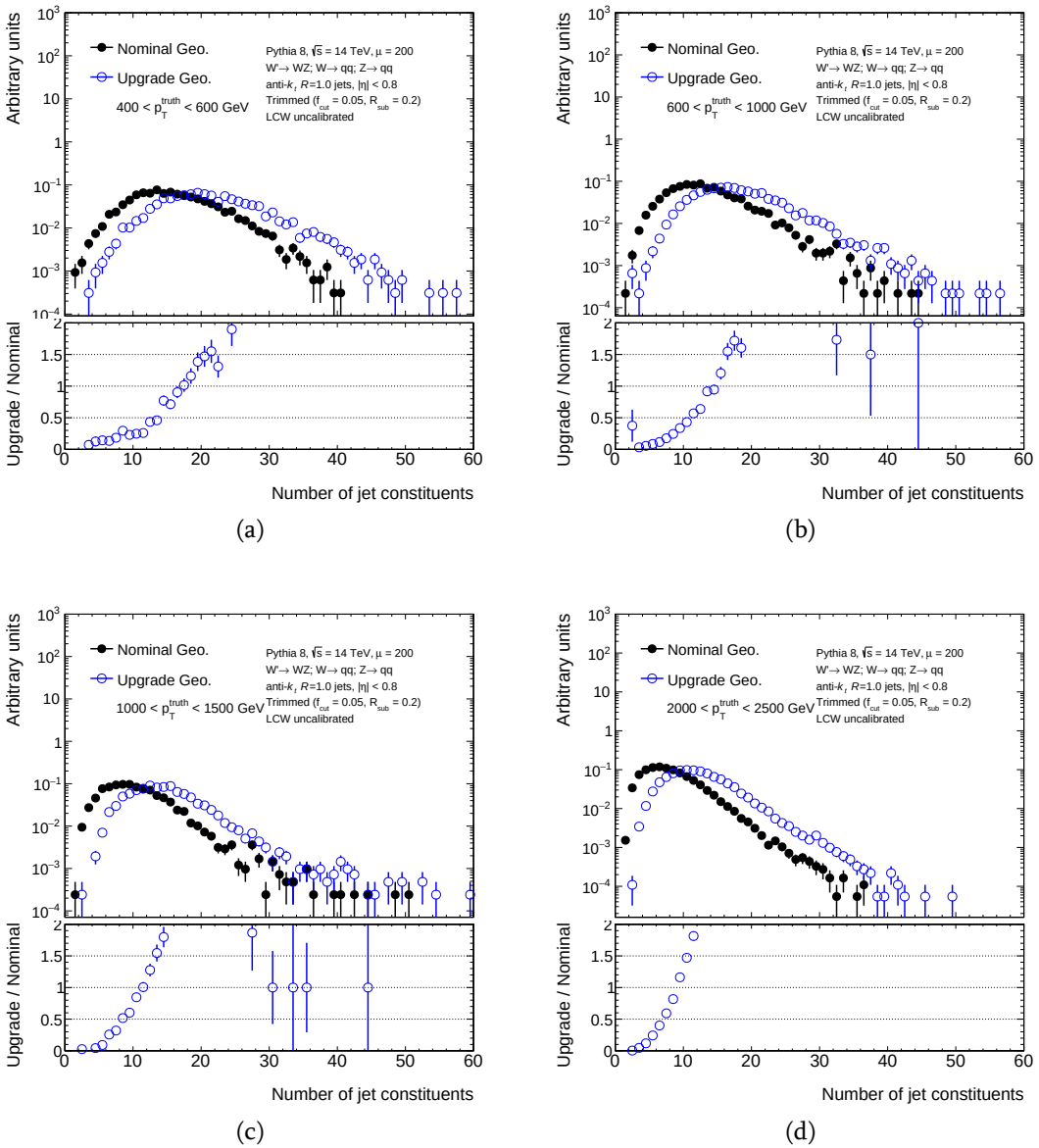

Figure 3.10.: Distribution of the number of jet constituents for the W/Z-jets in the nominal (black closed circles) and upgrade TileCal geometry (blue open circles). Results are obtained for the truth p_{T} ranges of a) [400,600] GeV, b) [600, 1000] GeV, c) [1000, 1500] GeV and d) [2000, 2500] GeV in the $|\eta| < 0.8$ region.

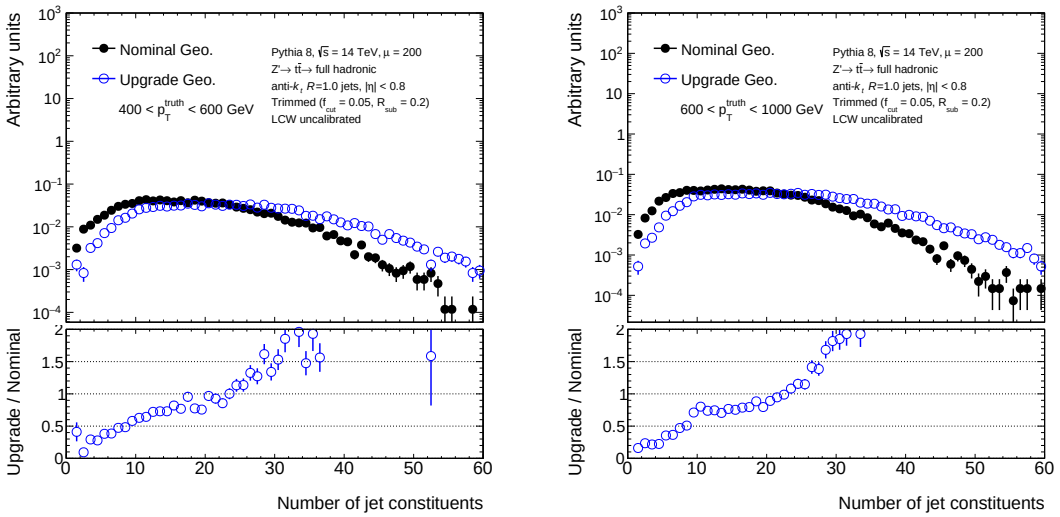

Figure 3.11.: Distribution of the number of jet constituents for the top-jets in the nominal (black closed circles) and upgrade (blue open circles) TileCal geometry. Results are obtained for the truth p_{T} ranges of a) [400,600] GeV, b) [600, 1000] GeV, c) [1000, 1500] GeV and d) [2000, 2500] GeV in the $|\eta| < 0.8$ region.

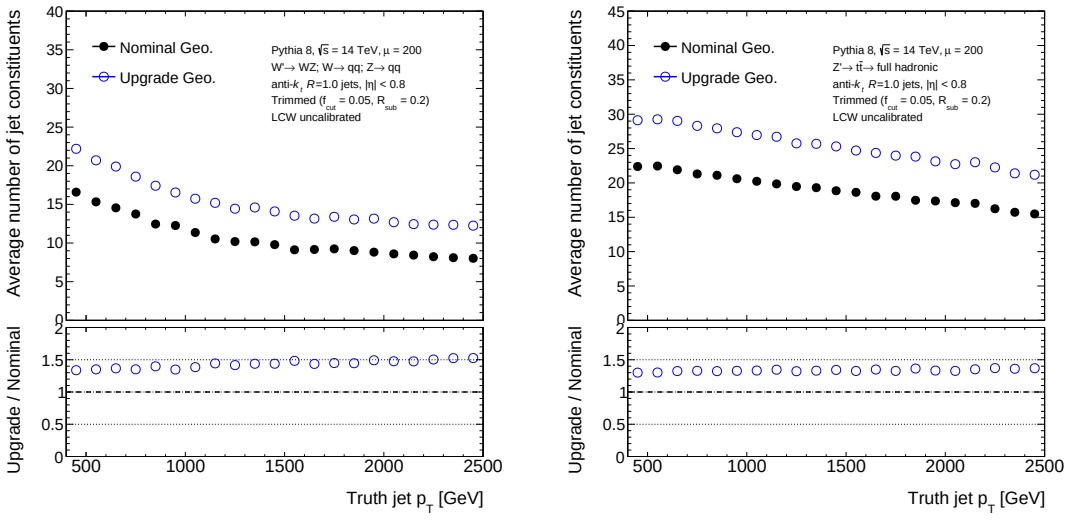

(a) (b)

Figure 3.12.: Average number of jet constituents as a function of the truth jet p_{T} for the a) W/Z-jets and b) top-jets in the nominal (black closed circles) and upgrade TileCal geometry (blue open circles). Results are obtained in the $|\eta| < 0.8$ region.

and cells of the A-layer divided into 4 independent cells in η (i.e. $\Delta\eta \times \Delta\phi = 0.025 \times 0.1$). The technical feasibility of this modification is not addressed in this study. In addition, modified topo-cluster splitting scheme is considered which is more optimized for the high granularity TileCal geometry setup.

The combination of both enhanced cell granularity and modified cluster splitting scheme leads to combined improvements of the small-radius jet angular resolution in η and large-radius jet calorimeter-based mass resolution of approximately 20%. In addition, a better measurements of the jet substructure variables allow for superior discrimination between QCD-jets and jets from boosted hadronically decaying heavy particles. The modified topo-cluster splitting scheme has non-negligible contributions to the improved performance, but an exact determination of the relative contributions of each of these additions is beyond the scope of this study. The results demonstrate that modified TileCal readout increasing the granularity could lead to significant improvements in the jet reconstruction performance that is important in the searches for new phenomena.

The considered Tile Calorimeter granularity upgrade is not a part of the ATLAS Phase-II upgrade plan, nevertheless it possibly turn into consideration and realization for the future collider at CERN [108].

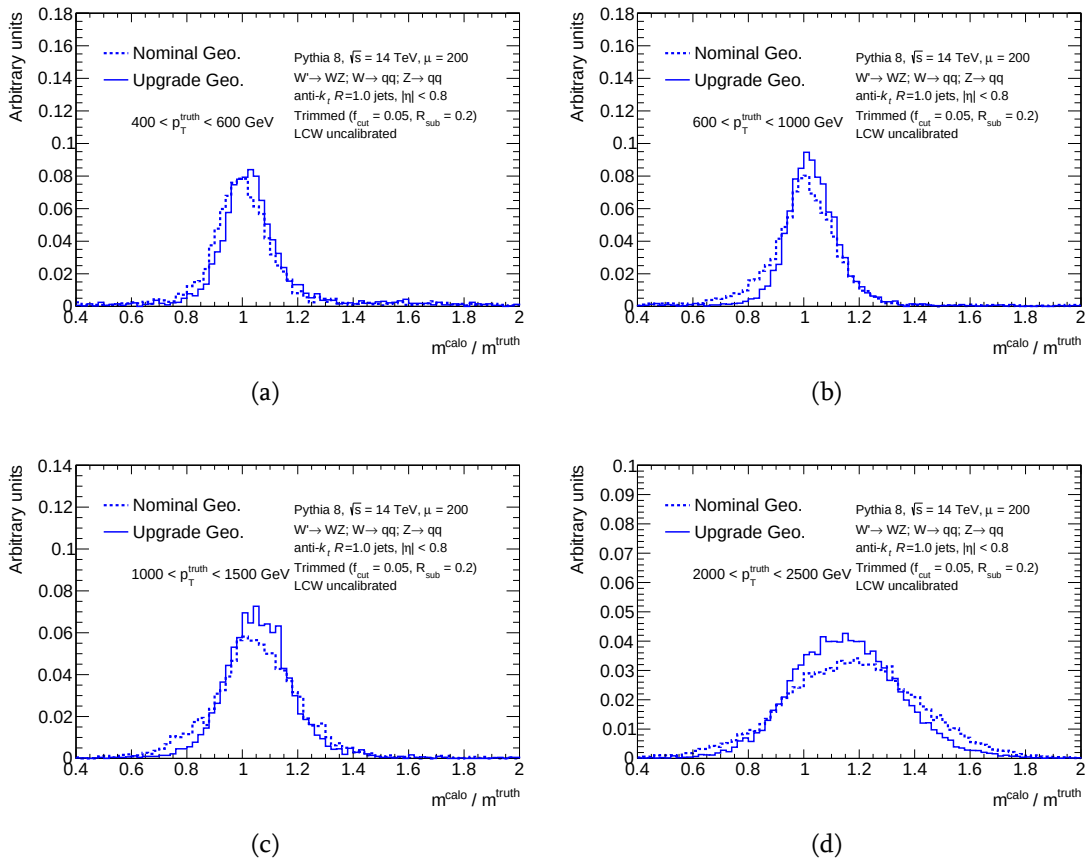

Figure 3.13.: Distributions of the calorimeter jet mass response for the W/Z-jets in the nominal (dashed line) and upgrade (solid line) TileCal geometry. Results are obtained for the truth p_{T} ranges of a) [400,600] GeV, b) [600, 1000] GeV, c) [1000, 1500] GeV and d) [2000, 2500] GeV in the $|\eta| < 0.8$ region.

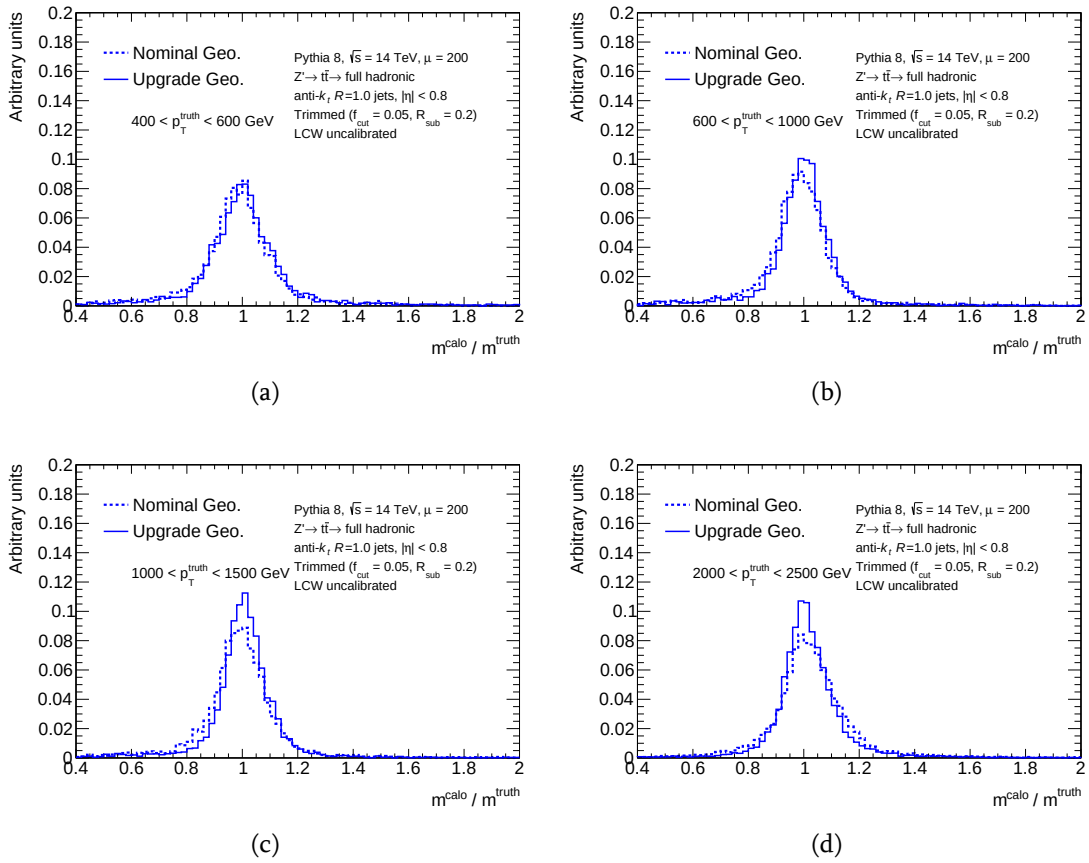

Figure 3.14.: Distributions of the calorimeter jet mass response for the top-jets in the nominal (dashed line) and upgrade (solid line) TileCal geometry. Results are obtained for the truth p_{T} ranges of a) [400,600] GeV, b) [600, 1000] GeV, c) [1000, 1500] GeV and d) [2000, 2500] GeV in the $|\eta| < 0.8$ region.

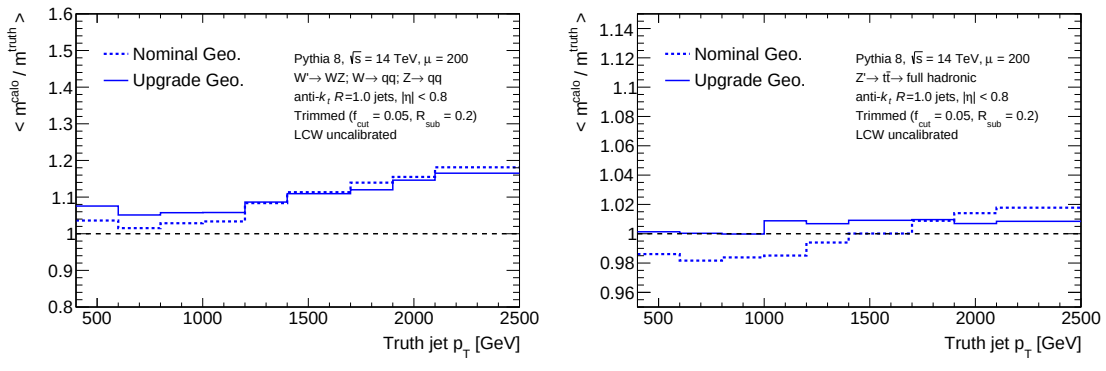

Figure 3.15.: The average calorimeter jet mass response as a function of the truth jet transverse momentum for the a) W/Z-jets and b) top-quark jets in the nominal (dashed line) and upgrade (solid line) geometry. Results are obtained in the $|\eta| < 0.8$ region.

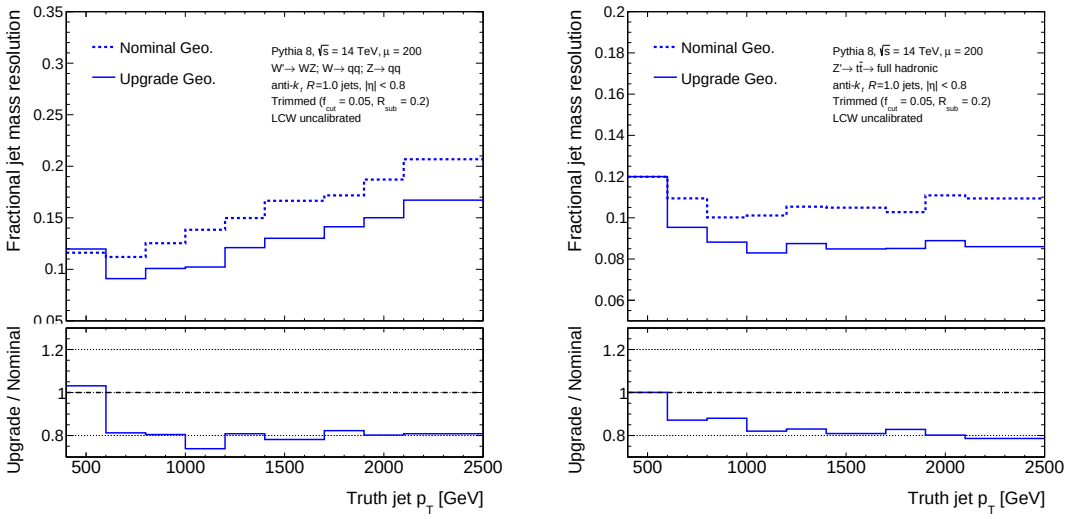

(a) (b)

Figure 3.16.: The fractional calorimeter-based jet mass resolution as a function of the truth jet transverse momentum for the a) W/Z-jets and b) top-quark jets in the nominal (dashed line) and upgrade (solid line) TileCal geometry. Results are obtained in the $|\eta| < 0.8$ region. The half of the 68% interquantile range divided by the median of the jet mass response is used as an outlier insensitive measure of the resolution.

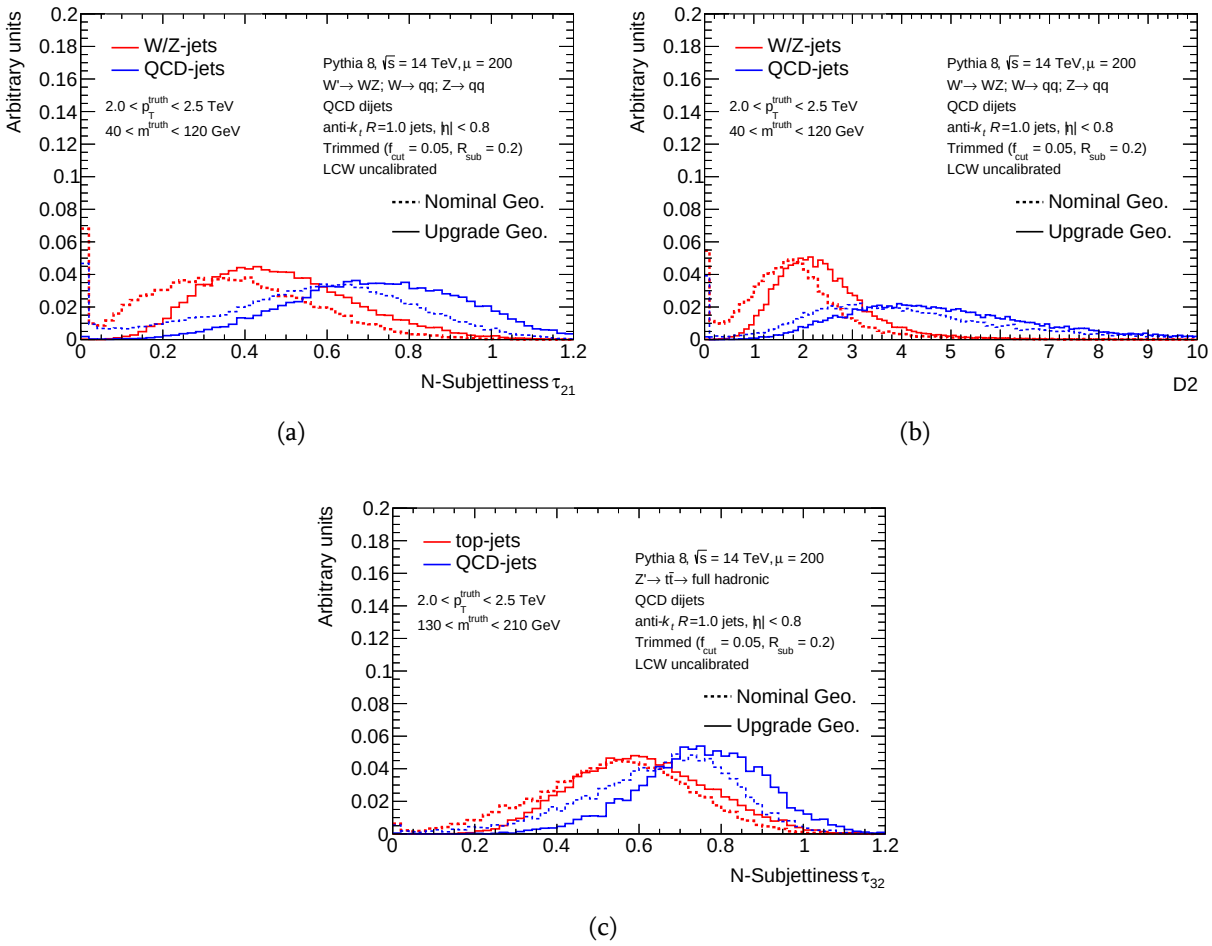

Figure 3.17.: The jet substructure variables a) τ_{21}, b) D_2 and c) τ_{32} for the simulated W/Z-jets (a,b) and top-jets (c) is compared to the QCD dijets in the nominal (dashed line) and upgrade (solid line) TileCal geometry. Results are obtained for the truth p_{T} range of [2000, 2500] GeV in the $|\eta| < 0.8$ region with $40 < m^{\mathrm{truth}} < 120$ GeV (a,b) and $130 < m^{\mathrm{truth}} < 210$ GeV (c).

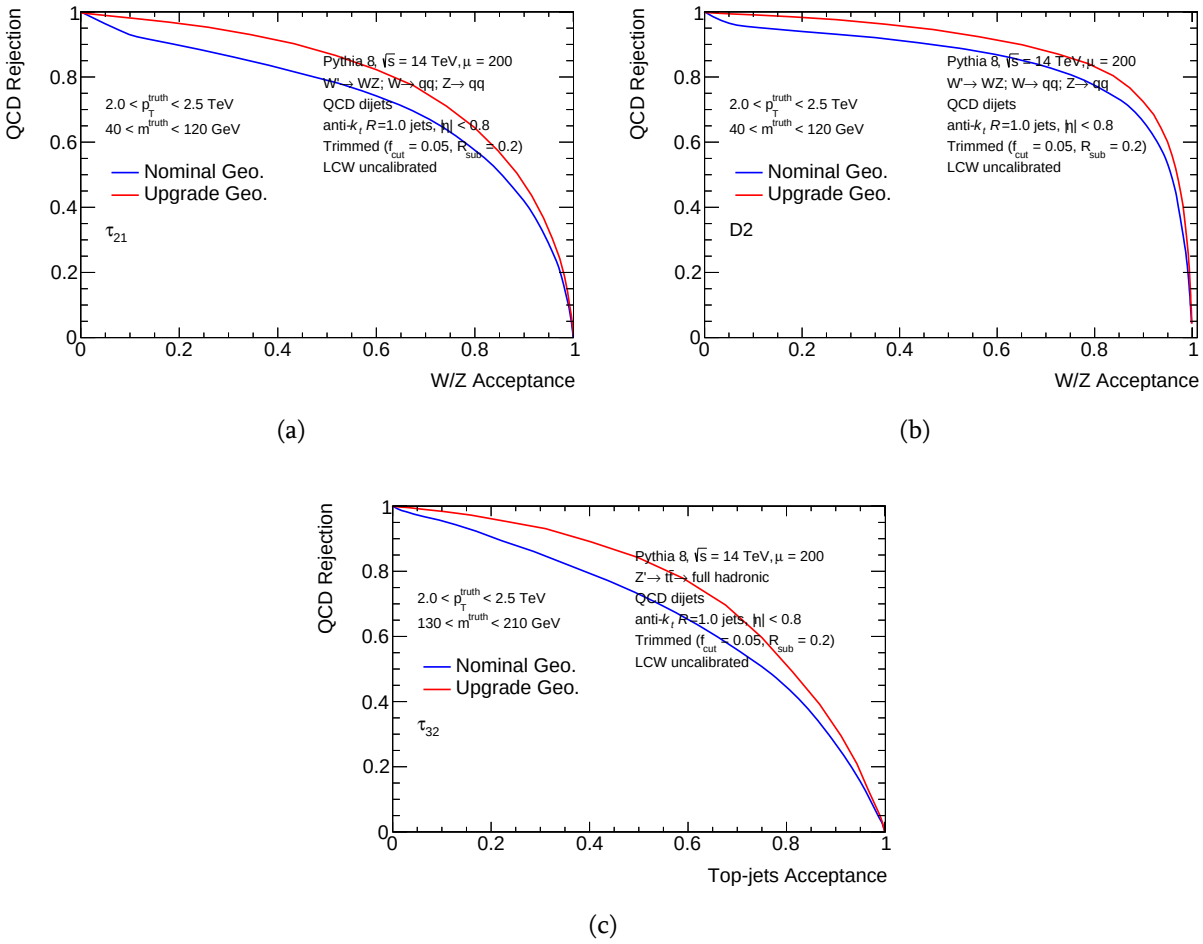

(a) (b)

(c)

Figure 3.18.: The ROC curves of the jet substructure variables a) τ_{21}, b) D_2 and c) τ_{32} for the simulated W/Z-jets (a,b) and top-jets (c) in the nominal (blue line) and upgrade (red line) TileCal geometry. Results are obtained for the truth p_{T} range of [2000, 2500] GeV in the $|\eta| < 0.8$ region with $40 < m^{\mathrm{truth}} < 120$ GeV (a,b) and $130 < m^{\mathrm{truth}} < 210$ GeV (c).

Chapter 4.

Electron energy calibration improvements in the crack region

In the LHC Run 1, the initial calibration procedure for the electron and photon energy measured with the ATLAS detector, was based on the calibration hit method [109, 110]. Later, this method was superseded with the method based on a multivariate analysis (MVA) techniques [111]. The performance of the MVA calibration on electrons in LHC Run 1, is presented in Figure 4.1, more details can be found in Ref. [111]. This figure shows the energy resolution for electrons as a function of pseudorapidity. The bins from $|\eta| = 1.37$ to $|\eta| = 1.52$ are not shown, where the initial calibration procedure was kept. This region is called a *crack* region, which covers a high amount of material (ranging from 5 to almost 10 radiation lengths (X_0)) traversed by a particle in front of the first active calorimeter layer, as it can be seen in Figure 4.2. Therefore, the electron and photon energy resolution is degraded significantly in the crack region. In the most of physics analysis, which have large statistics, the electrons from that region ($1.37 < |\eta| < 1.52$) are excluded, though the crack electrons are often used by analysis studying a rare processes (e.g. Higgs particle properties measurement analysis in 4 lepton decay channel [112]).

In this chapter, the electron energy calibration improvement in the crack region is investigated, using of the Tile Calorimeter E4 crack scintillators in the MVA calibration. Also, possible extension of crack scintillators up to $|\eta| \sim 1.75$ with E4′ counters is considered, to improve electron energy calibration performance in the region around $|\eta| = 1.7$, that is significantly affected with the high amount of dead material.

4.1. The ATLAS Electromagnetic Calorimeter

The ATLAS Electromagnetic Calorimeter [113, 114] (EM) is made of accordion-shaped electrodes and lead absorbers in liquid argon (LAr) as the active material. It covers the pseudorapidity range of $|\eta| < 3.2$, and contains a barrel part (EMB) covering $|\eta| < 1.475$, and two

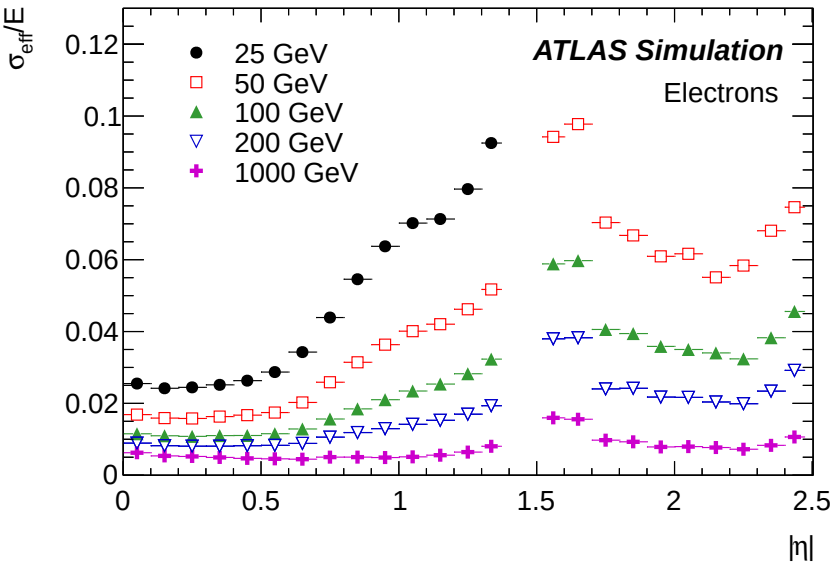

Figure 4.1.: Relative effective resolution σ_{eff}/E for electrons as a function of $|\eta|$ for different energies. The points at $E = 25$ GeV are shown only for $|\eta| < 1.37$, where they correspond to $E_{\text{T}} > 10$ GeV. Figure is taken from [111].

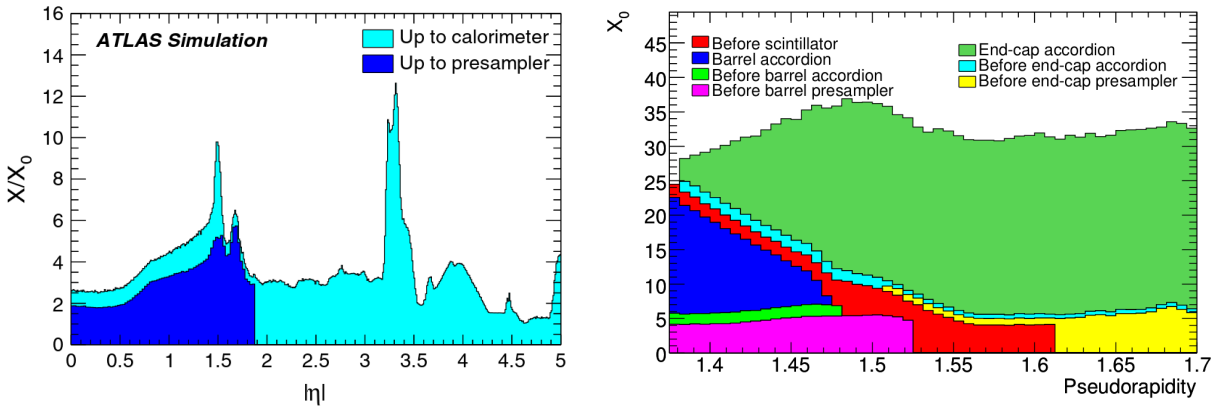

(a) (b)

Figure 4.2.: Cumulative amounts of material, in units of radiation length X_0 and as a function of $|\eta|$, in front of and in the electromagnetic calorimeters. Total amount of material in front of the presampler layer and in front of the accordion itself separately over the full η-coverage (a) and the details of the crack region between the barrel and end-cap cryostats (b) in terms of material in front of the active layers (including the crack scintillator) and of the total thickness of the active calorimeter. Figures are taken from [111] and [67].

endcaps (EMEC), that cover $1.375 < |\eta| < 3.2$ and are divided into two parts at $|\eta| = 2.5$. For $|\eta| < 1.8$, a presampler (PS) with an active LAr layer is installed directly in front of the EM calorimeters, which provides a measurement of the energy lost by a particle before reaching the calorimeter.

The barrel part and endcapes of the EM calorimeter are segmented transversally and divided in three samplings (two samplings in $2.5 < |\eta| < 3.2$) in depth. The granularity in the presampler and in each of the EM calorimeter samplings is summarized in Table 4.1 and shown in Figure 4.3.

The goal resolution for the electromagnetic calorimeter is $\sigma_E/E = 10\%/\sqrt{E} \oplus 0.7\%$.

η range	0 to 1.4	1.4 to 1.8	1.8 to 2.0	2.0 to 2.5	2.5 to 3.2
Presampler	0.025×0.1	0.025×0.1			
Sampling 1	0.003×0.1	0.003×0.1	0.004×0.1	0.006×0.1	0.1×0.1
Sampling 2	0.025×0.025	0.025×0.025	0.025×0.025	0.025×0.025	0.1×0.1
Sampling 3	0.050×0.025	0.050×0.025	0.050×0.025	0.050×0.025	

Table 4.1.: Granularity of the Presempler and EM calorimeter samplings (pseudorapidity, azimuth). Taken from [113].

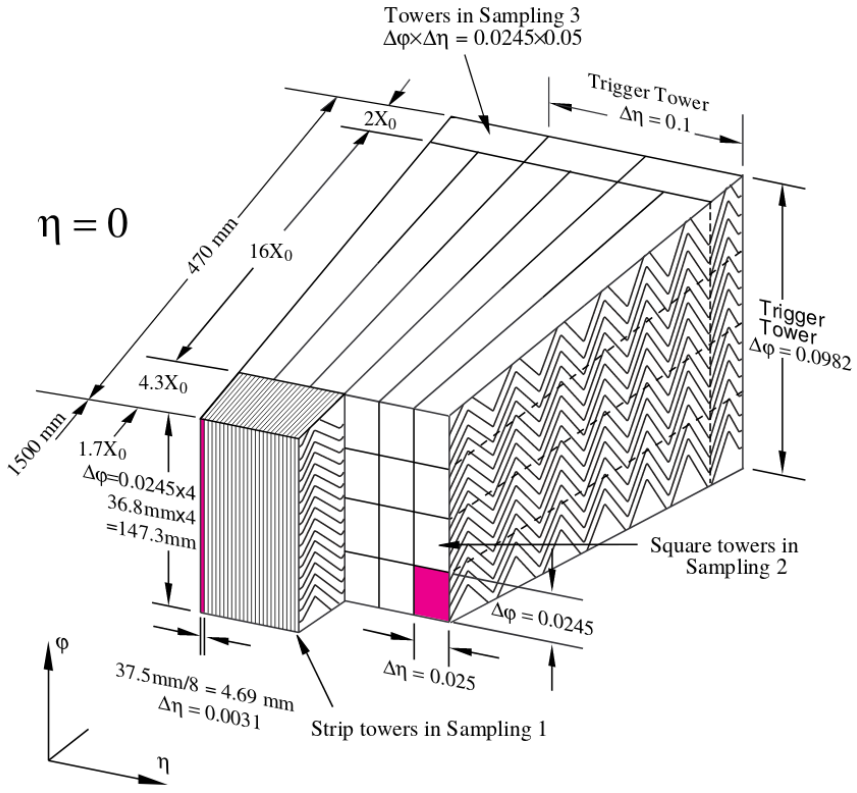

Figure 4.3.: Electromagnetic Calorimeter accordion structure. Figure is taken from [113].

4.2. E4 scintillators

E4 scintillators are the part of the Intermediate Tile Calorimeter (ITC) [85], which is a plug detector part of the TileCal. The ITC is located in the gap region, in between the long and the extended barrels of TileCal. There are six different groups of cells that belong to the ITC. There are two standard tile cell groups of the ITC named D4 and C10, and four groups of gap/crack cells with active material consisting of only one scintillator named E1, E2, E3, and E4, as shown in Figure 3.4. Each of these four groups in gap/crack cells has up to 64 instances of the same scintillator distribution covering the entire azimuth region (each module covers $\Delta\phi \approx 0.1$ rad) on each extended barrel. The differences between each of these scintillators are the geometries, pseudorapidity position, and size as described in Table 4.2. These gap/crack cells are read-out on one ϕ side of a module by wave-length shifting fibres into one photomultiplier (PMT). The ITC was designed to correct the energy lost in the passive material that fills the gap region.

The TileCal E4 crack scintillators are situated between Barrel (EMB) and Endcap (EMEC) of electromagnetic (EM) calorimeter. Electrons/photons in the crack region deposit energy in EMB, EMEC and in E4 scintillators as well. Such a position of the E4 scintillators gives a possibility to use it in the improvement of the electron and photon performance in the eta region $1.4 < |\eta| < 1.6$.

Scintillator type	η position	Thickness [mm]	Amount [X_0]
E1	1.0 - 1.1	12	0.04
E2	1.1 - 1.2	12	0.04
E3	1.2 - 1.4	6	0.026
E4	1.4 - 1.6	6	0.026

Table 4.2.: Gap/crack scintillators eta-positions, thickness and amount, in units of radiation length X_0, that includes two aluminum covers with the thickness of 0.5 mm for all the counters.

4.3. Sample and selection

The sample used in this analysis contains fully simulated single particles ($\sim$1 million electrons with $1.4 < |\eta| < 1.6$) with the wide range of E_{T} as it is presented in Figure 4.4.

The following selection criteria are applied on the used samples:

- Transverse energy in the EM calorimeter accordion $(E_{\mathrm{T}}^{\mathrm{acc}}) < 1$ TeV, $1.4 < |\eta_{\mathrm{cluster}}| < 1.6$;
- Matching between the generated particle and the reconstructed object (truth matching);

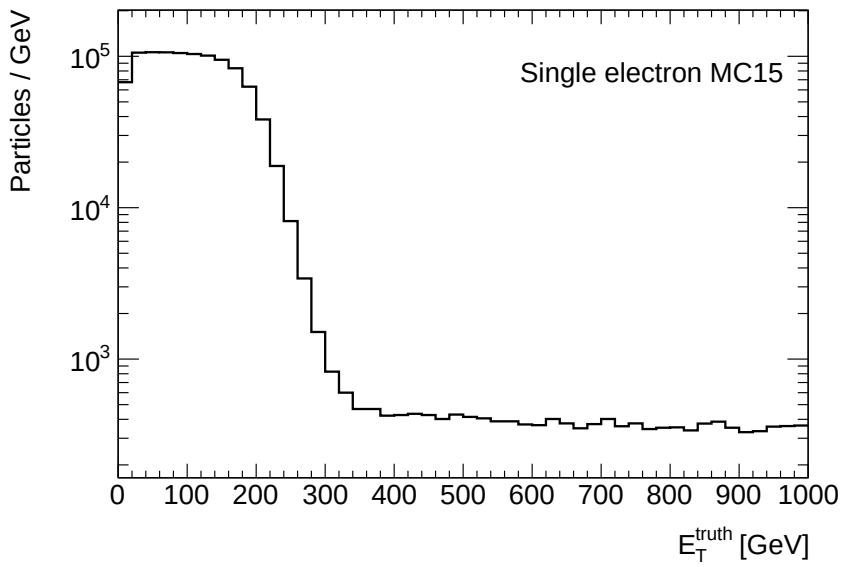

Figure 4.4.: Distribution of the true transverse energy of electrons used for the MVA calibration in the region $1.4 < |\eta| < 1.6$.

- Relative difference between the true and the reconstructed energy with the initial calibration procedure [109] below 50%. This requirement removes far outliers that can reduce the MVA performance.

4.4. Implementation and MVA algorithm

The MVA calibration scheme is implemented using the Toolkit for Multivariate Analysis (TMVA) framework [115]. The framework provides a ROOT-integrated machine learning environment for the processing and parallel evaluation of multivariate classification and regression techniques. A typical MVA classification or regression analysis consists of two distinct phases: the training and the evaluation.

For the training of the MVA, it is required to specify a training sample, a set of input variables, the quantity to be evaluated (target variable) and the MVA algorithm. The sample is described in previous section. The algorithm is boosted decision trees (BDT) with gradient boosting (BDTG). The target variable and input variables are discussed in the following paragraphs.

4.4.1. Target variable

The goal of the calibration is to estimate the true energy of the particle from the quantities measured by the detector. The MVA target must be either the energy or a quantity from which it is possible to compute this energy. The target that has used in this study is correction factor to the energy measured in the EM calorimeter accordion: $E_{\text{true}}/E_{\text{acc}}$.

4.4.2. Input variables

MVA algorithms give the possibility to use an arbitrary number of variables. The quantities used in this study are the following:

- **Total energy in the EM calorimeter accordion**: $E_{\text{acc}} = E_1 + E_2 + E_3$, defined as the sum of the uncalibrated energies in the EM calorimeter samplings;
- **Ratio of the energy in the presampler to the energy in the EM calorimeter accordion**: E_0/E_{acc};
- **Energy in first sampling of EM calorimeter accordion over the energy in second sampling of EM calorimeter accordion**: E_1/E_2;
- **Energy in three consecutive E4 scintillators over the energy in the EM calorimeter accordion**: $E_{3\times\text{E4}}/E_{\text{acc}}$. Electron shower width is wider than one E4 scintillator size in ϕ, so that for each electron the sum of energies from three consecutive E4 scintillators ($E_{3\times\text{E4}}$) is considered;
- **Pseudorapidity in the ATLAS frame**: η_{cluster} , i.e. taking into account the misalignment of the detector, in order to correct for the variation of the material in front of the accordion;
- ϕ **with respect to the EM calorimeter cell edge** in the frame of EM calorimeter,
- η **with respect to the EM calorimeter cell edge** in the frame of EM calorimeter.
- **Difference between ϕ angle of the electron cluster and azimuth position of the E4 scintillator**: $\Delta\phi = \phi_{\text{cluster}} - \phi_{\text{E4}}$.

4.4.3. Binning

In order to help the MVA to adjust the response as a function of many variables that have different behaviours in different regions of the phase space, the training sample was divided into bins in pseudorapidity ($|\eta_{\text{cluster}}|$). The binning was chosen to match approximately the non-uniformities of the detector and significant changes in the energy deposition in the EM calorimeter accordion and E4 scintillators (see Figure 4.5). Since the samples are limited in statistics, only three $|\eta_{\text{cluster}}|$ bins were chosen with the following edges: 1.4, 1.46, 1.52, 1.6, which approximately separate the bin where the amount of material traversed by a particle in front of first active calorimeter layer has a maximum (see Figure 4.2). Further splitting into bins in transverse energy gives no improvement given the small statistics in each bin.

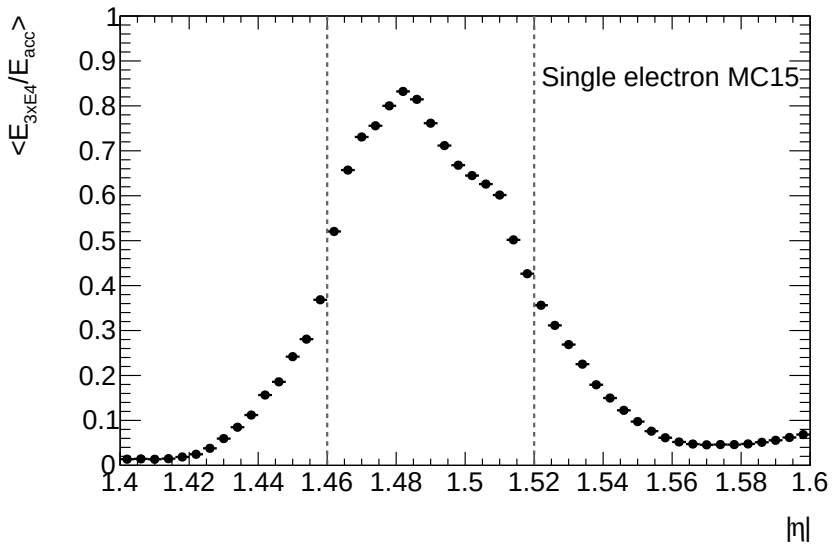

Figure 4.5.: Energy in three consecutive E4 scintillators over the energy in EM accordion as a function of pseudorapidity of the cluster. The vertical dashed lines indicate the chosen pseudorapidity bins.

4.5. Correction to the MVA output

Multivariate regression algorithms normally aim at minimizing the root mean square (RMS) of the target variable. In practice this leads to an optimization in which the mean value of the output energy E^{MVA} is close to E_{true}. However, the peak position of E/E_{true} can be shifted from unity due to the non symmetric shape of the distribution, which has a longer tail towards smaller values of E/E_{true} mostly due to the bremsstrahlung in the material upstream the calorimeter. In order to have a peak position closer to unity a set of shifts, defined as a inverse

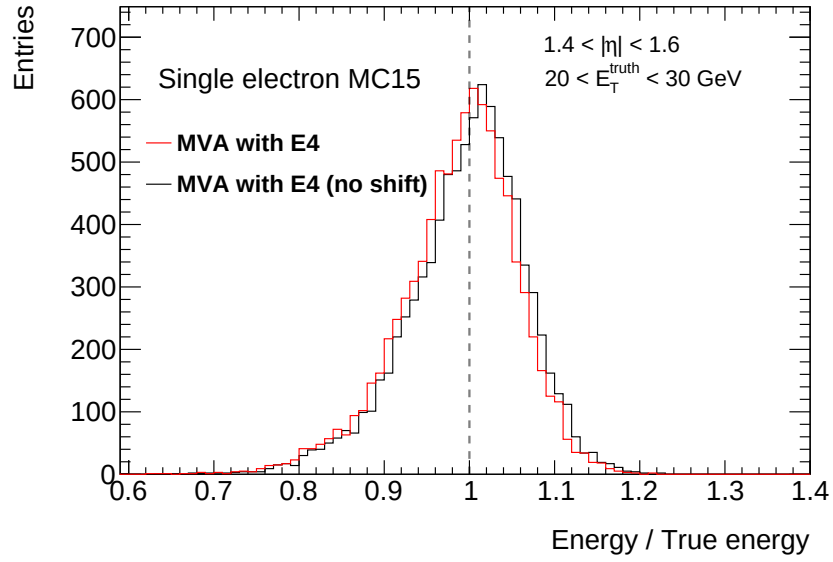

Figure 4.6.: Example of the shift effect for electrons. The distribution of E/E_{true} is compared before (black) and after (red) the shift.

of the peak position, were calculated and applied on top of the MVA output. An example of the shift effect is presented in Figure 4.6. The mean value of the smallest interval containing 10% of the events (Mean10) in each bin (defined below) was chosen to estimate the peak position. In each η bin used for the MVA training, the bins were defined according to the output transverse energy $E_{\mathrm{T}}^{\mathrm{MVA}} = E^{\mathrm{MVA}}/\cosh(\eta_{\mathrm{cluster}})$ and a linear interpolation was used to produce a continuous energy dependence. The chosen $E_{\mathrm{T}}^{\mathrm{MVA}}$ bin edges for the three different pseudorapidity regions (defined for the MVA training) are listed below:

- In the first η bin ($1.4 < |\eta_{\mathrm{cluster}}| < 1.46$): 15, 45, 160, 1000 GeV
- In the second η bin ($1.46 < |\eta_{\mathrm{cluster}}| < 1.52$): 17, 25, 500, 1000 GeV
- In the third η bin ($1.52 < |\eta_{\mathrm{cluster}}| < 1.6$): 100, 350, 1000 GeV

Figure 4.7 shows the shifts as a function of $E_{\mathrm{T}}^{\mathrm{MVA}}$.

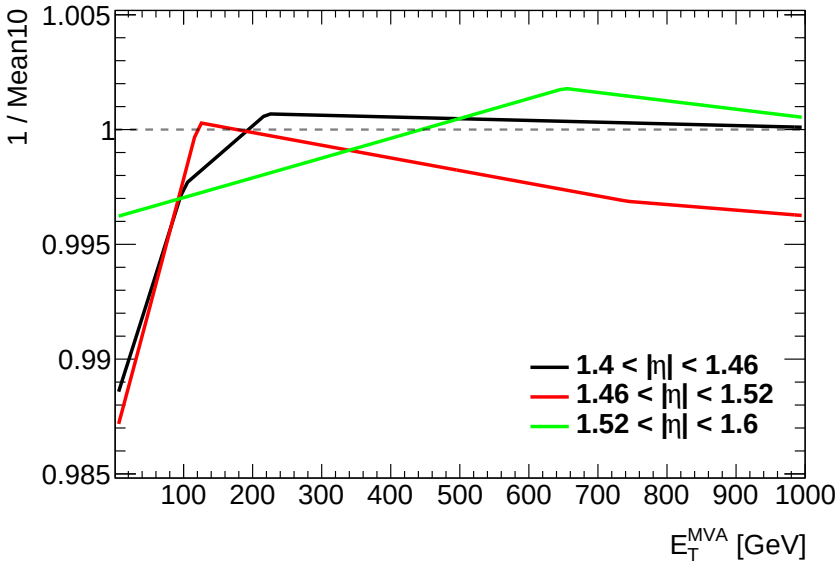

Figure 4.7.: Shifts applied to the MVA output for different $|\eta|$ regions as a function of $E_{\mathrm{T}}^{\mathrm{MVA}}$ for electrons.

4.6. Performance of the MVA calibration with E4 scintillators

In order to check the importance of E4 scintillators in the proposed MVA calibration for the crack region ($1.4 < |\eta| < 1.6$), an independent MVA training and calibration is performed, that do not use E4 scintillators information in the input variables. The performance of MVA calibration with and without E4 scintillators is compared in terms of linearity and resolution of the electron energy. The linearity is quantified by the peak position of E/E_{true} as a function of $E_{\mathrm{T}}^{\mathrm{truth}}$, estimated by the mean value of a Gaussian function fitted to the core of the distribution in each bin in $E_{\mathrm{T}}^{\mathrm{truth}}$ and $|\eta|$. The fits are restricted to the range $[-1, +2]$ standard deviations to avoid biases from the tails. The resolution is defined as the interquartile range of E/E_{true}, i.e.

the distance between the first and the last quarters of the data in each bin, divided by 1.349 in order to mimic the standard deviation in case of a normal distribution. The 1.349 value is derived from the number of standard deviations that encompasses 50% of the area under the curve of the normal distribution.

An example of distributions of E/E_{true} obtained using MVA calibration with and without E4 crack scintillators for electrons are presented in Figure 4.8 along with peak position and resolution.

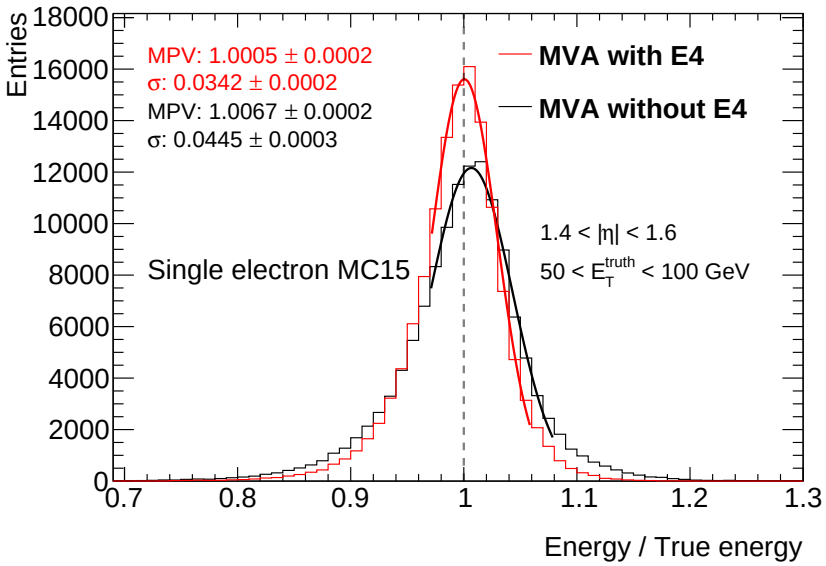

Figure 4.8.: Distributions of E/E_{true} obtained in the crack region ($1.4 < |\eta| < 1.6$) using MVA with (red) and without (black) E4 crack scintillators for electrons with truth transverse energy: $50 < E_{\text{T}}^{\text{truth}} < 100$ GeV. A Gaussian function is fitted to the distributions in the range [-1, +2] standard deviations. Most probable value (MPV), estimated from a Gaussian fit and resolution (σ) from the effective interquartile range (see text) are shown on the plot.

4.6.1. Linearity, uniformity vs. $|\eta|$ and resolution on single particles

The linearity for electrons with $E_{\text{T}}^{\text{truth}}$ ranging from 0 to 1 TeV is shown in Figure 4.9, obtained in different bins in $|\eta|$. The non-linearity with the MVA calibration with E4 scintillators is below few per mil for $E_{\text{T}}^{\text{truth}}$ above 20 GeV, and typically better than 1.5% at lower transverse energies. The situation is slightly worse in case of MVA calibration without E4 scintillators, the non-linearity reaches up to 3% at lower transverse energies in higher bin in $|\eta|$, however in that case the energy shifts are not applied, which expects a little improvement. In general, there is an improvement of about a factor two when the E4 scintillators are included in the MVA calibration. The uniformity as a function of pseudorapidity is shown in various intervals of $E_{\text{T}}^{\text{truth}}$ in Figure 4.10. One observes, that the values are closer to unity and stable within few per mil in case of MVA with E4.

The resolution as a function of $E_{\text{T}}^{\text{truth}}$ (pseudorapidity) is shown in various intervals of pseudorapidity ($E_{\text{T}}^{\text{truth}}$) in Figure 4.11 (Figure 4.12). The ratio between the results obtained with and

without E4 scintillators are shown in the lower part of each figure. After inclusion of E4 scintillators information in the MVA calibration, improvements of about 10% to 50% are observed depending on the bins in $E_{\mathrm{T}}^{\mathrm{truth}}$ and $|\eta|$.

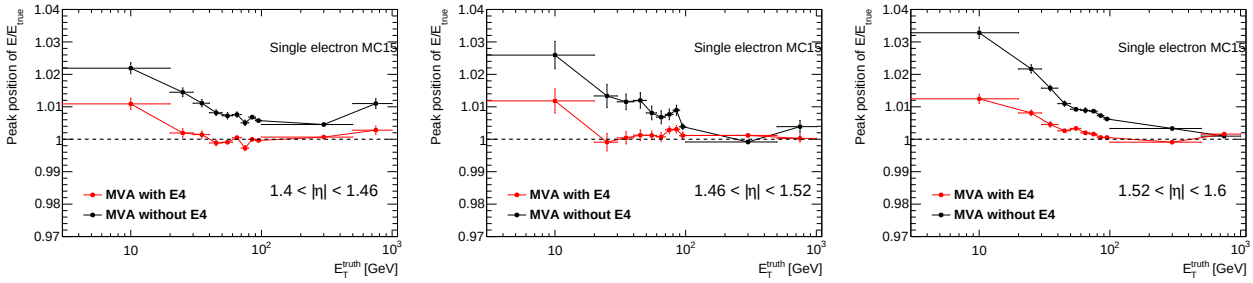

(a) (b) (c)

Figure 4.9.: Linearity, given by the peak position of E/E_{true} as a function of truth transverse energy ($E_{\mathrm{T}}^{\mathrm{truth}}$), comparing the MVA calibration with (red) and without (black) E4 scintillators for electrons. The values are obtained in three bins in $|\eta_{\mathrm{cluster}}|$: [1.4, 1.46] (a), [1.46, 1.52] (b) and [1.52, 1.6] (c).

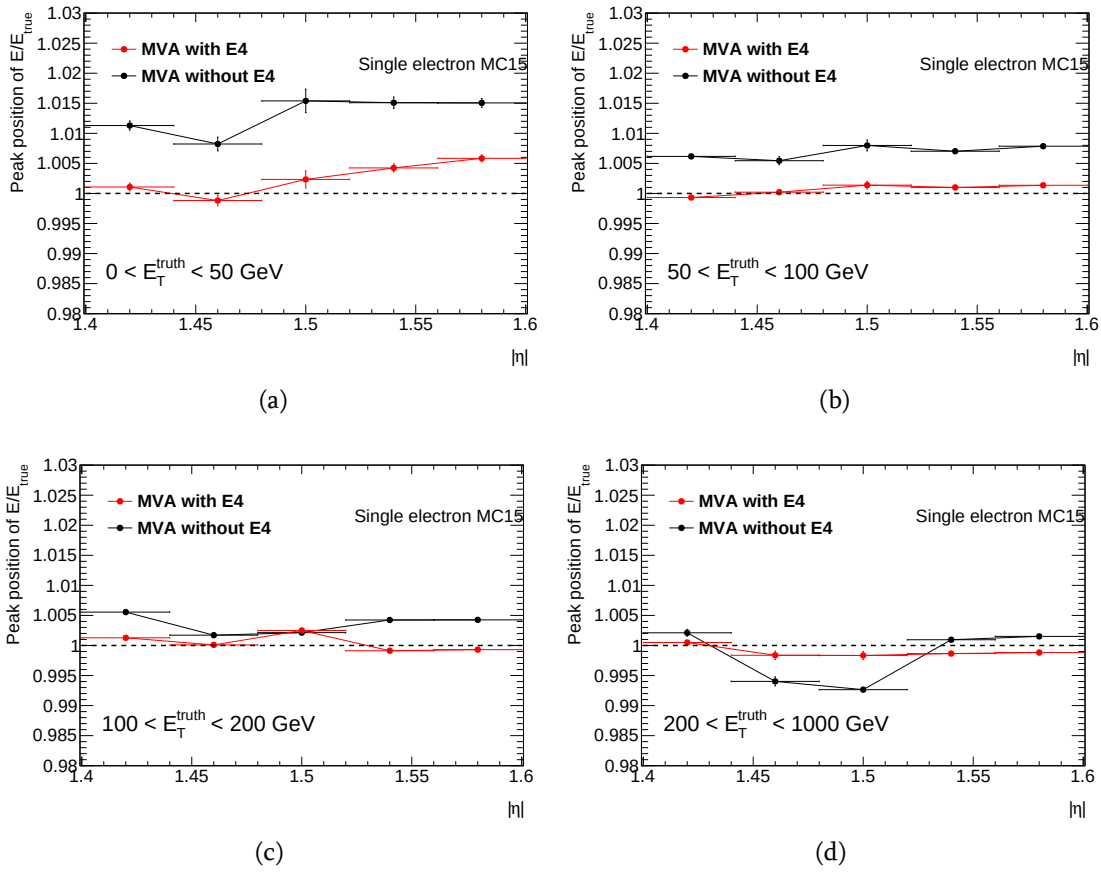

(a) (b) (c) (d)

Figure 4.10.: Peak position of E/E_{true} as a function of pseudorapidity ($|\eta_{\mathrm{cluster}}|$), comparing the MVA calibration with (red) and without (black) E4 scintillators for electrons. The values are obtained in four bins in $E_{\mathrm{T}}^{\mathrm{truth}}$: a) [0, 50] GeV, b) [50, 100] GeV, c) [100, 200] GeV and d) [200, 1000] GeV.

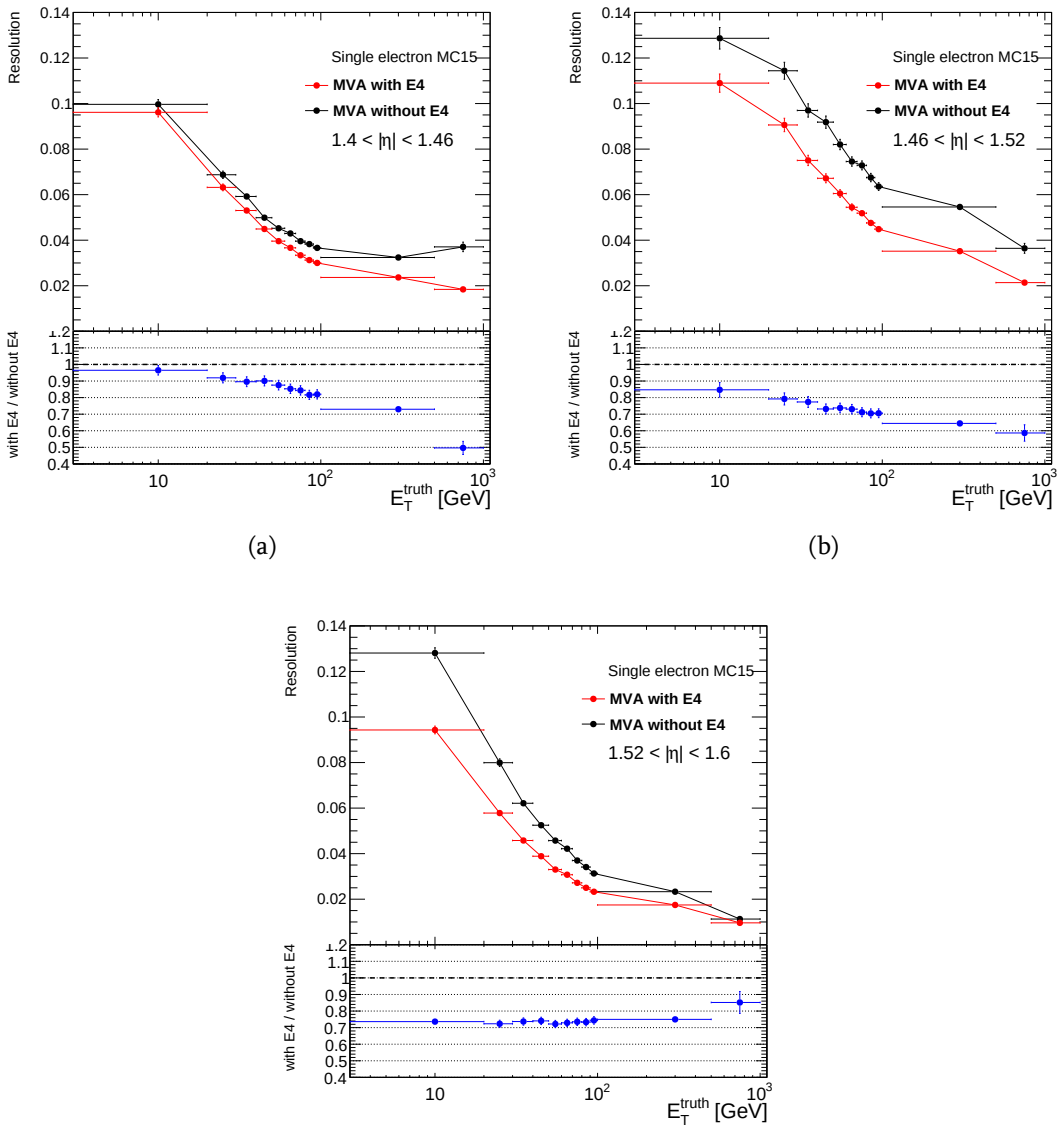

Figure 4.11.: Energy resolution of the electrons as a function of truth transverse energy ($E_{\mathrm{T}}^{\mathrm{truth}}$), comparing the MVA calibration with (red) and without (black) E4 scintillators. The values are obtained in three bins in $|\eta_{\mathrm{cluster}}|$: [1.4, 1.46] (a), [1.46, 1.52] (b) and [1.52, 1.6] (c). The lower part of the figures show the ratio of the values from MVA with E4 to the values from MVA without E4.

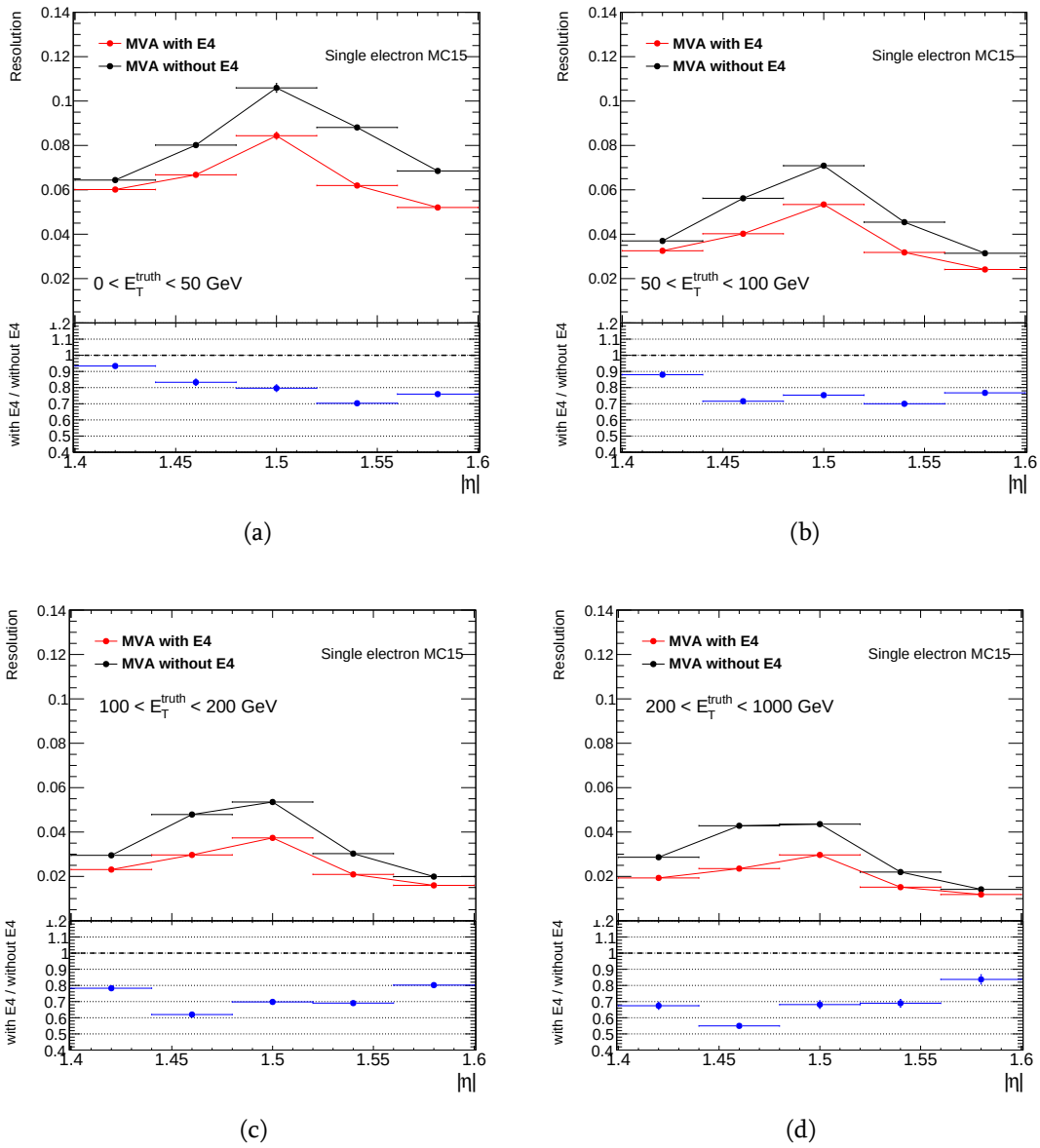

Figure 4.12.: Energy resolution of the electrons as a function of pseudorapidity ($|\eta_{\text{cluster}}|$), comparing the MVA calibration with (red) and without (black) E4 scintillators. The values are obtained in four bins in $E_{\text{T}}^{\text{truth}}$: a) [0, 50] GeV, b) [50, 100] GeV, c) [100, 200] GeV and d) [200, 1000] GeV. The lower part of the figures show the ratio of the values from MVA with E4 to the values from MVA without E4.

4.6.2. Stability

In order to check if the input variables related to the E4 crack scintillators are correctly used in the MVA training, the behaviour of the MVA calibrated energy as a function of that input variables has been investigated.

Figure 4.13 (Figure 4.14) shows the residual dependence of the peak position of E/E_{true} for the MVA with E4 on the energy in three consecutive E4 scintillators over the energy in EM accordion (difference between ϕ coordinate of the electron cluster and azimuth position of the E4 scintillator). The plots are obtained in different η regions for $E_{\text{T}}^{\text{truth}} < 100$ GeV and $E_{\text{T}}^{\text{truth}} > 100$ GeV. The histograms of the corresponding input variable are presented in yellow for illustration purposes. No strong residual dependence are observed on that input variables, the values are varying within few per mil.

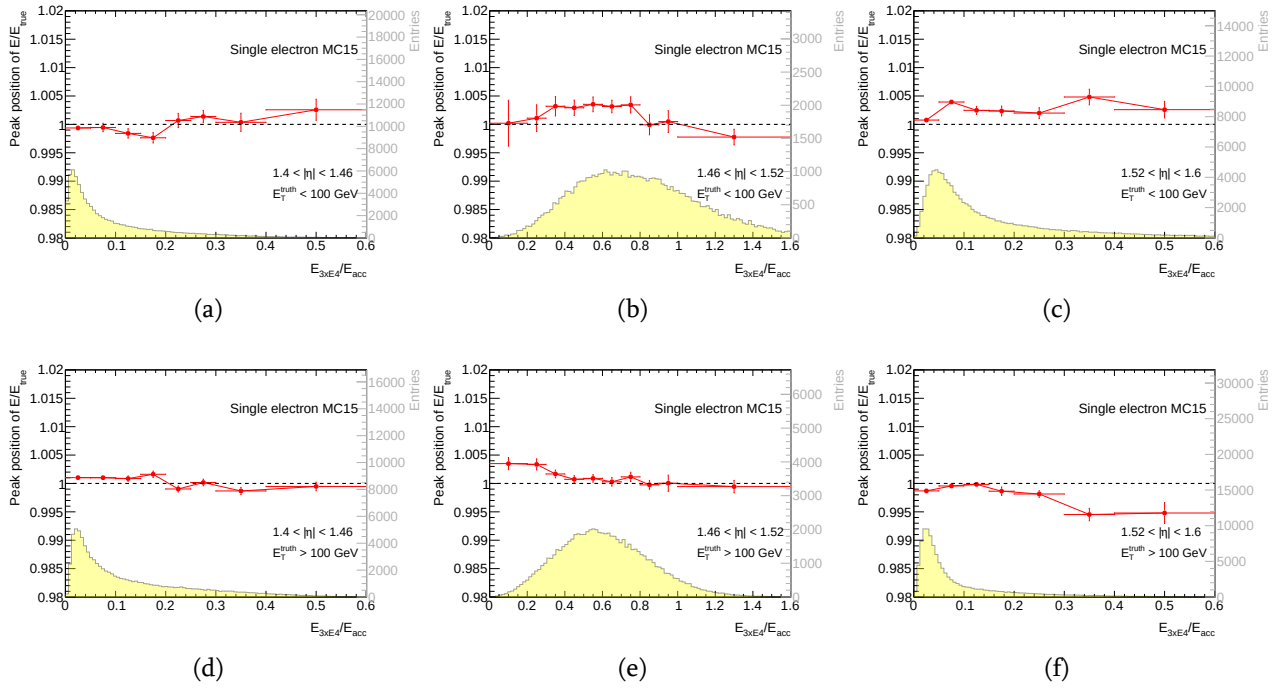

Figure 4.13.: Peak position of E/E_{true} as a function of $E_{3\times\text{E4}}/E_{\text{acc}}$ (energy in three consecutive E4 scintillators over the energy in EM accordion). Top plots are obtained for $E_{\text{T}}^{\text{truth}} < 100$ GeV and bottom plots are obtained for $E_{\text{T}}^{\text{truth}} > 100$ GeV in three bins in $|\eta_{\text{cluster}}|$: [1.4, 1.46] (a,d), [1.46, 1.52] (b,e) and [1.52, 1.6] (c,f). Each histogram (in yellow) illustrates the distribution of the corresponding variable.

4.6.3. MVA energy sensitivity to E4 energy bias

The input variable participating with E4 crack scintillators in the MVA calibration can lead to the additional systematic uncertainty on the calibrated electron energy. In order to check the effect of the E4 energy systematic uncertainty on the MVA energy, the sensitivity to the E4 energy bias has been investigated.

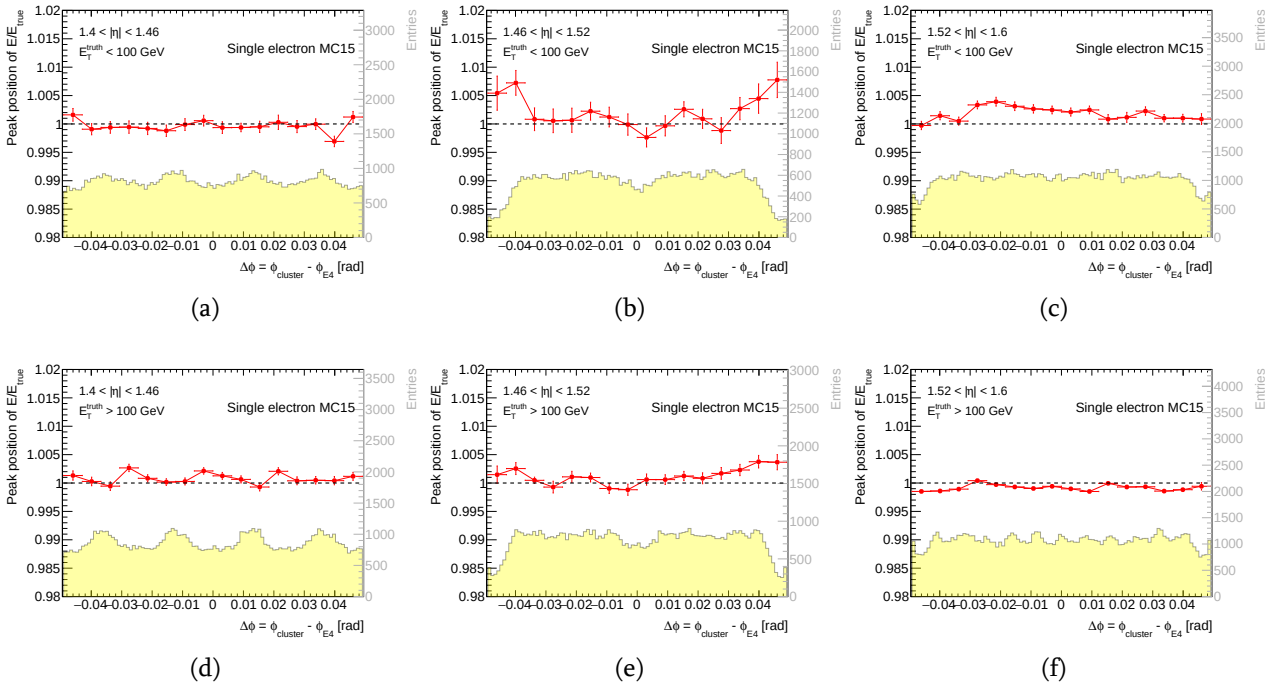

Figure 4.14.: Peak position of E/E_{true} as a function of $\Delta\phi$ (difference between ϕ coordinate of the electron cluster and azimuth position of the E4 scintillator). Top plots are obtained for $E_{\text{T}}^{\text{truth}} < 100$ GeV and bottom plots are obtained for $E_{\text{T}}^{\text{truth}} > 100$ GeV in three bins in $|\eta_{\text{cluster}}|$: [1.4, 1.46] (a,d), [1.46, 1.52] (b,e) and [1.52, 1.6] (c,f). Each histogram (in yellow) illustrates the distribution of the corresponding variable.

For a given population of electrons the following function is defined:

$$f(\alpha) = \langle E^{\text{MVA}}(\alpha)/E^{\text{MVA}} \rangle - 1 \, , \tag{4.1}$$

where E^{MVA} is the MVA calibrated energy of electron, while $E^{\text{MVA}}(\alpha)$ is the MVA calibrated energy when a bias α is introduced in the energy measured with E4 crack scintillators:

$$E'_{3\times\text{E4}} = E_{3\times\text{E4}} \cdot (1+\alpha) \tag{4.2}$$

and $\langle E^{\text{MVA}}(\alpha)/E^{\text{MVA}} \rangle$ is the average value of the relative difference between MVA energies obtained with and without E4 energy bias, in a given population of electrons. The value of $f(\alpha)$ is the variation of MVA energy scale. As shown in Figure 4.15 we can assume that it is a linear function of α, so if we have a slope of that function, we can evaluate the MVA energy scale variation for any reasonable value of E4 energy bias α. For each E_{T}/η bins, $f(\alpha)$ is plotted for the several values of α and a linear fit is done in order to extract the slope. Figure 4.15 shows an example of the linear fit to $f(\alpha)$ function. Slopes of $f(\alpha)$ as a function of truth transverse energy is presented in Figure 4.16. Here we can find that in the most sensitive η bin ($1.46 < |\eta_{\text{cluster}}| < 1.52$) at $E_{\text{T}}^{\text{truth}} = 100$ GeV, 10% bias ($\alpha = 0.1$) of the energy from E4 crack scintillators gives about 3% variation of the final MVA energy scale.

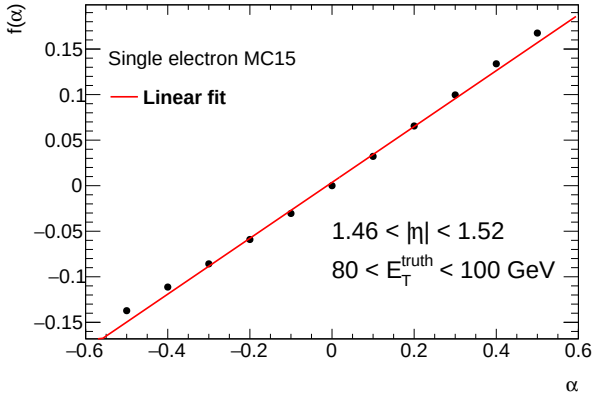

Figure 4.15.: Example of $f(\alpha)$ function in the bin $1.46 < |\eta_{\text{cluster}}| < 1.52$. The slope is extracted from the linear fit shown with read line.

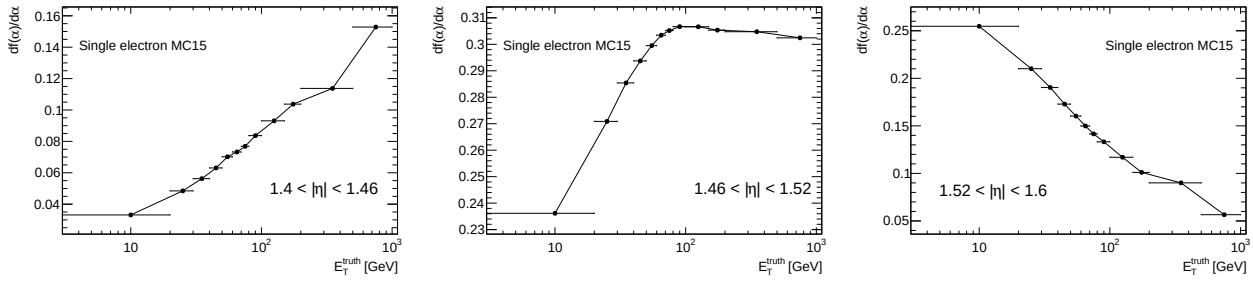

(a) (b) (c)

Figure 4.16.: Sensitivity, given by a slope of $f(\alpha)$ as a function of truth transverse energy ($E_{\text{T}}^{\text{truth}}$). The values are obtained in three bins in $|\eta_{\text{cluster}}|$: [1.4, 1.46] (a), [1.46, 1.52] (b) and [1.52, 1.6] (c).

4.7. MVA calibration with E4′ scintillators

In LHC Run 2 a few E4′ counter prototypes covering the range $-1.72 < \eta < -1.6$ have been installed to check possibility to improve the electron energy resolution in the region $|\eta| \sim 1.7$, which is the second most critical region affected with the high amount of dead material (see Figures 4.1 and 4.2). This may allow in Phase I upgrade to improve the layout of TileCal gap/crack scintillators and enlarge the coverage to $\eta \sim 1.72$.

Possible improvement in the electron energy calibration with E4′ scintillators is investigated with the simulated single electron sample, where E4′ counters are implemented in the full 2π geometry up to $|\eta| \sim 1.75$ in the extension of E4 counters. Similarly to MVA calibration with E4 scintillators, energy deposited by the electron in E4′ scintillators is added in the set of the MVA input variables. Figure 4.17 illustrates the improvement with E4′ scintillators for simulated electrons with truth transverse energy between 50 GeV and 100 GeV. An improvement of about 30% in the resolution is found in the wide range of truth transverse energy, as it can be seen in Figure 4.18(a). Figure 4.18(b) shows that the peak position of E/E_{true} is stable mostly within few per mil from unity as a function of truth transverse energy for both MVA with and without E4′ scintillators. The corrections to the MVA output, that is described in Section 4.5, are not applied to shift the peak position closer to unity.

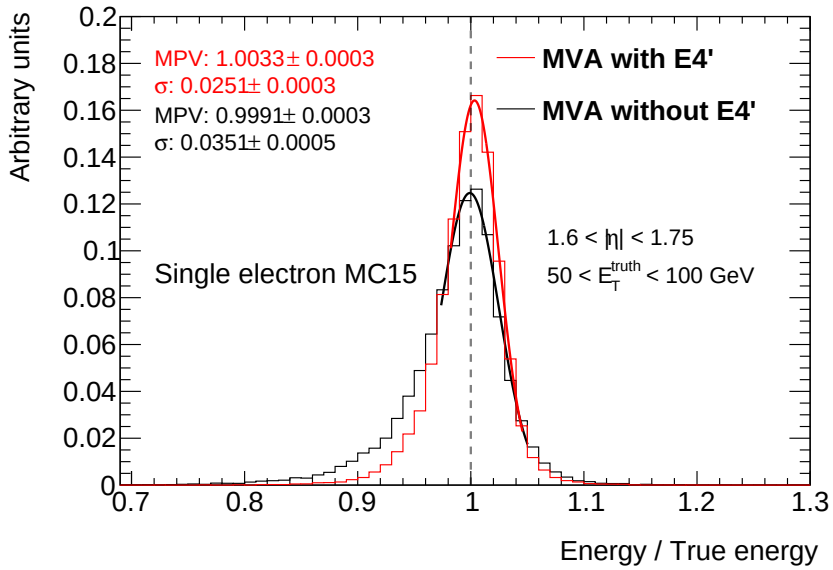

Figure 4.17.: Distributions of E/E_{true} obtained in the region $1.6 < |\eta| < 1.75$ using MVA with (red) and without (black) E4′ scintillators for electrons with truth transverse energy: $50 < E_{\text{T}}^{\text{truth}} < 100$ GeV. A Gaussian function is fitted to the distributions in the range [-1, +2] standard deviations. Most probable value (MPV), estimated from a Gaussian fit and resolution (σ) from the effective interquartile range (see text) are shown on the plot.

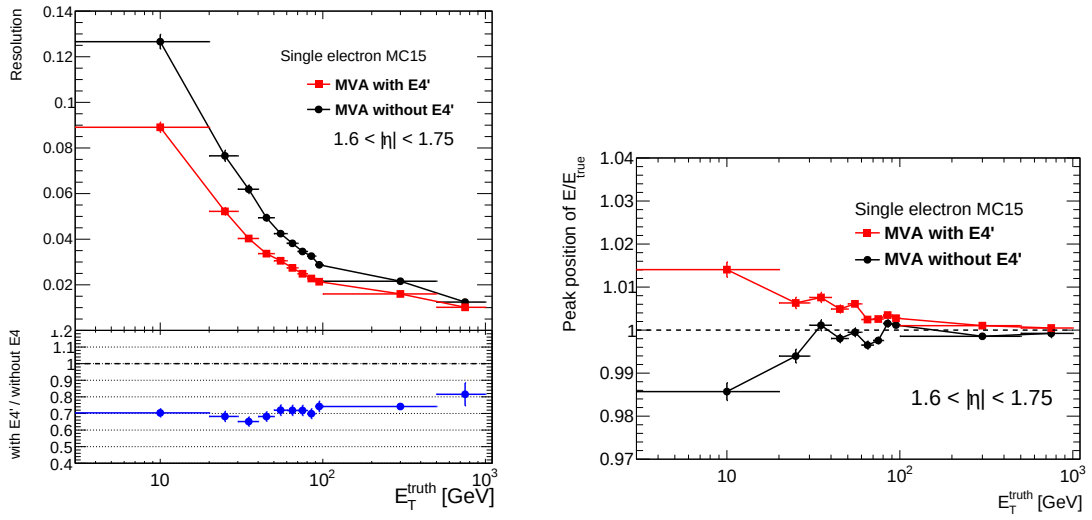

(a) (b)

Figure 4.18.: Energy resolution (a) and peak position of E/E_{true} (b) for electrons as a function of truth transverse energy ($E_{\mathrm{T}}^{\mathrm{truth}}$), comparing the MVA calibration with (red) and without (black) E4′ scintillators.

4.8. Comparison to MC15 MVA

The comparison of MVA calibration with E4 scintillators for the crack region to the initial MVA calibration used for MC15 (Monte Carlo samples for 2015 data analysis) is presented in Figure 4.19. In the region $1.6 < |\eta| < 1.75$, calibration with E4′ scinitllators is presented as well. Results are obtained using the simulated single electron sample with the transverse energy spectrum shown in Figure 4.4, independent from pseudorapidity. MVA calibration methods (with/without E4 scintillators and with E4′ scinitllators), used in this study, all are significantly better than MC15 MVA.

In case of MVA without E4 crack scintillators and MC15 MVA, the largest deviation from unity of the peak position of E/E_{true} is observed in the pseudorapidity region which corresponds to the largest amount of material in front of first active EM calorimeter layer (see Figure 4.2). In that region, the degradation of the resolution is also observed, as it can be seen from Figure 4.19(b). MVA calibration with E4 crack scintillators gives peak position of E/E_{true} closer to unity and significantly improves the resolution. The peak position of E/E_{true} in the region $1.6 < |\eta| < 1.75$ is more deviated from unity for the MVA calibration with E4′ scinitllators than for the MC15 MVA calibration, however for the former one corrections to the MVA output are not applied, which expects a little improvement. Figure 4.19(b) shows a significant improvement in the energy resolution for the region $1.6 < |\eta| < 1.75$ with the E4′ scinitllators compared to the initial MVA calibration used for MC15.

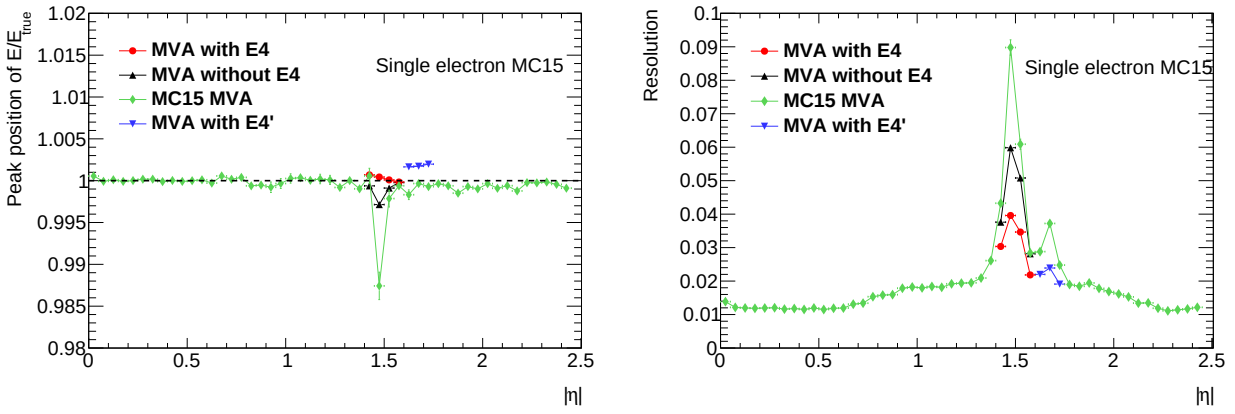

(a) (b)

Figure 4.19.: Peak position of E/E_{true} (a) and resolution (b) as a function of pseudorapidity for electrons, comparing the MVA calibration with (red)/without (black) E4 scintillators and MVA calibration used for MC15 samples (green). In the region $1.6 < |\eta| < 1.75$ the results of MVA calibration with E4′ scinitllators (blue) are shown as well.

4.9. Conclusions

The electron energy calibration improvement in the crack region is investigated. Information from the Tile Calorimeter E4 crack scintillators is included in the MVA based electron energy calibration procedure in order to correct energy losses in the passive material before and between Barrel and Endcape of the Electromagnetic Calorimeter. The performance of the calibration is checked on the simulated single electron sample. MVA calibration with and without E4 crack scintillators have been compared in terms of linearity and resolution. Results show that E4 crack scintillators improve the energy resolution by about 10% to 50% depending on η and E_{T} bins in the range $1.4 < |\eta| < 1.6$. Peak position of E/E_{true} is within few per mil from unit for the MVA with E4, slightly better than without E4 crack scintillators. MVA energy sensitivity to E4 energy bias has been investigated and found that 10% bias of the energy from E4 crack scintillators gives about 3% variation of the final MVA energy of electrons.

Possible improvement of the electron performance in the region $1.6 < |\eta| < 1.75$ is investigated using the simulated single electron sample with E4′ scinitllators implemented in the extension of E4 counters. The study shows that extending of TileCal gap/crack scintillators up to $|\eta| \sim 1.75$ would improve the electron energy resolution by about 30%, assuming that scintillators are radiation hard and well calibrated.

This study led to very important decisions in the Tile Calorimeter phase I upgrades of the tile crack counters as well as in the ATLAS e/γ performance group. In the long shutdown LS2, all the TileCal crack scintillators were replaced with new ones that have the extended pseudorapidity coverage up to $\eta \sim 1.72$, as motivated by the results obtained in this thesis. For the analysis with full LHC run 2 dataset, the ATLAS e/γ performance group used E4 crack scintillators as suggested in the thesis, leading to better electron/photon performance in the pseudorapidity region $1.4 < |\eta| < 1.6$ [1]. Figure 4.20 shows the improvement with the Tile-

Cal E4 crack scintillators for simulated electrons generated with transverse energy between 50 GeV and 100 GeV. The electron energy resolution as a function of $|\eta|$, covering the region $|\eta| < 2.5$, is illustrated in Figure 4.21.

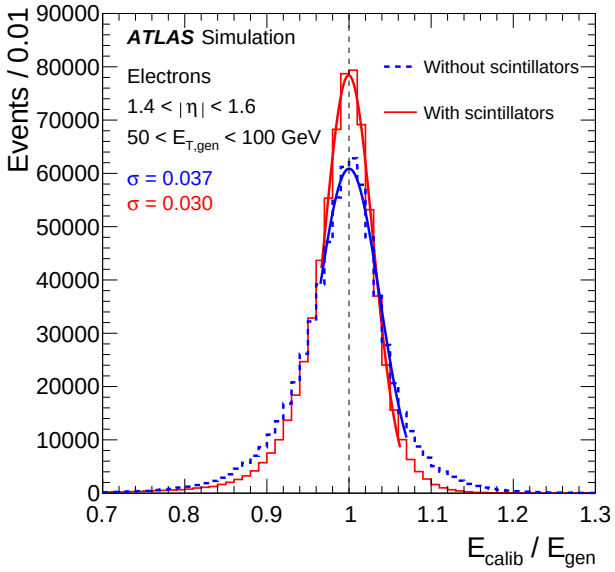

Figure 4.20.: Distributions of the calibrated energy, E_{calib}, divided by the generated energy, E_{gen}, for electrons with $1.4 < |\eta| < 1.6$ and $50 < E_{\text{T,gen}} < 100$ GeV. The dashed (solid) histogram shows the results based on the energy calibration without (with) the scintillator information. The curves represent Gaussian fits to the cores of the distributions. b) Adapted from [1].

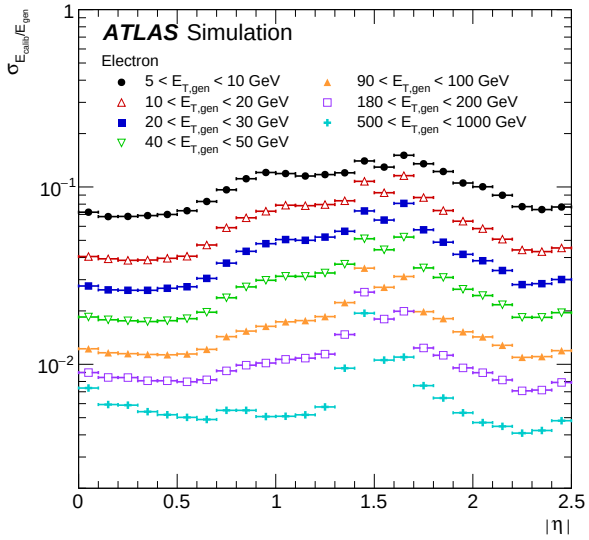

Figure 4.21.: Energy resolution, $\sigma_{E_{\text{calib}}/E_{\text{gen}}}$, estimated from the interquartile range of $E_{\text{calib}}/E_{\text{gen}}$ as a function of $|\eta|$ for electrons in different E_{T} ranges. Adapted from [1].

Chapter 5.

Search for FCNC top-quark decays $t \to qZ$ at $\sqrt{s} = 8$ TeV

In this chapter, the search for top-quark flavour-changing neutral current (FCNC) decays (see Section 1.3.2) using the proton-proton (pp) collision data at $\sqrt{s} = 8$ TeV is presented. The search is performed using the top-quark–top-antiquark pair production events, with one top quark decaying through the $t \to qZ$ ($q = u, c$) FCNC channel, and the other through the dominant Standard Model mode $t \to bW$. Only Z boson decays into charged leptons and hadronic and leptonic W boson decays are considered. Consequently, two channels are used in the search: dilepton and trilepton. The final state topology in dilepton channel is characterized by the presence of two isolated charged leptons and at least four jets, one of the jets originating from a b-quark. The trilepton final state topology is characterized by the presence of three isolated charged leptons, at least two jets, one of the jets originating from a b-quark, and missing transverse momentum from the undetected neutrino.

5.1. Data and Monte Carlo samples

This section describes the data and Monte Carlo simulated samples used in this analysis.

The software packages are used to generate and simulate the event sample of different physics processes. These software packages incorporate the knowledge of the physics of a given process and use Monte Carlo (MC) statistical techniques to generate and simulate the event of that process. MC simulated event samples are used to study the detector sensitivity to the signal processes and to estimate contribution from the expected background processes.

The detector and trigger simulations are performed with standard ATLAS software using GEANT4 [95, 116]. The same offline reconstruction methods used on data are applied to the simulated samples.

5.1.1. Data sample

The full 2012 dataset recorded by the ATLAS from pp collisions at $\sqrt{s} = 8$ TeV is used. The analysed events were recorded by single-electron or single-muon triggers and fulfil standard data-quality requirements. Triggers with different transverse momentum thresholds are used to increase the overall efficiency. The triggers using a low transverse momentum (p_{T}) threshold ($p_{\mathrm{T}}^{e,\mu} > 24$ GeV) also have an isolation requirement. Efficiency losses at higher $p_{\mathrm{T}}^{e,\mu}$ values are recovered by higher threshold triggers ($p_{\mathrm{T}}^{e} > 60$ GeV or $p_{\mathrm{T}}^{\mu} > 36$ GeV) without any isolation requirement. The integrated luminosity of the analyzed data sample is 20.3 fb^{-1}.

5.1.2. Signal sample

The Monte Carlo simulation samples of top-quark pair production, with one of the top quarks decaying through FCNC to qZ, while the other decays according to the SM, were generated with PROTOS 2.2 (PROgram for TOp Simulations) [117, 118], which includes effects of new physics at an energy scale Λ by adding dimension-six effective operators to the SM Lagrangian, written in terms of anomalous couplings, as described in Section 1.3.2. The FCNC Ztq vertex involves a minimum of four anomalous couplings X_{qt}^{L}, X_{qt}^{R} and $\kappa_{qt}^{L}, \kappa_{qt}^{R}$. Each of them are set to 0.01.

Different samples are generated for dilepton and trilepton channels. Only Z boson decays to charged leptons and hadronic (leptonic) decays of W boson are generated at the matrix-element level by PROTOS for dilepton (trilepton) signal sample. The CTEQ6L1 [119] leading order parton distribution function (PDF) was used with PROTOS. After the generation, events are hadronized using PYTHIA 6.426 [120] with tunes from Perugia2011C (P2011C) [121] and with τ decays being generated with TAUOLA [122]. The mass of the top quark was set to $m_{top} = 172.5$ GeV, while the masses of the W boson and Z boson were set to their measured values $m_W = 80.399$ GeV and $m_Z = 91.1876$ GeV [123], respectively.

5.1.3. Background samples

Several SM processes have final-state topologies similar to the signal, they are considered as background processes. The background processes in dilepton (trilepton) channel can be events with two (three) reconstructed isolated charged leptons, that are prompt leptons[1] as well as "fake leptons" (non-prompt leptons or jets misidentified as isolated charged leptons).

Background events with fake leptons are estimated from a data-driven method using a parameterization of the prompt- and fake-lepton efficiencies. In dilepton channel, such background arises mostly from W+jets and SM $t\bar{t}$ processes, while in trilepton channel - mostly from Z+jets and SM $t\bar{t}$ processes.

[1] Prompt leptons are leptons from the decay of W or Z bosons, either directly or through an intermediate $\tau \to \ell\nu\nu$ decay, or from the semileptonic decay of top quarks.

MC simulated samples are produced for the dominant background processes with prompt leptons. In dilepton channel, dominant background with prompt leptons arises from Z+jets production process, while in trilepton channel it is comprised mostly with diboson (WZ,ZZ) and $t\bar{t}V$ (V is W or Z) production processes. Small background contribution arises from tZ, Wt, WW, triboson (WWW, ZWW, ZZZ), VH, gluon-gluon fusion Higgs (ggH) and $t\bar{t}H$ production processes.

The Z+jets production events are generated using the Alpgen v2.14 [124] leading-order (LO) generator and the CTEQ6L1 PDF set. Parton shower and fragmentation are modelled with Pythia 6.425. To avoid double-counting of partonic configurations generated by both the matrix-element calculation and the parton-shower evolution, a parton-jet matching scheme ("MLM matching") is employed [125]. Events are generated with up to five additional partons, separately for Z+light jets (denoted in this analysis as Z+LF), $Zb\bar{b}$+jets and $Zc\bar{c}$+jets (denoted in this analysis as Z+HF).

For $t\bar{t}$ and single top (Wt-channel) the events are generated using the MC@NLO generator v4.03 [126] with the CT10 [127] PDF set. The parton shower and the underlying event are added using the Herwig generator v6.5 [128] with the AUET2-CT10 [129] tune.

The $WW/WZ/ZZ$+jets samples are generated with Alpgen 2.14 use the CTEQ6L1 PDF set and are interfaced with Herwig to add the parton shower with the AUET2 tune. Up to three additional partons from the matrix element are simulated. Another samples for diboson events (WZ and ZZ) are produced using Sherpa v1.4.3 [130] containing up to three additional partons.

The $Z\gamma$ background events are generated with Sherpa generator v1.4.1 with the CT10 PDF set. Events with $t\bar{t}W$, $t\bar{t}Z$ and $t\bar{t}\gamma$ production, including those with extra jets in the final state as well as triboson samples and tZ with up to one additional parton, are generated using MadGraph5 [131] with CTEQ6L1 PDF set. Parton showering is added using Pythia 6.426 with AUET2B tune.

The $t\bar{t}H$ and VH samples are generated with Pythia 8.165 [93] using CTEQ6L1 PDF and AU2 [97] set of tuned parameters. The ggH sample is generated using Powheg [132, 133] generator with CTEQ6L1 PDF set. It is interfaced to the Pythia 8.1 with the CT10 PDF set and AU2 tune.

5.2. Reconstructed physics objects

The primary objects considered in this analysis are electrons, muons, missing transverse momentum (with magnitude $E_{\mathrm{T}}^{\mathrm{miss}}$), jets, and b-tagged jets. Tau leptons are not explicitly reconstructed, although the τ decay products are reconstructed as electrons, muons or jets and as an additional contribution to the missing transverse momentum.

5.2.1. Electrons

Electron candidates are reconstructed as clustered energy deposits in the electromagnetic calorimeter that are associated to a well-measured charged particle tracks in the inner detector. The candidates are required to have a transverse energy E_{T} greater than 15 GeV and a pseudorapidity of the calorimeter cluster associated with the electron candidate $|\eta_{cluster}| < 2.47$. Candidates in the transition region between the barrel and endcap calorimeters, $1.37 \leq |\eta_{\mathrm{cluster}}| \leq 1.52$, have poorer energy resolution and are excluded. Electron candidates in this analysis satisfy "tight" quality requirements on the electromagnetic cluster and associated track that provide separation between isolated electrons and jets. Also, in order to suppress QCD multi-jet background, it is required that there is little calorimeter activity in the space surrounding the electron. Two isolation variables are employed: the energy deposited around the electron in the calorimeter in a cone size of 0.2, and the scalar sum of the p_{T} of tracks around the electron candidate in a cone size of 0.3. Cuts on these two quantities are used to select isolated electrons, chosen to have 90% isolation efficiency in simulation. Additionally, the longitudinal impact parameter of the electron track with respect to the selected primary vertex of the event, z_0, is required to be less than 2 mm. Jets within $\Delta R < 0.2$ of the selected electron are removed from the events. If an additional selected jet is found within $\Delta R < 0.2$, then the electron is discarded. A looser electron selection, used for the estimation of backgrounds with fake leptons, is defined by removing the isolation requirements.

5.2.2. Muons

Muon candidate reconstruction [134] is done by searching for track segments in layers of the muon chambers and combining these segments, starting from the outermost layer and fitted to account for material effects. Then the track is matched with tracks reconstructed in the inner detector. The candidates were refitted using the complete track information from both detector systems. The hit pattern in the inner detector must be consistent with a well reconstructed track, and the longitudinal impact parameter of the muon track with respect to the selected primary vertex of the event, z_0, is required to be less than 2 mm. All muons are required to pass $p_{\mathrm{T}} > 15$ GeV, $|\eta| < 2.5$ and to be separated by $\Delta R < 0.4$ from any selected jet. Additionally, the sum of the momenta of tracks inside a cone around the muon candidate, with variable size such that it is smaller for higher muon p_{T} [135], must be less than 5% of the muon energy. For the estimation of backgrounds with fake leptons, a looser selection is applied by removing the isolation requirement.

5.2.3. Jets

Jets are reconstructed with the anti-k_t algorithm [99] with a radius parameter $R = 0.4$, starting from energy clusters in the calorimeter reconstructed using the energy scale established

for electromagnetic objects. Prior to jet finding, a local cluster calibration scheme is applied to correct the topological cluster energies for the effects of non-compensation, dead material, and out-of-cluster leakage [136]. The corrections are obtained from simulation of charged and neutral particles.These jets are then calibrated to the hadronic energy scale using p_{T}- and η-dependent correction factors [137]. In a very small fraction of events, jets can be incorrectly reconstructed from a few noisy cells so event cleaning cuts are applied to remove events with jets flagged as 'bad'. Selected jets were required to have $p_{\mathrm{T}} > 25$ GeV and $|\eta| < 2.5$. To reduce the number of selected jets that originate from secondary pp interactions, for jets with $p_{\mathrm{T}} < 50$ GeV and $|\eta| < 2.4$, the scalar sum of the p_{T} of tracks matched to a jet and originating from the primary vertex must be at least 50% of the scalar sum of the p_{T} of all tracks matched to the jet.

5.2.4. *b*-tagging

Jets are identified as originating from the hadronization of a b-quark [138] (b-tagging) and not a light quark, mainly because their significant longer flight path, due to their relative long life time. This is done using multivariate techniques to combine information from the impact parameters of displaced tracks as well as topological properties of secondary and tertiary decay vertices reconstructed within the jet. It is determined with simulated $t\bar{t}$ events that, for the chosen working point, the tagging efficiency for b-jets with $p_{\mathrm{T}} > 20$ GeV is 70%, while the rejection factors for light-quark or gluon jets (light jets), charm jets and τ leptons are 137, 5 and 13, respectively.

5.2.5. Missing transverse energy

The measurement of $E_{\mathrm{T}}^{\mathrm{miss}}$ is based [139] on the energy deposits in the calorimeter with $|\eta| < 4.9$. The energy deposits associated with reconstructed jets and electrons are calibrated accordingly. Energy deposits not associated with a reconstructed object are calibrated according to their energy sharing between the electromagnetic and hadronic calorimeters. The momentum associated with each reconstructed muon, estimated using the momentum measurement of its reconstructed track, is taken into account in the calculation of $E_{\mathrm{T}}^{\mathrm{miss}}$.

5.3. Event selection and reconstruction

5.3.1. Preselection

The preselection of events for dilepton and trilepton analysis is same as follows.

At least one of the selected leptons must be matched, with $\Delta R < 0.15$ to the appropriate trigger object and have $p_{\mathrm{T}} > 25$ GeV. The trigger efficiencies for the leptons are approximately

93% for electrons, 70% for muons with $|\eta| < 1.05$ and 86% for muons with $1.05 < |\eta| < 2.4$ [140, 141]. The events are required to have at least one primary vertex with more than four associated tracks, each with $p_{\mathrm{T}} > 400$ MeV. The primary vertex is chosen as the one with the highest $\sum p_{\mathrm{T}}^2$ over all associated tracks. Leptons from cosmic rays are rejected by removing muon pairs with large, oppositely signed transverse impact parameters ($|d_0| > 0.5$ mm) and consistent with being back-to-back in the $r - \phi$ plane. Events with noise bursts and readout errors in the LAr calorimeter are also rejected.

5.3.2. Dilepton event selection and reconstruction

The final stage topology of $t\bar{t} \to bW(\to q\bar{q})qZ(\to \ell^+\ell^-)$ signal events includes two charged leptons and at least 4 jets with one b-jet. Accordingly, selected events are required to have exactly two reconstructed isolated charged leptons, at least 4 jets, with one of them being b-tagged. The two leptons must have the same flavour and opposite-sign charge. Invariant mass of the leptons pair must be within 10 GeV of the Z boson mass (m_Z). In addition, selected jets are required to have $p_{\mathrm{T}} > 30$ GeV.

In order to reconstruct the kinematics of $t\bar{t}$ event with SM top-quark ($t \to bW \to j_a j_b j_c$) and FCNC top-quark ($t \to qZ \to j_d \ell_a \ell_b$), one need to associate selected jets to quarks from W boson decay, light-quark from FCNC top decay (denoted as q-quark) and b-quark. This is done by assigning the b-tagged jet to the b-quark and selecting the jets combination assigned to quarks from W boson decay and q-quark which gives the minimum value of the following expression:

$$\chi^2 = \frac{(m^{reco}_{j_a j_b j_c} - m_t)^2}{\sigma^2_{t_{SM}}} + \frac{(m^{reco}_{j_d \ell_a \ell_b} - m_t)^2}{\sigma^2_{t_{FCNC}}} + \frac{(m^{reco}_{j_b j_c} - m_W)^2}{\sigma^2_W}, \tag{5.1}$$

where $m^{reco}_{j_a j_b j_c}$, $m^{reco}_{j_d \ell_a \ell_b}$ and $m^{reco}_{j_b j_c}$, are the reconstructed masses of the SM top-quark, the FCNC top-quark and the W boson from the SM top-quark decay. Central values of the masses of the top quarks and W boson are taken as $m_t = 172.5$ GeV, $m_W = 80.4$ GeV. The widths ($\sigma_{t_{\mathrm{FCNC}}}$, $\sigma_{t_{\mathrm{SM}}}$, σ_W) are taken from simulated signal events. This is done by matching the particles in the simulated events to the reconstructed ones and then performing Bukin fits[2] [142] to the masses of the matched reconstructed top quarks and W boson. The obtained values are $\sigma_{t_{\mathrm{FCNC}}} = 9.8$ GeV, $\sigma_{t_{\mathrm{SM}}} = 21.5$ GeVand $\sigma_W = 12.1$ GeV.

After the event reconstruction, following requirements are applied: $|m^{\mathrm{reco}}_{j_a j_b j_c} - 172.5\ \mathrm{GeV}| < 40$ GeV, $|m^{\mathrm{reco}}_{j_d \ell_a \ell_b} - 172.5\ \mathrm{GeV}| < 40$ GeV, and $|m^{\mathrm{reco}}_{j_b j_c} - 80.4\ \mathrm{GeV}| < 30$ GeV. In the retained events, the fraction of correct assignments between the reconstructed top quarks and the true simulated particles (evaluated as a match within a cone of $\Delta R < 0.4$) is $\epsilon_{tops} = 71.6\%$.

[2]These fits use a piecewise function with a Gaussian function in the centre and two asymmetric tails. Five parameters determine the overall normalization, the peak position, the width of the core, the asymmetry, the size of the lower tail, and the size of the higher tail. From these parameters, only the width enters the χ^2.

The selection of the signal region (SR) is concluded with the requirement on the multivariate discriminant $\mathcal{D} > 0.75$, that optimizes the signal significance, as described in Section 5.5.

5.3.3. Trilepton event selection and reconstruction

The final stage topology of $t\bar{t} \to bW(\to \ell\nu)qZ(\to \ell^+\ell^-)$ signal events includes three charged leptons, at least 2 jets, one of the jets originating from a b-quark, and missing transverse momentum from the undetected neutrino.

Selected events are required to have exactly three reconstructed isolated charged leptons. Two of the leptons are required to have the same flavour, opposite charge and a reconstructed mass within 15 GeV of the Z boson mass. If more than one compatible lepton-pair is found, the one with the reconstructed mass closest to m_Z is chosen as the Z boson candidate. According to the signal topology, the events are then required to have $E_{\mathrm{T}}^{\mathrm{miss}} > 20$ GeV and two jets, although an additional third jet from initial- or final-state radiation is allowed. One or two of the jets must be b-tagged. Only one b-tagged jet is expected in the signal events, nevertheless a second one can arise from a misidentified c-jet associated with the FCNC decay of the top quark. Allowing for the additional b-tagged jet increases the signal efficiency without compromising the signal-to-background ratio. In addition, selected jets are required to have $p_{\mathrm{T}} > 35$ GeV.

Applying energy–momentum conservation, the kinematics of the top quarks can be reconstructed from the corresponding decay particles. Since the neutrino from the semileptonic decay of the top quark ($t \to bW \to b\ell\nu$) is undetected, its four-momentum must be estimated. This can be done by assuming that the lepton not previously assigned to the Z boson, and the b-tagged jet (labelled b-jet) originate from the W boson and SM top-quark decays, respectively, and that $E_{\mathrm{T}}^{\mathrm{miss}}$ is the neutrino's transverse momentum. The longitudinal component of the neutrino's momentum (p_z^ν) is then determined by minimizing, the following expression:

$$\chi^2 = \frac{\left(m^{\mathrm{reco}}_{j_a\ell_a\ell_b} - m_{t_{\mathrm{FCNC}}}\right)^2}{\sigma^2_{t_{\mathrm{FCNC}}}} + \frac{\left(m^{\mathrm{reco}}_{j_b\ell_c\nu} - m_{t_{\mathrm{SM}}}\right)^2}{\sigma^2_{t_{\mathrm{SM}}}} + \frac{\left(m^{\mathrm{reco}}_{\ell_c\nu} - m_W\right)^2}{\sigma^2_W}, \tag{5.2}$$

where $m^{\mathrm{reco}}_{j_a\ell_a\ell_b}$, $m^{\mathrm{reco}}_{j_b\ell_c\nu}$, and $m^{\mathrm{reco}}_{\ell_c\nu}$ are the reconstructed masses of the qZ, bW, and $\ell\nu$ systems, respectively. The central value for the masses and the widths of the top quarks and W boson are taken from reconstructed simulated signal events. This is done by matching the true particles in the simulated events to the reconstructed ones, setting the longitudinal momentum of the neutrino to the p_z of the true simulated neutrino and then performing Bukin fits to the masses of the matched reconstructed top quarks and W boson. The values are $m_{t_{\mathrm{FCNC}}} = 173$ GeV, $\sigma_{t_{\mathrm{FCNC}}} = 10$ GeV, $m_{t_{\mathrm{SM}}} = 168$ GeV, $\sigma_{t_{\mathrm{SM}}} = 23$ GeV, $m_W = 82$ GeV and $\sigma_W = 15$ GeV.

For each jet combination, where any jet can be assigned to j_a , while j_b must correspond to a b-tagged jet, the χ^2 minimization gives the most probable value for p_z^ν. From all combinations, the one with the minimum χ^2 is chosen, along with the corresponding p_z^ν value. The fractions of correct assignments between the reconstructed top quarks and the true simulated particles (evaluated as a match within a cone of size ΔR = 0.4) are $\epsilon_{t_{\mathrm{FCNC}}} = 79.9\%$ and $\epsilon_{t_{\mathrm{SM}}} = 56.3\%$.

The selection of the signal region (SR) is concluded with the requirement of $\chi^2 < 6$, which optimizes the search sensitivity discussed in Section 5.7.

5.4. Background estimation

In this section, estimation of expected contributions from the background processes is described. As already mentioned in Section 5.1.3, MC simulated samples are used for estimation of backgrounds containing only prompt leptons, while backgrounds containing fake leptons are estimated from a data-driven method using a parameterization of the prompt- and fake-lepton efficiencies. The MC samples are normalized to their theoretical cross sections.

The background control regions are defined to check the modelling of the simulated background samples. In the dilepton channel analysis, scaling factors are extracted from the control regions for the dominant background processes and are applied in the signal region. No scaling factors are derived from the control regions in the trilepton channel analysis, however they are used to estimate the background modelling uncertainties.

5.4.1. Background control regions for dilepton channel

In the dilepton channel analysis, the tight cut on the reconstructed Z boson candidate mass significantly reduces non-Z boson production processes. Due to the high value of the Z+jets production cross-section compared to other backgrounds cross sections [143], Z+jets production is expected to dominate the background contribution in the dilepton signal region.

One of the known weakness of the leading order MC generators is the ability to correctly predict heavy flavour content of the vector boson production in association with jets. Since the Z+light and Z+heavy flavour jets samples are generated separately, it is possible to perform the normalization of Z+jets samples by simultaneous fit in two control regions enriched with Z+light and Z+heavy flavour jets events.

The control region selection for the Z+LF events includes requirement of at least 4 jets with $p_{\mathrm{T}} > 30$ GeV and non of them being b-tagged, having exactly two leptons with the same flavour, opposite-sign charge and reconstructed dilepton mass within 10 GeV of the Z boson mass. Additionally, the $t\bar{t} \to bW(\to q\bar{q})qZ(\to \ell^+\ell^-)$ events are reconstructed, as described in Section 5.3.2, and required $|m^{\mathrm{reco}}_{j_a j_b j_c} - 172.5\ \mathrm{GeV}| > 40$ GeV, $|m^{\mathrm{reco}}_{j_d \ell_a \ell_b} - 172.5\ \mathrm{GeV}| > 40$ GeV, and $|m^{\mathrm{reco}}_{j_b j_c} - 80.4\ \mathrm{GeV}| > 30$ GeV.

For the Z+HF control region definition, events are required to have at least 4 jets with $p_{\mathrm{T}} > 30$ GeV and at least one of them being b-tagged, exactly two leptons with the same flavour, opposite-sign charge and reconstructed dilepton mass within 10 GeV of the Z boson mass. The $t\bar{t} \to bW(\to q\bar{q})qZ(\to \ell^+\ell^-)$ events are reconstructed and required $|m^{\mathrm{reco}}_{j_d \ell_a \ell_b} - 172.5\ \mathrm{GeV}| > 40$ GeV.

Figures 5.1 and 5.2 present distributions for the transverse momentum of reconstructed q-

quark and Z boson candidates in the Z+LF and Z+HF control regions, respectively. MC samples are normalized to their theoretical cross sections and no further corrections are applied. The data is about 10% lower and about 10% higher than the background prediction in the Z+LF and Z+HF control regions, respectively.

In order to improve the normalization of the Z+jets samples, the Z+LF and Z+HF samples are fitted to data using simultaneous likelihood fit in the Z+LF and Z+HF control regions. The correction factors 0.78 ± 0.11 and 1.32 ± 0.21 are obtained for Z+LF and Z+HF background samples, respectively, which are then applied in the dilepton signal region.

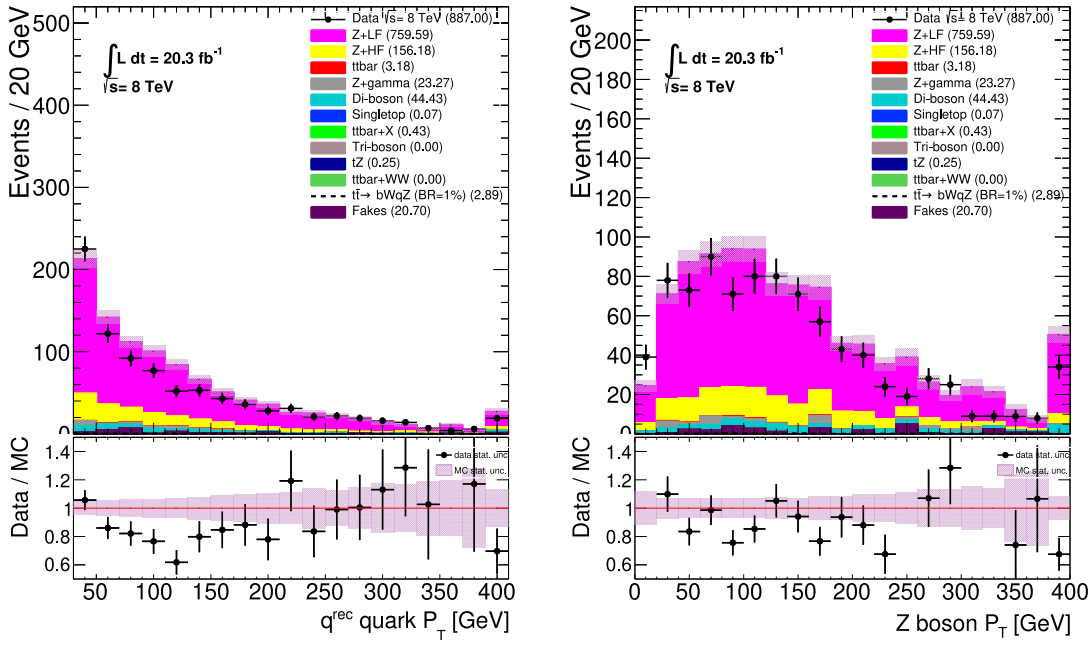

(a) (b)

Figure 5.1.: Expected (filled histogram) and observed (points with error bars) distributions for the p_{T} of the reconstructed a) q-quark and b) Z boson candidates in the Z+LF control region. Background statistical uncertainties associated with the number of events in the samples are represented by the hatched areas.

5.4.2. Background control regions for trilepton channel

Three control regions are defined to check the agreement between data and simulated samples of the ZZ, WZ and $t\bar{t}Z$ backgrounds.

The ZZ control region is defined by requiring two pairs of leptons with the same flavour, opposite charge and a reconstructed mass within 15 GeV of the Z boson mass. The expected and observed yields are shown in Table 5.1. There is a well agreement between data and expectation.

To define the control region for WZ, events are required to have three leptons, two of them

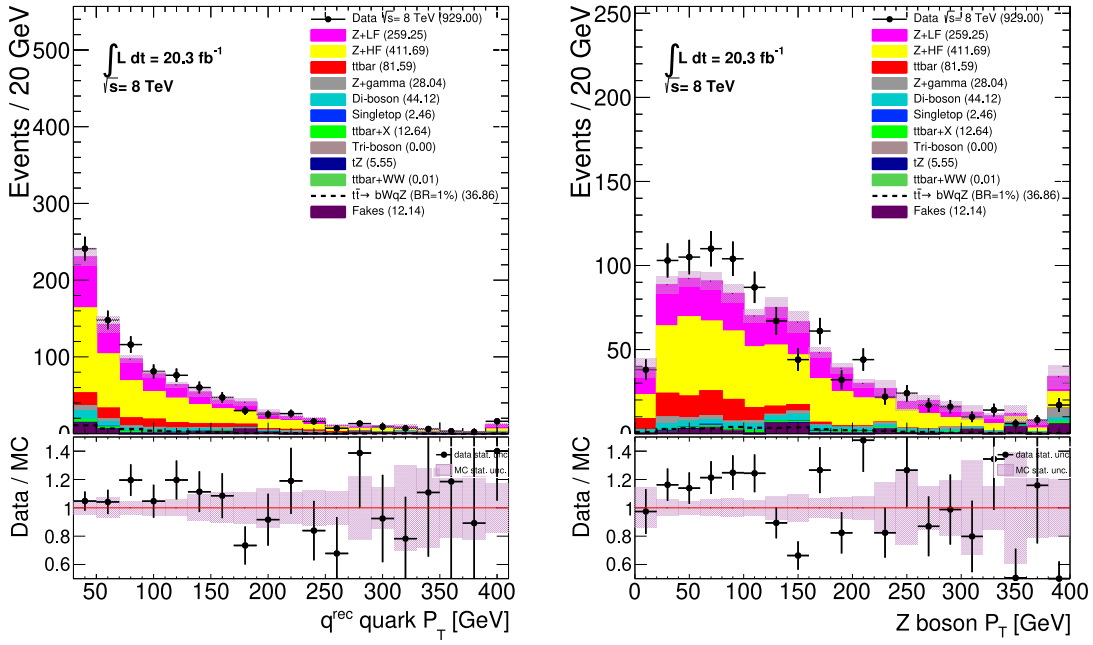

Figure 5.2.: Expected (filled histogram) and observed (points with error bars) distributions for the p_{T} of the reconstructed a) q-quark and b) Z boson candidates in the Z+HF control region. Background statistical uncertainties associated with the number of events in the samples are represented by the hatched areas.

with the same flavour, opposite charge and a reconstructed mass within 15 GeV of the Z boson mass. Presence of at least one jet with $p_{\mathrm{T}} > 35$ GeV and no b-tagged jets with $p_{\mathrm{T}} > 35$ GeV are also required. Additionally, a W boson transverse mass, built with the residual lepton and $E_{\mathrm{T}}^{\mathrm{miss}}$, is required to be greater than 50 GeV. Table 5.2 shows the expected and observed yields in this control region. The data number agrees well with the background expectation.

The $t\bar{t}Z$ control region is defined by requiring at least three leptons, two of them with the same flavour, opposite charge and a reconstructed mass within 15 GeV of the Z boson mass. Furthermore the events are required to have at least two jets with $p_{\mathrm{T}} > 25$ GeV and at least two b-tagged jets if there are three leptons in the event, or at least one b-tagged jet if there are four or more leptons in the event. Since the signal contribution for events with three leptons and two b-tagged jets is small, the overlap between signal and background regions is not removed, increasing the $t\bar{t}Z$ sensitivity in this control region. The yields in this control region are presented in Table 5.3. Background yields agree well with the data within the given uncertainty.

Backgrounds from events which contain at least one fake lepton are estimated from data using the matrix method [144]. This is based on the measurement of the efficiencies of real (prompt) and fake loose leptons to pass the nominal selection, ϵ_R and ϵ_F, and on the selection of two orthogonal sets of events in the signal region. For the first of these sets, the nominal requirements are used for the leptonic selection, while for the second one, only the leptons which satisfy the looser selection (as described in Section 5.2) but without meeting the nominal requirements are considered. For the single-lepton case, the number of events with one fake nominal lepton is $N_F^{\mathrm{nominal}} = (\epsilon_F/\epsilon_R{-}\epsilon_F)((\epsilon_R{-}1)N_T + \epsilon_R N_L)$, where N_T (N_L) represents the number of selected events in the first (second) set defined above. The method is extrapolated to the three-lepton topology, with a 8×8 matrix that is inverted using a numerical method to obtain the number of events with at least one fake lepton. The efficiencies for real and fake leptons are estimated as a function of the lepton transverse momentum by a fit of the matrix method results to two dedicated samples enriched with events of real and fake leptons: a sample of $Z \to \ell^+\ell^-, \ell = e, \mu$ and a same-sign dilepton sample (excluding same-flavour events with a reconstructed mass compatible with a Z boson). In both samples, in order to improve the modelling of fake leptons originating from heavy-flavour decays, only events with at least one additional b-tagged jet are considered. The efficiency ϵ_R ranges from 0.74 to 0.88 (0.80 to 0.99) and ϵ_F from 0.010 to 0.13 (0.035 to 0.18) for electrons (muons). The relevant uncertainties are calculated from the discrepancy between predicted and observed number of events in the control region detailed below.

A control region to test the performance of the fake-lepton estimation method and derive its uncertainty is defined. It requires three leptons with $p_{\mathrm{T}} < 50$ GeV (the third one with $p_{\mathrm{T}} < 30$ GeV), two of them having the same flavour, opposite charge and a reconstructed mass within 15 GeV of the Z boson mass, at least one b-tagged jet with $p_{\mathrm{T}} > 35$ GeV and $E_{\mathrm{T}}^{\mathrm{miss}} < 40$ GeV. As for the $t\bar{t}Z$ control region, there is a small overlap with the signal region, which is not removed in order to increase the sensitivity to the fake-lepton backgrounds. The observed and

expected yields are in agreement within the given uncertainties, as shown in Table 5.4.

Figure 5.3 shows the p_{T} of the leading lepton for the ZZ, WZ and $t\bar{t}Z$ control regions, and the reconstructed mass of the two leptons with the same flavour and opposite charge for the fake-lepton control region.

Sample	Yield
ZZ	$87 \pm 4 \pm 5$
Other backgrounds	$0.48 \pm 0.05 \pm 0.08$
Total background	$88 \pm 4 \pm 5$
Data	95

Table 5.1.: Event yields in the ZZ control region for all significant sources of background. The ZZ Sherpa sample is taken as reference. The first uncertainty is the statistical one associated with the number of events in the simulated samples, the second uncertainty is systematic and is described in Section 5.6. The entry labelled "other backgrounds" includes all the remaining backgrounds described in Section 5.1.3.

Sample	Yield
WZ	$333 \pm 5 \pm 17$
ZZ	$35 \pm 3 \pm 6$
Fake leptons	$15 \pm 3 \pm 5$
Other backgrounds	$9.5 \pm 0.3 \pm 2.4$
Total background	$392 \pm 7 \pm 19$
Data	405

Table 5.2.: Event yields in the WZ control region for all significant sources of background. The WZ Sherpa sample is taken as reference. The first uncertainty is the statistical one associated with the number of events in the simulated samples, the second uncertainty is systematic and is described in Section 5.6. The entry labelled "other backgrounds" includes all the remaining backgrounds described in Section 5.1.3.

5.5. Signal-to-background discrimination

Following the dilepton signal event kinematics reconstruction and applying the mass windows, as described in Section 5.3.2, a multivariate discriminant is built for signal-to-background discrimination.

Signal and background probabilities, P_s and P_b, are computed for each event using probability density functions (pdf), constructed from the physical variables that have different distributions for signal and background processes. The chosen variables are shown in Figure 5.4:

Sample	Yield
$t\bar{t}V$	$8.3 \pm 0.2 \pm 2.7$
tZ	$2.0 \pm 0.1 \pm 1.0$
WZ	$1.8 \pm 0.3 \pm 0.4$
Other backgrounds	$1.8 \pm 0.4 \pm 0.4$
Total background	$13.9 \pm 0.6 \pm 3.0$
Data	12

Table 5.3.: Event yields in the $t\bar{t}Z$ control region for all significant sources of background. The first uncertainty is the statistical one associated with the number of events in the simulated samples, the second uncertainty is systematic and is described in Section 5.6. The entry labelled "other backgrounds" includes all the remaining backgrounds described in Section 5.1.3.

Sample	Yield
Fake leptons	$7 \pm 1 \pm 4$
WZ	$2.7 \pm 0.4 \pm 0.7$
ZZ	$1.7 \pm 0.6 \pm 0.8$
Other backgrounds	$1.7 \pm 0.1 \pm 0.6$
Total background	$13 \pm 1 \pm 4$
Data	17

Table 5.4.: Event yields in the fake-lepton control region for all significant sources of background. The first uncertainty is the statistical one associated with the number of events in the simulated samples, the second uncertainty is systematic and is described in Section 5.6. The entry labelled "other backgrounds" includes all the remaining backgrounds described in Section 5.1.3.

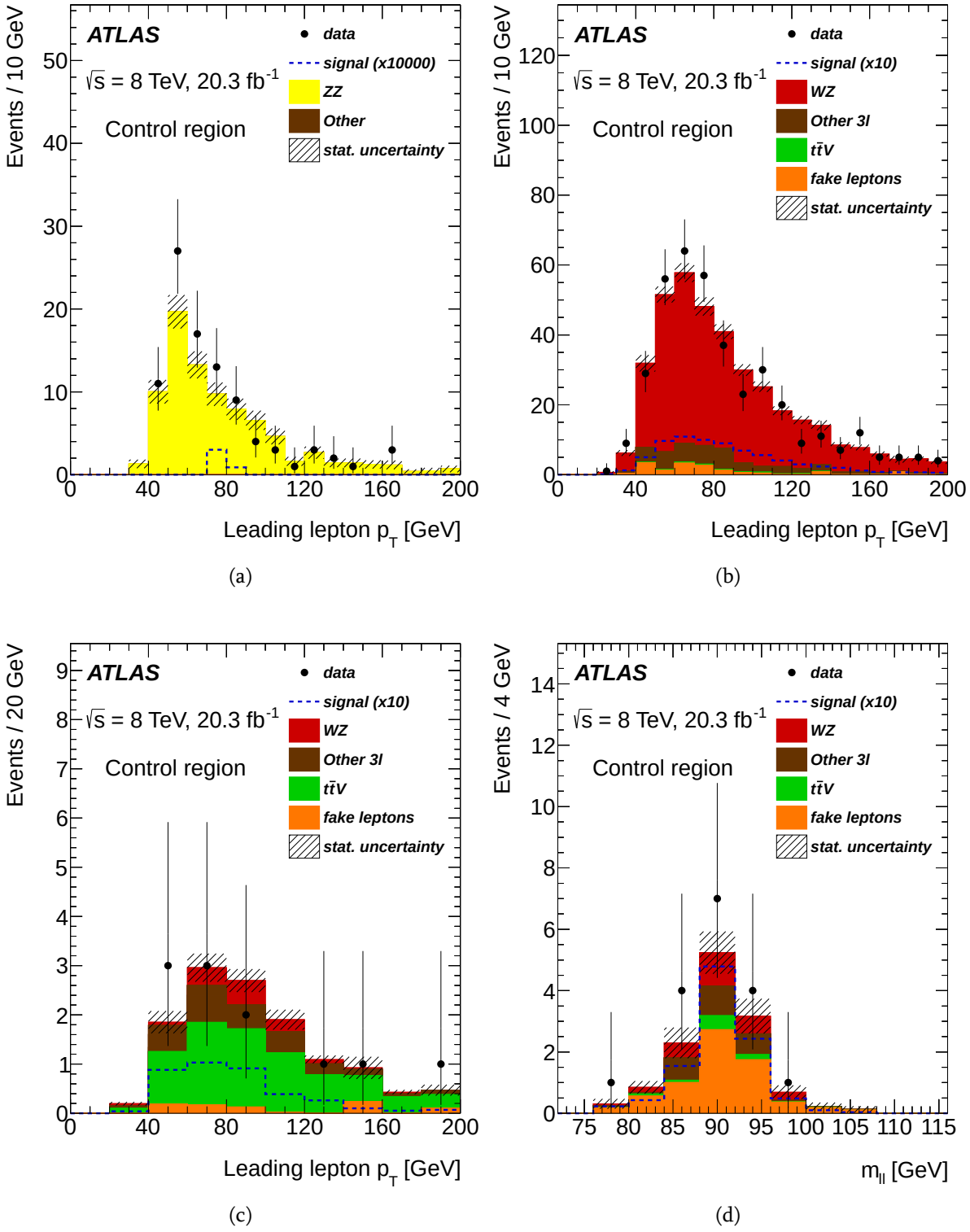

Figure 5.3.: Expected (filled histogram) and observed (points with error bars) distributions for the p_{T} of the leading lepton in the (a) ZZ, (b) WZ and (c) $t\bar{t}Z$ control regions and (d) reconstructed mass of the two leptons with the same flavour and opposite charge in the fake-lepton control region. For comparison, distributions for the FCNC $t\bar{t} \to bWqZ$ signal (dashed line), scaled to 10^4 or 10 times the observed 95% CL limit, are also shown. Background statistical uncertainties associated with the number of events in the samples are represented by the hatched areas. Adapted from [2].

the reconstructed mass of top quark from the FCNC decay, sum of the transverse momentum of the reconstructed q and b quarks coming from top quarks decays, the reconstructed mass of W boson, sum of the transverse momentum of the reconstructed W and Z bosons, the cosine of the angle between the reconstructed W and Z bosons. Correlation matrix of the chosen variables is presented in Figure 5.5. Assuming uncorrelated variables, signal and background probabilities for each event are:

$$P_s = \prod_{i=1}^{n} p_i^s(x_i), \; P_b = \prod_{i=1}^{n} p_i^b(x_i) \tag{5.3}$$

where $n = 5$ is the number of used pdfs and p_i^s (p_i^b) is the probability of an event to have the x_i value for the physical variable i, which corresponds to the signal (background) pdf. If the probability P_s is higher than P_b, then the event is signal-like, or if $P_s < P_b$ - background-like, so the multivariate discriminant can be the following:

$$\mathcal{D} = \log\left(\frac{P_s}{P_b}\right) \tag{5.4}$$

Signal-like events have higher $\mathcal{D}$ values than background-like ones. The obtained multivariate discriminant distribution is shown in Figure 5.6.

The definition of dilepton signal region is concluded by setting the cut on the $\mathcal{D}$, which optimizes the signal significance defined as $S/\sqrt{B}$, where S is the number of signal events and B - number of background events. Figure 5.7 shows the signal significance as a function of the cut on the multivariate discriminant ($\mathcal{D}^{cut}$), from this figure it can be seen that the maximum signal significance $s/\sqrt{b} = 13.66$ (signal number is normalized to the $BR(t \to qZ) = 1\%$) is achieved at the value of $\mathcal{D}^{cut} = 0.75$.

In the trilepton channel analysis, the signal-to-background discrimination is done by setting the cut on the value of χ^2 from the event kinematics reconstruction. The distribution of the χ^2 is presented in Figure 5.8. Events are required $\chi^2 < 6$, which optimizes the search sensitivity discussed in Section 5.7.

5.6. Systematic uncertainties

The effect of each source of systematic uncertainty is studied by independently varying the corresponding central value and propagating this through the full analysis chain. The relative impact of each type of systematic uncertainty on the total background and signal yields in the dilepton and trilepton signal regions is summarized in Table 5.5.

In both dilepton and trilepton channel, event modeling and experimental uncertainties re-

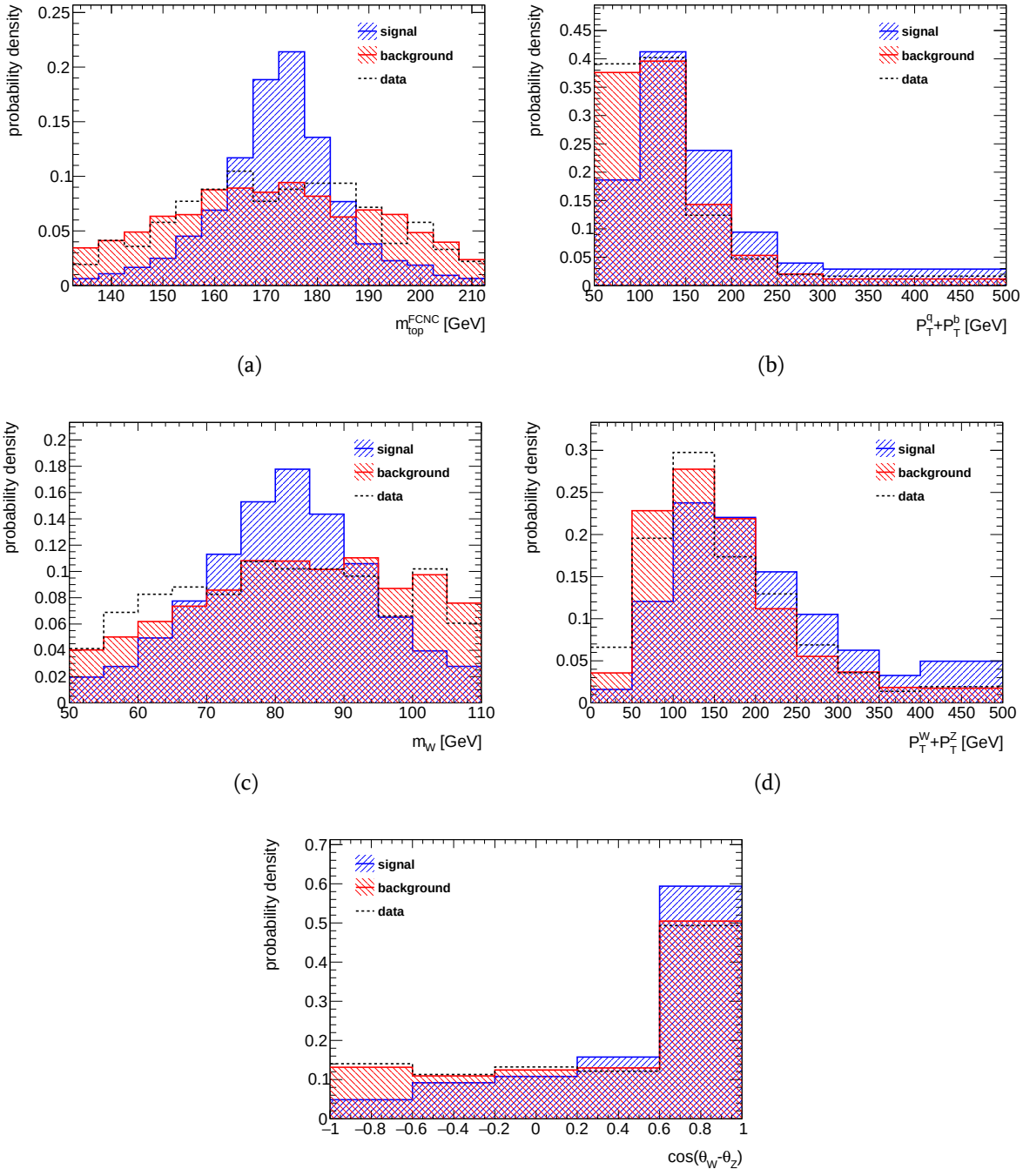

Figure 5.4.: Probability density functions for the physical variable a) the reconstructed mass of the top quark from the FCNC decay, b) sum of the transverse momentum of the reconstructed q and b quarks, c) the reconstructed mass of W boson, d) sum of the transverse momentum of the reconstructed W and Z bosons, e) the cosine of the angle between the reconstructed W and Z bosons from which the multivariate discriminant was built.

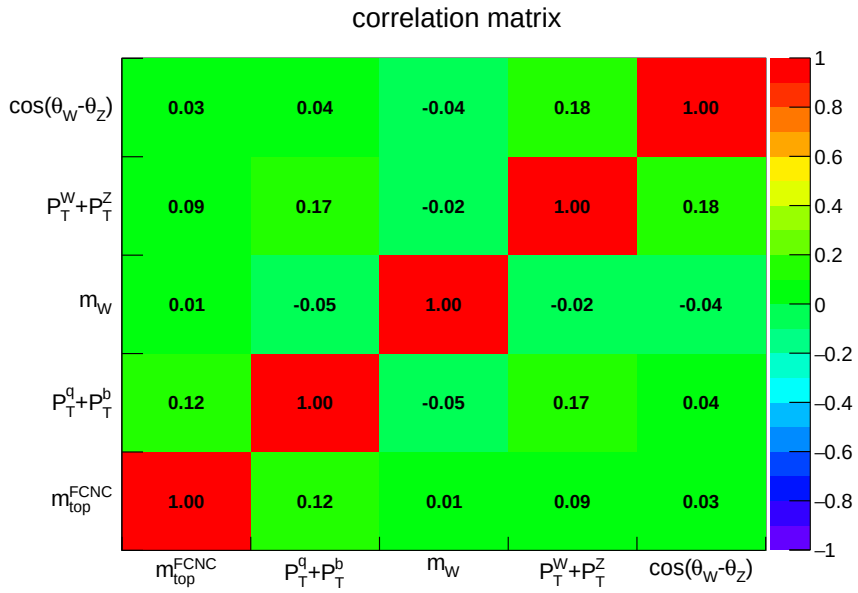

Figure 5.5.: Correlation matrix of the chosen physical variables for the multivariate discriminant.

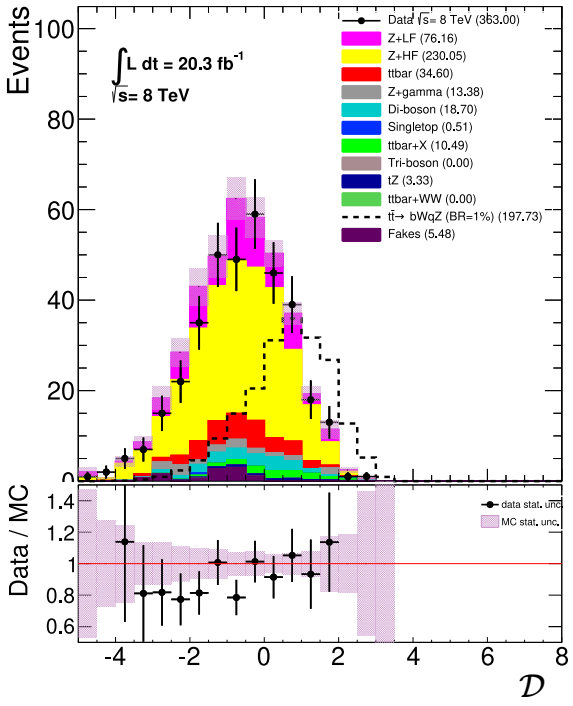

Figure 5.6.: Expected (filled histogram) and observed (points with error bars) distributions for the discriminant variable $\mathcal{D}$ in the dilepton channel. For comparison, distribution for the FCNC $t\bar{t} \to bWqZ$ signal (dashed line) normalized to the BR($t \to qZ$) = 1%, is also shown. Background statistical uncertainties associated with the number of events in the samples are represented by the hatched areas.

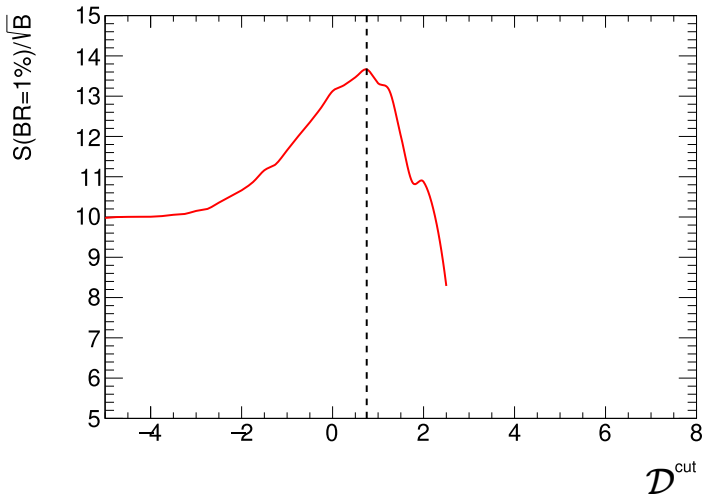

Figure 5.7.: Dependence of the signal number (normalized to a branching ratio of $t \to qZ$ of 1%) over the square root from background number on the cut on the multivariate discriminant. The vertical dashed line indicates the point where the cut is placed ($\mathcal{D}^{cut} = 0.75$ or $\mathcal{D} > 0.75$).

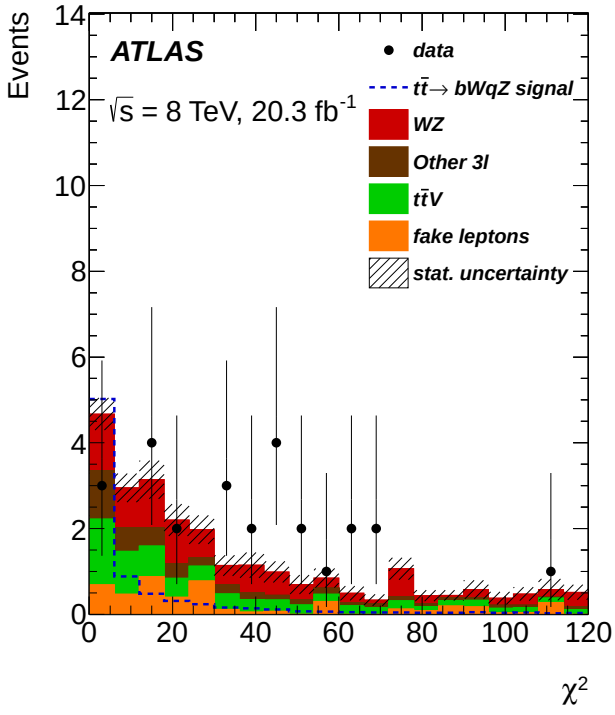

Figure 5.8.: Expected (filled histogram) and observed (points with error bars) distributions for the χ^2 of the event kinematics reconstruction in the trilepton channel. For comparison, distribution for the FCNC $t\bar{t} \to bWqZ$ signal (dashed line) normalized to the extracted observed 95% CL limit, is also shown. Background statistical uncertainties associated with the number of events in the samples are represented by the hatched areas. Adapted from [2].

sulting from detector effects are considered. Experimental uncertainties have a higher impact on the background yields in the dilepton channel, while event modeling – in the trilepton channel.

Event modeling uncertainties on the background yield in the dilepton channel includes 14.4% and 16% uncertainties of the Z+LF and Z+HF contributions due to the data-driven normalization described in Section 5.4.1. The $t\bar{t}$ background cross section uncertainty of +5.1/-5.9% is also included as well as 5% [145] and 30% [146, 147] uncertainties on the diboson and $t\bar{t}V$ normalization, respectively. In the trilepton channel it includes the following two contributions. The uncertainties on the main backgrounds are estimated using the level of agreement with data of the reference samples in the dedicated control regions described in Section 5.4.2. The uncertainties are estimated to be 6.3%, 12%, 42% and 62%, for the WZ, ZZ, $t\bar{t}Z$ and fake-lepton backgrounds, respectively. The other contribution comes from the uncertainty on the theoretical prediction in the signal region and is estimated using the alternative WZ and ZZ simulated samples. The corresponding uncertainties are 17% and 100%, respectively. Similarly, for $t\bar{t}Z$, tZ and Higgs samples, conservative values of 30% [146, 147], 50% [148] and 15% [149] respectively, are used, in order to account for the theoretical uncertainties.

The theoretical uncertainty of the signal modeling is taken as 5.5%, which takes into account the $t\bar{t}$ production cross section.

For both the estimated signal and background event yields, the lepton reconstruction, identification and trigger efficiencies, as well as lepton momentum scales and resolutions [111, 150, 151] are considered. The uncertainties affecting the jet energy scale and resolution [136, 152] are considered as well. The uncertainties on the b-tagging performance, which includes the uncertainty of the b-, c-, mistagged- and τ-jet scale factors are evaluated by varying the η-, p_{T} - and flavour-dependent scale factors applied to each jet in the simulated samples. In the trilepton channel, the $E_{\mathrm{T}}^{\mathrm{miss}}$ scale uncertainty is considered as well. All these detector systematic uncertainties are treated as fully correlated between signal and background. The evaluated values can be found in Table 5.5.

The uncertainty related to the integrated luminosity for the dataset used in this analysis is 2.8%. It is derived following the methodology described in Ref. [153]. It only affects the estimations obtained from simulated samples.

5.7. Results

Table 5.6 and 5.7 show the expected number of background events and number of selected data events in the dilepton and trilepton signal regions, respectively. The distributions of the reconstructed masses of the top quarks and Z boson in the dilepton and trilepton signal regions are presented in Figure 5.9 and 5.10, respectively. Good agreement between observed data and background expectations is observed in both channels. No evidence for the $t \to qZ$ decay is found, therefore a 95% confidence level (CL) upper limit on the number of signal events is

Source	Dilepton SR		Trilepton SR	
	B [%]	S [%]	B [%]	S [%]
Event modelling	10	5.5	17	5.5
Leptons	3.9	1.7	4.7	2.9
Jets	16	8.9	7.7	4.9
b-tagging	4.7	6.3	3.9	7.2
$E_{\mathrm{T}}^{\mathrm{miss}}$	—	—	3.2	1.5
Luminosity	2.8	2.8	2.4	2.8
Statistical	6.0	2.0	8.1	1.5

Table 5.5.: Summary of the relative impact of each type of uncertainty on the total background (B) and signal (S) yields in the dilepton and trilepton signal regions.

derived using the modified frequentist likelihood method [154, 155].

In the dilepton channel, the statistical analysis is based on a likelihood function $L(\mu, \theta)$ constructed as a product of one Poisson probability term for the number of observed events and several Gaussian constraint terms for θ, a set of nuisance parameters that parametrize the effects of MC statistical and systematic uncertainties on the signal and background expectations. This function depends on the parameter μ, which is a multiplicative factor for the number of signal events normalized to the reference branching ratio of $t \to qZ$ of 1%. Constraining the $\mathrm{BR}(t \to bW) = 1 - \mathrm{BR}(t \to qZ)$, the relationship between μ and the corresponding $\mathrm{BR}(t \to qZ)$ is

$$\mu = \frac{\mathrm{BR}(t \to qZ)(1 - \mathrm{BR}(t \to qZ))}{\mathrm{BR}_{\mathrm{ref}}(t \to qZ)(1 - \mathrm{BR}_{\mathrm{ref}}(t \to qZ))}. \tag{5.5}$$

The test statistic q_μ is defined using the profile likelihood ratio as follows:

$$q_\mu = \begin{cases} -2 \ln \lambda(\mu) & \hat{\mu} \leq \mu \\ 0 & \hat{\mu} > \mu \end{cases} \tag{5.6}$$

with

$$\lambda(\mu) = \frac{L(\mu, \hat{\hat{\theta}})}{L(\hat{\mu}, \hat{\theta})}, \tag{5.7}$$

where $\hat{\mu}$ and $\hat{\theta}$ are the values of the parameters that maximize the likelihood function (with the constraints $0 \leq \hat{\mu} \leq \mu$), and $\hat{\hat{\theta}}$ are the values of the nuisance parameters that maximize the likelihood function for a given value of μ. This test statistic is used to measure the compatibility of the observed data with the background-only hypothesis (i.e. for $\mu = 0$), and to make statistical inferences about μ, such as upper limits using the CL_s method [154, 155]. The CL of

the extracted limit is defined as:

$$\mathrm{CL} = 1 - \mathrm{CL}_s \tag{5.8}$$

with

$$\mathrm{CL}_s = \frac{\int_{q_\mu^{obs}}^{\infty} f(q_\mu|\mu) dq_\mu}{\int_{q_\mu^{obs}}^{\infty} f(q_\mu|0) dq_\mu}, \tag{5.9}$$

where $f(q_\mu|\mu)$ is the pdf of q_μ, and q_μ^{obs} is the test statistic observed from data for a given value of μ. The expected upper limit on μ is the one which would be obtained if the data events were perfectly described by the expected background and it can be computed by replacing q_μ^{obs} with the median value of q_μ assuming a parameter $\mu = 0$. The CL_s was calculated using the asymptotic properties of $\lambda(\mu)$ [156] as implemented in RooStats [157].

In the tripelton channel, the test-statistic X_d, which compares the number of observed data events with background and signal expectations, is defined as:

$$X_d = n \ln\left(1 + \frac{s}{b}\right), \tag{5.10}$$

where n, b and s are the numbers of data, expected background and signal events, respectively. The X_d statistical test is then compared to 10^5 pseudo-experiments for the hypotheses of signal plus background (X_{s+b}) and background-only (X_b), which are obtained by replacing n with the corresponding number of events produced by each pseudo-experiment. The statistical fluctuations of the pseudo-experiments are implemented assuming that the number of events follows a Poisson distribution. All statistical and systematic uncertainties on the expected backgrounds and signal efficiencies, as described in Section 5.6, are taken into account and implemented assuming Gaussian distributions. The CL for a given signal hypothesis s is defined as [154]:

$$\mathrm{CL} = 1 - \frac{\int_0^{X_d} P_{s+b}(X) dX}{\int_0^{X_d} P_b(X) dX}, \tag{5.11}$$

where P_{s+b} and P_b are the probability density functions obtained from the pseudo-experiments for the X_{s+b} and X_b values, respectively, and are functions of s and b. For the calculation of expected limit the X_d is replaced with the median of the statistical test for the background hypothesis (X_b).

In both channels, the upper limit on the number of signal events is determined as the value of the signal number that corresponds to the CL of 95%. The limits on the number of signal events are converted into upper limits on the BR($t \to qZ$) assuming that only one FCNC mode contributes. Table 5.8 shows the observed limits on BR($t \to qZ$) together with the expected limits and corresponding $\pm 1\sigma$ bounds. The observed limits are in agreement with the expected sensitivity, assuming that the data are described correctly by the SM background expectations. The expected sensitivity in the trilepton channel is about 3 times better than the one in the

dilepton channel, while the observed limit is about 4 times stringent. Uncertainties are limited by data statistics.

Sample	Yield
Z+LF	9.1 ± 1.6
Z+HF	28.5 ± 1.8
$t\bar{t}$	4.0 ± 0.8
Other backgrounds	8.6 ± 1.5
Total background	$50 \pm 3 \pm 10$
Data	53

Table 5.6.: Expected number of background events and number of observed data events in the dilepton signal region. Quoted uncertainties on individual background samples are statistical uncertainties in the simulated samples. The first uncertainty on the total background yield is the statistical one associated with the number of events in the simulated samples, the second uncertainty is systematic and is described in Section 5.6. The entry labelled "other backgrounds" includes all the remaining backgrounds described in Section 5.1.3.

Sample	Yield
WZ	$1.3 \pm 0.2 \pm 0.6$
$t\bar{t}V$	$1.5 \pm 0.1 \pm 0.5$
tZ	$1.0 \pm 0.1 \pm 0.5$
Fake leptons	$0.7 \pm 0.3 \pm 0.4$
Other backgrounds	$0.2 \pm 0.1 \pm 0.1$
Total background	$4.7 \pm 0.4 \pm 1.0$
Data	3

Table 5.7.: Expected number of background events and number of observed data events in the trilepton signal region. The first uncertainty is the statistical one associated with the number of events in the simulated samples, the second uncertainty is systematic and is described in Section 5.6. The entry labelled "other backgrounds" includes all the remaining backgrounds described in Section 5.1.3.

Channel	Observed	-1σ	Expected	$+1\sigma$
Dilepton	2.9×10^{-3}	1.9×10^{-3}	2.7×10^{-3}	3.9×10^{-3}
Trilepton	7×10^{-4}	6×10^{-4}	8×10^{-4}	12×10^{-4}

Table 5.8.: Observed and expected 95% CL upper limits on the FCNC top quark decay $t \to qZ$ branching ratios obtained in the dilepton and trilepton channels. The expected central value is shown together with the $\pm 1\sigma$ bands. Contribution from the statistical and systematic uncertainties are included.

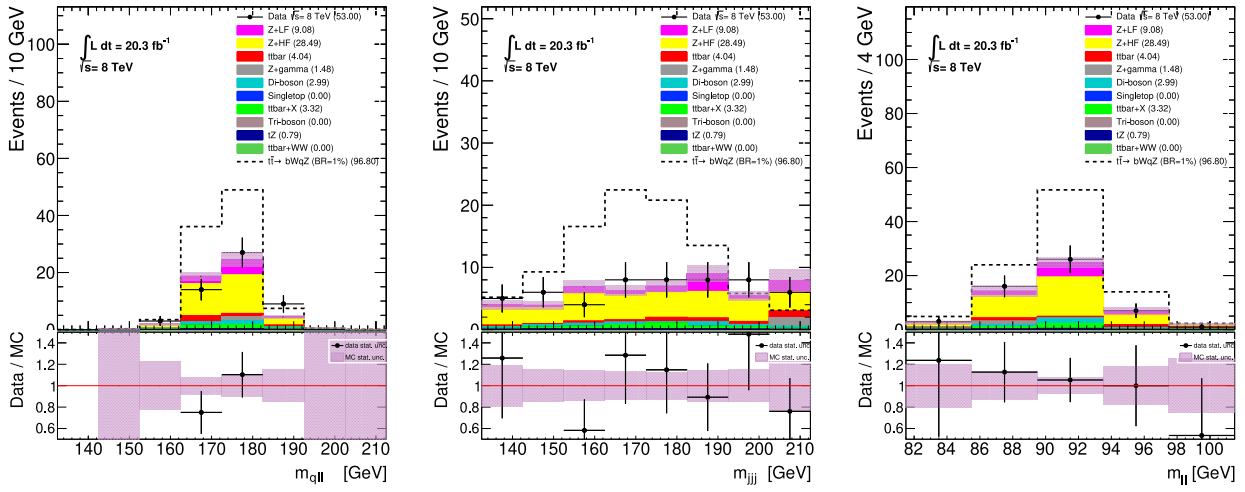

Figure 5.9.: Expected (filled histogram) and observed (points with error bars) distributions in the dilepton signal region for the reconstructed masses of the (a) top quark from the FCNC decay, (b) top quark from the SM decay and (c) Z boson. For comparison, distributions for the FCNC $t\bar{t} \to bWqZ$ signal (dashed line) normalized to the BR($t \to qZ$) = 1%, are also shown. Background statistical uncertainties associated with the number of events in the samples are represented by the hatched areas.

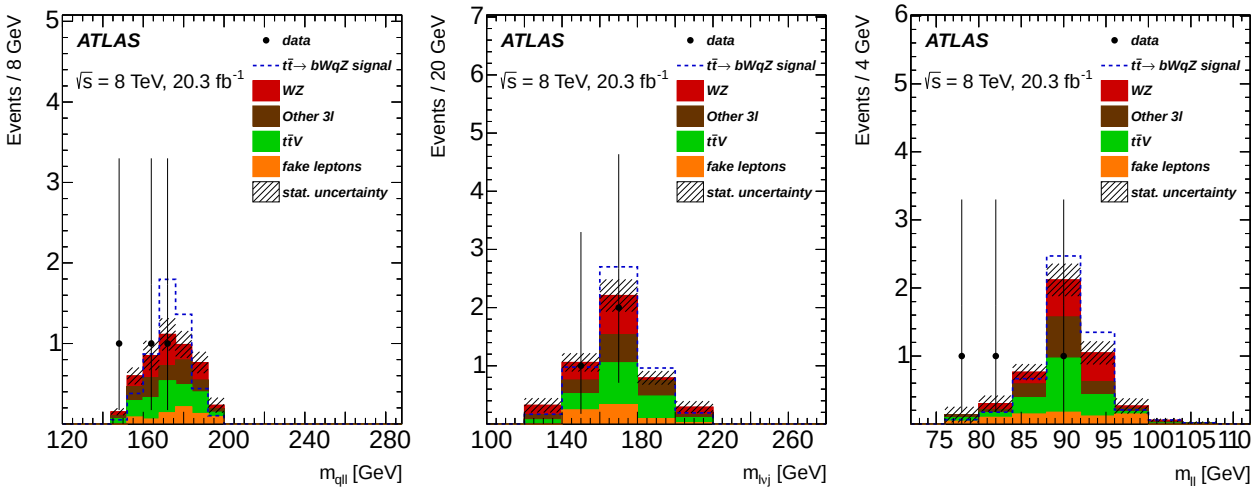

Figure 5.10.: Expected (filled histogram) and observed (points with error bars) distributions in the trilepton signal region for the reconstructed masses of the (a) top quark from the FCNC decay, (b) top quark from the SM decay and (c) Z boson. For comparison, distributions for the FCNC $t\bar{t} \to bWqZ$ signal (dashed line) normalized to the extracted observed 95% CL limit, are also shown. Background statistical uncertainties associated with the number of events in the samples are represented by the hatched areas. Adapted from [2].

5.8. Conclusions

A search for the FCNC top-quark decay $t \to qZ$ is presented, using the data collected by the ATLAS detector during 2012 from proton–proton collisions at the Large Hadron Collider at a centre-of-mass energy of $\sqrt{s} = 8$ TeV, corresponding to an integrated luminosity of 20.3 fb^{-1}. The search is performed using the top-quark–top-antiquark pair production events, with one top quark decaying through the $t \to qZ$ ($q = u, c$) FCNC channel, and the other through the dominant Standard Model mode $t \to bW$. Only Z boson decays into charged leptons and hadronic and leptonic W boson decays are considered. Consequently, two channels are used in the search: dilepton and trilepton. No evidence for the FCNC $t \to qZ$ decay is found. A 95% CL upper limit on the $t \to qZ$ branching ratio is established at BR($t \to qZ$) $< 7 \times 10^{-4}$ using the trilepton channel, which is about 4 times stringent than the limit of BR($t \to qZ$) $< 2.9 \times 10^{-3}$ obtained in the dilepton channel. Observed limits are in agreement with expected limits of BR($t \to qZ$) $< 8 \times 10^{-4}$ and BR($t \to qZ$) $< 2.7 \times 10^{-3}$ within the $\pm 1\sigma$ bands in trilepton and dilepton channels, respectively.

Chapter 6.

Search for FCNC top-quark decays $t \to qZ$ at $\sqrt{s} = 13$ TeV

A search for flavour-changing neutral-current top-quark decays $t \to qZ$ using $\sqrt{s} = 13$ TeV proton–proton collisions data is presented in this chapter. The search is performed using top-quark pair events, with one top quark decaying through the $t \to qZ$ $(q = u, c)$ flavour-changing neutral-current channel, and the other through the dominant Standard Model mode $t \to bW$. Only Z boson decays into charged leptons and leptonic W boson decays are considered as signal. Consequently, the final-state topology is characterized by the presence of three isolated charged leptons (electrons or muons) and at least two jets, one of the jets originating from a b-quark, and missing transverse momentum from the undetected neutrino.

6.1. Data and Monte Carlo samples

6.1.1. Data sample

In this analysis, the combined 2015 and 2016 datasets from proton–proton (pp) collisions at $\sqrt{s} = 13$ TeV corresponding to an integrated luminosity of 36.1 fb^{-1} are used. Analysed events are selected by either a single-electron or a single-muon trigger. Triggers with different transverse-momentum thresholds are used to increase the overall efficiency. The triggers using a low electron transverse momentum (p_{T}^{e}) or muon transverse momentum (p_{T}^{μ}) threshold ($p_{\mathrm{T}}^{e} > 24$ GeV or $p_{\mathrm{T}}^{\mu} > 20$ GeV for 2015 data and $p_{\mathrm{T}}^{e,\mu} > 26$ GeV for 2016 data) also have isolation requirements. At high p_{T} the isolation requirements incur small efficiency losses which are recovered by higher-threshold triggers ($p_{\mathrm{T}}^{e} > 60$ GeV, $p_{\mathrm{T}}^{e} > 120$ GeV, or $p_{\mathrm{T}}^{\mu} > 50$ GeV for 2015 data and $p_{\mathrm{T}}^{e} > 60$ GeV, $p_{\mathrm{T}}^{e} > 140$ GeV, or $p_{\mathrm{T}}^{\mu} > 50$ GeV for 2016 data) without isolation requirements.

6.1.2. Monte Carlo simulated samples

Monte-Carlo simulation samples (MC) are used to model the signal and several background processes. The generated samples containing top-quarks are produced with the m_{top} parameter set to 172.5 GeV. The heavy flavour decays are modelled using the EvtGen [158] program. The response of the detector to stable[1] particles is emulated by a dedicated simulation [89] based on GEANT4 [95]. A set of minimum-bias interactions generated with Pythia 8.186 [93] using the A2 set of tuned parameters [97] and the MSTW2008LO [98] PDF set were overlaid on the hard-scattering event to account for additional pp collisions in the same or nearby bunch crossings (pile-up). Simulated samples were reweighted to match the pile-up conditions in data. Detailed or fast simulations of the detector and trigger system were performed with standard ATLAS software using GEANT4 [89, 95] or ATLFASTII [89], respectively. The same offline reconstruction methods used on data are also applied to the samples of simulated events. Simulated events are corrected so that the object identification, reconstruction, and trigger efficiencies; the energy scales; and the energy resolutions match those determined from data control samples.

Table 6.1 summarizes information about the generators, parton shower, and PDFs used to simulate the different event samples considered in the analysis.

Signal samples

The next-to-leading-order (NLO) simulation of signal events was performed with the event generator MG5_aMC@NLO [159] interfaced to Pythia8 [160] with the A14 [94] set of tuned parameters and the NNPDF2.3LO PDF set [43]. Dynamic factorization and renormalization scales were used. The factorization and renormalization scales were set equal to $\sqrt{m_t^2 + (p_{\text{T},t}^2 + p_{\text{T},\bar{t}}^2)/2}$ where $p_{\text{T},t}$ ($p_{\text{T},\bar{t}}$) is the transverse momentum of the top quark (top antiquark). For the matrix element, the PDF set NNPDF3.0NLO [161] was used. For the top-quark FCNC decay, the effects of new physics at an energy scale Λ were included by adding dimension-six effective terms to the SM Lagrangian (see Section 1.3.2). No differences between the kinematical distributions from the $bWuZ$ and $bWcZ$ processes are observed. Due to the different b-tagging mistag rates for u- and c-quarks, the signal efficiencies differ after applying requirements on the b-tagged jet multiplicity. Hence limits on BR($t \to qZ$) are set separately for $q = u, c$. Only decays of the W and Z bosons with charged leptons were generated at the matrix-element level ($Z \to e^+e^-$, $\mu^+\mu^-$, or $\tau^+\tau^-$ and $W \to e\nu$, $\mu\nu$, or $\tau\nu$).

The number of signal events presented in this analysis is normalized to a reference branching ratio of $\text{BR}_{\text{ref}}(t \to qZ) = 0.1\%$, constraining $\text{BR}(t \to bW) = 1 - \text{BR}(t \to qZ)$ and using the predicted $t\bar{t}$ production cross section $\sigma_{t\bar{t}}$ = 831.76 pb as calculated with the `Top++2.0` program to next-to-next-to-leading order in perturbative QCD, including soft-gluon resummation to next-to-next-to-leading-log order (see [39] and references therein), and assuming a top-quark mass m_{top} = 172.5 GeV.

[1] A particle is considered stable if $c\tau \geqslant 1$ cm.

Background samples

Several SM processes have final-state topologies similar to the signal, with at least three prompt charged leptons, especially dibosons (WZ and ZZ), $t\bar{t}V$ (V is W or Z), $t\bar{t}\,WW$, $t\bar{t}H$, gluon–gluon fusion (ggF) H, vector-boson fusion (VBF) H, VH, tZ, WtZ, $ttt(t)$, and triboson (WWW, ZWW and ZZZ) production. The theoretical estimates for these backgrounds are further constrained by the simultaneous fit to the signal and control regions described below. Events with non-prompt leptons or events in which at least one jet is misidentified as an isolated charged lepton (labelled as fake leptons) can also fulfil the event selection requirements. These events, typically Z+jets (including γ emission), $t\bar{t}$, and single-top (Wt), are estimated with the semi-data-driven method explained in Section 6.6, which also uses simulated samples which for the Z+jets events include Z production in association with heavy-flavour quarks.

$t\bar{t} + Z/W$ production: The associated production of a $t\bar{t}$ pair with one vector boson was generated at NLO with MG5_aMC@NLO interfaced to Pythia8 with the A14 set of tuned parameters and the NNPDF2.3LO PDF set. The $t\bar{t}Z$ and $t\bar{t}W$ samples were normalized to the NLO QCD+electroweak cross-section calculation using a fixed scale ($m_t + m_V/2$) [162]. In the case of the $t\bar{t}Z$ sample with the $Z \to \ell^+\ell^-$ decay mode, the Z/γ^* interference was included with the criterion $m_{\ell\ell} > 5$ GeV applied. Alternative $t\bar{t}Z$ sample is generated with Sherpa v2.2 using LO ME with up to one additional parton included in the ME calculation and merged with the Sherpa parton shower using the ME+PS@NLO prescription [163].

tZ production: The t-channel production of a single top-quark in association with a Z boson (tZ) is generated using MG5_aMC@NLO interfaced with Pythia6 [120] with the CTEQ6L1 PDF [119] set and the Perugia2012 (P2012) [121] tune. The four-flavour PDF scheme is used in the computation. Alternative MG5_aMC@NLO_Pythia6 samples with additional radiation were considered in order to estimate the effect of QCD radiation.

WtZ production: Production of a single top quark in the Wt-channel together with a Z boson (WtZ) was generated with MG5_aMC@NLO with the parton shower simulated using Pythia8, the PDF set NNPDF2.3LO, and the A14 set of tuned parameters. The diagram removal technique [164] was employed to handle the overlap of WtZ with $t\bar{t}Z$ and $t\bar{t}$ production followed by a three-body top-quark decay ($t \to WZb$). The procedure also removes the interference between WtZ and these two processes.

Diboson production: Diboson processes with four charged leptons (4ℓ), three charged leptons and one neutrino ($\ell\ell\ell\nu$), two charged leptons and two neutrinos ($\ell\ell\nu\nu$), and diboson processes having additional hadronic contributions ($\ell\ell\ell\nu jj$, $\ell\ell\ell\ell jj$, $gg\ell\ell\ell\ell$, $\ell\ell\nu\nu jj$) were simulated using the Sherpa 2.1.1 [130] generator. The matrix elements contain all diagrams with four electroweak vertices. They were calculated for up to one (4ℓ, $2\ell + 2\nu$) or no additional partons ($3\ell + 1\nu$) at NLO and up to three partons at LO using the Comix [165] and OpenLoops [166] matrix element generators and were merged with the Sherpa parton shower using the ME+PS@NLO prescription. The CT10 PDF set was used in conjunction

with a dedicated parton shower tuning developed by the Sherpa authors. The NLO cross sections calculated by the generator are used to normalize diboson processes. Alternative diboson samples are simulated using the PowhegBox v2 [132, 133] generator, interfaced to the Pythia8 parton shower model. The CT10nlo set is used in the matrix element while the CTEQL1 PDF set is used for the parton shower along with the AZNLO [167] tune.

Higgs samples: Samples of $t\bar{t}H$ are generated using NLO matrix elements in MG5_aMC@NLO with the `NNPDF3.0` PDF set interfaced to the Pythia8 parton shower model using the PDF set NNPDF2.3LO and the A14 tune. Higgs boson production via gluon fusion and vector boson fusion (VBF) is generated using Powheg-Box v2 generator with CT10 PDF. The parton shower, fragmentation, and the underlying event are simulated using Pythia8with the CTEQ6L1 PDF set and AZNLO tune. Higgs boson production in association with a boson (VH) is generated at LO using Pythia8 with the PDF set NNPDF2.3LO and the A14 tune. All Higgs samples are normalized to the theoretical calculations of Ref. [162].

Z+jets production: Events containing Z bosons are simulated using PowhegBox v2 interfaced to the Pythia8 parton shower model. The CT10 PDF set is used in the matrix element. The AZNLO tune is used, with PDF set CTEQ6L1, for the modelling of non-perturbative effects. Photos++ version 3.52 [168] is used for QED emissions from electroweak vertices and charged leptons.

$t\bar{t}$ and Wt production: The generation of $t\bar{t}$ and single top quarks in the Wt-channel was done with Powheg-Box v2 and Powheg-Box v1, respectively. The parton shower, fragmentation and the underlying event are simulated using the Pythia8 with the A14 tune for $t\bar{t}$ sample, and using the Pythia6 with the CTEQ6L1 PDF set and the Perugia2012 tune for Wt sample. Due to the high lepton-multiplicity requirement of the event selection and to increase the sample size, the $t\bar{t}$ sample was produced by selecting only true dilepton events in the final state. To evaluate the uncertainty due to the choice of NLO generator, $t\bar{t}$ sample generated using MadGraph5_aMC@NLO interfaced to Pythia8 is used. To evaluate the uncertainty due to the choice of the parton shower algorithm, $t\bar{t}$ sample generated using Powheg interfaced to Herwig7 [169, 170] is used. In order to estimate the effect of QCD radiation on the $t\bar{t}$ samples, alternative samples generated with Powheg+Pythia8 were considered where the factorization and renormalization scale was varied up and down by a factor of two and the A14 tune variant was changed correspondingly to `A14v3cUp` and `A14v3cDo` [94].

Rare SM background: The SM production of three or four top-quarks and the associated production of a top-quark pair with two W bosons are generated at LO with `MG5_aMC+Pythia8`, using the `A14` tune together with the `NNPDF2.3LO` PDF set. The production of three massive vector bosons with subsequent leptonic decays of all three bosons is modelled at LO with the `Sherpa 2.1` generator. Up to two additional partons are included in the matrix element at LO.

Sample	Generator	Parton shower	ME PDF	PS PDF	Tune parameters
$t\bar{t} \to bWqZ$	MG5_aMC@NLO [159]	Pythia8 [160]	NNPDF3.0NLO [161]	NNPDF2.3LO [43]	A14 [94]
$t\bar{t}V$,$t\bar{t}H$	MG5_aMC@NLO	Pythia8	NNPDF3.0NLO	NNPDF2.3LO	A14
$t\bar{t}Z$ (alternative)	Sherpa 2.2.0 [130]	Sherpa 2.2.0	NNPDF3.0NNLO	NNPDF3.0NNLO	Sherpa default
WZ, ZZ	Sherpa 2.1.1	Sherpa 2.1.1	CT10 [127]	CT10	Sherpa default
WZ (alternative)	Powheg-Box v2 [133]	Pythia8	CT10nlo	CTEQ6L1 [119]	AZNLO [167]
tZ	MG5_aMC@NLO	Pythia6 [120]	NNPDF3.0NLO	CTEQ6L1	Perugia2012 [121]
tZ (rad. syst.)	MG5_aMC@NLO	Pythia6	NNPDF3.0NLO	CTEQ6L1	P2012RadHi/Lo [121]
WtZ	MG5_aMC@NLO	Pythia8	NNPDF3.0NLO	NNPDF2.3LO	A14
WtZ (alternative)	MG5_aMC@NLO	Herwig++ [169]	CT10	CTEQ6L1	UE-EE-5 [171]
ggF H, VBF H	Powheg-Box v2	Pythia8	CT10	CTEQ6L1	AZNLO
WH, ZH	Pythia8	Pythia8	NNPDF2.3LO	NNPDF2.3LO	A14
$3t$, $4t$, $t\bar{t}WW$	MG5_aMC@NLO	Pythia8	NNPDF3.0NLO	NNPDF2.3LO	A14
Tribosons	Sherpa 2.1.1	Sherpa 2.1.1	CT10	CT10	Sherpa default
Z+jets	Powheg-Box v2, Photos++ [168]	Pythia8	CT10	CTEQ6L1	AZNLO
$t\bar{t} \to bWbW$	Powheg-Box v2	Pythia8	CT10	NNPDF2.3LO	A14
$t\bar{t} \to bWbW$ (rad. syst.)	Powheg-Box v2	Pythia8	CT10	NNPDF2.3LO	A14v3cUp/Do [94]
$t\bar{t} \to bWbW$ (PS syst.)	Powheg-Box v2	Herwig7 [170]	NNPDF3.0NLO	MMHT2014lo68cl [172]	H7-UE-MMHT [170]
$t\bar{t} \to bWbW$ (ME syst.)	MG5_aMC@NLO	Pythia8	NNPDF3.0NLO	NNPDF2.3LO	A14
Wt	Powheg-Box v1	Pythia6	CT10f4	CTEQ6L1	Perugia2012

Table 6.1.: Generators, parton shower simulation, parton distribution functions, and tune parameters used to produce simulated samples for this analysis. The acronyms ME and PS stand for matrix element and parton shower, respectively.

6.2. Object reconstruction

The final states of interest for this search include electrons, muons, jets, b-tagged jets and missing transverse momentum. This section briefly describes the reconstruction of each of these objects. Tau leptons are not explicitly reconstructed, although the τ decay products are reconstructed as electrons, muons or jets and as an additional contribution to the missing transverse momentum.

Electrons: Electron candidates are reconstructed [173] from energy deposits (clusters) in the electromagnetic calorimeter matched to reconstructed charged-particle tracks in the inner detector. The candidates are required to have a transverse energy $E_{\mathrm{T}} > 15$ GeV and the pseudorapidity of the calorimeter energy cluster associated with the electron candidate must satisfy $|\eta_{\mathrm{cluster}}| < 2.47$. Clusters in the transition region between the barrel and endcap calorimeters, $1.37 \leq |\eta_{\mathrm{cluster}}| \leq 1.52$, have poorer energy resolution and are excluded. To reduce the background from non-prompt sources, electron candidates are also required to satisfy $|d_0|/\sigma(d_0) < 5$ and $|z_0 \sin(\theta)| < 0.5$ mm criteria, where d_0 is the transverse impact parameter, with uncertainty $\sigma(d_0)$, and z_0 is the longitudinal impact parameter with respect to the primary vertex (defined in Section 6.3.1). The sum of transverse energies of clusters in the calorimeter within a cone of $\Delta R = 0.2$ around the electron candidate, excluding the p_{T} of the electron candidate, is required to be less than 6% of the electron p_{T}. The scalar sum of particle transverse momenta around the elec-

tron candidate within a cone of min(10 GeV/p_{T}, 0.2) must be less than 6% of the electron candidate's p_{T}.

Muons: Muon candidates are reconstructed from tracks in the inner detector and muon spectrometer, which are combined to improve the reconstruction precision and to increase the background rejection [174]. They are required to have $p_{\mathrm{T}} > 15$ GeV and $|\eta| < 2.5$. Muons are also required to satisfy $|d_0|/\sigma(d_0) < 3$ and $|z_0 \sin(\theta)| < 0.5$ mm criteria. Additionally, the scalar sum of particle transverse momenta around the muon candidate within a cone of min(10 GeV/p_{T}, 0.3) must be less than 6% of the muon candidate's p_{T}.

Jets: Jets are reconstructed from topological clusters of calorimeter cells that are noise-suppressed and calibrated to the electromagnetic scale [92] using the anti-k_t algorithm [99] with a radius parameter $R = 0.4$ as implemented in FastJet [101]. Corrections that change the angles and the energy are applied to the jets, starting with a subtraction procedure that uses the jet area to estimate and remove the average energy contributed by pile-up interactions [103]. This is followed by a jet-energy-scale calibration that restores the jet energy to the mean response of a particle-level simulation by using a global sequential calibration to correct finer variations due to jet flavour and detector geometry and in situ corrections that match the data to the simulation energy scale [175]. Jets in the analysis have $p_{\mathrm{T}} > 25$ GeV and $|\eta| < 2.5$. To reduce the number of selected jets that originate from pile-up, an additional selection criterion based on a jet-vertex tagging technique is applied. Jet-vertex tagging is a likelihood discriminant combining information from several track-based variables [176] and is only applied to jets with $p_{\mathrm{T}} < 60$ GeV and $|\eta| < 2.4$.

b-tagging: Jets containing b-hadrons are identified (b-tagged) [177, 178] using an algorithm based on multivariate techniques. It combines information from the impact parameters of displaced tracks and from topological properties of secondary and tertiary decay vertices reconstructed within the jet. Using simulated $t\bar{t}$ events, the b-tagging efficiency for jets originating from a b-quark is determined to be 77% for the chosen working point, while the rejection factors for light-flavour jets and charm jets are 134 and 6, respectively.

Missing transverse momentum The missing transverse momentum $\vec{p}_{\mathrm{T}}^{\,\mathrm{miss}}$ is the negative vector sum of the p_{T} of all selected and calibrated objects in the event, including a term to account for soft particles in the event that are not associated with any of the selected objects [139, 179]. To reduce contamination from pile-up interactions, the soft term is calculated from inner detector tracks matched to the selected primary vertex. The magnitude of the missing transverse momentum is $E_{\mathrm{T}}^{\mathrm{miss}}$.

Overlap removal: To avoid double counting of single final-state objects, such as an isolated electron being reconstructed as both an electron and a jet, the following procedures are applied in the order given. Electron candidates which share a track with a muon candidate are removed. If the distance in ΔR between a jet and an electron candidate is $\Delta R < 0.2$, then the jet is dropped. If, for the same electron, multiple jets are found with this

requirement, only the closest one is dropped. If the distance in ΔR between a jet and an electron is $0.2 < \Delta R < 0.4$, then the electron is dropped. If the distance in ΔR between a jet and a muon candidate is $\Delta R < 0.4$ and if the jet has more than two associated tracks, the muon is dropped; otherwise the jet is removed.

6.3. Event selection and reconstruction

6.3.1. Preselection

All events considered in the analysis are required to pass the following selection requirements.

Data quality: Data events must be recorded in a luminosity block that is part of the good runs list. Data events in which the LAr or Tile calorimeters are flagged to be in error state are removed from the analysis.

Vertex selection: Events are required to have a primary vertex, which must have at least two associated tracks, each with $p_{\mathrm{T}} > 400$ MeV. The primary vertex with the highest sum of p_{T}^2 over all associated tracks is chosen.

Bad jet cleaning: Events containing fake jets (arising from non-collision background or cosmic events) or fake signals in the calorimeter (either from noise bursts or from the presence of coherent noise) are removed.

Trigger: All events are required to have triggered one of the single electron or single muon triggers listed in Table 6.2.

Trigger matching: At least one of the selected leptons must be matched, with $\Delta R < 0.15$, to the appropriate trigger object and have transverse momentum greater than 25 GeV or 27 GeV for the data collected in 2015 or 2016, respectively.

6.3.2. Event selection and kinematics reconstruction

The final state corresponding to top-quark pair production events with one of the top-quarks decaying via FCNC into qZ with Z boson decays into charged leptons, and the other through the dominant SM decay mode $t \to bW$ with leptonic W boson decays, is characterized by the presence of three isolated charged leptons, at least two jets, one of the jets originated from a b-quark, and missing transverse momentum from the undetected neutrino.

According to the considered final state topology, selected events are required to have exactly three leptons (electrons and/or muons), at least one pair of leptons with same flavour, opposite charge and a reconstructed mass within 15 GeV of the Z boson mass, at least two jets with only one being b-tagged and missing transverse momentum greater than 20 GeV.

Triggers in 2015 [180]	
HLT_e24_lhmedium_L1EM20VH	Software-based high level electron trigger that requires $E_{\mathrm{T}} > 24$ GeV and likelihood-based medium identification criteria. The trigger is seeded by first level trigger L1_EM20VH.
HLT_e60_lhmedium	Software-based high level electron trigger that requires $E_{\mathrm{T}} > 60$ GeV and likelihood-based medium identification criteria.
HLT_e120_lhloose	Software-based high level electron trigger that requires $E_{\mathrm{T}} > 120$ GeV and likelihood-based loose identification criteria.
HLT_mu20_iloose_L1MU15	Software-based high level muon trigger that requires $E_{\mathrm{T}} > 20$ GeV and loose isolation criteria. The trigger is seeded by first level trigger L1_MU15.
Triggers in 2016 [181]	
HLT_e26_lhtight_nod0_ivarloose	Software-based high level electron trigger that requires $E_{\mathrm{T}} > 26$ GeV and likelihood-based tight identification criteria without applying transverse impact parameter requirements, but applying variable-size cone isolation.
HLT_e60_lhmedium_nod0	Software-based high level electron trigger that requires $E_{\mathrm{T}} > 60$ GeV and likelihood-based medium identification criteria without applying transverse impact parameter and isolation requirements.
HLT_e140_lhloose_nod0	Software-based high level electron trigger that requires $E_{\mathrm{T}} > 140$ GeV and likelihood-based loose identification criteria without applying transverse impact parameter and isolation requirements.
HLT_mu26_ivarmedium	Software-based high level muon trigger that requires $E_{\mathrm{T}} > 26$ GeV and medium isolation criteria.
HLT_mu50	Software-based high level muon trigger that requires $E_{\mathrm{T}} > 50$ GeV and without applying isolation requirements.

Table 6.2.: Description of single electron and single muon triggers used in this analysis.

The kinematics of the top-quarks can be reconstructed from the corresponding decay particles. Two leptons coming from top-quark FCNC decay ($t \to qZ \to q\ell\ell$) are determined as a opposite sign and same flavour (OSSF) leptons pair which gives the closest mass to 91.2 GeV. The remaining lepton is assigned to the charged lepton from Standard Model semileptonic decay of the top-quark ($t \to bW \to b\ell\nu$). Since the neutrino from the W decay is undetected, its four-momentum needs to be estimated. This can be done by assuming the missing transverse momentum to be the neutrino transverse momentum. The longitudinal component of the neutrino momentum (p_z^ν) is then determined by minimizing, the following expression:

$$\chi^2 = \frac{\left(m^{\text{reco}}_{j_a\ell_a\ell_b} - m_{t_{\text{FCNC}}}\right)^2}{\sigma^2_{t_{\text{FCNC}}}} + \frac{\left(m^{\text{reco}}_{j_b\ell_c\nu} - m_{t_{\text{SM}}}\right)^2}{\sigma^2_{t_{\text{SM}}}} + \frac{\left(m^{\text{reco}}_{\ell_c\nu} - m_W\right)^2}{\sigma^2_W}, \tag{6.1}$$

where $m^{\text{reco}}_{j_a\ell_a\ell_b}$, $m^{\text{reco}}_{j_b\ell_c\nu}$, and $m^{\text{reco}}_{\ell_c\nu}$ are the reconstructed masses of the qZ, bW, and $\ell\nu$ systems, respectively. The central value for the masses and the widths of the top quarks and W boson are taken from reconstructed simulated signal events. This is done by matching the true particles in the simulated events to the reconstructed ones, setting the longitudinal momentum of the neutrino to the p_z of the true simulated neutrino and then performing Bukin fits[2] [142] to the masses of the matched reconstructed top quarks and W boson (more details are in Appendix B). The values are $m_{t_{\text{FCNC}}} = 169.6$ GeV, $m_{t_{\text{SM}}} = 167.2$ GeV, $m_W = 81.2$ GeV, $\sigma_{t_{\text{FCNC}}} = 12.0$ GeV, $\sigma_{t_{\text{SM}}} = 24.0$ GeV and $\sigma_W = 15.1$ GeV. Studies show that the final result, expected limit on BR($t \to qZ$), is weakly sensitive to these values.

For each jet combination, where any jet can be assigned to j_a, while j_b must correspond to a b-tagged jet, the χ^2 minimization gives the most probable value for p_z^ν. From all combinations, the one with the minimum χ^2 is chosen, along with the corresponding p_z^ν value. The jet associated to the top-quark from the SM decay is labeled as the b-quark jet. The jet from the top-quark with the FCNC decay is denoted as the light (q) quark jet.

6.4. Signal region

Following the event selection and kinematics reconstruction, described in the previous section, the signal region (SR) is defined by applying the mass windows on the reconstructed objects, as can be found in Table 6.3.

The expected yields in the signal region can be found in Table 6.4. Presented uncertainties include statistical and systematic components which are discussed in Section 6.8. The dominant backgrounds come from $t\bar{t}Z$, WZ and fake leptons. These backgrounds are studied in detail in the following sections.

Figures 6.1-6.2 show the expected distributions for the invariant masses of the reconstructed

[2]These fits use a piecewise function with a Gaussian function in the centre and two asymmetric tails. Five parameters determine the overall normalization, the peak position, the width of the core, the asymmetry, the size of the lower tail, and the size of the higher tail. From these parameters, only the peak position and the width enter the χ^2.

Z boson, W boson and the top-quarks, while in Figure 6.3 the distributions of the missing transverse momentum, p_{T} of the b-quark and q-quark jets are presented. Figure 6.4 shows the resulting χ^2 after the reconstruction. For these plots, the data are blinded. The distributions with unblinded data can be found in Section 6.10.3.

6.5. Background control and validation regions

The backgrounds considered are the ones that contain three reconstructed leptons in the final state, which can be real or fake-leptons[3]. Backgrounds that can produce three real leptons in the final states come primarily from WZ, $t\bar{t}Z$ and tZ processes. Such backgrounds were estimated using MC simulation, while backgrounds containing at least one fake-lepton were estimated using the semi-data-driven technique that is described later in Section 6.6.

In order to check the estimation of the main background processes, several control regions are defined. Later these control regions are used in the combined fit with the signal region, as described in Section 6.10.1, to allow a tighter constraint of background expectations and systematic uncertainties for the statistical analysis. To validate the fit procedure, two validation regions (VRs), not included in the combined fit, are defined.

The selection requirements applied in all regions defined in this analysis are summarized in Table 6.3, which includes the Fake Scale Factors fit regions (see Section 6.6), background control and signal regions included in the final fit (see Section 6.10.1), and the validation regions that are not included in the fit. The details of the selection requirements are explained in the following sections.

	Fakes SFs Fit Regions		Final Fit Regions					Validation Regions	
Selection	Z+jets CR	$t\bar{t}$ CR	Fakes CR0(CR1)	$t\bar{t}Z$ CR	WZ CR	ZZ CR	SR	Side-band VR	WZ VR
N leptons	= 3	= 3	= 3	= 3	= 3	= 4	=3	= 3	= 3
OSSF	Yes	No	Yes	Yes	Yes	Yes	Yes	Yes	Yes
$\lvert m_z$ - 91.2$\rvert$	< 15 GeV	-	> 15 GeV	< 15 GeV	< 15 GeV	< 15 GeV	< 15 GeV	< 15 GeV	< 15 GeV
N jets	≥ 1	≥ 2	≥ 2	≥ 4	≥ 2	≥ 1	≥ 2	≥ 2	= 1
N b-tags	≤ 1	≤ 1	= 0 (= 1)	= 2	= 0	= 0	= 1	= 1	= 1
$E_{\mathrm{T}}^{\mathrm{miss}}$	< 40 GeV	-	> 20 GeV	> 20 GeV	> 40 GeV	> 20 GeV	> 20 GeV	> 20 GeV	> 20 GeV
m_{T}^{w}	< 50 GeV	-	-	-	> 50 GeV	-	-	-	> 50 GeV
$\lvert m_w$ - 80.4$\rvert$	-	-	-	-	-	-	< 30 GeV	-	-
$\lvert m_{\mathrm{top}}^{\mathrm{SM}}$ - 172.5$\rvert$	-	-	-	-	-	-	< 40 GeV	-	-
$\lvert m_{\mathrm{top}}^{\mathrm{FCNC}}$ - 172.5$\rvert$	-	-	-	-	-	-	< 40 GeV	> 40 GeV	-

Table 6.3.: The selection requirements applied for the Fake Scale Factor fit regions, background control and signal regions included in the combined fit, and the validation regions.

[3]The "fake-lepton" denotes a reconstructed lepton not coming from a W, Z or τ decay. Typically it arises from the decay of a bottom or charm hadron, an electron from a photon conversion, a jet misidentified as an electron, or a muon produced from an in-flight decay of a pion or kaon.

6.5.1. Control region for backgrounds with fake-leptons

To study the backgrounds with fake-leptons the following control region was tested: exactly three leptons, at least one pair of leptons with the opposite sign charge and same flavour, at least two jets. To enrich contribution from fake-leptons it is also required that $|m_{\ell\ell} - 91.2| > 15$ GeV, where $m_{\ell\ell}$ is the reconstructed mass of OSSF leptons pair giving the value closest to 91.2 GeV. This cut makes the CR orthogonal to the SR. To be closer to the signal region in phase space, $E_{\mathrm{T}}^{\mathrm{miss}}$ is required to be greater than 20 GeV. In the different control/signal regions different number of b-tags is used. Since the fake lepton rate depends on the b-jet multiplicity, it is important to control this background in the used b-tag multiplicity bins separately. Therefore the fakes control region is split into two regions depending on b-tag multiplicity: no b-tag (CR0) and one b-tag (CR1). Defining fakes control region with two b-tags is not important since events with two b-tags are used only in $t\bar{t}Z$ CR where fake-leptons contribution is not significant (see following section).

The expected and observed event yields can be found in Table 6.4, while the distributions of leading lepton p_{T}, leading jet p_{T}, missing transverse energy and jet multiplicity in these CRs are presented in Figures 6.5-6.8. Agreement between data and background is within uncertainty.

6.5.2. Control region for $t\bar{t}Z$ background

Another important background of the analysis comes from $t\bar{t}Z$ production and for this reason it is important to control the corresponding MC. The selection consists of requiring three leptons with at least one pair of leptons with the same flavour and opposite charge, at least four jets, two b-tagged jets and missing transverse energy greater than 20 GeV. The Z boson is reconstructed using the OSSF leptons pair giving the mass closest to 91.2 GeV, requiring $|m_Z - 91.2| < 15$ GeV.

The expected and observed event yields in this CR can be found in Table 6.4, while the distributions of reconstructed Z boson mass, missing transverse energy, leading lepton p_{T} and leading jet p_{T} can be found in Figure 6.9 and 6.10. A good agreement between data and prediction is observed in this CR.

6.5.3. Control region for WZ background

To define a control region dominated by the WZ background the following selection is applied: exactly 3 leptons with at least one OSSF pair of leptons, at least two jets (leading jet with $p_{\mathrm{T}} > 35$ GeV), none of which pass the b-tagging requirement, and missing transverse energy greater than 40 GeV. The Z boson is reconstructed using the OSSF leptons pair giving the mass closest to 91.2 GeV, requiring $|m_Z - 91.2| < 15$ GeV. Additionally a cut on the W boson trans-

verse mass[4], $m_{\mathrm{T}} > 50$ GeV, is required to ensure the purity of the WZ samples.

Expected and observed event yields are presented in Table 6.4 and Figures 6.11-6.12 show the distributions of the W boson transverse mass, Z boson mass, missing transverse energy, leading lepton p_{T}, leading jet p_{T} and jet multiplicity. Total background is underestimated, though the agreement between data and prediction is within less than one sigma uncertainty of total expected background.

6.5.4. Control region for ZZ background

In order to control correctly the diboson (WZ, ZZ) normalization in the simultaneous likelihood fit (see Section 6.10.1), it is important to define a control region for ZZ background. Requiring exactly 4 leptons with at least 2 OSSF pair of leptons giving the mass compatible with that of the Z boson within a 15 GeV window, it is possible to select almost only ZZ events. To be closer to the signal region at least one jet and $E_{\mathrm{T}}^{\mathrm{miss}} > 20$ GeV are required in addition.

Expected and observed event yields in this CR are presented in Table 6.4, while Figure 6.13 presents the distributions of the reconstructed mass of the ZZ system, p_{T} of the leading jet and jet multiplicity. The data and prediction agree within the uncertainty.

6.5.5. Side-band validation region

As already mentioned, the background control regions defined above are used in the simultaneous likelihood fit to calibrate the estimation of the main background processes, as described in Section 6.10.1. In order to validate the background calibration procedure the side-band validation region is defined by inverting the signal region window cut on FCNC top-quark mass, keeping the window on the Z boson mass and not applying any cut on the W boson and SM top-quark masses. This region is not included in the fit.

The expected and observed event yields are shown in Table 6.5, while Figure 6.14 shows the distributions of the W and Z boson masses and the leading lepton p_{T}. The distribution of the χ^2 is presented in Figure 6.15.

6.5.6. Validation region for WZ background

In addition to the side-band validation region, the WZ validation region is defined to validate the WZ background normalization in one b-tag events. This region is not included in the combined fit. Selection requirements are the following: exactly 3 leptons with at least one OSSF pair of leptons, exactly one jet which passes the b-tagging requirement, and missing transverse

[4]The transverse mass is calculated using the momentum of the lepton associated with the W boson, $E_{\mathrm{T}}^{\mathrm{miss}}$ and azimuthal angle,ϕ, between them: $m_{\mathrm{T}} = \sqrt{2p_{\mathrm{T}}^{\ell} E_{\mathrm{T}}^{\mathrm{miss}} (1 - \cos\Delta\phi)}$

energy greater than 20 GeV. The Z boson is reconstructed using the OSSF leptons pair giving the mass closest to 91.2 GeV, requiring $|m_Z - 91.2| < 15$ GeV. A cut on the W boson transverse mass, $m_{\mathrm{T}} > 50$ GeV, is required.

Expected and observed event yields are presented in Table 6.5. Figure 6.16 shows the distributions of the W boson transverse mass, Z boson mass and missing transverse energy. Agreement between data and prediction is within uncertainty.

Sample	WZ CR	ZZ CR	$t\bar{t}Z$ CR	Fakes CR0	Fakes CR1	SR
$t\bar{t}Z$	16.3 ± 3.13	0 ± 0	60.8 ± 8.71	6.08 ± 1.24	22.1 ± 3.19	36.7 ± 5.02
$t\bar{t}W$	0.813 ± 0.177	0 ± 0	0.966 ± 0.232	3.65 ± 0.726	15.5 ± 2.17	1.12 ± 0.198
WZ	559 ± 238	0 ± 0	8.95 ± 8.75	150 ± 67.8	20.4 ± 9.24	32.4 ± 18.8
ZZ	48.3 ± 10.7	91.8 ± 20.4	0.0704 ± 0.0265	58.0 ± 15.6	9.02 ± 2.28	6.21 ± 3.18
tZ	6.25 ± 2.04	0 ± 0	3.61 ± 1.20	0.632 ± 0.220	1.98 ± 0.627	12.5 ± 3.80
WtZ	5.48 ± 1.28	0 ± 0	6.09 ± 1.99	1.28 ± 0.457	2.55 ± 0.575	7.03 ± 1.53
Other MC	9.26 ± 4.78	0.967 ± 0.602	2.73 ± 1.39	11.8 ± 6.11	12.0 ± 6.05	2.29 ± 1.24
Fakes	28.4 ± 16.1	0 ± 0	3.28 ± 5.54	150 ± 50.3	143 ± 68.5	25.6 ± 10.8
Total bkg.	674 ± 241	92.8 ± 20.4	86.5 ± 14.9	382 ± 91.7	226 ± 69.7	124 ± 25.7
$t\bar{t} \to bWuZ$	35.5 ± 3.58	0 ± 0	4.41 ± 0.823	3.66 ± 0.632	7.98 ± 0.809	101 ± 7.95
$t\bar{t} \to bWcZ$	29.2 ± 3.30	0 ± 0	8.94 ± 1.41	3.72 ± 0.607	7.49 ± 0.746	85.5 ± 6.90
Data	734	87	81	433	260	—
Data/Bkg	1.09 ± 0.392	0.938 ± 0.230	0.936 ± 0.191	1.13 ± 0.278	1.15 ± 0.360	—

Table 6.4.: The expected and observed event yields in the background control regions. In the signal region only the expected yields are shown. Unblinded data can be found in Section 6.10.3. The number of signal events is normalized to an arbitrary branching ratio of BR$(t \to qZ) = 0.1\%$. Shown uncertainties include statistical and systematic components which are discussed in Section 6.8.

	Side-band VR	WZ VR
$t\bar{t}Z$	34.3 ± 4.67	2.77 ± 0.658
$t\bar{t}W$	1.54 ± 0.252	0.995 ± 0.197
WZ	59.9 ± 24.4	52.0 ± 17.1
ZZ	11.3 ± 9.91	4.16 ± 1.96
tZ	20.5 ± 6.25	13.8 ± 4.27
WtZ	8.30 ± 1.73	1.01 ± 0.471
Other MC	2.24 ± 1.44	1.66 ± 1.84
Fakes	43.5 ± 17.6	43.1 ± 12.7
Total bkg.	182 ± 33.7	120 ± 22.6
$t\bar{t} \to bWuZ$	12.5 ± 1.10	7.69 ± 0.885
$t\bar{t} \to bWcZ$	16.6 ± 1.37	11.7 ± 1.44
Data	185	123
Data/Bkg	1.02 ± 0.203	1.03 ± 0.215

Table 6.5.: The expected and observed event yields in the side-band and WZ validation regions. The number of signal events is normalized to an arbitrary branching ratio of BR$(t \to qZ) = 0.1\%$. Shown uncertainties include statistical and systematic components which are discussed in Section 6.8.

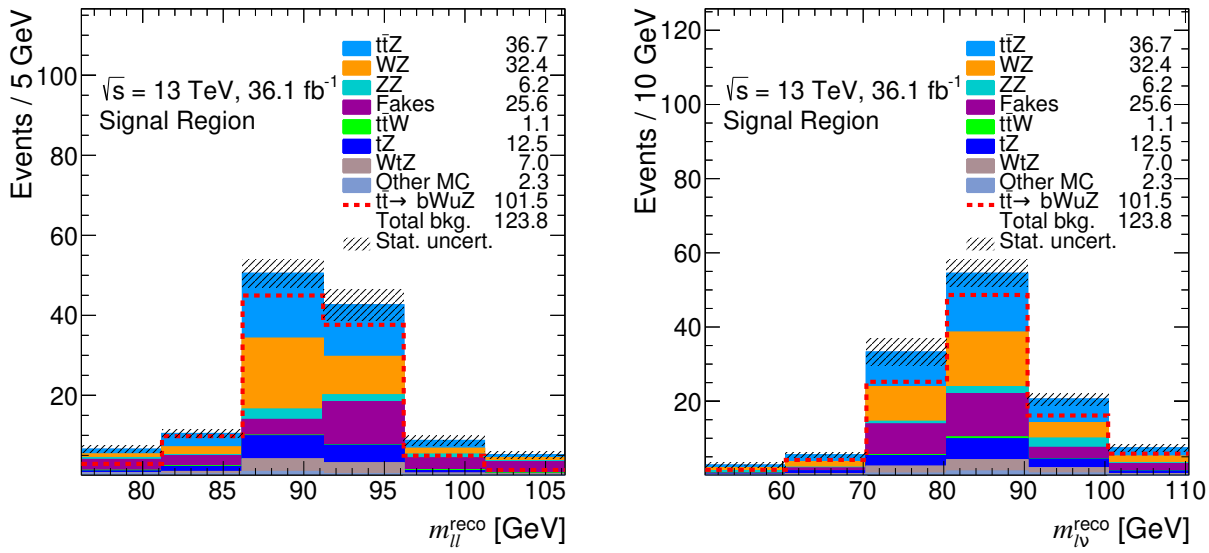

(a) (b)

Figure 6.1.: Expected distributions in the signal region for the invariant masses of the a) Z boson and the b) W boson candidates.

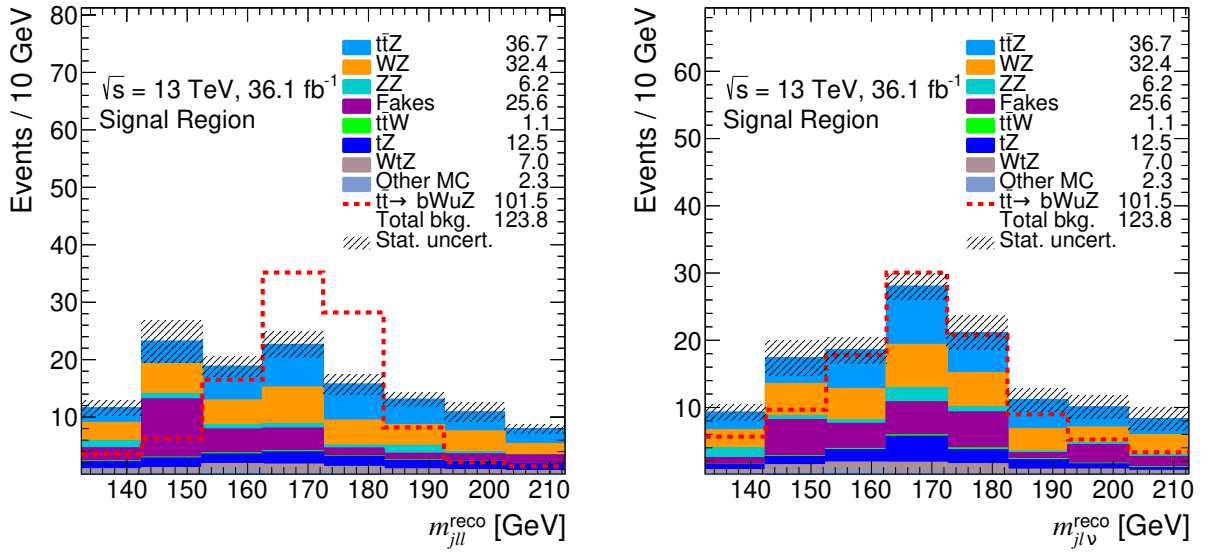

(a) (b)

Figure 6.2.: Expected distributions in the signal region for the invariant masses of the a) FCNC top and the b) SM top candidates.

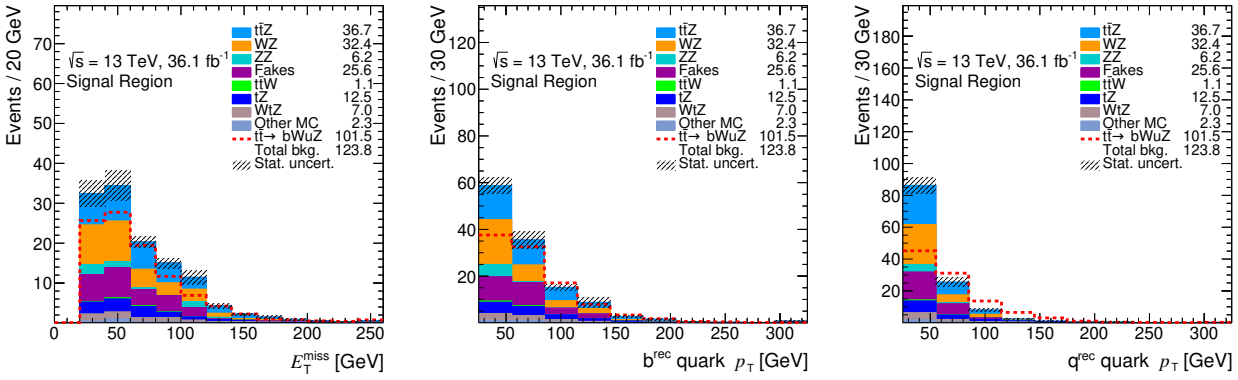

(a) (b) (c)

Figure 6.3.: Expected distributions in the signal region for the a) missing transverse momentum, p_{T} of the b) b-quark and c) q-quark jets.

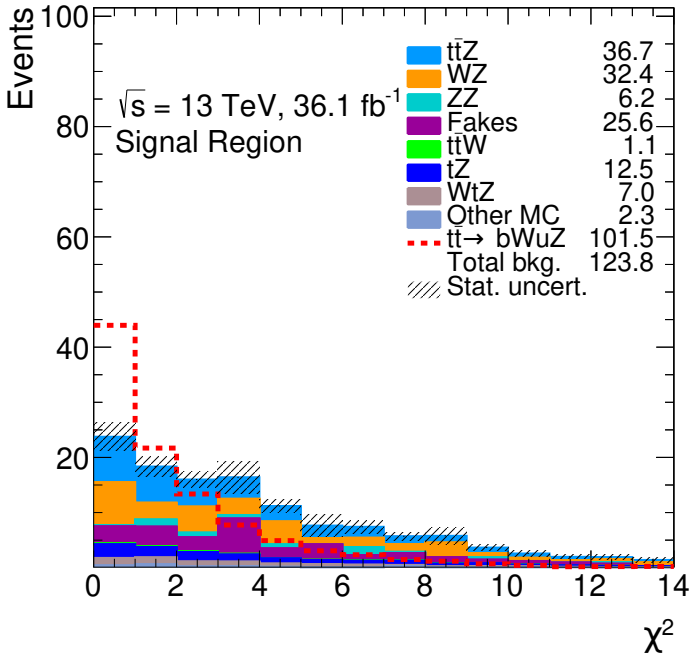

Figure 6.4.: χ^2 distributions for the signal and background expectations in the signal region.

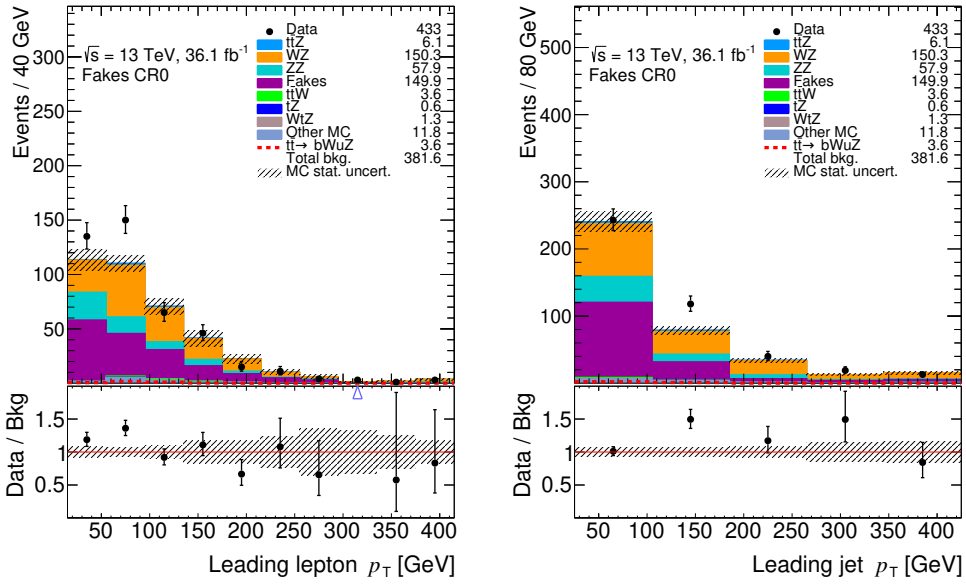

(a) (b)

Figure 6.5.: Expected and observed distributions in the fakes CR0 for a) p_T of the leading lepton and b) p_T of the leading jet.

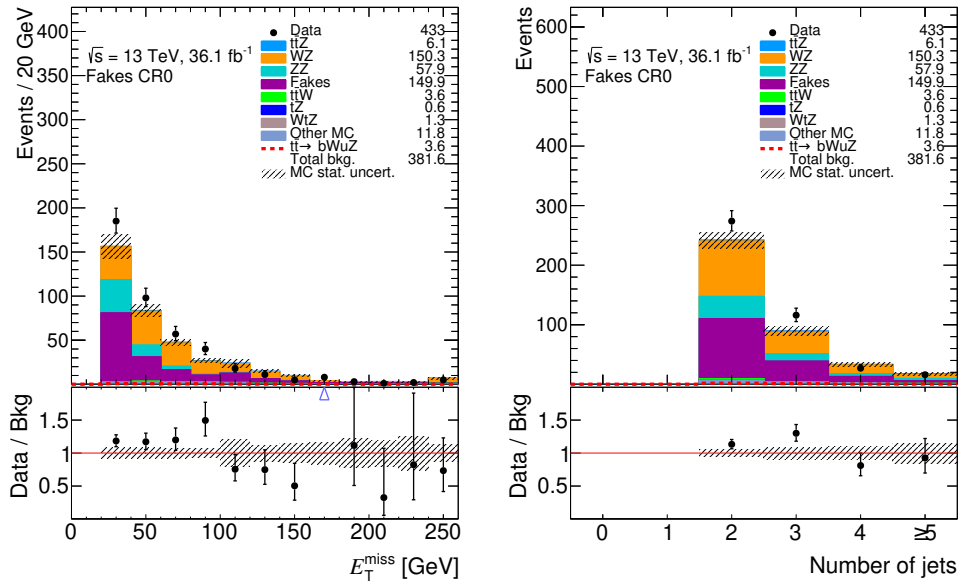

(a) (b)

Figure 6.6.: Expected and observed distributions in the fakes CR0 for a) missing transverse energy and b) jet multiplicity.

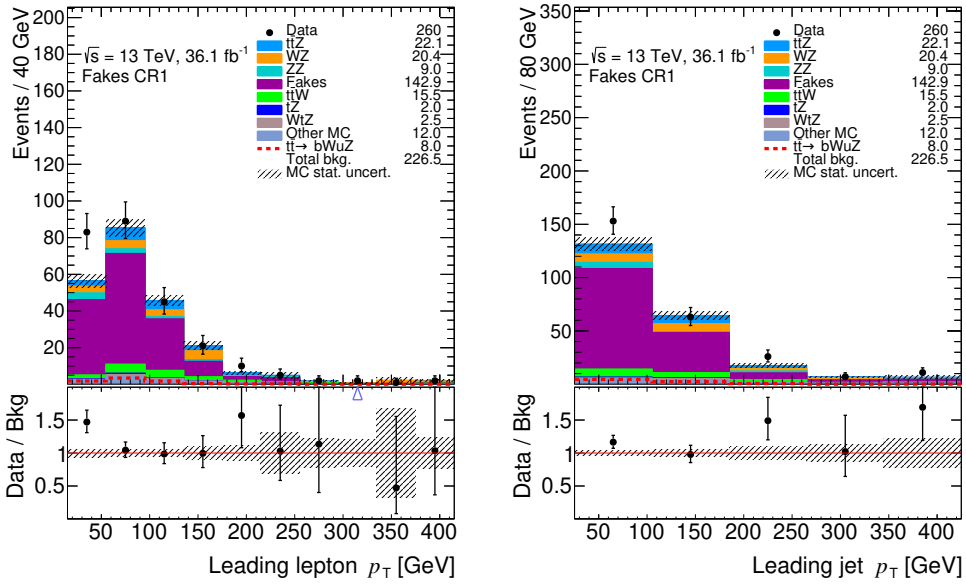

(a) (b)

Figure 6.7.: Expected and observed distributions in the fakes CR1 for a) p_T of the leading lepton and b) p_T of the leading jet.

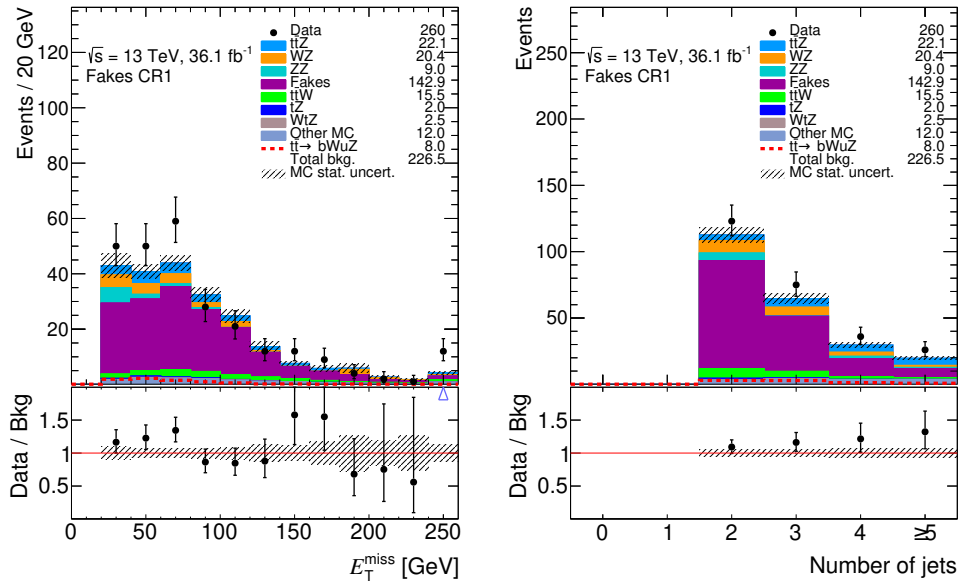

(a) (b)

Figure 6.8.: Expected and observed distributions in the fakes CR0 for a) missing transverse energy and b) jet multiplicity.

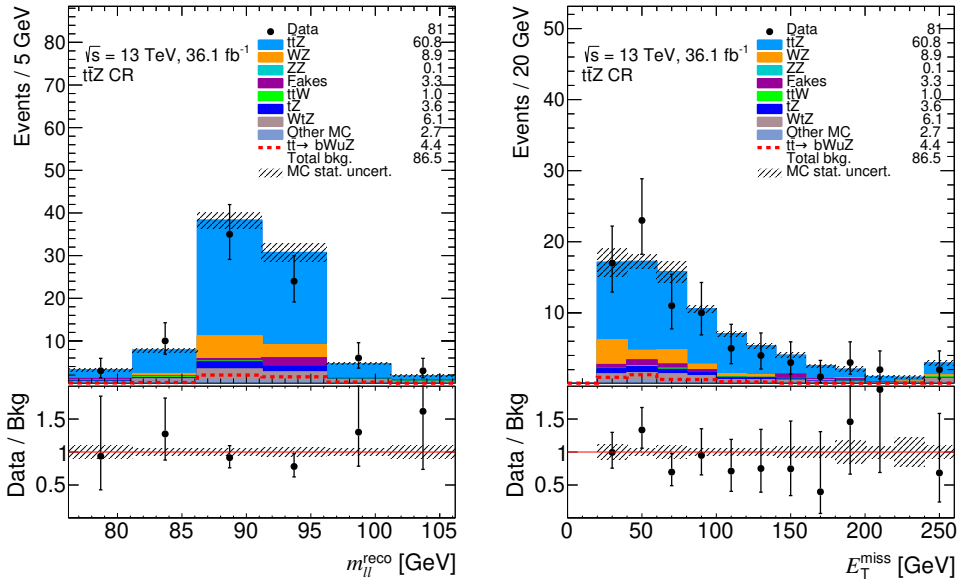

(a) (b)

Figure 6.9.: Expected and observed distributions in the $t\bar{t}Z$ control region for the a) mass of the reconstructed Z boson and b) missing transverse energy.

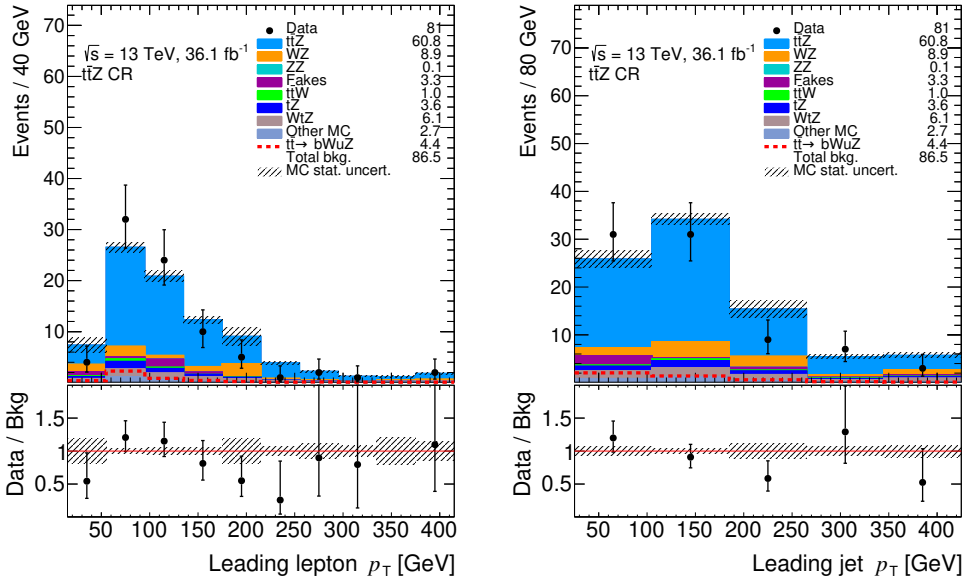

(a) (b)

Figure 6.10.: Expected and observed distributions in the $t\bar{t}Z$ control region for a) p_T of the leading lepton and b) p_T of the leading jet.

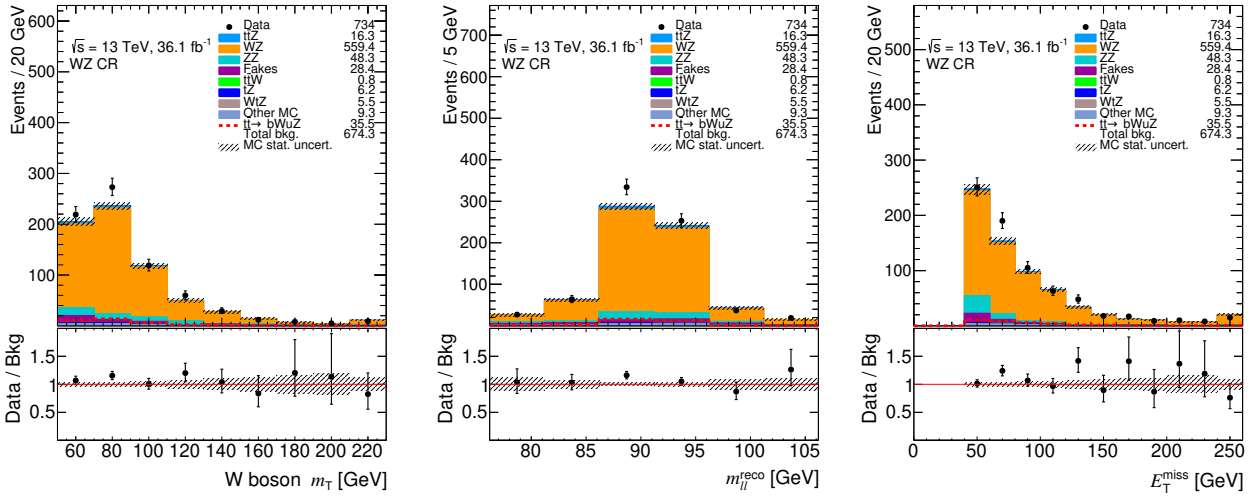

(a) (b) (c)

Figure 6.11.: Expected and observed distributions in the WZ control region for the a) transverse mass of the W boson, b) mass of the reconstructed Z boson and c) missing transverse energy.

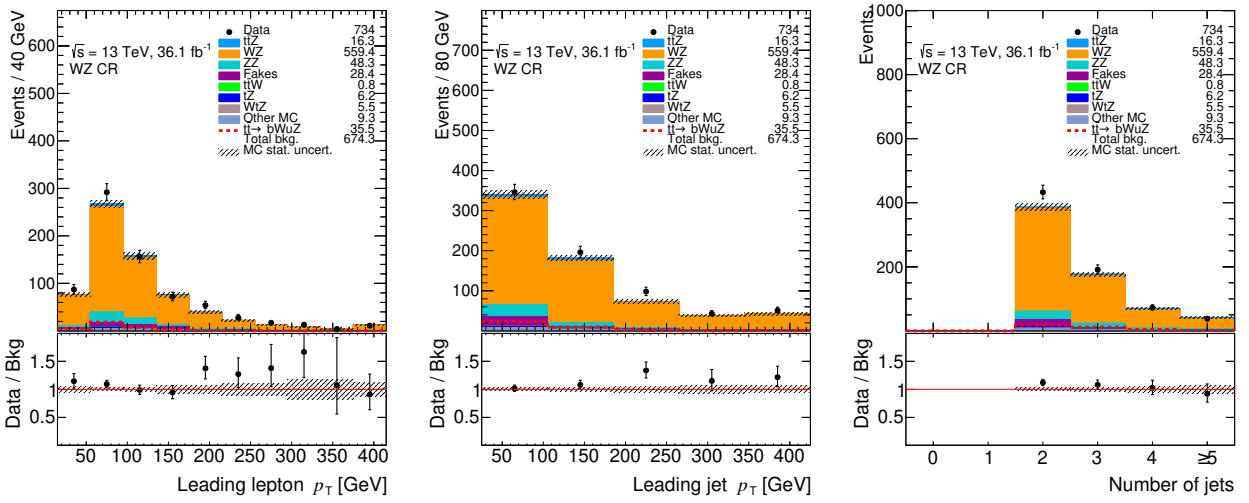

(a) (b) (c)

Figure 6.12.: Expected and observed distributions in the WZ control region for a) p_T of the leading lepton, b) p_T of the leading jet and c) jet multiplicity.

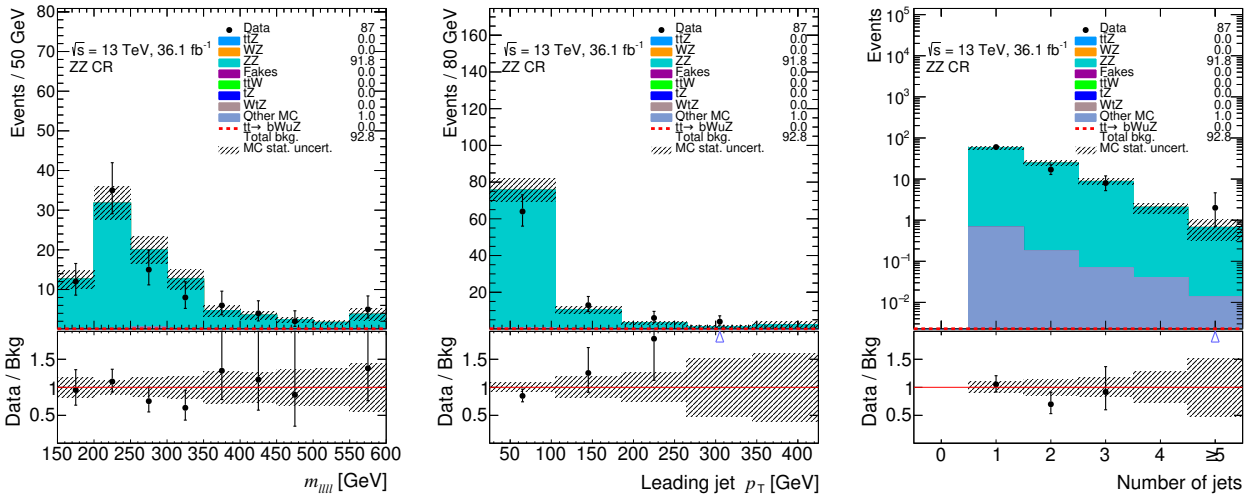

(a) (b) (c)

Figure 6.13.: Expected and observed distributions in the ZZ control region for a) the reconstructed mass of the ZZ system b) p_{T} of the leading jet and c) jet multiplicity.

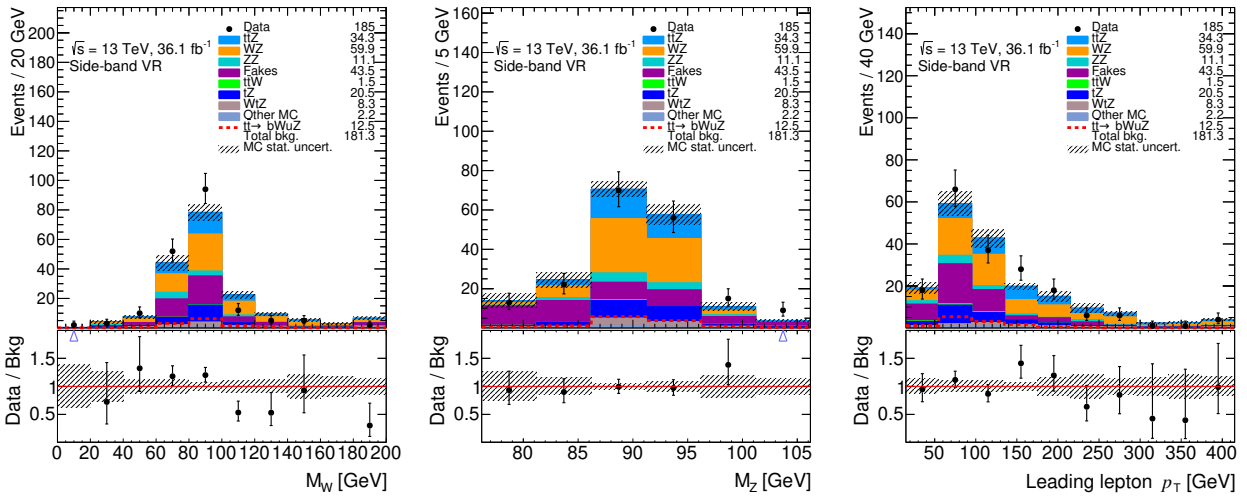

(a) (b) (c)

Figure 6.14.: Expected and observed distributions in the side-band validation region for the invariant mass of the a) W and b) Z boson and c) p_{T} of the leading lepton.

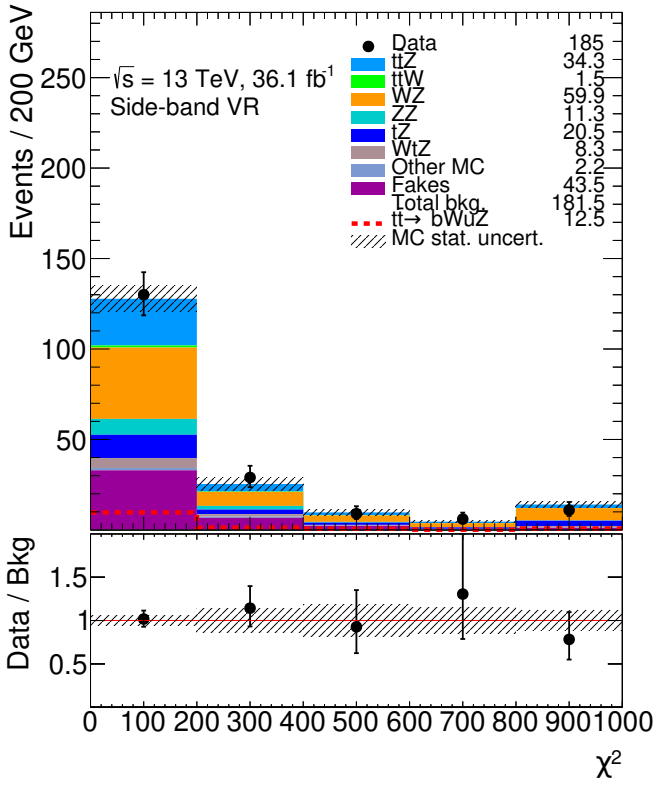

Figure 6.15.: Expected and observed distributions of the χ^2 in the side-band validation region.

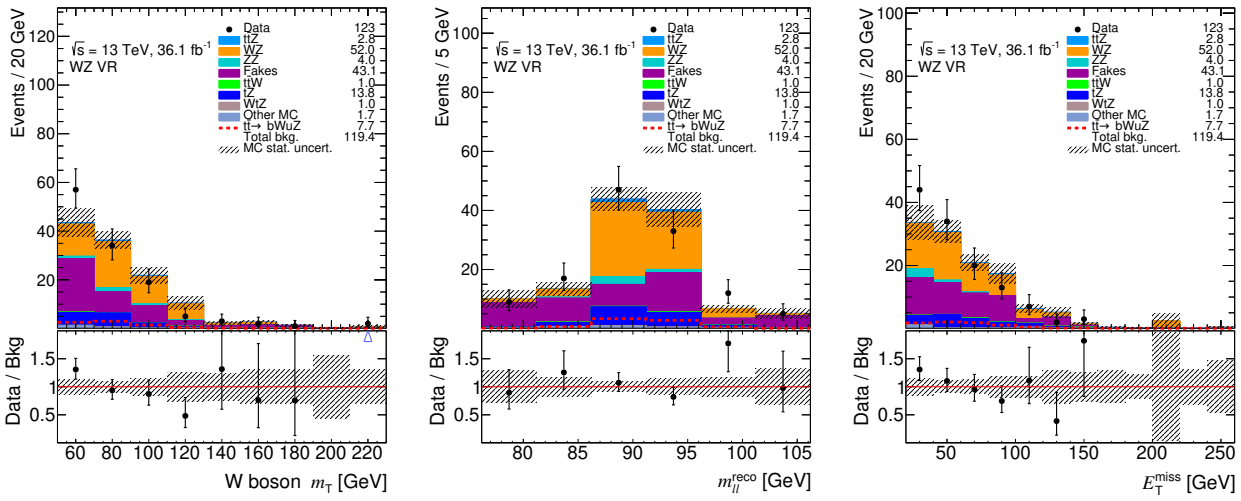

(a) (b) (c)

Figure 6.16.: Expected and observed distributions in the WZ validation region for the a) transverse mass of the W boson, b) mass of the reconstructed Z boson and c) missing transverse energy.

6.6. Estimation of the fake-lepton background

The "Fake Scale Factor" method is used for estimation of the fake-lepton background. The method explained in this section is a semi-data-driven technique, since it takes advantage of both data and Monte Carlo simulation. The underlying idea of the Fake Scale Factor method is to correct Monte Carlo prediction of fake rates according to the candidate fake-lepton flavour and the nature of the environment in which the fake-lepton is produced. Two environments are considered: "light" environment (Z+jets events) and "heavy" environment ($t\bar{t}$ events). Therefore we define two different sets of control regions with three leptons orthogonal to signal, background control and validation regions. One set of CRs enriched with e/μ fakes in Z+jets events and the other one in $t\bar{t}$ events. In Z+jets events dominant sources of fake-leptons are photon conversion and heavy hadrons, while in $t\bar{t}$ events fake-leptons are originated mostly from heavy hadrons. Having two flavours and two different environments we define four different Fake Scale Factors (FSFs), namely corrections to Monte Carlo prediction of fake-lepton rates in the Z+jets and $t\bar{t}$ events:

- $\lambda^{e}_{\text{Zjets}}$ — applied to Z+jets events with electron fake;
- $\lambda^{\mu}_{\text{Zjets}}$ — applied to Z+jets events with muon fake;
- $\lambda^{e}_{t\bar{t}}$ — applied to $t\bar{t}$ events with electron fake;
- $\lambda^{\mu}_{t\bar{t}}$ — applied to $t\bar{t}$ events with muon fake.

The particle truth information is used for the identification of the fake-leptons in the Z+jets and $t\bar{t}$ MC samples, then the events with N_e fake electrons and N_μ fake muons are reweighted by

$$(\lambda^{e})^{N_e} \cdot (\lambda^{\mu})^{N_\mu}.$$

More details about the event categories that are corrected using the scale factors are discussed in Appendix C.

6.6.1. Fake Scale Factors fit regions

The CR of Z+jets events enriched with electron (muon) fakes is defined as follows:

- Three leptons and at least one jet;
- No or one b-tagged jet;
- $e\mu\mu$ (μee) or eee ($\mu\mu\mu$) channel with OSSF;
- $|m_{\ell^+\ell^-} - 91.2| < 15$ GeV;

- $E_{\mathrm{T}}^{\mathrm{miss}} < 40$ GeV;
- $m_{\mathrm{T}}^{\ell\nu} < 50$ GeV.

where transverse mass $m_{\mathrm{T}}^{\ell\nu}$ is calculated for the candidate fake-lepton (the one which does not reconstruct a Z boson). The events that are in overlap with the signal region and the side-band validation region are vetoed.

The CR of $t\bar{t}$ events enriched with electron (muon) fakes is defined as follows:

- Three leptons and at least two jets;
- No or one b-tagged jet;
- μee ($e\mu\mu$);
- Veto any opposite-sign same-flavour lepton pair;
- One OS lepton pair.

Observed yields and Monte Carlo predictions in FSF control regions can be found in Table 6.6.

Sample	Z+jets CR e-fakes	Z+jets CR μ-fakes	$t\bar{t}$ CR e-fakes	$t\bar{t}$ CR μ-fakes
$t\bar{t}Z$	4.62 ± 0.158	5.10 ± 0.163	2.67 ± 0.126	2.34 ± 0.122
$t\bar{t}W$	0.251 ± 0.0391	0.306 ± 0.0444	4.11 ± 0.190	4.41 ± 0.190
WZ	221 ± 7.00	270 ± 8.24	5.39 ± 1.27	1.88 ± 0.554
ZZ	259 ± 10.7	134 ± 15.9	0.859 ± 0.512	0.0339 ± 0.0137
tZ	4.40 ± 0.217	5.45 ± 0.236	0.139 ± 0.0384	0.0800 ± 0.0366
WtZ	1.27 ± 0.180	1.30 ± 0.187	0.721 ± 0.119	0.363 ± 0.0944
Other MC	16.6 ± 3.00	18.7 ± 2.80	5.85 ± 0.530	6.74 ± 0.827
e-fakes ($t\bar{t}$)	6.02 ± 0.988	2.31 ± 0.592	47.6 ± 2.80	0 ± 0
e-fakes (Zjets)	286 ± 19.1	0 ± 0	0 ± 0	0 ± 0
μ-fakes ($t\bar{t}$)	2.30 ± 0.589	6.83 ± 1.07	0.122 ± 0.441	35.8 ± 2.53
μ-fakes (Zjets)	0 ± 0	129 ± 11.9	0 ± 0	0 ± 0
Total MC	801 ± 23.2	573 ± 21.7	67.4 ± 3.21	51.7 ± 2.73
Data	1131	686	73	54
Data/MC	1.41 ± 0.0586	1.20 ± 0.0645	1.08 ± 0.137	1.04 ± 0.152

Table 6.6.: The expected and observed event yields in the Z+jets and $t\bar{t}$ control regions. Shown uncertainties are purely statistical.

6.6.2. Determination of Fake Scale Factors

Since none of the control regions is perfectly pure with respect to the process under consideration, Fake Scale Factors are determined by a simultaneous likelihood fit in all fake scale factors fit regions. One bin (total yield) per control region is used for the fit. Statistical and systematic uncertainties discussed in Section 6.8 are included in the likelihood as described in Section 6.9. Extracted FSFs are as follow:

- $\lambda^{e}_{\text{Zjets}}$ = 2.16 $\pm$ 0.835
- $\lambda^{\mu}_{\text{Zjets}}$ = 1.88 $\pm$ 0.915
- $\lambda^{e}_{t\bar{t}}$ = 1.12 $\pm$ 0.273
- $\lambda^{\mu}_{t\bar{t}}$ = 1.07 $\pm$ 0.716

Errors on FSFs are from the fit taking into account statistical and systematic uncertainties (see Section 6.8). The leading 10 systematic uncertainty sources according to their impact on each of the fake scale factors are presented in Tables 6.7-6.10. The impact of each systematic source is defined as the $\Delta\lambda = \lambda' - \lambda$, where λ' is the FSF calculated using the event yields set to corresponding up/down systematic variation, while λ is the FSF extracted from the nominal yields, as presented above. For example, up (down) variation of Z+jets yield with electron fakes by its 35% normalization uncertainty gives ${\lambda^{e}_{\text{Zjets}}}'$ = 1.59 (3.32) and accordingly $\Delta\lambda^{e}_{\text{Zjets}} = {\lambda^{e}_{\text{Zjets}}}' - \lambda^{e}_{\text{Zjets}}$ = -0.57 (1.16), that is presented in Table 6.7.

The summary of relative impact of each source of uncertainty on the event yields in the fake scale factors fit regions can be found in Tables 6.11-6.14. The distributions from the $t\bar{t}$ and Z+jets control regions, before and after applying FSFs, are presented in Figures 6.17-6.29: the distributions of b-tag and jet multiplicity are shown in Figures 6.17-6.20, while Figures 6.21-6.26 present leading, sub-leading and third lepton transverse momentum distributions. The distributions of missing transverse momentum in the $t\bar{t}$ CRs are shown in Figure 6.27. The distributions of the variables that are constructed using the candidate fake-lepton, such as transverse mass $m^{\ell\nu}_{\text{T}}$ in the Z+jets CRs and invariant mass of the same flavour lepton pair in the $t\bar{t}$ CRs, are presented in Figure 6.28 and Figure 6.29, respectively. These plots show how well modelled are the fake-leptons. Agreement between data and prediction is significantly improved after applying FSFs on the MC. Since data-to-MC ratio is flat as a function of lepton p_{T} we can assume that FSFs do not depend on it.

Source	$\Delta\lambda^{e}_{\text{Zjets}}$
Z+jets normalization	–0.57 / 1.2
WZ_1_Jet	–0.10 / 0.12
ZZ normalization	–0.10 / 0.11
JET_21NP_JET_Pileup_RhoTopology	–0.077 / 0.11
WZ normalization	–0.087 / 0.10
EL_SF_ID	–0.088 / 0.10
JET_21NP_JET_Flavor_Composition	–0.060 / 0.082
WZ_2_Jet	–0.062 / 0.081
JET_JER_SINGLE_NP	0.080 / –0.067
WZ modelling	0.076 / –0.056

Table 6.7.: Leading 10 systematic uncertainty sources according to the impact on the $\lambda^{e}_{\text{Zjets}}$ are presented. The impact of each systematic source is defined as the $\Delta\lambda = \lambda' - \lambda$, where λ' is the FSF calculated using the event yields set to corresponding up/down systematic variation, while λ is the FSF extracted from the nominal yields.

Source	$\Delta\lambda^{\mu}_{Zjets}$
Z+jets normalization	–0.49 / 1.0
WZ_1_Jet	–0.31 / 0.31
WZ normalization	–0.26 / 0.26
WZ modelling	0.24 / –0.23
WZ_2_Jet	–0.19 / 0.19
ZZ normalization	–0.13 / 0.12
$t\bar{t}$ NLO generator	0.046 / –0.084
MU_SF_ID_SYST	–0.078 / 0.081
pileup	–0.069 / 0.078
WZ_3_Jet	–0.076 / 0.076

Table 6.8.: Leading 10 systematic uncertainty sources according to the impact on the $\lambda^{\mu}_{\text{Zjets}}$ are presented. The impact of each systematic source is defined as the $\Delta\lambda = \lambda' - \lambda$, where λ' is the FSF calculated using the event yields set to corresponding up/down systematic variation, while λ is the FSF extracted from the nominal yields.

Source	$\Delta\lambda^{e}_{t\bar{t}}$
$t\bar{t}$ QCD radiation	0.099 / –0.084
$t\bar{t}$ NLO generator	–0.075 / 0.085
Other bkg. normalization	–0.062 / 0.061
$t\bar{t}$ PS	–0.058 / 0.059
$\sigma_{t\bar{t}}$(PDF+α_S)	–0.045 / 0.049
pileup	0.048 / –0.044
EL_SF_ID	–0.044 / 0.046
$\sigma_{t\bar{t}}$(scale)	–0.026 / 0.040
JET_21NP_JET_Flavor_Composition	–0.037 / 0.039
JET_21NP_JET_Pileup_RhoTopology	–0.037 / 0.038

Table 6.9.: Leading 10 systematic uncertainty sources according to the impact on the $\lambda^{e}_{t\bar{t}}$ are presented. The impact of each systematic source is defined as the $\Delta\lambda = \lambda' - \lambda$, where λ' is the FSF calculated using the event yields set to corresponding up/down systematic variation, while λ is the FSF extracted from the nominal yields.

Source	$\Delta\lambda^{\mu}_{t\bar{t}}$
$t\bar{t}$ PS	–0.35 / 1.0
$t\bar{t}$ NLO generator	–0.24 / 0.46
$t\bar{t}$ QCD radiation	–0.15 / 0.21
JET_JER_SINGLE_NP	–0.090 / 0.12
Other bkg. normalization	–0.091 / 0.094
$\sigma_{t\bar{t}}$(PDF+α_S)	–0.041 / 0.047
pileup	0.045 / –0.040
$\sigma_{t\bar{t}}$(scale)	–0.023 / 0.039
JET_21NP_JET_Flavor_Composition	–0.033 / 0.036
EL_SF_ID	–0.011 / 0.025

Table 6.10.: Leading 10 systematic uncertainty sources according to the impact on the $\lambda^{\mu}_{t\bar{t}}$ are presented. The impact of each systematic source is defined as the $\Delta\lambda = \lambda' - \lambda$, where λ' is the FSF calculated using the event yields set to corresponding up/down systematic variation, while λ is the FSF extracted from the nominal yields.

Source	$t\bar{t}Z$	$t\bar{t}W$	WZ	ZZ	tZ	WtZ	Other MC	e-fakes ($t\bar{t}$)	e-fakes (Zjets)	μ-fakes ($t\bar{t}$)
pileup	-0.4 / 0.4	-1.6 / 1.6	-3.8 / 3.8	-2.2 / 2.2	-1.5 / 1.5	-2.7 / 2.7	2.5 / -2.5	-1.9 / 1.9	-0.6 / 0.6	1.6 / -1.6
EL_SF_ID	1.7 / -1.7	1.8 / -1.8	1.8 / -1.8	2.0 / -2.0	1.6 / -1.6	1.5 / -1.5	2.4 / -2.4	3.3 / -3.3	3.1 / -3.1	0.9 / -0.9
bTagSF_77_eigenvars_B_0	5.0 / -5.0	6.1 / -6.1	0.1 / -0.1	-0.0 / 0.0	1.9 / -1.9	2.6 / -2.6	0.3 / -0.3	1.9 / -1.9	0.1 / -0.1	3.3 / -3.3
EG_SCALE_ALL	0.0 / -0.0	-0.9 / 0.9	-0.2 / 0.2	-0.7 / 0.7	0.6 / -0.6	-0.5 / 0.5	-0.4 / 0.4	2.0 / -2.0	0.4 / -0.4	0.1 / -0.1
JET_21NP_JET_BJES_Response	-1.4 / 1.4	2.5 / -2.5	0.1 / -0.1	0.1 / -0.1	0.1 / -0.1	1.2 / -1.2	0.1 / -0.1	-3.8 / 3.8	0.1 / -0.1	-2.3 / 2.3
JET_21NP_JET_EffectiveNP_1	-2.4 / 2.4	-10.0 / 10.0	0.8 / -0.8	0.3 / -0.3	-2.1 / 2.1	-0.8 / 0.8	1.7 / -1.7	-1.9 / 1.9	1.8 / -1.8	-0.0 / 0.0
JET_21NP_JET_EffectiveNP_6	-0.1 / 0.1	-1.5 / 1.5	-0.1 / 0.1	0.3 / -0.3	-0.4 / 0.4	1.0 / -1.0	-0.0 / 0.0	3.0 / -3.0	-0.0 / 0.0	-0.0 / 0.0
JET_21NP_JET_EffectiveNP_7	0.3 / -0.3	-1.4 / 1.4	-0.1 / 0.1	-0.1 / 0.1	0.4 / -0.4	-1.7 / 1.7	0.1 / -0.1	-2.0 / 2.0	0.0 / -0.0	-0.0 / 0.0
JET_21NP_JET_EtaIntercalibration_Modelling	-1.0 / 1.0	-3.6 / 3.6	-0.5 / 0.5	-0.5 / 0.5	-1.3 / 1.3	-1.3 / 1.3	0.7 / -0.7	0.1 / -0.1	0.1 / -0.1	5.3 / -5.3
JET_21NP_JET_EtaIntercalibration_NonClosure	-0.8 / 0.8	-0.7 / 0.7	0.1 / -0.1	-0.7 / 0.7	-1.5 / 1.5	0.7 / -0.7	-0.1 / 0.1	1.0 / -1.0	0.6 / -0.6	-3.0 / 3.0
JET_21NP_JET_EtaIntercalibration_TotalStat	-1.4 / 1.4	-2.3 / 2.3	0.4 / -0.4	-0.2 / 0.2	-0.9 / 0.9	0.2 / -0.2	0.4 / -0.4	-0.9 / 0.9	0.2 / -0.2	0.0 / -0.0
JET_21NP_JET_Flavor_Composition	-1.0 / 1.0	-4.9 / 4.9	0.9 / -0.9	0.2 / -0.2	-3.9 / 3.9	-2.5 / 2.5	5.7 / -5.7	-1.7 / 1.7	2.9 / -2.9	-0.5 / 0.5
JET_21NP_JET_Flavor_Response	1.0 / -1.0	2.6 / -2.6	-0.2 / 0.2	-0.3 / 0.3	1.3 / -1.3	0.6 / -0.6	-1.2 / 1.2	-1.1 / 1.1	-0.5 / 0.5	-5.2 / 5.2
JET_21NP_JET_Pileup_OffsetMu	0.4 / -0.4	8.3 / -8.3	-0.3 / 0.3	-0.3 / 0.3	-0.6 / 0.6	0.7 / -0.7	0.4 / -0.4	-0.1 / 0.1	-0.6 / 0.6	-2.5 / 2.5
JET_21NP_JET_Pileup_OffsetNPV	-0.9 / 0.9	-1.2 / 1.2	-0.2 / 0.2	-0.7 / 0.7	-0.6 / 0.6	3.2 / -3.2	-0.8 / 0.8	0.2 / -0.2	0.2 / -0.2	-0.0 / 0.0
JET_21NP_JET_Pileup_RhoTopology	-3.2 / 3.2	-7.5 / 7.5	0.5 / -0.5	0.1 / -0.1	-2.3 / 2.3	-1.4 / 1.4	4.9 / -4.9	3.2 / -3.2	4.1 / -4.1	-2.7 / 2.7
JET_JER_SINGLE_NP	-1.4 / 1.4	23.9 / -23.9	2.7 / -2.7	-3.2 / 3.2	-1.9 / 1.9	7.7 / -7.7	-20.0 / 20.0	13.3 / -13.3	-2.7 / 2.7	-4.9 / 4.9
MET_SoftTrk_ResoPara	1.8 / -1.8	5.7 / -5.7	1.6 / -1.6	3.5 / -3.5	-1.0 / 1.0	5.2 / -5.2	3.6 / -3.6	2.6 / -2.6	0.6 / -0.6	-5.9 / 5.9
MET_SoftTrk_ResoPerp	0.4 / -0.4	0.2 / -0.2	0.4 / -0.4	2.1 / -2.1	-0.9 / 0.9	1.7 / -1.7	-15.1 / 15.1	5.2 / -5.2	2.0 / -2.0	0.0 / 0.0
MET_SoftTrk_Scale	1.0 / -1.0	2.6 / -2.6	0.8 / -0.8	2.3 / -2.3	-0.1 / 0.1	0.1 / -0.1	1.9 / -1.9	1.6 / -1.6	1.6 / -1.6	-0.7 / 0.7
MUON_MS	-0.2 / 0.2	-0.6 / 0.6	-0.2 / 0.2	-0.4 / 0.4	-0.4 / 0.4	0.9 / -0.9	-0.0 / 0.0	0.9 / -0.9	-0.3 / 0.3	2.5 / -2.5
Luminosity	2.1 / -2.1	2.1 / -2.1	2.1 / -2.1	2.1 / -2.1	2.1 / -2.1	2.1 / -2.1	2.1 / -2.1	2.1 / -2.1	2.1 / -2.1	2.1 / -2.1
$t\bar{t}Z$ normalization	12.0 / -12.0	0.0 / 0.0	0.0 / 0.0	0.0 / 0.0	0.0 / 0.0	0.0 / 0.0	0.0 / 0.0	0.0 / 0.0	0.0 / 0.0	0.0 / 0.0
$t\bar{t}Z$ modelling	-2.1 / 2.1	0.0 / 0.0	0.0 / 0.0	0.0 / 0.0	0.0 / 0.0	0.0 / 0.0	0.0 / 0.0	0.0 / 0.0	0.0 / 0.0	0.0 / 0.0
$t\bar{t}W$ normalization	0.0 / 0.0	13.0 / -13.0	0.0 / 0.0	0.0 / 0.0	0.0 / 0.0	0.0 / 0.0	0.0 / 0.0	0.0 / 0.0	0.0 / 0.0	0.0 / 0.0
WZ normalization	0.0 / 0.0	0.0 / 0.0	12.5 / -12.5	0.0 / 0.0	0.0 / 0.0	0.0 / 0.0	0.0 / 0.0	0.0 / 0.0	0.0 / 0.0	0.0 / 0.0
WZ modelling	0.0 / 0.0	0.0 / 0.0	-8.6 / 8.6	0.0 / 0.0	0.0 / 0.0	0.0 / 0.0	0.0 / 0.0	0.0 / 0.0	0.0 / 0.0	0.0 / 0.0
WZ_1_Jet	0.0 / 0.0	0.0 / 0.0	14.6 / -14.6	0.0 / 0.0	0.0 / 0.0	0.0 / 0.0	0.0 / 0.0	0.0 / 0.0	0.0 / 0.0	0.0 / 0.0
WZ_2_Jet	0.0 / 0.0	0.0 / 0.0	9.5 / -9.5	0.0 / 0.0	0.0 / 0.0	0.0 / 0.0	0.0 / 0.0	0.0 / 0.0	0.0 / 0.0	0.0 / 0.0
WZ_3_Jet	0.0 / 0.0	0.0 / 0.0	4.1 / -4.1	0.0 / 0.0	0.0 / 0.0	0.0 / 0.0	0.0 / 0.0	0.0 / 0.0	0.0 / 0.0	0.0 / 0.0
ZZ normalization	0.0 / 0.0	0.0 / 0.0	0.0 / 0.0	12.5 / -12.5	0.0 / 0.0	0.0 / 0.0	0.0 / 0.0	0.0 / 0.0	0.0 / 0.0	0.0 / 0.0
tZ normalization	0.0 / 0.0	0.0 / 0.0	0.0 / 0.0	0.0 / 0.0	30.0 / -30.0	0.0 / 0.0	0.0 / 0.0	0.0 / 0.0	0.0 / 0.0	0.0 / 0.0
tZ QCD radiation	0.0 / 0.0	0.0 / 0.0	0.0 / 0.0	0.0 / 0.0	-4.6 / 4.6	0.0 / 0.0	0.0 / 0.0	0.0 / 0.0	0.0 / 0.0	0.0 / 0.0
WtZ normalization	0.0 / 0.0	0.0 / 0.0	0.0 / 0.0	0.0 / 0.0	0.0 / 0.0	10.0 / -28.0	0.0 / 0.0	0.0 / 0.0	0.0 / 0.0	0.0 / 0.0
WtZ PS	0.0 / 0.0	0.0 / 0.0	0.0 / 0.0	0.0 / 0.0	0.0 / 0.0	34.6 / -34.6	0.0 / 0.0	0.0 / 0.0	0.0 / 0.0	0.0 / 0.0
Other bkg. normalization	0.0 / 0.0	0.0 / 0.0	0.0 / 0.0	0.0 / 0.0	0.0 / 0.0	0.0 / 0.0	50.0 / -50.0	0.0 / 0.0	0.0 / 0.0	0.0 / 0.0
$\sigma_{t\bar{t}}$(scale)	0.0 / 0.0	0.0 / 0.0	0.0 / 0.0	0.0 / 0.0	0.0 / 0.0	0.0 / 0.0	0.0 / 0.0	2.4 / -3.5	0.0 / 0.0	2.4 / -3.5
$\sigma_{t\bar{t}}$(PDF+α_S)	0.0 / 0.0	0.0 / 0.0	0.0 / 0.0	0.0 / 0.0	0.0 / 0.0	0.0 / 0.0	0.0 / 0.0	4.2 / -4.2	0.0 / 0.0	4.2 / -4.2
$t\bar{t}$ PS	0.0 / 0.0	0.0 / 0.0	0.0 / 0.0	0.0 / 0.0	0.0 / 0.0	0.0 / 0.0	0.0 / 0.0	0.5 / -0.5	0.0 / 0.0	5.4 / -5.4
$t\bar{t}$ NLO generator	0.0 / 0.0	0.0 / 0.0	0.0 / 0.0	0.0 / 0.0	0.0 / 0.0	0.0 / 0.0	0.0 / 0.0	111.6 / -100	0.0 / 0.0	-5.9 / 5.9
$t\bar{t}$ QCD radiation	0.0 / 0.0	0.0 / 0.0	0.0 / 0.0	0.0 / 0.0	0.0 / 0.0	0.0 / 0.0	0.0 / 0.0	-34.6 / 34.6	0.0 / 0.0	-38.8 / 38.8
Z+jets normalization	0.0 / 0.0	0.0 / 0.0	0.0 / 0.0	0.0 / 0.0	0.0 / 0.0	0.0 / 0.0	0.0 / 0.0	0.0 / 0.0	35.0 / -35.0	0.0 / 0.0

Table 6.11.: Summary of the relative impact of each source of uncertainty on the event yields in the Z+jets control region enriched with electron fakes for each individual sample (shown in percentage). Only the systematic sources are shown which have the effect above 2% on at least one sample.

Source	$t\bar{t}Z$	$t\bar{t}W$	WZ	ZZ	tZ	WtZ	Other MC	e-fakes ($t\bar{t}$)	μ-fakes ($t\bar{t}$)	μ-fakes (Zjets)
pileup	-4.3 / 4.3	-8.2 / 8.2	-1.5 / 1.5	0.5 / -0.5	-3.3 / 3.3	-5.4 / 5.4	5.7 / -5.7	-7.8 / 7.8	-5.5 / 5.5	5.2 / -5.2
EL_SF_ID	0.7 / -0.7	0.6 / -0.6	0.7 / -0.7	0.6 / -0.6	0.7 / -0.7	0.6 / -0.6	0.8 / -0.8	3.4 / -3.4	0.3 / -0.3	0.6 / -0.6
bTagSF_77_eigenvars_B_0	5.2 / -5.2	3.2 / -3.2	0.1 / -0.1	-0.0 / 0.0	0.6 / -0.6	3.8 / -3.8	0.2 / -0.2	-1.8 / 1.8	0.3 / -0.3	0.3 / -0.3
EG_RESOLUTION_ALL	-0.3 / 0.3	-0.0 / 0.0	-0.0 / 0.0	-0.0 / 0.0	0.0 / -0.0	2.1 / -2.1	0.0 / -0.0	-3.1 / 3.1	-0.9 / 0.9	-0.3 / 0.3
JET_21NP_JET_BJES_Response	0.2 / -0.2	-0.8 / 0.8	-0.0 / 0.0	-0.1 / 0.1	1.2 / -1.2	0.4 / -0.4	0.1 / -0.1	-3.0 / 3.0	-0.2 / 0.2	-0.5 / 0.5
JET_21NP_JET_EffectiveNP_1	-1.8 / 1.8	3.0 / -3.0	1.0 / -1.0	0.8 / -0.8	0.1 / -0.1	-4.4 / 4.4	-0.1 / 0.1	-0.4 / 0.4	-1.9 / 1.9	-3.8 / 3.8
JET_21NP_JET_EffectiveNP_3	0.2 / -0.2	1.0 / -1.0	0.4 / -0.4	-0.2 / 0.2	-0.5 / 0.5	0.4 / -0.4	0.1 / -0.1	-2.9 / 2.9	-0.0 / 0.0	-0.4 / 0.4
JET_21NP_JET_EffectiveNP_6	-0.1 / 0.1	-1.1 / 1.1	-0.0 / 0.0	-0.1 / 0.1	0.5 / -0.5	-0.7 / 0.7	-0.1 / 0.1	3.0 / -3.0	0.0 / -0.0	0.0 / -0.0
JET_21NP_JET_EffectiveNP_7	-0.0 / 0.0	-1.2 / 1.2	-0.1 / 0.1	0.2 / -0.2	-0.3 / 0.3	0.2 / -0.2	-0.0 / 0.0	2.9 / -2.9	0.0 / -0.0	0.5 / -0.5
JET_21NP_JET_EtaIntercalibration_Modelling	-1.6 / 1.6	-0.1 / 0.1	1.2 / -1.2	-0.9 / 0.9	0.5 / -0.5	-0.4 / 0.4	1.4 / -1.4	4.2 / -4.2	-3.1 / 3.1	0.7 / -0.7
JET_21NP_JET_EtaIntercalibration_NonClosure	0.9 / -0.9	0.4 / -0.4	0.3 / -0.3	-0.7 / 0.7	0.3 / -0.3	-5.7 / 5.7	-0.3 / 0.3	6.0 / -6.0	0.2 / -0.2	0.7 / -0.7
JET_21NP_JET_EtaIntercalibration_TotalStat	-1.2 / 1.2	1.7 / -1.7	0.6 / -0.6	-0.2 / 0.2	0.6 / -0.6	-0.2 / 0.2	-0.0 / 0.0	-2.9 / 2.9	0.3 / -0.3	-1.0 / 1.0
JET_21NP_JET_Flavor_Composition	-3.5 / 3.5	0.6 / -0.6	2.5 / -2.5	3.9 / -3.9	-0.2 / 0.2	-5.9 / 5.9	2.1 / -2.1	-3.9 / 3.9	6.1 / -6.1	-2.3 / 2.3
JET_21NP_JET_Flavor_Response	1.1 / -1.1	-0.4 / 0.4	-1.2 / 1.2	0.1 / -0.1	-0.1 / 0.1	-0.8 / 0.8	-2.3 / 2.3	5.9 / -5.9	0.2 / -0.2	1.8 / -1.8
JET_21NP_JET_Pileup_OffsetMu	0.1 / -0.1	1.7 / -1.7	-0.3 / 0.3	-0.9 / 0.9	-1.1 / 1.1	2.2 / -2.2	1.1 / -1.1	-7.9 / 7.9	3.1 / -3.1	1.2 / -1.2
JET_21NP_JET_Pileup_OffsetNPV	-0.1 / 0.1	4.8 / -4.8	0.4 / -0.4	-0.5 / 0.5	-1.1 / 1.1	0.8 / -0.8	-0.4 / 0.4	-7.3 / 7.3	-1.2 / 1.2	-2.5 / 2.5
JET_21NP_JET_Pileup_PtTerm	-0.3 / 0.3	-0.8 / 0.8	-0.2 / 0.2	-0.3 / 0.3	1.7 / -1.7	0.5 / -0.5	1.6 / -1.6	-2.8 / 2.8	0.0 / -0.0	0.9 / -0.9
JET_21NP_JET_Pileup_RhoTopology	-2.6 / 2.6	2.8 / -2.8	1.3 / -1.3	1.6 / -1.6	0.8 / -0.8	-3.8 / 3.8	0.8 / -0.8	-2.7 / 2.7	-0.9 / 0.9	-3.5 / 3.5
JET_JER_SINGLE_NP	3.7 / -3.7	-33.9 / 33.9	-0.3 / 0.3	-3.6 / 3.6	-0.2 / 0.2	16.3 / -16.3	7.1 / -7.1	-13.6 / 13.6	5.4 / -5.4	-2.1 / 2.1
MET_SoftTrk_ResoPara	0.4 / -0.4	-3.7 / 3.7	-0.4 / 0.4	1.3 / -1.3	0.8 / -0.8	2.7 / -2.7	2.3 / -2.3	-8.3 / 8.3	2.5 / -2.5	0.5 / -0.5
MET_SoftTrk_ResoPerp	1.0 / -1.0	-5.2 / 5.2	0.5 / -0.5	1.6 / -1.6	-0.2 / 0.2	-2.8 / 2.8	2.0 / -2.0	0.2 / -0.2	5.2 / -5.2	2.1 / -2.1
MET_SoftTrk_Scale	0.9 / -0.9	-2.1 / 2.1	0.2 / -0.2	1.6 / -1.6	-0.4 / 0.4	1.8 / -1.8	1.1 / -1.1	9.1 / -9.1	2.3 / -2.3	1.7 / -1.7
MUON_ID	-0.7 / 0.7	-0.4 / 0.4	-0.2 / 0.2	0.1 / -0.1	-0.7 / 0.7	1.8 / -1.8	-0.1 / 0.1	5.7 / -5.7	-0.8 / 0.8	-0.0 / 0.0
MUON_MS	0.2 / -0.2	1.5 / -1.5	0.2 / -0.2	-0.6 / 0.6	-0.1 / 0.1	1.8 / -1.8	0.0 / -0.0	-3.0 / 3.0	0.7 / -0.7	0.2 / -0.2
Luminosity	2.1 / -2.1	2.1 / -2.1	2.1 / -2.1	2.1 / -2.1	2.1 / -2.1	2.1 / -2.1	2.1 / -2.1	2.1 / -2.1	2.1 / -2.1	2.1 / -2.1
$t\bar{t}Z$ normalization	12.0 / -12.0	0.0 / 0.0	0.0 / 0.0	0.0 / 0.0	0.0 / 0.0	0.0 / 0.0	0.0 / 0.0	0.0 / 0.0	0.0 / 0.0	0.0 / 0.0
$t\bar{t}W$ normalization	0.0 / 0.0	13.0 / -13.0	0.0 / 0.0	0.0 / 0.0	0.0 / 0.0	0.0 / 0.0	0.0 / 0.0	0.0 / 0.0	0.0 / 0.0	0.0 / 0.0
WZ normalization	0.0 / 0.0	0.0 / 0.0	12.5 / -12.5	0.0 / 0.0	0.0 / 0.0	0.0 / 0.0	0.0 / 0.0	0.0 / 0.0	0.0 / 0.0	0.0 / 0.0
WZ modelling	0.0 / 0.0	0.0 / 0.0	-11.3 / 11.3	0.0 / 0.0	0.0 / 0.0	0.0 / 0.0	0.0 / 0.0	0.0 / 0.0	0.0 / 0.0	0.0 / 0.0
WZ_1_Jet	0.0 / 0.0	0.0 / 0.0	14.9 / -14.9	0.0 / 0.0	0.0 / 0.0	0.0 / 0.0	0.0 / 0.0	0.0 / 0.0	0.0 / 0.0	0.0 / 0.0
WZ_2_Jet	0.0 / 0.0	0.0 / 0.0	9.3 / -9.3	0.0 / 0.0	0.0 / 0.0	0.0 / 0.0	0.0 / 0.0	0.0 / 0.0	0.0 / 0.0	0.0 / 0.0
WZ_3_Jet	0.0 / 0.0	0.0 / 0.0	3.7 / -3.7	0.0 / 0.0	0.0 / 0.0	0.0 / 0.0	0.0 / 0.0	0.0 / 0.0	0.0 / 0.0	0.0 / 0.0
WZ_4_Jet	0.0 / 0.0	0.0 / 0.0	2.2 / -2.2	0.0 / 0.0	0.0 / 0.0	0.0 / 0.0	0.0 / 0.0	0.0 / 0.0	0.0 / 0.0	0.0 / 0.0
ZZ normalization	0.0 / 0.0	0.0 / 0.0	0.0 / 0.0	12.5 / -12.5	0.0 / 0.0	0.0 / 0.0	0.0 / 0.0	0.0 / 0.0	0.0 / 0.0	0.0 / 0.0
tZ normalization	0.0 / 0.0	0.0 / 0.0	0.0 / 0.0	0.0 / 0.0	30.0 / -30.0	0.0 / 0.0	0.0 / 0.0	0.0 / 0.0	0.0 / 0.0	0.0 / 0.0
tZ QCD radiation	0.0 / 0.0	0.0 / 0.0	0.0 / 0.0	0.0 / 0.0	-2.4 / 2.4	0.0 / 0.0	0.0 / 0.0	0.0 / 0.0	0.0 / 0.0	0.0 / 0.0
WtZ normalization	0.0 / 0.0	0.0 / 0.0	0.0 / 0.0	0.0 / 0.0	0.0 / 0.0	10.0 / -28.0	0.0 / 0.0	0.0 / 0.0	0.0 / 0.0	0.0 / 0.0
WtZ PS	0.0 / 0.0	0.0 / 0.0	0.0 / 0.0	0.0 / 0.0	0.0 / 0.0	25.3 / -25.3	0.0 / 0.0	0.0 / 0.0	0.0 / 0.0	0.0 / 0.0
Other bkg. normalization	0.0 / 0.0	0.0 / 0.0	0.0 / 0.0	0.0 / 0.0	0.0 / 0.0	0.0 / 0.0	50.0 / -50.0	0.0 / 0.0	0.0 / 0.0	0.0 / 0.0
$\sigma\_t\bar{t}$(scale)	0.0 / 0.0	0.0 / 0.0	0.0 / 0.0	0.0 / 0.0	0.0 / 0.0	0.0 / 0.0	0.0 / 0.0	2.4 / -3.5	2.4 / -3.5	0.0 / 0.0
$\sigma_{t\bar{t}}$(PDF+α_S)	0.0 / 0.0	0.0 / 0.0	0.0 / 0.0	0.0 / 0.0	0.0 / 0.0	0.0 / 0.0	0.0 / 0.0	4.2 / -4.2	4.2 / -4.2	0.0 / 0.0
$t\bar{t}$ PS	0.0 / 0.0	0.0 / 0.0	0.0 / 0.0	0.0 / 0.0	0.0 / 0.0	0.0 / 0.0	0.0 / 0.0	-37.6 / 37.6	40.2 / -40.2	0.0 / 0.0
$t\bar{t}$ NLO generator	0.0 / 0.0	0.0 / 0.0	0.0 / 0.0	0.0 / 0.0	0.0 / 0.0	0.0 / 0.0	0.0 / 0.0	-4.2 / 4.2	-71.8 / 71.8	0.0 / 0.0
$t\bar{t}$ QCD radiation	0.0 / 0.0	0.0 / 0.0	0.0 / 0.0	0.0 / 0.0	0.0 / 0.0	0.0 / 0.0	0.0 / 0.0	-7.0 / 7.0	12.1 / -12.1	0.0 / 0.0
Z+jets normalization	0.0 / 0.0	0.0 / 0.0	0.0 / 0.0	0.0 / 0.0	0.0 / 0.0	0.0 / 0.0	0.0 / 0.0	0.0 / 0.0	0.0 / 0.0	35.0 / -35.0

Table 6.12.: Summary of the relative impact of each source of uncertainty on the event yields in the Z+jets control region enriched with muon fakes for each individual sample (shown in percentage). Only the systematic sources are shown which have the effect above 2% on at least one sample.

Source	$t\bar{t}Z$	$t\bar{t}W$	WZ	ZZ	tZ	WtZ	Other MC	e-fakes ($t\bar{t}$)	μ-fakes ($t\bar{t}$)
pileup	0.0 / -0.0	0.5 / -0.5	5.6 / -5.6	0.3 / -0.3	4.5 / -4.5	1.2 / -1.2	-5.0 / 5.0	-4.2 / 4.2	-20.1 / 20.1
EL_SF_ID	2.0 / -2.0	1.8 / -1.8	2.5 / -2.5	1.9 / -1.9	1.8 / -1.8	1.9 / -1.9	2.4 / -2.4	3.2 / -3.2	0.6 / -0.6
bTagSF_77_eigenvars_B_0	4.1 / -4.1	4.8 / -4.8	0.0 / 0.0	-1.0 / 1.0	-1.2 / 1.2	2.1 / -2.1	2.7 / -2.7	1.8 / -1.8	-11.3 / 11.3
JET_21NP_JET_EffectiveNP_1	0.3 / -0.3	0.1 / -0.1	1.1 / -1.1	6.3 / -6.3	0.7 / -0.7	0.6 / -0.6	0.4 / -0.4	1.2 / -1.2	0.1 / -0.1
JET_21NP_JET_EtaIntercalibration_Modelling	0.4 / -0.4	0.3 / -0.3	0.0 / -0.0	6.2 / -6.2	0.0 / -0.0	0.6 / -0.6	-0.1 / 0.1	1.2 / -1.2	0.0 / -0.0
JET_21NP_JET_Flavor_Composition	1.1 / -1.1	0.5 / -0.5	0.6 / -0.6	6.5 / -6.5	-0.6 / 0.6	2.3 / -2.3	2.0 / -2.0	2.9 / -2.9	0.3 / -0.3
JET_21NP_JET_Flavor_Response	-0.4 / 0.4	-0.3 / 0.3	0.1 / -0.1	-6.3 / 6.3	0.2 / -0.2	0.0 / -0.0	-0.1 / 0.1	-1.2 / 1.2	-0.0 / 0.0
JET_21NP_JET_Pileup_RhoTopology	0.2 / -0.2	0.2 / -0.2	1.7 / -1.7	6.3 / -6.3	0.7 / -0.7	1.4 / -1.4	1.5 / -1.5	2.9 / -2.9	0.1 / -0.1
JET_JER_SINGLE_NP	2.4 / -2.4	1.6 / -1.6	3.8 / -3.8	-18.9 / 18.9	2.8 / -2.8	-2.9 / 2.9	9.0 / -9.0	0.8 / -0.8	-0.9 / 0.9
Luminosity	2.1 / -2.1	2.1 / -2.1	2.1 / -2.1	2.1 / -2.1	2.1 / -2.1	2.1 / -2.1	2.1 / -2.1	2.1 / -2.1	2.1 / -2.1
$t\bar{t}Z$ normalization	12.0 / -12.0	0.0 / 0.0	0.0 / 0.0	0.0 / 0.0	0.0 / 0.0	0.0 / 0.0	0.0 / 0.0	0.0 / 0.0	0.0 / 0.0
$t\bar{t}W$ normalization	0.0 / 0.0	13.0 / -13.0	0.0 / 0.0	0.0 / 0.0	0.0 / 0.0	0.0 / 0.0	0.0 / 0.0	0.0 / 0.0	0.0 / 0.0
WZ normalization	0.0 / 0.0	0.0 / 0.0	12.5 / -12.5	0.0 / 0.0	0.0 / 0.0	0.0 / 0.0	0.0 / 0.0	0.0 / 0.0	0.0 / 0.0
WZ modelling	0.0 / 0.0	0.0 / 0.0	8.2 / -8.2	0.0 / 0.0	0.0 / 0.0	0.0 / 0.0	0.0 / 0.0	0.0 / 0.0	0.0 / 0.0
WZ_2_Jet	0.0 / 0.0	0.0 / 0.0	15.7 / -15.7	0.0 / 0.0	0.0 / 0.0	0.0 / 0.0	0.0 / 0.0	0.0 / 0.0	0.0 / 0.0
WZ_3_Jet	0.0 / 0.0	0.0 / 0.0	5.8 / -5.8	0.0 / 0.0	0.0 / 0.0	0.0 / 0.0	0.0 / 0.0	0.0 / 0.0	0.0 / 0.0
ZZ normalization	0.0 / 0.0	0.0 / 0.0	0.0 / 0.0	12.5 / -12.5	0.0 / 0.0	0.0 / 0.0	0.0 / 0.0	0.0 / 0.0	0.0 / 0.0
tZ normalization	0.0 / 0.0	0.0 / 0.0	0.0 / 0.0	0.0 / 0.0	30.0 / -30.0	0.0 / 0.0	0.0 / 0.0	0.0 / 0.0	0.0 / 0.0
tZ QCD radiation	0.0 / 0.0	0.0 / 0.0	0.0 / 0.0	0.0 / 0.0	12.4 / -12.4	0.0 / 0.0	0.0 / 0.0	0.0 / 0.0	0.0 / 0.0
WtZ normalization	0.0 / 0.0	0.0 / 0.0	0.0 / 0.0	0.0 / 0.0	0.0 / 0.0	10.0 / -28.0	0.0 / 0.0	0.0 / 0.0	0.0 / 0.0
WtZ PS	0.0 / 0.0	0.0 / 0.0	0.0 / 0.0	0.0 / 0.0	0.0 / 0.0	-39.4 / 39.4	0.0 / 0.0	0.0 / 0.0	0.0 / 0.0
Other bkg. normalization	0.0 / 0.0	0.0 / 0.0	0.0 / 0.0	0.0 / 0.0	0.0 / 0.0	0.0 / 0.0	50.0 / -50.0	0.0 / 0.0	0.0 / 0.0
$\sigma_{t\bar{t}}$(scale)	0.0 / 0.0	0.0 / 0.0	0.0 / 0.0	0.0 / 0.0	0.0 / 0.0	0.0 / 0.0	0.0 / 0.0	2.4 / -3.5	2.4 / -3.5
$\sigma_{t\bar{t}}$(PDF+α_S)	0.0 / 0.0	0.0 / 0.0	0.0 / 0.0	0.0 / 0.0	0.0 / 0.0	0.0 / 0.0	0.0 / 0.0	4.2 / -4.2	4.2 / -4.2
$t\bar{t}$ PS	0.0 / 0.0	0.0 / 0.0	0.0 / 0.0	0.0 / 0.0	0.0 / 0.0	0.0 / 0.0	0.0 / 0.0	5.8 / -5.8	-100.0 / 100.0
$t\bar{t}$ NLO generator	0.0 / 0.0	0.0 / 0.0	0.0 / 0.0	0.0 / 0.0	0.0 / 0.0	0.0 / 0.0	0.0 / 0.0	7.5 / -7.5	-100.0 / 100.0
$t\bar{t}$ QCD radiation	0.0 / 0.0	0.0 / 0.0	0.0 / 0.0	0.0 / 0.0	0.0 / 0.0	0.0 / 0.0	0.0 / 0.0	-8.1 / 8.1	0.0 / 0.0

Table 6.13.: Summary of the relative impact of each source of uncertainty on the event yields in the $t\bar{t}$ control region enriched with electron fakes for each individual sample (shown in percentage). Only the systematic sources are shown which have the effect above 2% on at least one sample.

Source	$t\bar{t}Z$	$t\bar{t}W$	WZ	ZZ	tZ	WtZ	Other MC	μ-fakes ($t\bar{t}$)
pileup	1.6 / -1.6	-2.3 / 2.3	-10.9 / 10.9	1.8 / -1.8	3.9 / -3.9	-2.6 / 2.6	-0.3 / 0.3	-3.3 / 3.3
EL_SF_ID	0.9 / -0.9	0.9 / -0.9	1.2 / -1.2	2.1 / -2.1	1.2 / -1.2	0.9 / -0.9	0.8 / -0.8	0.7 / -0.7
bTagSF_77_extrapolation	-0.1 / 0.1	-0.0 / 0.0	-0.0 / 0.0	-0.0 / 0.0	-3.3 / 3.3	0.1 / -0.1	-0.1 / 0.1	-0.0 / 0.0
bTagSF_77_eigenvars_B_0	5.0 / -5.0	4.8 / -4.8	0.0 / 0.0	-0.1 / 0.1	6.2 / -6.2	4.6 / -4.6	3.8 / -3.8	0.1 / -0.1
bTagSF_77_eigenvars_B_1	1.5 / -1.5	1.5 / -1.5	0.0 / 0.0	0.1 / -0.1	5.0 / -5.0	1.4 / -1.4	0.9 / -0.9	0.1 / -0.1
bTagSF_77_eigenvars_B_2	-0.7 / 0.7	-0.7 / 0.7	0.0 / 0.0	-0.1 / 0.1	3.6 / -3.6	-0.4 / 0.4	-0.4 / 0.4	-0.1 / 0.1
EG_RESOLUTION_ALL	-0.2 / 0.2	0.2 / -0.2	-0.0 / 0.0	0.0 / 0.0	-0.2 / 0.2	-2.4 / 2.4	-0.0 / 0.0	-0.0 / 0.0
JET_21NP_JET_BJES_Response	-0.3 / 0.3	0.1 / -0.1	0.0 / 0.0	-0.0 / 0.0	-0.0 / 0.0	-2.1 / 2.1	-0.1 / 0.1	-0.2 / 0.2
JET_21NP_JET_EffectiveNP_1	0.1 / -0.1	0.3 / -0.3	3.4 / -3.4	5.3 / -5.3	-0.3 / 0.3	-2.0 / 2.0	1.1 / -1.1	0.8 / -0.8
JET_21NP_JET_EtaIntercalibration_Modelling	-0.3 / 0.3	0.2 / -0.2	3.3 / -3.3	3.8 / -3.8	0.1 / -0.1	-2.9 / 2.9	-0.1 / 0.1	0.4 / -0.4
JET_21NP_JET_Flavor_Composition	0.8 / -0.8	0.2 / -0.2	6.3 / -6.3	4.0 / -4.0	6.4 / -6.4	-0.7 / 0.7	1.3 / -1.3	2.7 / -2.7
JET_21NP_JET_Flavor_Response	-0.1 / 0.1	-0.1 / 0.1	-3.3 / 3.3	-5.3 / 5.3	0.1 / -0.1	0.9 / -0.9	-1.0 / 1.0	-0.7 / 0.7
JET_21NP_JET_Pileup_OffsetMu	-0.2 / 0.2	0.0 / -0.0	-3.3 / 3.3	0.3 / -0.3	0.0 / -0.0	-1.6 / 1.6	1.1 / -1.1	-0.2 / 0.2
JET_21NP_JET_Pileup_OffsetNPV	-0.4 / 0.4	-0.2 / 0.2	0.0 / -0.0	2.4 / -2.4	0.1 / -0.1	-4.2 / 4.2	1.0 / -1.0	-0.3 / 0.3
JET_21NP_JET_Pileup_RhoTopology	0.3 / -0.3	0.3 / -0.3	4.3 / -4.3	5.3 / -5.3	-0.2 / 0.2	-2.7 / 2.7	1.3 / -1.3	1.2 / -1.2
JET_JER_SINGLE_NP	-1.9 / 1.9	-2.1 / 2.1	17.2 / -17.2	409.9 / -100.0	16.1 / -16.1	1.0 / -1.0	-5.9 / 5.9	10.5 / -10.5
MUON_MS	0.3 / -0.3	-0.1 / 0.1	0.0 / 0.0	-1.3 / 1.3	-4.0 / 4.0	1.3 / -1.3	0.0 / -0.0	-0.6 / 0.6
Luminosity	2.1 / -2.1	2.1 / -2.1	2.1 / -2.1	2.1 / -2.1	2.1 / -2.1	2.1 / -2.1	2.1 / -2.1	2.1 / -2.1
$t\bar{t}Z$ normalization	12.0 / -12.0	0.0 / 0.0	0.0 / 0.0	0.0 / 0.0	0.0 / 0.0	0.0 / 0.0	0.0 / 0.0	0.0 / 0.0
$t\bar{t}Z$ modelling	-13.1 / 13.1	0.0 / 0.0	0.0 / 0.0	0.0 / 0.0	0.0 / 0.0	0.0 / 0.0	0.0 / 0.0	0.0 / 0.0
$t\bar{t}W$ normalization	0.0 / 0.0	13.0 / -13.0	0.0 / 0.0	0.0 / 0.0	0.0 / 0.0	0.0 / 0.0	0.0 / 0.0	0.0 / 0.0
WZ normalization	0.0 / 0.0	0.0 / 0.0	12.5 / -12.5	0.0 / 0.0	0.0 / 0.0	0.0 / 0.0	0.0 / 0.0	0.0 / 0.0
WZ modelling	0.0 / 0.0	0.0 / 0.0	-41.7 / 41.7	0.0 / 0.0	0.0 / 0.0	0.0 / 0.0	0.0 / 0.0	0.0 / 0.0
WZ_2_Jet	0.0 / 0.0	0.0 / 0.0	13.5 / -13.5	0.0 / 0.0	0.0 / 0.0	0.0 / 0.0	0.0 / 0.0	0.0 / 0.0
WZ_3_Jet	0.0 / 0.0	0.0 / 0.0	8.6 / -8.6	0.0 / 0.0	0.0 / 0.0	0.0 / 0.0	0.0 / 0.0	0.0 / 0.0
WZ_4_Jet	0.0 / 0.0	0.0 / 0.0	2.9 / -2.9	0.0 / 0.0	0.0 / 0.0	0.0 / 0.0	0.0 / 0.0	0.0 / 0.0
ZZ normalization	0.0 / 0.0	0.0 / 0.0	0.0 / 0.0	12.5 / -12.5	0.0 / 0.0	0.0 / 0.0	0.0 / 0.0	0.0 / 0.0
tZ normalization	0.0 / 0.0	0.0 / 0.0	0.0 / 0.0	0.0 / 0.0	30.0 / -30.0	0.0 / 0.0	0.0 / 0.0	0.0 / 0.0
tZ QCD radiation	0.0 / 0.0	0.0 / 0.0	0.0 / 0.0	0.0 / 0.0	-42.2 / 42.2	0.0 / 0.0	0.0 / 0.0	0.0 / 0.0
WtZ normalization	0.0 / 0.0	0.0 / 0.0	0.0 / 0.0	0.0 / 0.0	0.0 / 0.0	10.0 / -28.0	0.0 / 0.0	0.0 / 0.0
Other bkg. normalization	0.0 / 0.0	0.0 / 0.0	0.0 / 0.0	0.0 / 0.0	0.0 / 0.0	0.0 / 0.0	50.0 / -50.0	0.0 / 0.0
$\sigma_{t\bar{t}}$(scale)	0.0 / 0.0	0.0 / 0.0	0.0 / 0.0	0.0 / 0.0	0.0 / 0.0	0.0 / 0.0	0.0 / 0.0	2.4 / -3.5
$\sigma_{t\bar{t}}$(PDF+α_S)	0.0 / 0.0	0.0 / 0.0	0.0 / 0.0	0.0 / 0.0	0.0 / 0.0	0.0 / 0.0	0.0 / 0.0	4.2 / -4.2
$t\bar{t}$ PS	0.0 / 0.0	0.0 / 0.0	0.0 / 0.0	0.0 / 0.0	0.0 / 0.0	0.0 / 0.0	0.0 / 0.0	49.2 / -49.2
$t\bar{t}$ NLO generator	0.0 / 0.0	0.0 / 0.0	0.0 / 0.0	0.0 / 0.0	0.0 / 0.0	0.0 / 0.0	0.0 / 0.0	30.1 / -30.1
$t\bar{t}$ QCD radiation	0.0 / 0.0	0.0 / 0.0	0.0 / 0.0	0.0 / 0.0	0.0 / 0.0	0.0 / 0.0	0.0 / 0.0	16.3 / -16.3

Table 6.14.: Summary of the relative impact of each source of uncertainty on the event yields in the $t\bar{t}$ control region enriched with muon fakes for each individual sample (shown in percentage). Only the systematic sources are shown which have the effect above 2% on at least one sample.

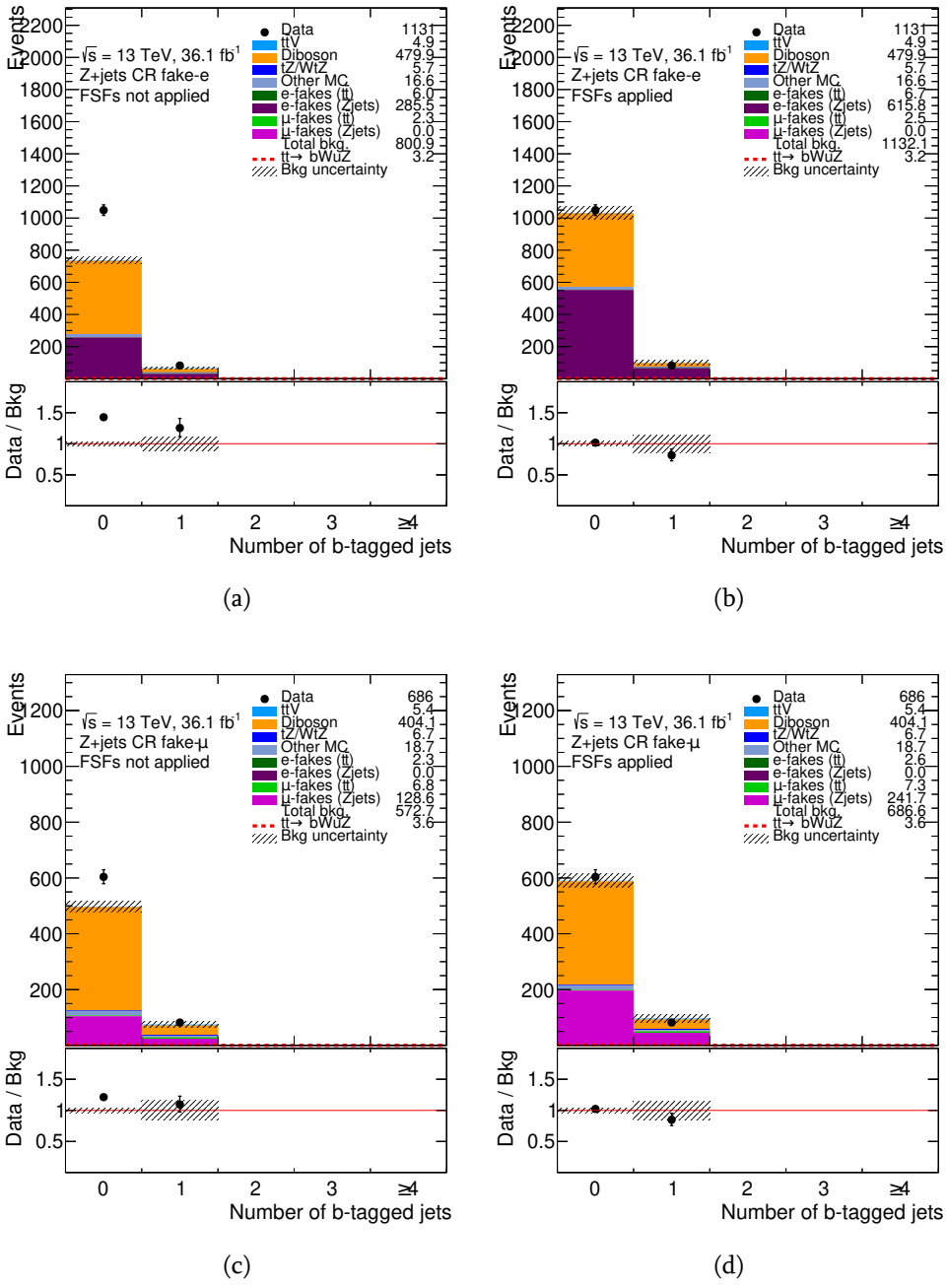

Figure 6.17.: Expected and observed distributions of the b-tag multiplicity in the Z+jets CR with fake electron (a,b) and with fake muon (c,d) before (left) and after (right) applying the fake scale factors. The number of signal events is normalized to the expected 95% CL limit. The dashed area represents statistical uncertainty on the background prediction.

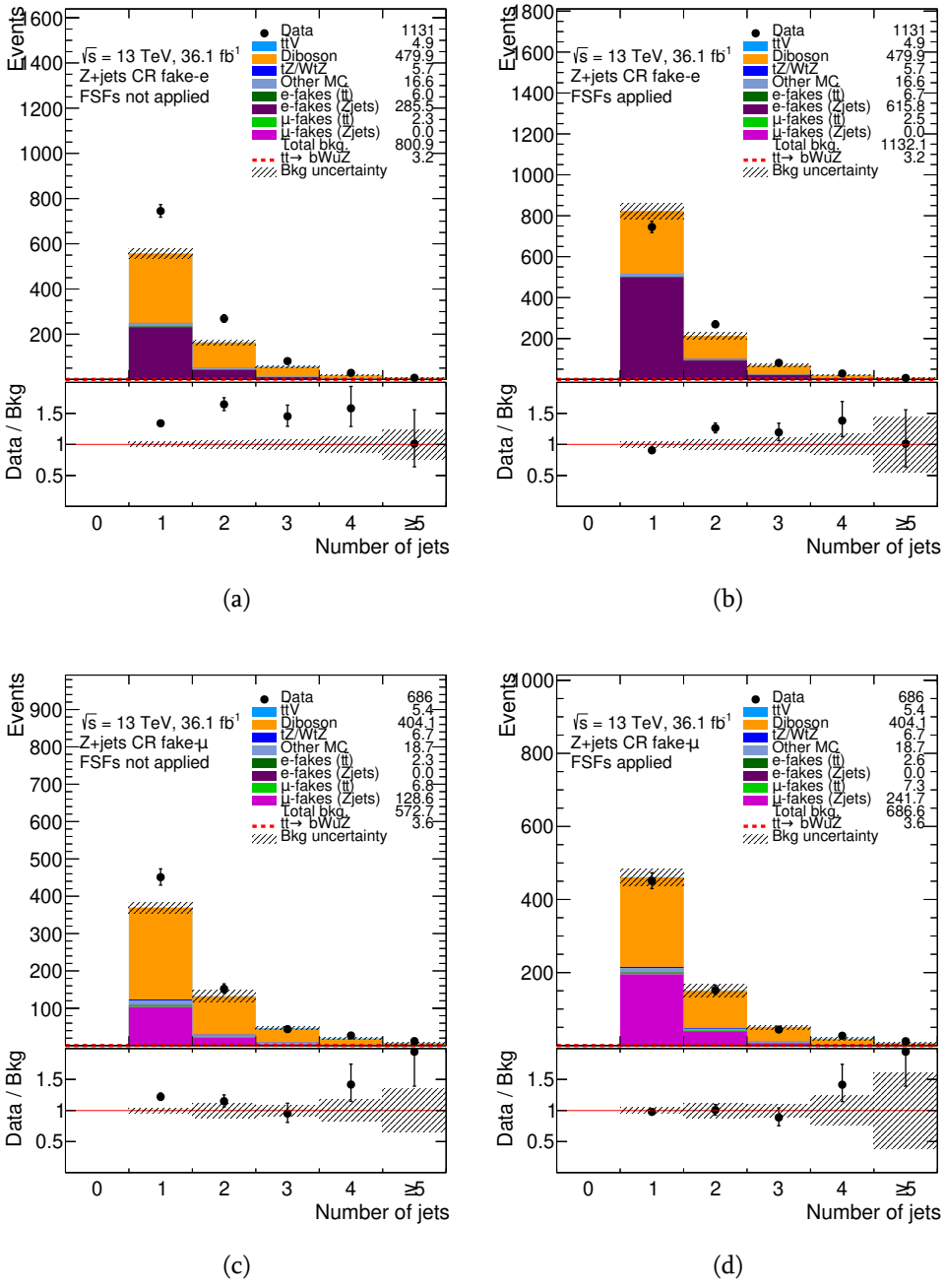

Figure 6.18.: Expected and observed distributions of the jet multiplicity in the Z+jets CR with fake electron (a,b) and with fake muon (c,d) before (left) and after (right) applying the fake scale factors. The number of signal events is normalized to the expected 95% CL limit. The dashed area represents statistical uncertainty on the background prediction.

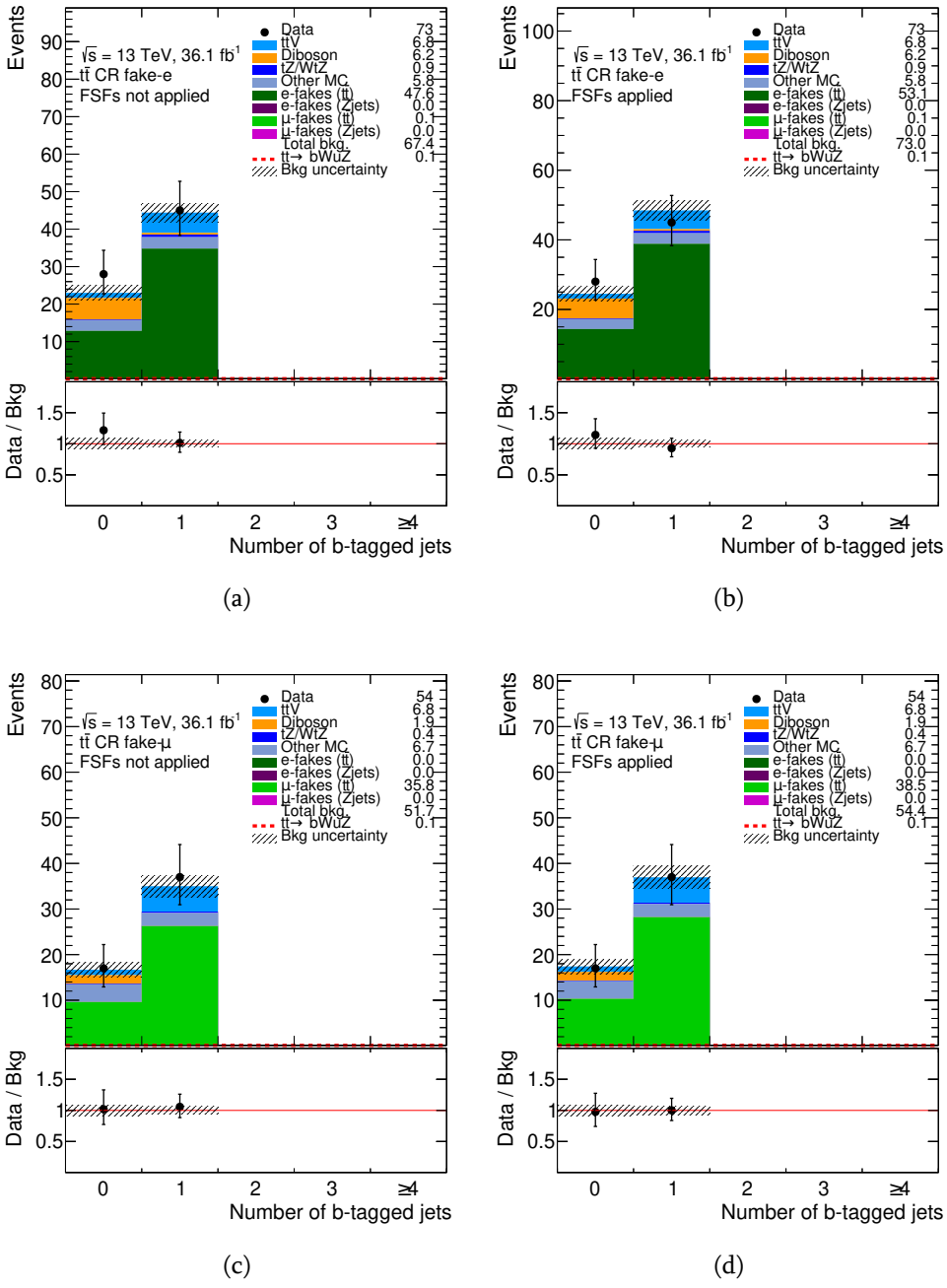

Figure 6.19.: Expected and observed distributions of the b-tag multiplicity in the $t\bar{t}$ CR with fake electron (a,b) and with fake muon (c,d) before (left) and after (right) applying the fake scale factors. The number of signal events is normalized to the expected 95% CL limit. The dashed area represents statistical uncertainty on the background prediction.

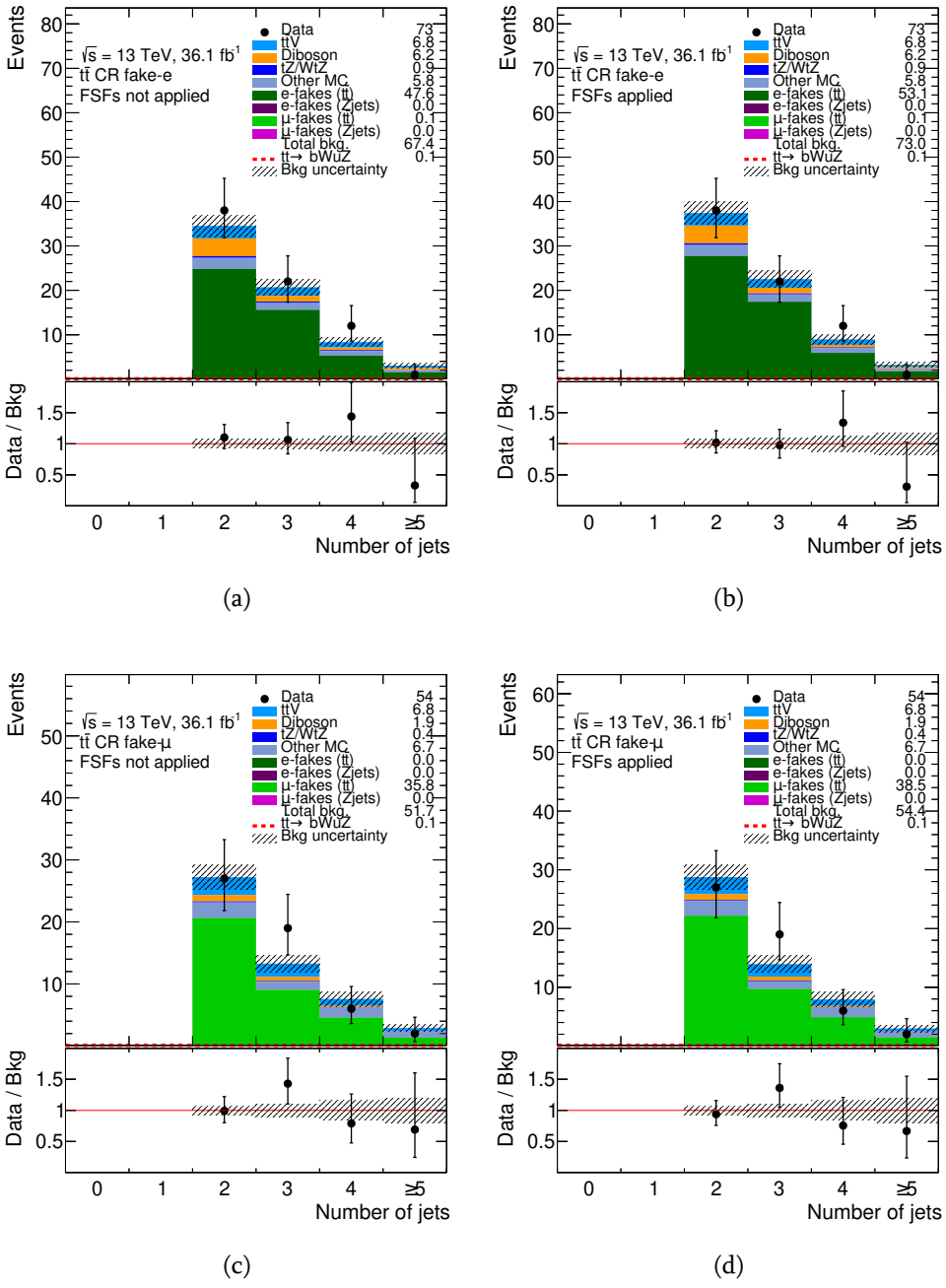

Figure 6.20.: Expected and observed distributions of the jet multiplicity in the $t\bar{t}$ CR with fake electron (a,b) and with fake muon (c,d) before (left) and after (right) applying the fake scale factors. The number of signal events is normalized to the expected 95% CL limit. The dashed area represents statistical uncertainty on the background prediction.

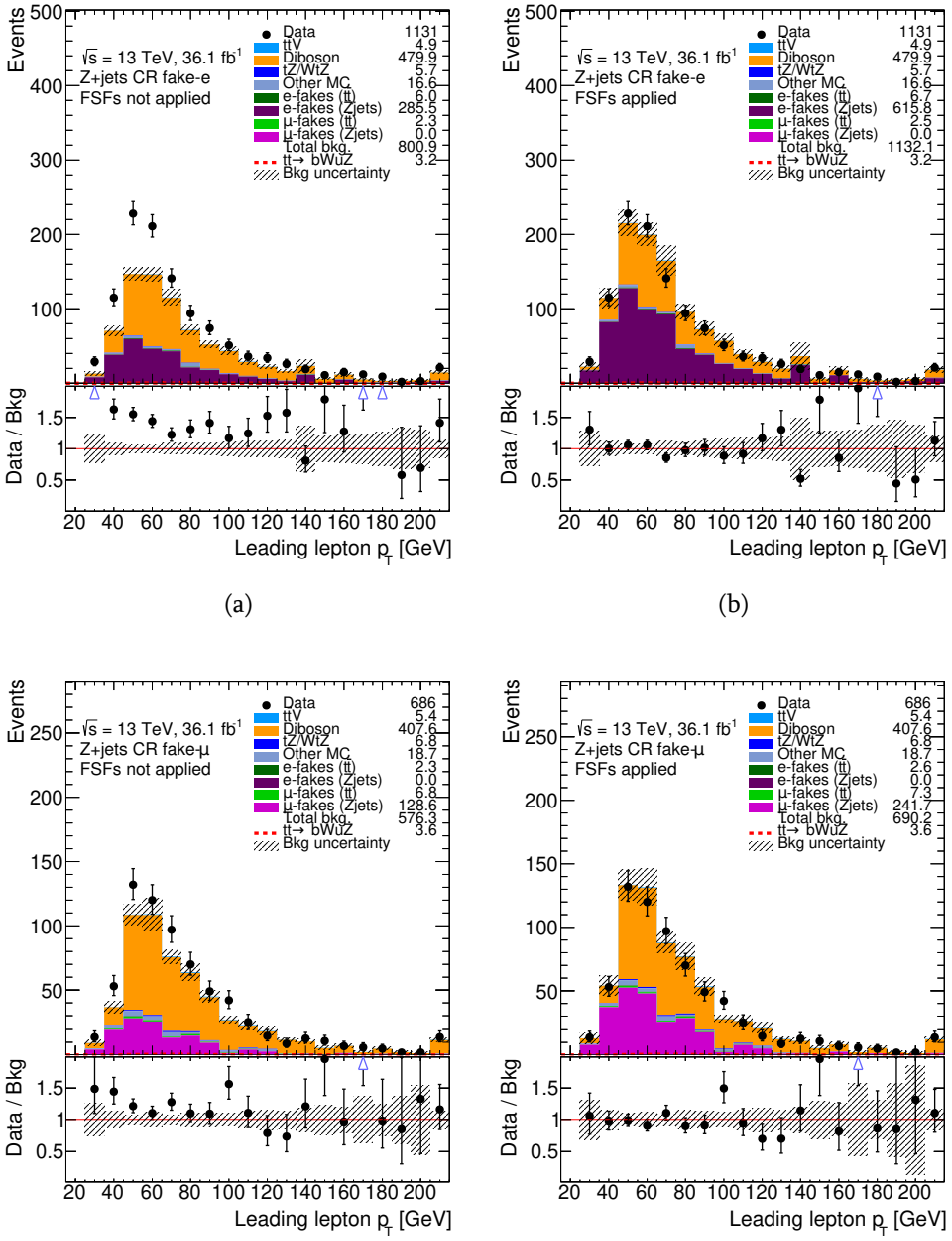

Figure 6.21.: Expected and observed distributions of the leading lepton p_{T} in the Z+jets CR with fake electron (a,b) and with fake muon (c,d) before (left) and after (right) applying the fake scale factors. The number of signal events is normalized to the expected 95% CL limit. The dashed area represents statistical uncertainty on the background prediction.

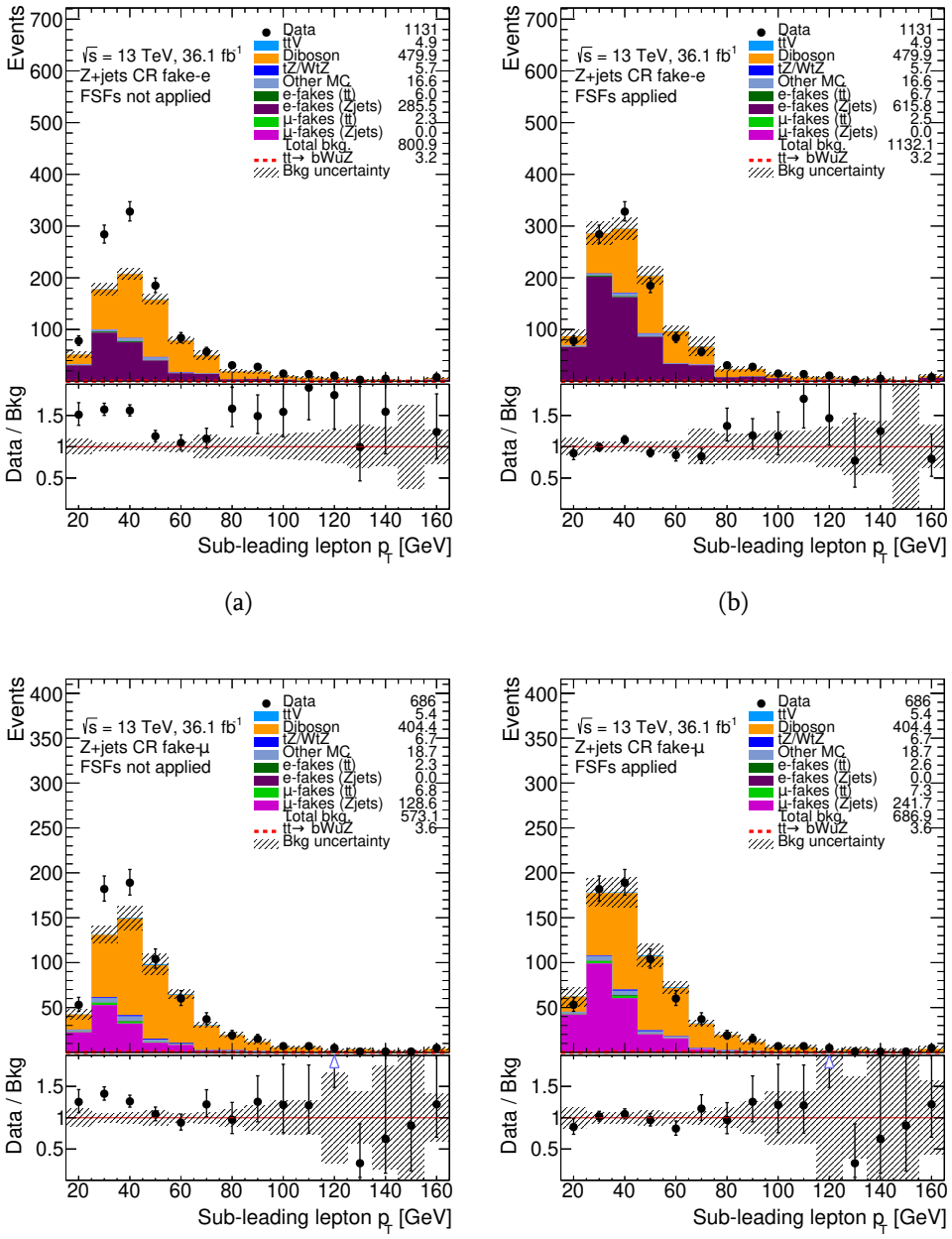

Figure 6.22.: Expected and observed distributions of the sub-leading lepton p_{T} in the Z+jets CR with fake electron (a,b) and with fake muon (c,d) before (left) and after (right) applying the fake scale factors. The number of signal events is normalized to the expected 95% CL limit. The dashed area represents statistical uncertainty on the background prediction.

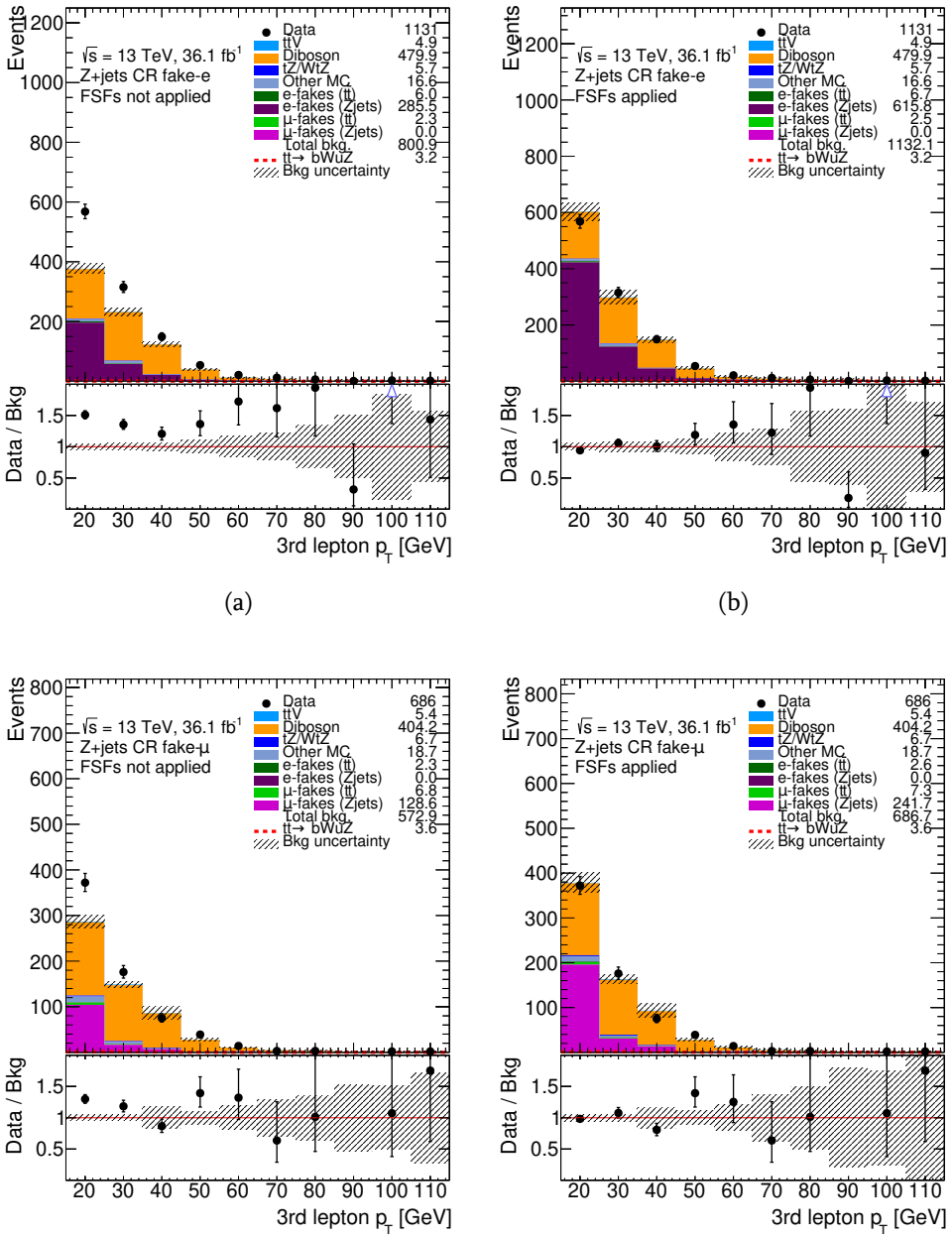

Figure 6.23.: Expected and observed distributions of the third lepton p_{T} in the Z+jets CR with fake electron (a,b) and with fake muon (c,d) before (left) and after (right) applying the fake scale factors. The number of signal events is normalized to the expected 95% CL limit. The dashed area represents statistical uncertainty on the background prediction.

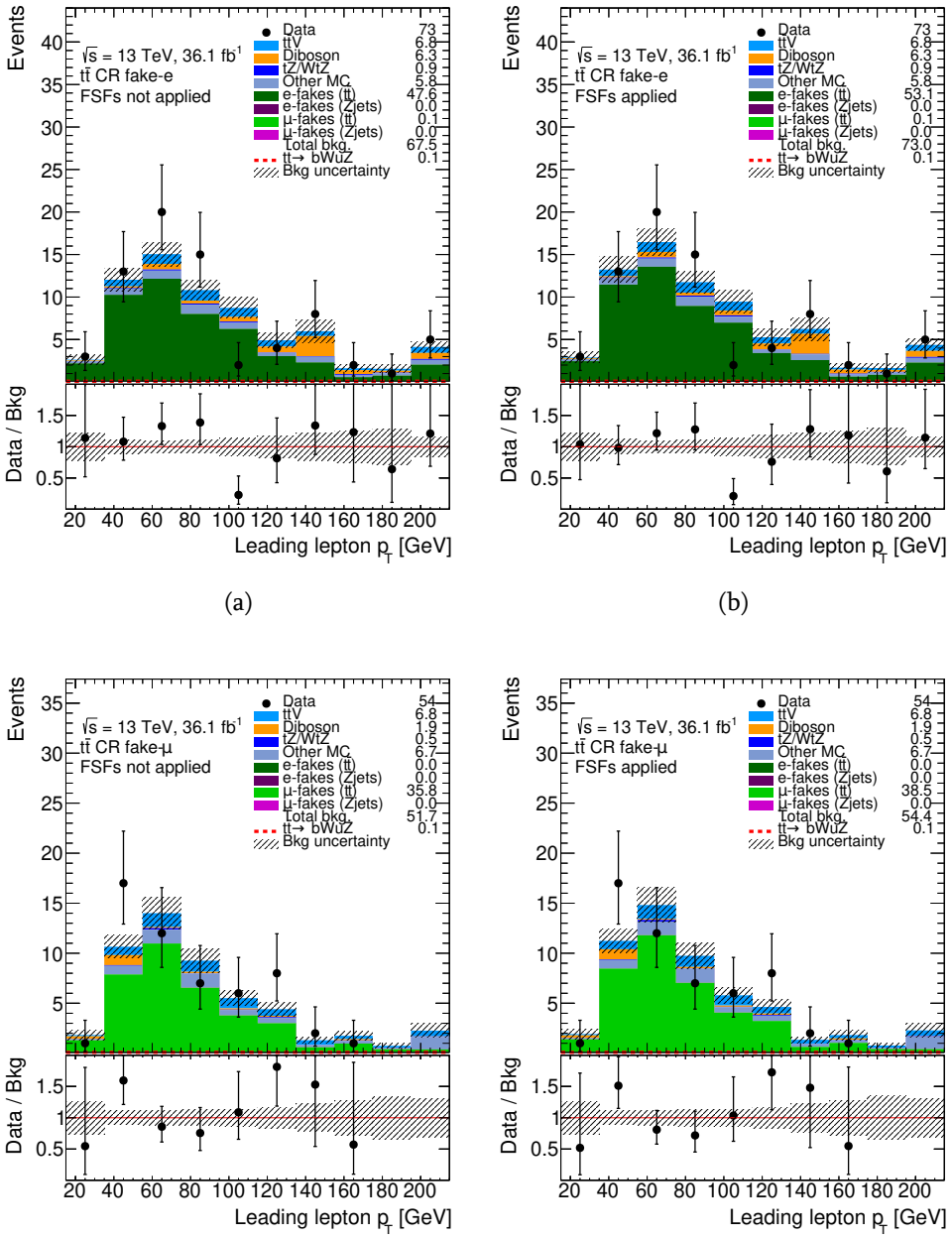

Figure 6.24.: Expected and observed distributions of the leading lepton p_{T} in the $t\bar{t}$ CR with fake electron (a,b) and with fake muon (c,d) before (left) and after (right) applying the fake scale factors. The number of signal events is normalized to the expected 95% CL limit. The dashed area represents statistical uncertainty on the background prediction.

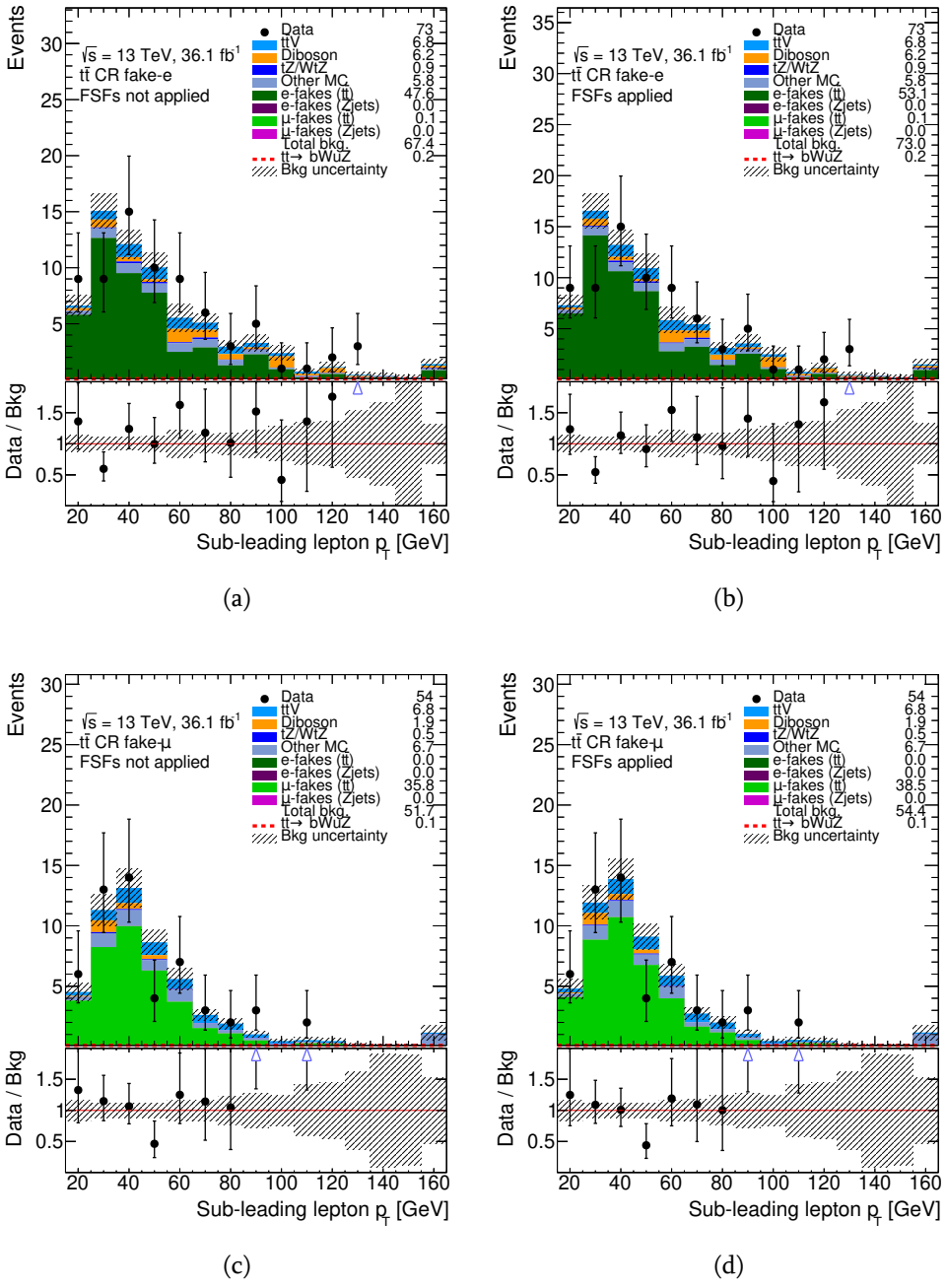

Figure 6.25.: Expected and observed distributions of the sub-leading lepton p_{T} in the $t\bar{t}$ CR with fake electron (a,b) and with fake muon (c,d) before (left) and after (right) applying the fake scale factors. The number of signal events is normalized to the expected 95% CL limit. The dashed area represents statistical uncertainty on the background prediction.

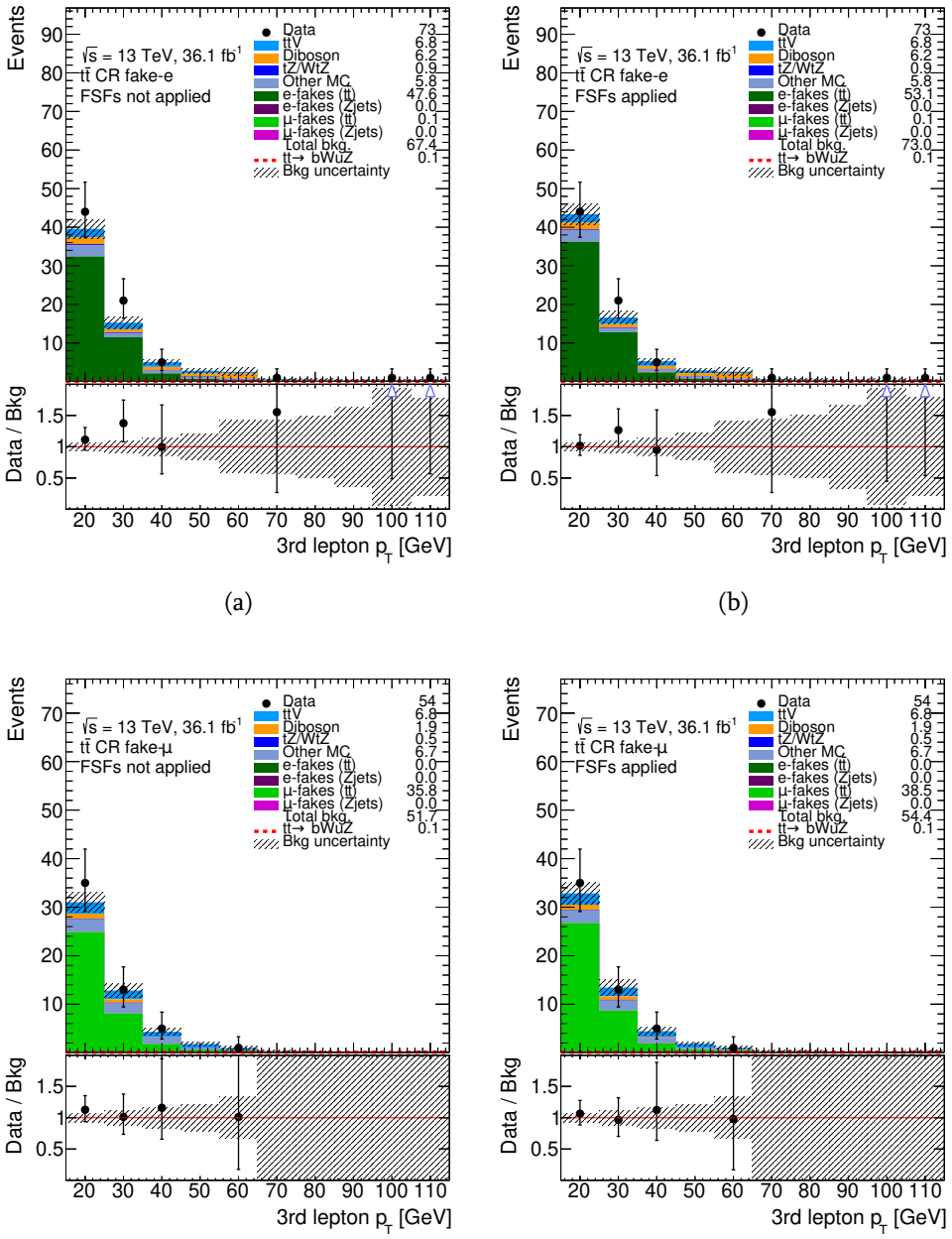

Figure 6.26.: Expected and observed distributions of the 3rd lepton p_{T} in the $t\bar{t}$ CR with fake electron (a,b) and with fake muon (c,d) before (left) and after (right) applying the fake scale factors. The number of signal events is normalized to the expected 95% CL limit. The dashed area represents statistical uncertainty on the background prediction.

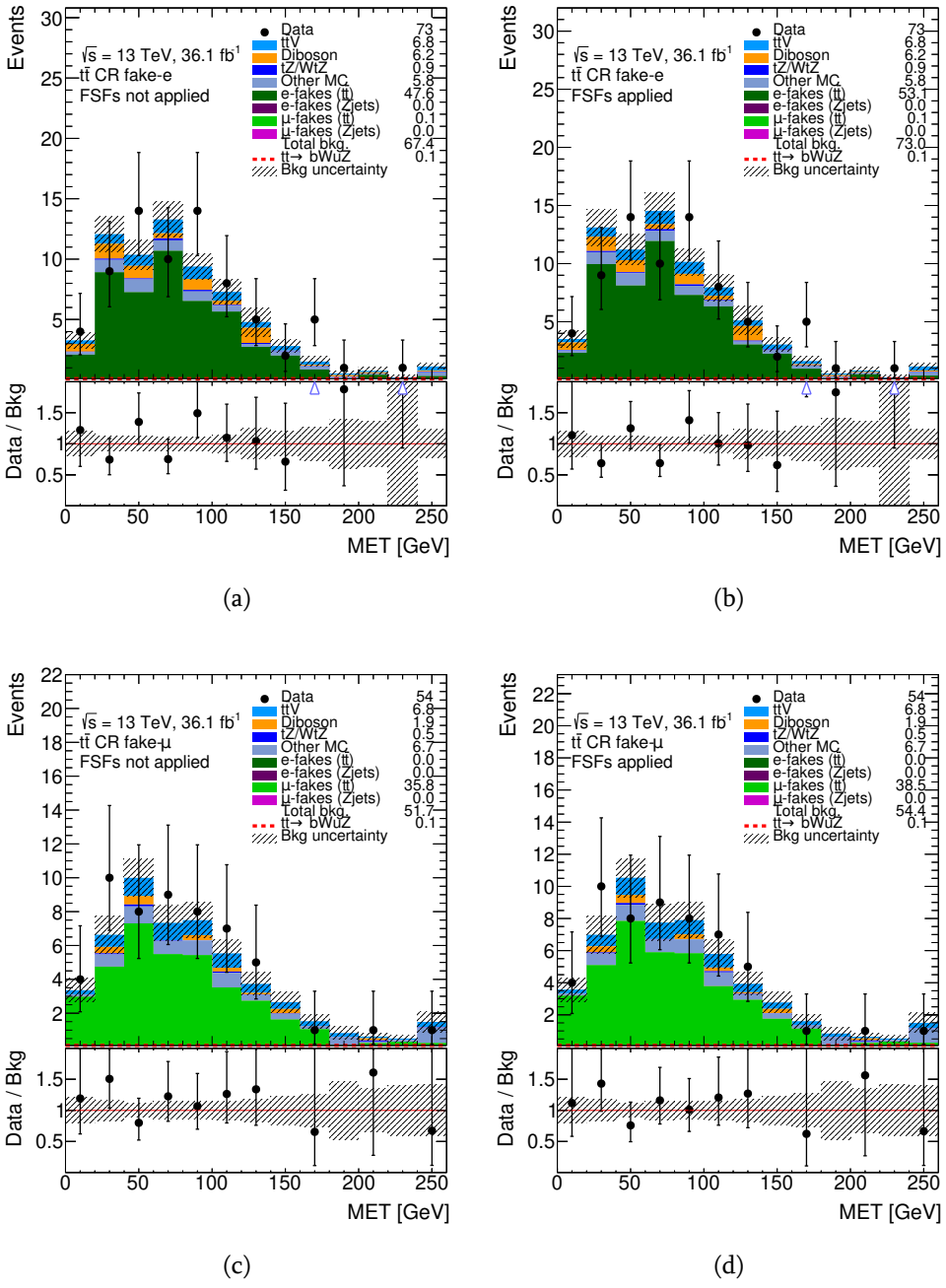

Figure 6.27.: Expected and observed distributions of the $E_{\mathrm{T}}^{\mathrm{miss}}$ in the $t\bar{t}$ CR with fake electron (a,b) and with fake muon (c,d) before (left) and after (right) applying the fake scale factors. The number of signal events is normalized to the expected 95% CL limit. The dashed area represents statistical uncertainty on the background prediction.

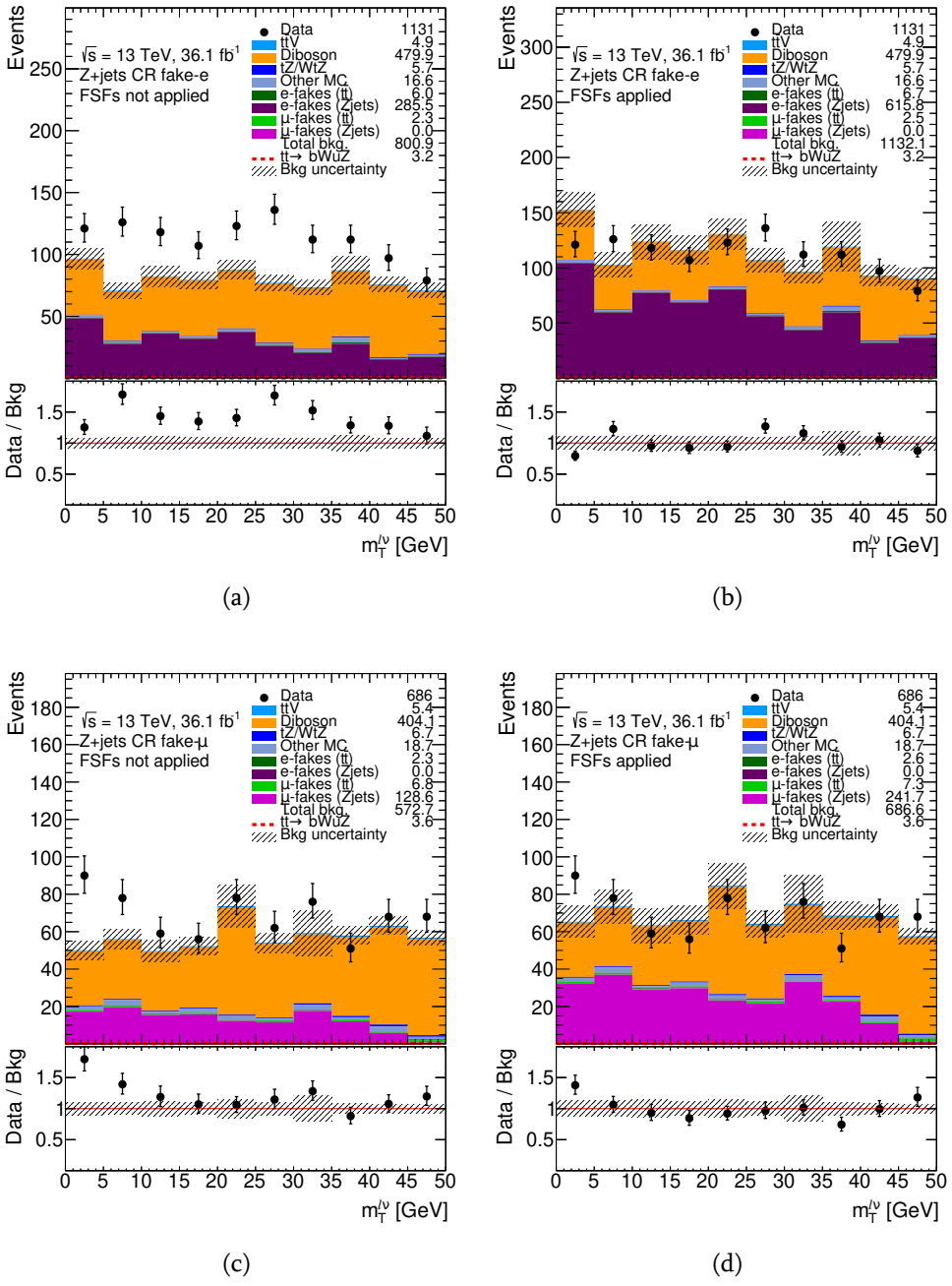

Figure 6.28.: Expected and observed distributions of the transverse mass $m_{\mathrm{T}}^{\ell\nu}$ in the Z+jets CR with fake electron (a,b) and with fake muon (c,d) before (left) and after (right) applying the fake scale factors. The number of signal events is normalized to the expected 95% CL limit. The dashed area represents statistical uncertainty on the background prediction.

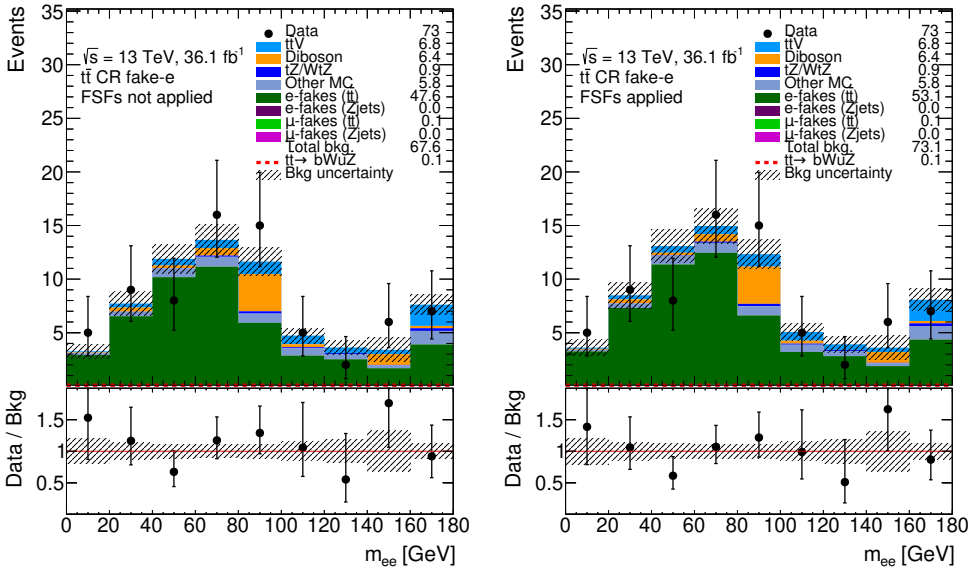

(a) (b)

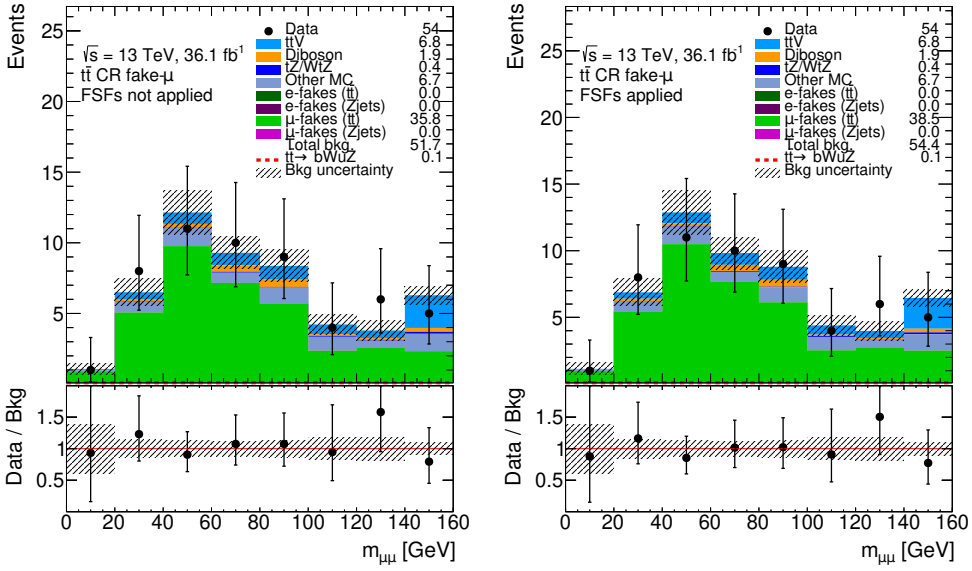

(c) (d)

Figure 6.29.: Expected and observed distributions of the invariant mass of the same flavour lepton pair in the $t\bar{t}$ CR with fake electron (a,b) and with fake muon (c,d) before (left) and after (right) applying the fake scale factors. The number of signal events is normalized to the expected 95% CL limit. The dashed area represents statistical uncertainty on the background prediction.

6.7. Signal-to-background discrimination

As described in Section 6.3.2, kinematics of signal events are reconstructed using a χ^2 minimization method. By selecting a jets combination and longitudinal component of neutrino momentum, this method would try to reconstruct a background event as a signal-like, however in average resulting χ^2 value would be higher for the background events than for the signal since background events do not contain the FCNC top-quark. As can be seen from Figure 6.4 the χ^2 distribution has a good signal-to-background separation power. It is used as a discriminant variable.

6.8. Systematic uncertainties

6.8.1. Experimental Systematics

Luminosity

The luminosity estimate has an uncertainty of 2.1% in $\sqrt{s} = 13$ TeV analyses. It is derived, following a methodology similar to that detailed in Ref. [182], from a calibration of the luminosity scale using x-y beam-separation scans performed in August 2015 and May 2016. This systematic uncertainty is applied to all processes determined from Monte Carlo simulations.

Pile-up reweighting

An uncertainty related to the scaling factors applied in MC to account for differences in pile-up distributions between MC and data is considered.

Lepton Reconstruction, Identification and Trigger

The reconstruction, identification and isolation efficiency of electrons and muons, as well as the efficiency of the triggers used to record the events, differ between data and simulation. Scale factors and their uncertainties are derived using a tag-and-probe method applied to electrons and muons from Z and W bosons and J/ψ particles [1, 174].

Lepton Momentum Scale and Resolution

The accuracy of lepton momentum scale and resolution in simulation is checked using reconstructed distributions of the $Z \to l^+l^-$ and $J/\psi \to l^+l^-$ masses [1, 174]. Small discrepancies are observed between data and simulation, and corrections for the lepton energy scale and res-

olution are implemented. Uncertainties on both the momentum scale and resolutions in the muon spectrometer and the tracking systems are considered, and varied separately.

Jet Vertex Tagger Efficiency

The uncertainty related to the Jet Vertex Tagger (JVT) scaling factors applied to the MC simulation includes the statistical uncertainty, a 30% uncertainty on the estimation of the residual contamination from pile-up jets after pileup suppression [176]. It is included in the fit as one nuisance parameter (NP).

Jet Energy Scale

The jet energy scale (JES) and its uncertainty have been derived combining information from test-beam data, LHC collision data and simulation [175]. The 75 parameters from the in situ analyses have been combined to form 8 NPs (7 dominant eigenvectors and 1 residual term of remainder). Further sources of uncertainties (η inter-calibration, pileup, single-hadron high-p_{T}, flavour and topology) round out JES uncertainty configuration for a total of 21 parameters (1 parameter is not applied to full simulation samples).

Jet Energy Resolution

The jet energy resolution has been measured separately for data and simulation using two in-situ techniques [175]. The expected fractional p_{T} resolution for a given jet is obtained as a function of its p_{T} and rapidity. A systematic uncertainty is defined as the quadratic difference between the jet energy resolutions for data and simulation. To estimate the corresponding systematic uncertainty in the analysis, the energy of jets in the simulation is smeared by this residual difference, and the changes in the normalization and shape of the distributions are compared to the default prediction. Since jets in the simulation can not be under-smeared, by definition the resulting uncertainty on the normalization and shape of the distributions is one-sided. This uncertainty is then symmetrized.

Heavy- and Light-Flavour Tagging

The effects of uncertainties in efficiencies for the heavy flavour identification of jets by the b-tagging algorithm have been evaluated. These efficiencies are measured from data and depend on the jet flavour. Efficiencies for tagging jets in the simulation have to be corrected by p_{T}-dependent factors; for jets from light quarks and gluons, the factors also depend on η. The scale factors and their uncertainties are applied to each jet in the simulation depending on its flavour and p_{T} [183].

Missing transverse energy

The lepton and jet energy scale and resolution uncertainties are propagated to the missing transverse momentum through the re-computation of its corresponding terms [179]. Their impact on the missing transverse momentum is therefore evaluated when the event selections are re-applied after having shifted the lepton energy. The effects of the energy scale and resolution uncertainties on the cell-out and soft-jet terms which also enter the $E_{\mathrm{T}}^{\mathrm{miss}}$ calculation are estimated by varying the scales and resolutions up and down by 1σ before re-doing the selection of the simulation samples.

Fake Scale Factors

Uncertainties of Fake Scale Factors are propagated to the fake-lepton background expectation by varying each FSF up and down by 1σ independently in the jet multiplicity bins: =1, =2, =3, =4, ≥ 5 and the corresponding NP is treated as uncorrelated in the b-veto and b-tag regions. Similarly, each of Fake Scale Factors is varied by $\pm 1\sigma$ uncertainty independently in the $E_{\mathrm{T}}^{\mathrm{miss}}$ bins: [20,40] GeV, [40,60] GeV, [60,80] GeV, $\geq$ 100 GeV and the corresponding NP is treated as uncorrelated in the b-veto and b-tag regions. Titles of NPs corresponding to the variations in the jet multiplicity bins are: `EL_Fake_SF_Zjets_*j`, `EL_Fake_SF_ttbar_*j`, `MU_Fake_SF_Zjets_*j`, `MU_Fake_SF_ttbar_*j`, where the star (*) stands to the number of jets in the corresponding bin. Titles of NPs corresponding to the variations in the $E_{\mathrm{T}}^{\mathrm{miss}}$ bins are: `EL_Fake_SF_Zjets_MET*`, `EL_Fake_SF_ttbar_MET*`, `MU_Fake_SF_Zjets_MET*`, `MU_Fake_SF_ttbar_MET*`, where the star (*) stands to the low edge of the corresponding $E_{\mathrm{T}}^{\mathrm{miss}}$ bin.

6.8.2. Theoretical and modelling uncertainties

Nuisance parameter for each of the uncertainties described below is included in the combined fit using Gaussian prior term correlated across all regions, as described in Section 6.9. Exceptions are the $t\bar{t}$ and Z+jets background normalization uncertainties which are used only in the fake scale factors determination (see Section 6.6.2). These uncertainties are propagated to the fake-lepton background contribution in the combined fit using the fake scale factors uncertainties.

Signal normalization

The $t\bar{t}$ production cross section uncertainties ($\sigma_{t\bar{t}} = 831.76^{+19.77}_{-29.20}(\text{scale})^{+35.06}_{-35.06}(\text{PDF} + \alpha_S)$ pb) are considered for the signal normalization. The first uncertainty comes from the independent variation of the factorisation and renormalisation scales, while the second one is associated to

variations in the PDF and α_S, following the PDF4LHC prescription with the MSTW2008 68% CL NNLO, CT10 NNLO and NNPDF2.3 5f FFN PDF sets (see Ref. [40] and references therein, and Refs. [41–43]).

Titles of NPs: Signal normalization ($\sigma_{t\bar{t}}$(Scale)), Signal normalization ($\sigma_{t\bar{t}}$(PDF+α_S)).

Diboson background

For the WZ and ZZ processes, the uncertainties in the normalization of the cross section [184] and from the choice of values for the electroweak parameters [185] are added in quadrature, yielding a 12.5% uncertainty. Alternative sample of WZ background generated with Powheg+Pythia8 (see Section 6.1) is used for the systematic uncertainty due to a choice of the generator. Titles of NPs: ZZ normalization, WZ normalization, WZ modelling. The WZ normalization uncertainty NP is treated as uncorrelated in the b-veto and b-tag regions. In addition, WZ yield in each of the jet multiplicity bins: =1, =2, =3, =4, ≥ 5 is varied by $\pm 25\%$ added in quadrature per jet [186, 187] and the relative impact on the total WZ yield is considered as an uncertainty and it is input to the fit as an uncorrelated component. Titles of the corresponding NPs are: WZ_*_Jet, where the star (*) stands to the number of jets in the corresponding bin.

$t\bar{t}V$ background

Global 12% and 13% uncertainties including scale and PDF variations (rounded and symmetrized with respect to the reference) [159] are considered for $t\bar{t}Z$ and $t\bar{t}W$ processes, respectively. Alternative sample of $t\bar{t}Z$ background generated with Sherpa v2.2 (see Section 6.1) is used for the systematic uncertainty due to a choice of the generator. Uncertainties due to the renormalization (muR) and factorization (muF) scales choice for the $t\bar{t}Z$ background are evaluated using the multiple event weights that provided by the event generator. Titles of NPs: $t\bar{t}W$ normalization, $t\bar{t}Z$ normalization, $t\bar{t}Z$ modelling, $t\bar{t}Z$ muR, $t\bar{t}Z$ muF, $t\bar{t}Z$ muRF.

tZ background

A 30% normalization is considered for this background as it is measured in Ref. [188]. Alternative MG5_aMC@NLO_Pythia6 samples with additional radiation were used in order to estimate the effect of QCD radiation. Titles of NPs: tZ normalization, tZ QCD radiation.

WtZ background

An uncertainty of +10% and -28% is assigned to the WtZ background cross section following the methodology of Ref. [189]. The lower normalization uncertainty is produced with regular Diagram Removal to remove overlap between this process and the $t\bar{t}Z$ production. For

the upper normalization uncertainty theoretical computations on single top production in the t-channel are used [189], [148]. For the systematics related to parton showering, a sample interfaced with Herwig++ is used. Titles of NPs: `WtZ normalization`, `WtZ PS`.

$t\bar{t}$ background

As for the signal process the $t\bar{t}$ production cross section uncertainties ($\sigma_{t\bar{t}} = 831.76^{+19.77}_{-29.20}$(scale) $^{+35.06}_{-35.06}$(PDF + α_S) pb) are considered for the SM $t\bar{t}$ process normalization. These uncertainties are only included in the fit for the fake scale factors determination (see Section 6.6.2), which increases the uncertainty on the $t\bar{t}$ fake scale factors determined from the fit. Then the uncertainty of the $t\bar{t}$ fake scale factors are used in the final combined fit (see Section 6.10.1) as described in Section 6.8.1, thus the $t\bar{t}$ normalization uncertainty is propagated to the final combined fit. In order to evaluate the uncertainties due to the choice of NLO generator, parton showering algorithm and QCD radiation, the alternative samples were considered as described in Section 6.1.2. Since the fake scale factors determination fit use a single bin (total yield) per CR, only the acceptance component of the $t\bar{t}$ modelling uncertainties, i.e. relative difference in the $t\bar{t}$ yield due to the alternative sample, is considered in this fit. Both acceptance and shape components of the $t\bar{t}$ modelling uncertainties on the total fake-leptons background are considered in the final combined fit (see Section 6.10.1). Titles of NPs: $\sigma_{t\bar{t}}$`(Scale)`, $\sigma_{t\bar{t}}$`(PDF+`α_S`)`, $t\bar{t}$ `NLO generator`, $t\bar{t}$ `PS`, $t\bar{t}$ `QCD radiation`.

Z+jets background

The theoretical cross section uncertainty of 6% and additional 24% uncertainty added in quadrature per extra parton due to the extrapolation to higher jet multiplicity, was considered for Z+jets background normalization, which yields in total of ∼35% uncertainty. This uncertainty is only included in the fit for the fake scale factors determination (see Section 6.6.2), which increases the uncertainty on the Z+jets fake scale factors determined from the fit. Then the uncertainty of the Z+jets fake scale factors are used in the final combined fit (see Section 6.10.1) as described in Section 6.8.1, thus the Z+jets normalization uncertainty is propagated to the final combined fit. Title of NP: `Z+jets normalization`.

Other backgrounds

A 50% uncertainty is considered for other rare SM backgrounds, including $3t$, $4t$, $t\bar{t}WW$ production and Higgs samples. Title of NP: `Other bkg.normalization`.

6.9. Statistical analysis

The distributions from the background control and signal regions are combined to test for the presence of a signal. The χ^2 distribution is used in the signal region for signal-to-background discrimination (see Section 6.7), while in the background control regions no attempt is made to separate the signal from the background, but they allow a tighter constraint of backgrounds and systematic uncertainties in a combined fit with the signal region. Considered distributions in the background CRs are as follow: p_{T} of the leading lepton in fakes CRs (Figures 6.5(a),6.7(a)) and $t\bar{t}Z$ CR (Figure 6.10(a)), W boson transverse mass in WZ CR (Figure 6.11(a)) and 4-lepton system mass in ZZ CR (Figure 6.13(a)).

The statistical analysis is based on a binned likelihood function $L(\mu, \theta)$ constructed as a product of Poisson probability terms over all bins in each considered distribution, and several Gaussian constraint terms for θ, a set of nuisance parameters that parametrize effects of statistical uncertainty and all sources of systematics on the signal and background expectations. This function depends on the signal strength parameter μ, a multiplicative factor for the number of signal events normalized to a reference branching ratio $\mathrm{BR}_{\mathrm{ref}}(t \to qZ) = 0.1\%$. The relationship between μ and the corresponding $\mathrm{BR}(t \to qZ)$ in case of the signal events is

$$\mu = \frac{\mathrm{BR}(t \to qZ)(1 - \mathrm{BR}(t \to qZ))}{\mathrm{BR}_{\mathrm{ref}}(t \to qZ)(1 - \mathrm{BR}_{\mathrm{ref}}(t \to qZ))} \tag{6.2}$$

Therefore, the total number of expected events in a given bin depends on μ and θ. The nuisance parameters adjust the expectations for signal and background according to the corresponding systematic uncertainties, and their fitted values correspond to the amount that best fits the data.

The test statistic q_μ is defined as the profile likelihood ratio: $q_\mu = -2\ln(L(\mu, \hat{\hat{\theta}}_\mu)/L(\hat{\mu}, \hat{\theta}))$, where $\hat{\mu}$ and $\hat{\theta}$ are the values of the parameters that maximise the likelihood function (with the constraints $0 \leq \hat{\mu} \leq \mu$), and $\hat{\hat{\theta}}_\mu$ are the values of the nuisance parameters that maximise the likelihood function for a given value of μ. This test statistic is used to measure the compatibility of the observed data with the background-only hypothesis (i.e. for $\mu = 0$), and to make statistical inferences about μ, such as upper limits using the CL_s method [154, 155]. The CL_s is calculated using the asymptotic properties of q_μ [156] as it is implemented in the RooStats packages [157].

Technically, the likelihood fit is done using the TRExFitter framework.

6.10. Results

6.10.1. Likelihood fit using Asimov data

In order to study the expected behavior of the fit, the simultaneous likelihood fits are performed under the background-only (i.e. $\mu = 0$) and signal-plus-background hypothesis using "Asimov

data" in the signal region, defined as the total expected pre-fit background. All the defined background control regions with the real data are considered in the fits. The variables used in the combined fit are presented in Table 6.15. The systematic uncertainties used in the fit are listed in Section 6.8. Smoothing[5] and symmetrization are applied on the systematics histograms, then to ease the fit performance, a pruning of the systematics is performed before the fit: if a given systematic uncertainty does not change any bin by more than 0.5% from the nominal value, then the shape component of that systematic for that sample in that region is ignored. Normalization component for all systematic sources are kept. The result of the pruning is shown in Figures 6.30 and 6.31.

The fitted nuisance parameters for the background-only (i.e. $\mu = 0$) and signal-plus-background hypothesis are displayed in Figures 6.32 and 6.33. For each nuisance parameter, the fitted value represents the preferred shift with respect to the nominal prediction in units of its prior uncertainty, whereas the fitted error represents the post-fit uncertainty in units of the prior uncertainty. Therefore, a fitted value much different from 0 means that the data is not well described by a nominal prediction and a fitted error close to 1 indicates that the data did not have enough statistical power to reduce the original uncertainty. In Figures 6.32 and 6.33 we see that fitted nuisance parameters are within their prior uncertainties. The large available statistics in the background control regions is expected to significantly constrain the overall background uncertainty, primarily via anti-correlation among systematic uncertainties introduced by the fit. This is what we observe in Figures 6.32 and 6.33. More details of the systematic uncertainties that have a large pull/constrain can be found in Appendix D. Since in the background CRs the expected signal is negligible and in the SR the Asimov data are used, there is almost no difference in the fitted NPs from the background-only and signal-plus-background fits. The corresponding correlation matrices for the fitted nuisance parameters under the background-only and signal-plus-background hypothesis can be found in Figure 6.34 and 6.35, respectively. Figures 6.36-6.41 show the pre-fit and post-fit plots under the background-only hypothesis for the background control and signal regions respectively. Pre- and post-fit event yields are presented in Tables 6.16 and 6.17 respectively. As expected, pre-fit uncertainty on the background prediction is significantly reduced after the fit, agreement between data and prediction is improved as well.

For the validation of the fit procedure on the background predictions, the fitted nuisance parameters are propagated to the validation regions. Pre-fit and post-fit yields under the background-only hypothesis in the validation regions are presented in Table 6.18 and Table 6.19 respectively. Pre-fit and post-fit plots of the reconstructed Z boson in the WZ validation region are presented in Figure 6.42, while the pre-fit and post-fit plots of the χ^2 in the side-band VR are shown in Figure 6.43. In the WZ validation region we observe that the post-fit background and data stay in agreement within one sigma uncertainty, while in the side-band VR total post-fit background has increased, but stays in a good agreement with data.

Summary of the pre-fit and post-fit uncertainties on the event yields under the background-

[5]The smoothing is not applied to the systematic uncartainties that are originate from the scale factros variation, except pileup.

only hypothesis in the signal region can be found in Table 6.20 and 6.21, respectively. In order to gain insight on the impact of different systematic uncertainties on the signal extraction, a combined fit is performed under the signal-plus-background hypothesis. Using Asimov data in the signal region, defined as the total expected pre-fit background plus the FCNC signal with a 0.01% branching ratio, while using real data in the background CRs. Figure 6.44 illustrates the leading 15 uncertainties in the analysis according to their post-fit impact on the best-fit branching ratio.

Region	Variable
SR	χ^2
WZ CR	W boson transverse mass
ZZ CR	4-leptons system mass
$t\bar{t}Z$ CR	Leading lepton p_{T}
Fakes CR0	Leading lepton p_{T}
Fakes CR1	Leading lepton p_{T}

Table 6.15.: The variables used in the combined fit for the signal region, WZ, ZZ, $t\bar{t}Z$ and fakes control regions.

Sample	WZ CR	ZZ CR	$t\bar{t}Z$ CR	Fakes CR0	Fakes CR1	SR
$t\bar{t}Z$	16.3 ± 3.13	0 ± 0	60.8 ± 8.71	6.08 ± 1.24	22.1 ± 3.19	36.7 ± 5.02
$t\bar{t}W$	0.813 ± 0.177	0 ± 0	0.966 ± 0.232	3.65 ± 0.726	15.5 ± 2.17	1.12 ± 0.198
WZ	559 ± 238	0 ± 0	8.95 ± 8.75	150 ± 67.8	20.4 ± 9.24	32.4 ± 18.8
ZZ	48.3 ± 10.7	91.8 ± 20.4	0.0704 ± 0.0265	58.0 ± 15.6	9.02 ± 2.28	6.21 ± 3.18
tZ	6.25 ± 2.04	0 ± 0	3.61 ± 1.20	0.632 ± 0.220	1.98 ± 0.627	12.5 ± 3.80
WtZ	5.48 ± 1.28	0 ± 0	6.09 ± 1.99	1.28 ± 0.457	2.55 ± 0.575	7.03 ± 1.53
Other MC	9.26 ± 4.78	0.967 ± 0.602	2.73 ± 1.39	11.8 ± 6.11	12.0 ± 6.05	2.29 ± 1.24
Fakes	28.4 ± 16.1	0 ± 0	3.28 ± 5.54	150 ± 50.3	143 ± 68.5	25.6 ± 10.8
Total bkg.	674 ± 241	92.8 ± 20.4	86.5 ± 14.9	382 ± 91.7	226 ± 69.7	124 ± 25.7
Data	734	87	81	433	260	124
Data/Bkg	1.09 ± 0.392	0.938 ± 0.230	0.936 ± 0.191	1.13 ± 0.278	1.15 ± 0.360	1 ± 0.214

Table 6.16.: The expected and observed event yields in the WZ, ZZ, $t\bar{t}Z$, fakes control and signal regions before the fit under the background-only hypothesis. In the signal region "Asimov data" is presented, defined as the total expected pre-fit background. Shown uncertainties are total pre-fit uncertainties.

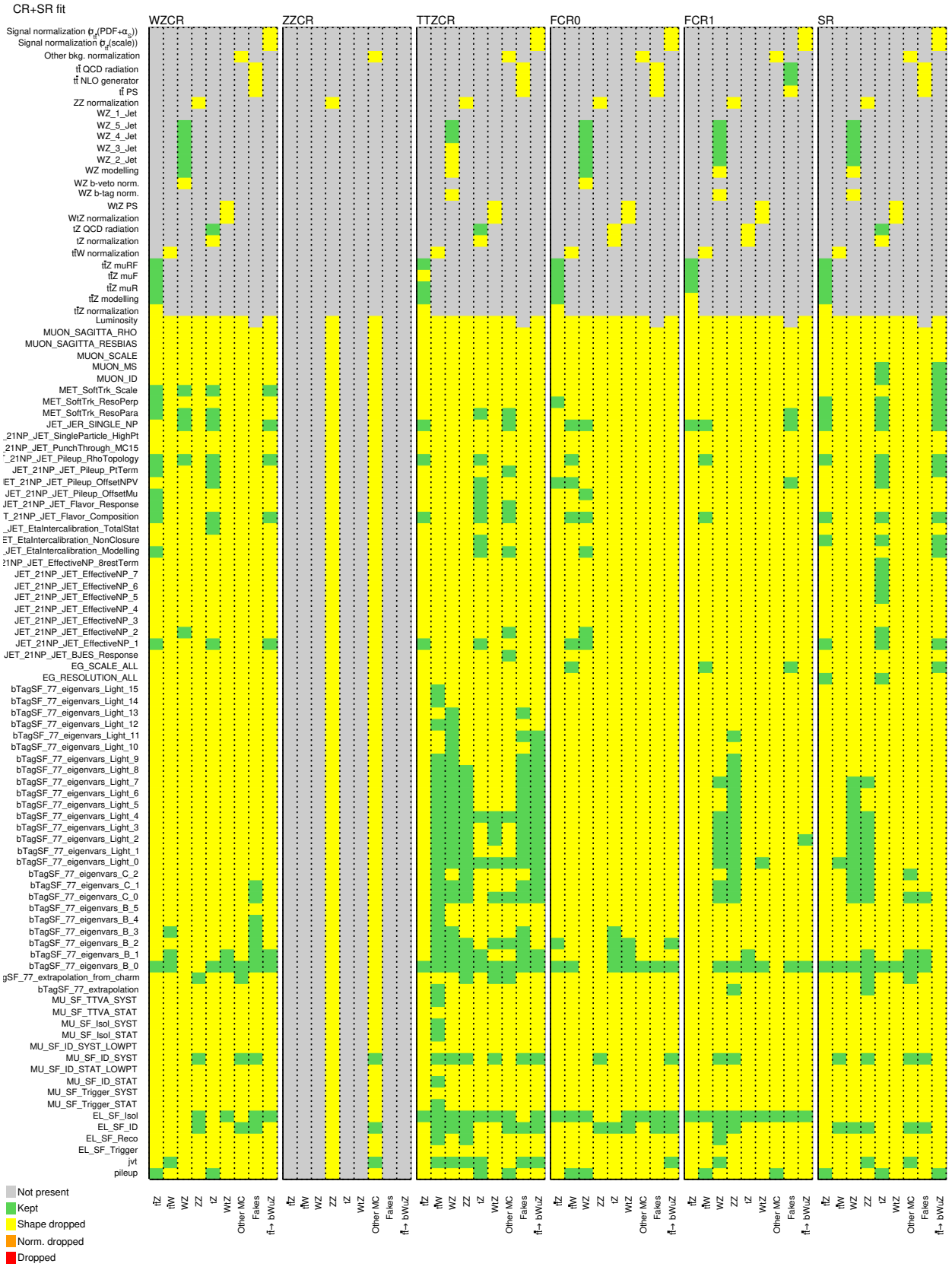

Figure 6.30.: Pruning of the instrumental and modelling systematic uncertainties based on the shape effect for each sample and region in the fit. Pruning algorithm is explained in the text.

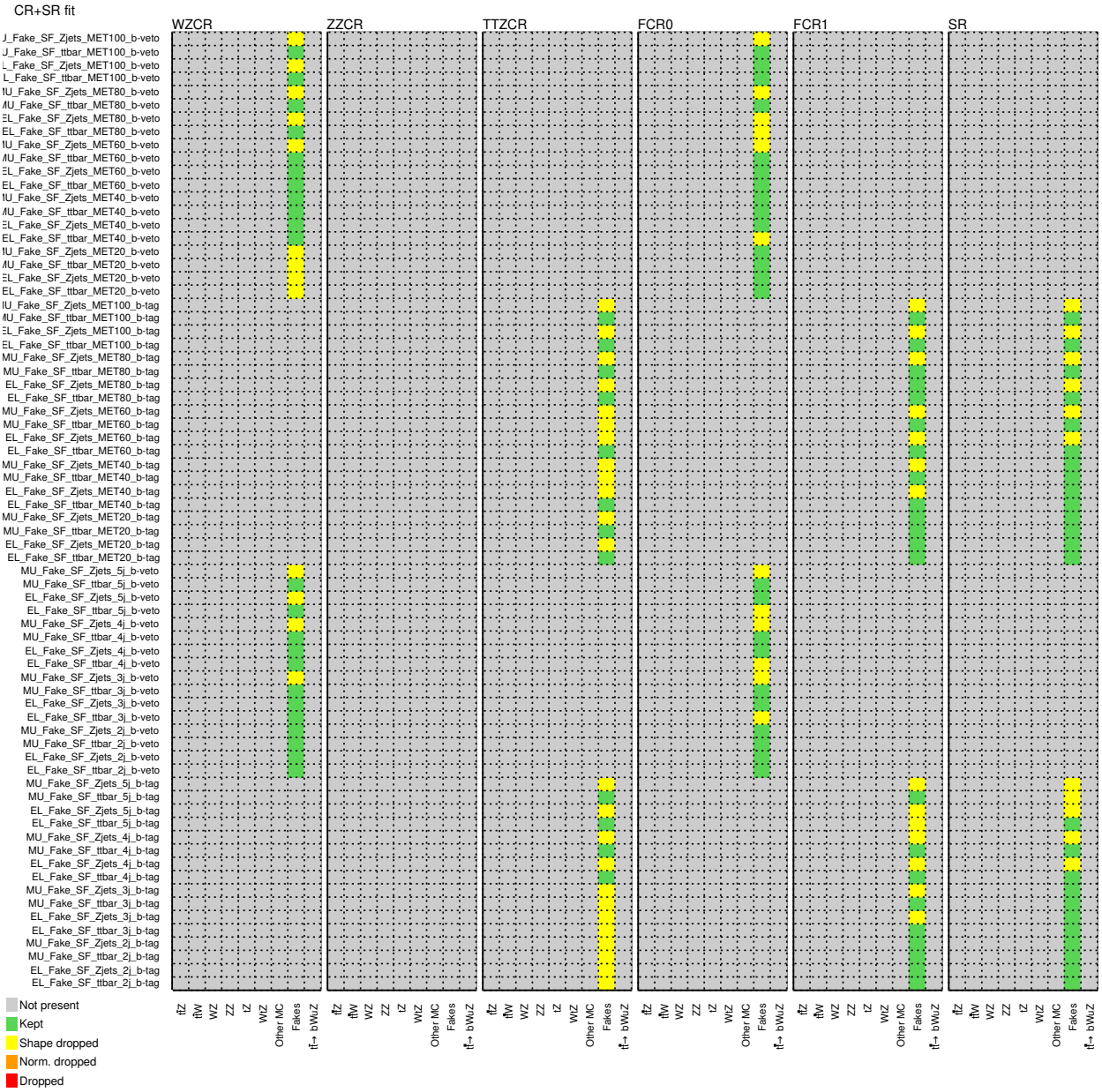

Figure 6.31.: Pruning of the instrumental and modelling systematic uncertainties based on the shape effect for each sample and region in the fit. Pruning algorithm is explained in the text.

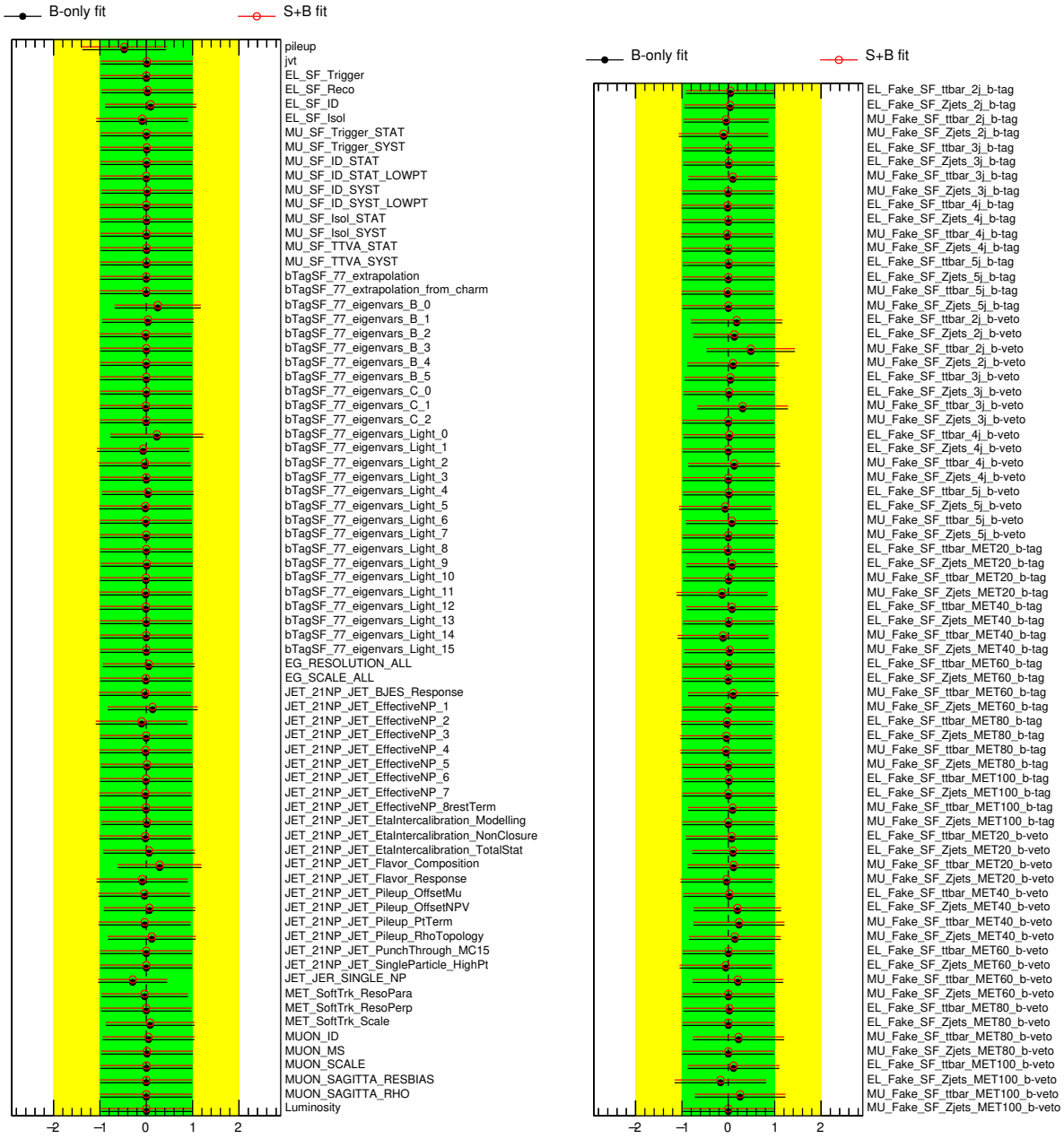

(a) (b)

Figure 6.32.: Fitted nuisance parameters corresponding to a) instrumental and b) fakes scale factors uncertainties under the background-only hypothesis (black closed circles) and under the signal-plus-background hypothesis (red open circles) in the background control and signal regions. In the signal region "Asimov data" is used, defined as the total expected pre-fit background.

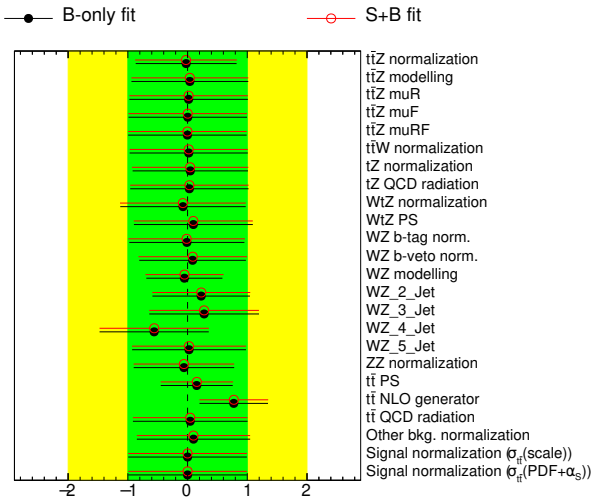

Figure 6.33.: Fitted nuisance parameters corresponding to the theoretical and modelling uncertainties under the background-only hypothesis (black closed circles) and under the signal-plus-background hypothesis (red open circles) in the background control and signal regions. In the signal region "Asimov data" is used, defined as the total expected pre-fit background.

Sample	WZ CR	ZZ CR	$t\bar{t}Z$ CR	Fakes CR0	Fakes CR1	SR
$t\bar{t}Z$	16.7 ± 3.10	0 ± 0	61.2 ± 6.48	6.22 ± 1.23	22.1 ± 2.94	37.6 ± 4.37
$t\bar{t}W$	0.860 ± 0.178	0 ± 0	1.00 ± 0.220	3.79 ± 0.715	15.8 ± 2.16	1.16 ± 0.200
WZ	610 ± 38.0	0 ± 0	6.18 ± 4.15	167 ± 13.3	20.4 ± 5.07	34.1 ± 8.28
ZZ	48.4 ± 9.05	89.1 ± 11.5	0.0684 ± 0.0227	59.7 ± 10.3	9.08 ± 2.21	6.86 ± 3.11
tZ	6.60 ± 2.07	0 ± 0	3.78 ± 1.18	0.681 ± 0.227	2.00 ± 0.611	12.7 ± 3.73
WtZ	5.45 ± 1.31	0 ± 0	5.79 ± 1.87	1.23 ± 0.443	2.47 ± 0.571	7.20 ± 1.61
Other MC	9.90 ± 4.84	1.04 ± 0.611	2.87 ± 1.38	13.0 ± 6.31	12.9 ± 6.13	2.37 ± 1.20
Fakes	40.1 ± 14.5	0 ± 0	2.07 ± 2.39	175 ± 32.1	174 ± 20.6	21.3 ± 7.28
Total bkg.	738 ± 33.5	90.1 ± 11.5	83.0 ± 7.23	426 ± 29.8	259 ± 19.8	123 ± 10.3
Data	734	87	81	433	260	124
Data/Bkg	0.995 ± 0.0583	0.966 ± 0.161	0.976 ± 0.138	1.02 ± 0.0863	1.01 ± 0.0990	1.00 ± 0.0987

Table 6.17.: The expected and observed event yields in the WZ, ZZ, $t\bar{t}Z$, fakes control and signal regions after the combined fit under the background-only hypothesis. In the signal region "Asimov data" is presented, defined as the total expected pre-fit background. Shown uncertainties are total post-fit uncertainties.

Sample	Side-band VR	WZ VR
$t\bar{t}Z$	34.3 ± 4.67	2.77 ± 0.658
$t\bar{t}W$	1.54 ± 0.252	0.995 ± 0.197
WZ	59.9 ± 24.4	52.0 ± 17.1
ZZ	11.3 ± 9.91	4.16 ± 1.96
tZ	20.5 ± 6.25	13.8 ± 4.27
WtZ	8.30 ± 1.73	1.01 ± 0.471
Other MC	2.24 ± 1.44	1.66 ± 1.84
Fakes	43.5 ± 17.6	43.1 ± 12.7
Total bkg.	182 ± 33.7	120 ± 22.6
Data	185	123
Data/Bkg	1.02 ± 0.203	1.03 ± 0.215

Table 6.18.: The expected and observed yields in the side-band and WZ validation regions before the fit. Shown uncertainties are total pre-fit uncertainties.

Sample	Side-band VR	WZ VR
$t\bar{t}Z$	34.0 ± 4.14	2.67 ± 0.586
$t\bar{t}W$	1.53 ± 0.246	0.949 ± 0.184
WZ	62.3 ± 11.8	51.2 ± 9.01
ZZ	7.54 ± 5.01	4.49 ± 1.95
tZ	20.7 ± 6.09	13.9 ± 4.14
WtZ	8.12 ± 1.77	1.03 ± 0.487
Other MC	2.39 ± 1.40	1.75 ± 1.68
Fakes	53.5 ± 16.6	43.8 ± 11.4
Total bkg.	190 ± 20.3	120 ± 16.5
Data	185	123
Data/Bkg	0.973 ± 0.126	1.03 ± 0.169

Table 6.19.: The expected and observed yields in the side-band and WZ validation regions after the combined fit under the background-only hypothesis. In the signal region "Asimov data" is used, defined as the total expected pre-fit background. Shown uncertainties are total post-fit uncertainties.

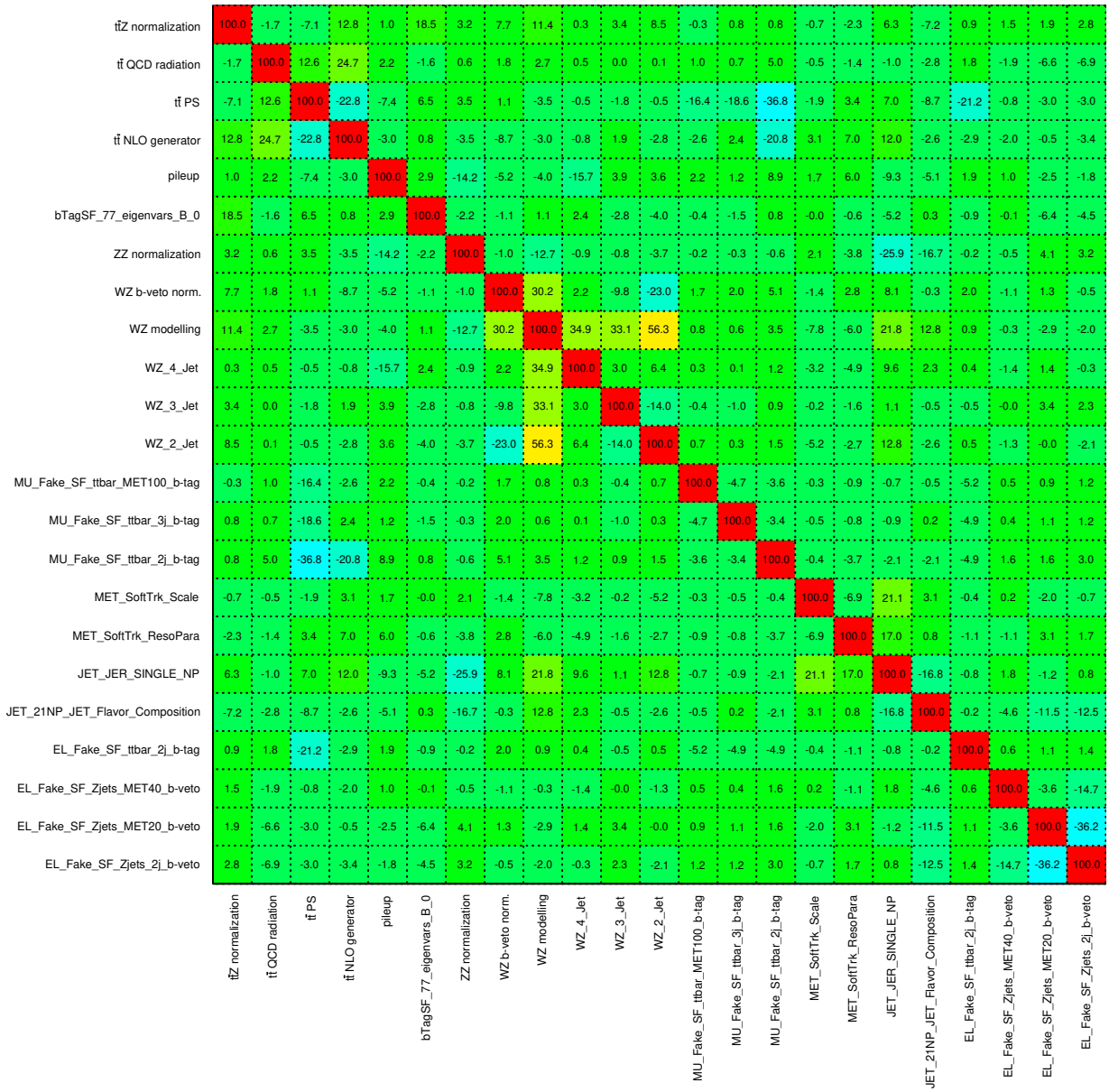

Figure 6.34.: Correlation matrix corresponding to the fit under the background-only hypothesis in the background control and signal regions. In the signal region "Asimov data" is used, defined as the total expected pre-fit background. Displayed values are in percentage. Only nuisance parameters with a correlation coefficient of at least 15% with any other parameter are displayed.

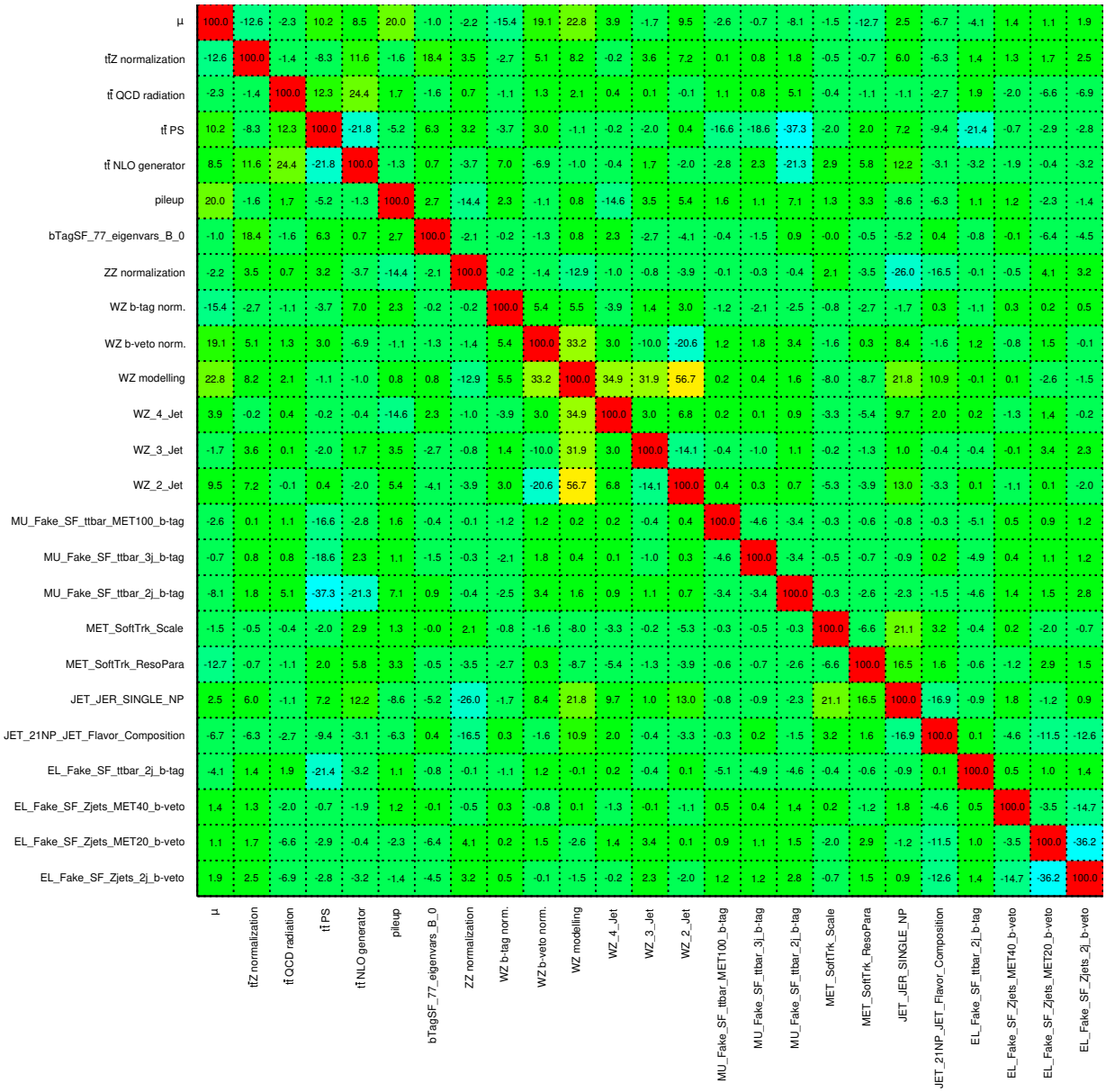

Figure 6.35.: Correlation matrix corresponding to the fit under the signal-plus-background hypothesis in the background control and signal regions. In the signal region "Asimov data" is used, defined as the total expected pre-fit background. Displayed values are in percentage. Only nuisance parameters with a correlation coefficient of at least 15% with any other parameter are displayed.

Source	$t\bar{t}Z$	$t\bar{t}W$	WZ	ZZ	tZ	WtZ	Other MC	Fakes	$t\bar{t}$ →bWuZ
pileup	-1.3 / 1.3	-4.1 / 4.1	-4.1 / 4.1	-10.7 / 10.7	1.0 / -1.0	-4.2 / 4.2	0.1 / -0.1	-6.9 / 6.9	-2.3 / 2.3
EL_SF_ID	1.2 / -1.2	1.2 / -1.2	1.2 / -1.2	2.0 / -2.0	1.2 / -1.2	1.1 / -1.1	1.2 / -1.2	2.1 / -2.1	1.1 / -1.1
bTagSF_77_extrapolation_from_charm	-0.1 / 0.1	0.0 / 0.0	0.0 / 0.0	-0.5 / 0.5	0.0 / 0.0	-0.1 / 0.1	3.0 / -3.0	0.0 / 0.0	0.0 / -0.0
bTagSF_77_eigenvars_B_0	2.5 / -2.5	4.5 / -4.5	-0.7 / 0.7	-3.3 / 3.3	-0.8 / 0.8	-1.0 / 1.0	1.2 / -1.2	-3.1 / 3.1	-3.2 / 3.2
bTagSF_77_eigenvars_C_0	0.4 / -0.4	0.1 / -0.1	-1.9 / 1.9	-0.6 / 0.6	0.1 / -0.1	0.3 / -0.3	-2.9 / 2.9	-0.4 / 0.4	0.0 / -0.0
bTagSF_77_eigenvars_Light_0	0.5 / -0.5	0.3 / -0.3	-6.0 / 6.0	-3.6 / 3.6	0.4 / -0.4	0.3 / -0.3	0.3 / -0.3	0.4 / -0.4	0.5 / -0.5
bTagSF_77_eigenvars_Light_1	-0.2 / 0.2	-0.1 / 0.1	2.3 / -2.3	1.8 / -1.8	-0.1 / 0.1	-0.1 / 0.1	-0.1 / 0.1	-0.2 / 0.2	-0.2 / 0.2
bTagSF_77_eigenvars_Light_2	-0.1 / 0.1	-0.1 / 0.1	1.6 / -1.6	3.5 / -3.5	-0.0 / 0.0	-0.0 / 0.0	0.1 / -0.1	-0.2 / 0.2	-0.1 / 0.1
bTagSF_77_eigenvars_Light_4	0.1 / -0.1	0.1 / -0.1	-3.1 / 3.1	-3.1 / 3.1	0.1 / -0.1	-0.1 / 0.1	0.1 / -0.1	0.1 / -0.1	0.1 / -0.1
EG_RESOLUTION_ALL	0.0 / -0.0	-0.2 / 0.2	-0.4 / 0.4	3.7 / -3.7	-0.2 / 0.2	-0.4 / 0.4	-0.8 / 0.8	-0.7 / 0.7	0.1 / -0.1
JET_21NP_JET_BJES_Response	-0.3 / 0.3	-1.3 / 1.3	0.2 / -0.2	3.4 / -3.4	-0.0 / 0.0	0.2 / -0.2	0.3 / -0.3	-0.2 / 0.2	0.1 / -0.1
JET_21NP_JET_EffectiveNP_1	0.7 / -0.7	0.5 / -0.5	2.4 / -2.4	1.4 / -1.4	1.3 / -1.3	0.7 / -0.7	0.7 / -0.7	1.2 / -1.2	0.4 / -0.4
JET_21NP_JET_EffectiveNP_2	-0.3 / 0.3	0.2 / -0.2	-1.4 / 1.4	-2.3 / 3.6	-0.6 / 0.6	-0.4 / 0.4	0.1 / -0.1	-2.3 / 2.3	-0.2 / 0.2
JET_21NP_JET_EffectiveNP_4	-0.1 / 0.1	-0.6 / 0.6	-0.6 / 0.6	7.2 / -4.2	-0.3 / 0.3	-0.6 / 0.6	0.1 / -0.1	0.8 / -0.8	-0.2 / 0.2
JET_21NP_JET_EffectiveNP_5	-0.0 / 0.0	0.9 / -0.9	1.0 / -1.0	-4.2 / 4.2	0.3 / -0.3	0.0 / -0.0	-0.5 / 0.5	0.2 / -0.2	0.1 / -0.1
JET_21NP_JET_EffectiveNP_6	0.2 / -0.2	-1.0 / 1.0	-0.6 / 0.6	0.1 / -0.1	0.4 / -0.4	-0.6 / 0.6	-0.7 / 0.7	-2.9 / 2.9	-0.1 / 0.1
JET_21NP_JET_EffectiveNP_8restTerm	0.0 / -0.0	-0.2 / 0.2	-0.1 / 0.1	1.4 / 5.1	-0.1 / 0.1	-0.6 / 0.6	0.2 / -0.2	-0.4 / 0.4	0.1 / -0.1
JET_21NP_JET_EtaIntercalibration_Modelling	0.4 / -0.4	1.3 / -1.3	1.7 / -1.7	3.3 / -3.3	0.5 / -0.5	0.7 / -0.7	-0.2 / 0.2	-3.8 / 3.8	0.0 / -0.0
JET_21NP_JET_EtaIntercalibration_NonClosure	-0.1 / 0.1	0.5 / -0.5	1.4 / -1.4	2.6 / -2.6	0.3 / -0.3	-0.3 / 0.3	-0.4 / 0.4	-1.3 / 1.3	-0.0 / 0.0
JET_21NP_JET_EtaIntercalibration_TotalStat	0.3 / -0.3	-1.8 / 1.8	1.2 / -1.2	-6.0 / 6.0	0.1 / -0.1	0.4 / -0.4	0.0 / -0.0	1.1 / -1.1	0.6 / -0.6
JET_21NP_JET_Flavor_Composition	1.2 / -1.2	0.7 / -0.7	1.9 / -1.9	14.7 / -14.7	2.1 / -2.1	1.1 / -1.1	0.1 / -0.1	8.9 / -8.9	0.1 / -0.1
JET_21NP_JET_Flavor_Response	-0.6 / 0.6	0.9 / -0.9	-0.5 / 0.5	7.3 / -6.0	-0.6 / 0.6	-0.4 / 0.4	0.4 / -0.4	-1.3 / 1.3	0.0 / -0.0
JET_21NP_JET_Pileup_OffsetNPV	0.4 / -0.4	-2.4 / 2.4	0.6 / -0.6	6.5 / -6.5	0.0 / -0.0	0.4 / -0.4	-0.2 / 0.2	1.2 / -1.2	0.4 / -0.4
JET_21NP_JET_Pileup_PtTerm	0.1 / -0.1	-0.4 / 0.4	-0.4 / 0.4	-8.5 / 8.5	-0.4 / 0.4	0.5 / -0.5	-0.5 / 0.5	0.2 / -0.2	-0.2 / 0.2
JET_21NP_JET_Pileup_RhoTopology	0.8 / -0.8	2.0 / -2.0	3.6 / -3.6	11.8 / -11.8	1.6 / -1.6	0.7 / -0.7	1.0 / -1.0	3.7 / -3.7	1.0 / -1.0
JET_JER_SINGLE_NP	-1.0 / 1.0	-0.6 / 0.6	8.0 / -8.0	-12.1 / 12.1	-0.4 / 0.4	-3.3 / 3.3	8.1 / -8.1	11.2 / -11.2	-2.2 / 2.2
MET_SoftTrk_ResoPara	0.2 / -0.2	0.1 / -0.1	4.0 / -4.0	22.8 / -22.8	0.3 / -0.3	-0.3 / 0.3	-0.2 / 0.2	-3.7 / 3.7	0.3 / -0.3
MET_SoftTrk_ResoPerp	0.2 / -0.2	-0.9 / 0.9	1.7 / -1.7	14.3 / -14.3	0.2 / -0.2	1.4 / -1.4	1.1 / -1.1	-5.3 / 5.3	0.3 / -0.3
MET_SoftTrk_Scale	0.3 / -0.3	0.5 / -0.5	-0.3 / 0.3	-6.6 / 6.6	0.1 / -0.1	1.0 / -1.0	0.4 / -0.4	-1.8 / 1.8	0.5 / -0.5
MUON_ID	0.0 / -0.0	-1.0 / 1.0	-1.0 / 1.0	-4.6 / 4.6	-0.0 / 0.0	0.6 / -0.6	0.3 / -0.3	0.3 / -0.3	-0.1 / 0.1
MUON_MS	0.1 / -0.1	1.7 / -1.7	0.5 / -0.5	3.9 / -3.9	-0.2 / 0.2	-0.5 / 0.5	0.4 / -0.4	0.6 / -0.6	0.1 / -0.1
MUON_SCALE	0.2 / -0.2	-0.5 / 0.5	0.1 / -0.1	-3.2 / 3.2	-0.4 / 0.4	-0.2 / 0.2	0.0 / -0.0	-0.5 / 0.5	-0.1 / 0.1
Luminosity	2.1 / -2.1	2.1 / -2.1	2.1 / -2.1	2.1 / -2.1	2.1 / -2.1	2.1 / -2.1	2.1 / -2.1	0.0 / 0.0	2.1 / -2.1
$t\bar{t}Z$ normalization	12.0 / -12.0	0.0 / 0.0	0.0 / 0.0	0.0 / 0.0	0.0 / 0.0	0.0 / 0.0	0.0 / 0.0	0.0 / 0.0	0.0 / 0.0
$t\bar{t}Z$ modelling	4.3 / -4.3	0.0 / 0.0	0.0 / 0.0	0.0 / 0.0	0.0 / 0.0	0.0 / 0.0	0.0 / 0.0	0.0 / 0.0	0.0 / 0.0
$t\bar{t}W$ normalization	0.0 / 0.0	13.0 / -13.0	0.0 / 0.0	0.0 / 0.0	0.0 / 0.0	0.0 / 0.0	0.0 / 0.0	0.0 / 0.0	0.0 / 0.0
WZ b-tag norm.	0.0 / 0.0	0.0 / 0.0	12.5 / -12.5	0.0 / 0.0	0.0 / 0.0	0.0 / 0.0	0.0 / 0.0	0.0 / 0.0	0.0 / 0.0
WZ modelling	0.0 / 0.0	0.0 / 0.0	-48.7 / 48.7	0.0 / 0.0	0.0 / 0.0	0.0 / 0.0	0.0 / 0.0	0.0 / 0.0	0.0 / 0.0
WZ_2_Jet	0.0 / 0.0	0.0 / 0.0	17.1 / -17.1	0.0 / 0.0	0.0 / 0.0	0.0 / 0.0	0.0 / 0.0	0.0 / 0.0	0.0 / 0.0
WZ_3_Jet	0.0 / 0.0	0.0 / 0.0	13.2 / -13.2	0.0 / 0.0	0.0 / 0.0	0.0 / 0.0	0.0 / 0.0	0.0 / 0.0	0.0 / 0.0
WZ_4_Jet	0.0 / 0.0	0.0 / 0.0	6.9 / -6.9	0.0 / 0.0	0.0 / 0.0	0.0 / 0.0	0.0 / 0.0	0.0 / 0.0	0.0 / 0.0
WZ_5_Jet	0.0 / 0.0	0.0 / 0.0	4.1 / -4.1	0.0 / 0.0	0.0 / 0.0	0.0 / 0.0	0.0 / 0.0	0.0 / 0.0	0.0 / 0.0
ZZ normalization	0.0 / 0.0	0.0 / 0.0	0.0 / 0.0	12.5 / -12.5	0.0 / 0.0	0.0 / 0.0	0.0 / 0.0	0.0 / 0.0	0.0 / 0.0
tZ normalization	0.0 / 0.0	0.0 / 0.0	0.0 / 0.0	0.0 / 0.0	30.0 / -30.0	0.0 / 0.0	0.0 / 0.0	0.0 / 0.0	0.0 / 0.0
WtZ normalization	0.0 / 0.0	0.0 / 0.0	0.0 / 0.0	0.0 / 0.0	0.0 / 0.0	10.0 / -28.0	0.0 / 0.0	0.0 / 0.0	0.0 / 0.0
WtZ PS	0.0 / 0.0	0.0 / 0.0	0.0 / 0.0	0.0 / 0.0	0.0 / 0.0	5.7 / -5.7	0.0 / 0.0	0.0 / 0.0	0.0 / 0.0
Other bkg. normalization	0.0 / 0.0	0.0 / 0.0	0.0 / 0.0	0.0 / 0.0	0.0 / 0.0	0.0 / 0.0	50.0 / -50.0	0.0 / 0.0	0.0 / 0.0
EL_Fake_SF_ttbar_2j_b-tag	0.0 / 0.0	0.0 / 0.0	0.0 / 0.0	0.0 / 0.0	0.0 / 0.0	0.0 / 0.0	0.0 / 0.0	4.6 / -4.6	0.0 / 0.0
EL_Fake_SF_Zjets_2j_b-tag	0.0 / 0.0	0.0 / 0.0	0.0 / 0.0	0.0 / 0.0	0.0 / 0.0	0.0 / 0.0	0.0 / 0.0	2.2 / -2.2	0.0 / 0.0
MU_Fake_SF_ttbar_2j_b-tag	0.0 / 0.0	0.0 / 0.0	0.0 / 0.0	0.0 / 0.0	0.0 / 0.0	0.0 / 0.0	0.0 / 0.0	12.9 / -12.9	0.0 / 0.0
MU_Fake_SF_Zjets_2j_b-tag	0.0 / 0.0	0.0 / 0.0	0.0 / 0.0	0.0 / 0.0	0.0 / 0.0	0.0 / 0.0	0.0 / 0.0	6.2 / -6.2	0.0 / 0.0
EL_Fake_SF_ttbar_3j_b-tag	0.0 / 0.0	0.0 / 0.0	0.0 / 0.0	0.0 / 0.0	0.0 / 0.0	0.0 / 0.0	0.0 / 0.0	3.5 / -3.5	0.0 / 0.0
MU_Fake_SF_ttbar_3j_b-tag	0.0 / 0.0	0.0 / 0.0	0.0 / 0.0	0.0 / 0.0	0.0 / 0.0	0.0 / 0.0	0.0 / 0.0	5.0 / -5.0	0.0 / 0.0
MU_Fake_SF_Zjets_3j_b-tag	0.0 / 0.0	0.0 / 0.0	0.0 / 0.0	0.0 / 0.0	0.0 / 0.0	0.0 / 0.0	0.0 / 0.0	2.4 / -2.4	0.0 / 0.0
MU_Fake_SF_ttbar_4j_b-tag	0.0 / 0.0	0.0 / 0.0	0.0 / 0.0	0.0 / 0.0	0.0 / 0.0	0.0 / 0.0	0.0 / 0.0	2.0 / -2.0	0.0 / 0.0
EL_Fake_SF_Zjets_MET20_b-tag	0.0 / 0.0	0.0 / 0.0	0.0 / 0.0	0.0 / 0.0	0.0 / 0.0	0.0 / 0.0	0.0 / 0.0	2.2 / -2.2	0.0 / 0.0
MU_Fake_SF_ttbar_MET20_b-tag	0.0 / 0.0	0.0 / 0.0	0.0 / 0.0	0.0 / 0.0	0.0 / 0.0	0.0 / 0.0	0.0 / 0.0	3.7 / -3.7	0.0 / 0.0
MU_Fake_SF_Zjets_MET20_b-tag	0.0 / 0.0	0.0 / 0.0	0.0 / 0.0	0.0 / 0.0	0.0 / 0.0	0.0 / 0.0	0.0 / 0.0	4.6 / -4.6	0.0 / 0.0
EL_Fake_SF_ttbar_MET40_b-tag	0.0 / 0.0	0.0 / 0.0	0.0 / 0.0	0.0 / 0.0	0.0 / 0.0	0.0 / 0.0	0.0 / 0.0	3.2 / -3.2	0.0 / 0.0
MU_Fake_SF_ttbar_MET40_b-tag	0.0 / 0.0	0.0 / 0.0	0.0 / 0.0	0.0 / 0.0	0.0 / 0.0	0.0 / 0.0	0.0 / 0.0	3.4 / -3.4	0.0 / 0.0
MU_Fake_SF_Zjets_MET40_b-tag	0.0 / 0.0	0.0 / 0.0	0.0 / 0.0	0.0 / 0.0	0.0 / 0.0	0.0 / 0.0	0.0 / 0.0	4.1 / -4.1	0.0 / 0.0
EL_Fake_SF_ttbar_MET60_b-tag	0.0 / 0.0	0.0 / 0.0	0.0 / 0.0	0.0 / 0.0	0.0 / 0.0	0.0 / 0.0	0.0 / 0.0	2.2 / -2.2	0.0 / 0.0
MU_Fake_SF_ttbar_MET60_b-tag	0.0 / 0.0	0.0 / 0.0	0.0 / 0.0	0.0 / 0.0	0.0 / 0.0	0.0 / 0.0	0.0 / 0.0	4.4 / -4.4	0.0 / 0.0
EL_Fake_SF_ttbar_MET80_b-tag	0.0 / 0.0	0.0 / 0.0	0.0 / 0.0	0.0 / 0.0	0.0 / 0.0	0.0 / 0.0	0.0 / 0.0	2.4 / -2.4	0.0 / 0.0
MU_Fake_SF_ttbar_MET80_b-tag	0.0 / 0.0	0.0 / 0.0	0.0 / 0.0	0.0 / 0.0	0.0 / 0.0	0.0 / 0.0	0.0 / 0.0	4.1 / -4.1	0.0 / 0.0
MU_Fake_SF_ttbar_MET100_b-tag	0.0 / 0.0	0.0 / 0.0	0.0 / 0.0	0.0 / 0.0	0.0 / 0.0	0.0 / 0.0	0.0 / 0.0	4.9 / -4.9	0.0 / 0.0
$t\bar{t}$ NLO generator	0.0 / 0.0	0.0 / 0.0	0.0 / 0.0	0.0 / 0.0	0.0 / 0.0	0.0 / 0.0	0.0 / 0.0	-24.8 / 24.8	0.0 / 0.0
$t\bar{t}$ QCD radiation	0.0 / 0.0	0.0 / 0.0	0.0 / 0.0	0.0 / 0.0	0.0 / 0.0	0.0 / 0.0	0.0 / 0.0	9.9 / -9.9	0.0 / 0.0
Signal normalization ($\sigma_{t\bar{t}}$(scale))	0.0 / 0.0	0.0 / 0.0	0.0 / 0.0	0.0 / 0.0	0.0 / 0.0	0.0 / 0.0	0.0 / 0.0	0.0 / 0.0	2.4 / -3.5
Signal normalization ($\sigma_{t\bar{t}}$(PDF+α_S))	0.0 / 0.0	0.0 / 0.0	0.0 / 0.0	0.0 / 0.0	0.0 / 0.0	0.0 / 0.0	0.0 / 0.0	0.0 / 0.0	4.2 / -4.2

Table 6.20.: Summary of the relative impact of each source of uncertainty on the event yields in the signal region for each individual sample (shown in percentage) before the fit. Only the systematic sources are shown which have the effect above 2% on at least one sample.

Source	$t\bar{t}Z$	$t\bar{t}W$	WZ	ZZ	tZ	WtZ	Other MC	Fakes	$t\bar{t}$ →bWuZ
pileup	-1.1 / 1.1	-3.7 / 3.7	-3.7 / 3.7	-9.6 / 9.6	0.9 / -0.9	-3.8 / 3.8	0.1 / -0.1	-6.3 / 6.3	-2.1 / 2.1
EL_SF_ID	1.2 / -1.2	1.2 / -1.2	1.2 / -1.2	2.0 / -2.0	1.2 / -1.2	1.1 / -1.1	1.2 / -1.2	2.1 / -2.1	1.1 / -1.1
bTagSF_77_extrapolation_from_charm	-0.1 / 0.1	0.0 / 0.0	0.0 / 0.0	-0.5 / 0.5	0.0 / 0.0	-0.1 / 0.1	3.0 / -3.0	0.0 / 0.0	0.0 / -0.0
bTagSF_77_eigenvars_B_0	2.3 / -2.3	4.2 / -4.2	-0.6 / 0.6	-3.1 / 3.1	-0.7 / 0.7	-1.0 / 1.0	1.1 / -1.1	-2.9 / 2.9	-2.9 / 2.9
bTagSF_77_eigenvars_C_0	0.4 / -0.4	0.1 / -0.1	-1.9 / 1.9	-0.6 / 0.6	0.1 / -0.1	0.3 / -0.3	-2.9 / 2.9	-0.4 / 0.4	0.0 / -0.0
bTagSF_77_eigenvars_Light_0	0.5 / -0.5	0.3 / -0.3	-6.0 / 6.0	-3.6 / 3.6	0.4 / -0.4	0.3 / -0.3	0.3 / -0.3	0.4 / -0.4	0.5 / -0.5
bTagSF_77_eigenvars_Light_1	-0.2 / 0.2	-0.1 / 0.1	2.2 / -2.2	1.8 / -1.8	-0.1 / 0.1	-0.1 / 0.1	-0.1 / 0.1	-0.2 / 0.2	-0.2 / 0.2
bTagSF_77_eigenvars_Light_2	-0.1 / 0.1	-0.1 / 0.1	1.5 / -1.5	3.4 / -3.4	-0.0 / 0.0	-0.0 / 0.0	0.1 / -0.1	-0.2 / 0.2	-0.1 / 0.1
bTagSF_77_eigenvars_Light_4	0.1 / -0.1	0.1 / -0.1	-3.1 / 3.1	-3.0 / 3.0	0.1 / -0.1	-0.1 / 0.1	0.1 / -0.1	0.1 / -0.1	0.1 / -0.1
EG_RESOLUTION_ALL	0.0 / -0.0	-0.2 / 0.2	-0.4 / 0.4	3.6 / -3.6	-0.2 / 0.2	-0.4 / 0.4	-0.8 / 0.8	-0.7 / 0.7	0.1 / -0.1
JET_21NP_JET_BJES_Response	-0.3 / 0.3	-1.3 / 1.3	0.2 / -0.2	3.4 / -3.4	-0.0 / 0.0	0.2 / -0.2	0.3 / -0.3	-0.2 / 0.2	0.1 / -0.1
JET_21NP_JET_EffectiveNP_1	0.6 / -0.6	0.5 / -0.5	2.3 / -2.3	1.4 / -1.4	1.2 / -1.2	0.7 / -0.7	0.7 / -0.7	1.2 / -1.2	0.4 / -0.4
JET_21NP_JET_EffectiveNP_2	-0.3 / 0.3	0.2 / -0.2	-1.4 / 1.4	-2.2 / 3.6	-0.6 / 0.6	-0.4 / 0.4	0.1 / -0.1	-2.3 / 2.3	-0.2 / 0.2
JET_21NP_JET_EffectiveNP_4	-0.1 / 0.1	-0.6 / 0.6	-0.6 / 0.6	7.2 / -4.1	-0.3 / 0.3	-0.6 / 0.6	0.1 / -0.1	0.7 / -0.7	-0.2 / 0.2
JET_21NP_JET_EffectiveNP_5	-0.0 / 0.0	0.9 / -0.9	1.0 / -1.0	-4.1 / 4.1	0.3 / -0.3	0.0 / -0.0	-0.5 / 0.5	0.2 / -0.2	0.1 / -0.1
JET_21NP_JET_EffectiveNP_6	0.2 / -0.2	-1.0 / 1.0	-0.6 / 0.6	0.1 / -0.1	0.4 / -0.4	-0.6 / 0.6	-0.6 / 0.6	-2.8 / 2.8	-0.1 / 0.1
JET_21NP_JET_EffectiveNP_8restTerm	0.0 / -0.0	-0.2 / 0.2	-0.1 / 0.1	1.4 / 5.0	-0.1 / 0.1	-0.5 / 0.5	0.2 / -0.2	-0.4 / 0.4	0.1 / -0.1
JET_21NP_JET_EtaIntercalibration_Modelling	0.4 / -0.4	1.3 / -1.3	1.6 / -1.6	3.2 / -3.2	0.5 / -0.5	0.7 / -0.7	-0.2 / 0.2	-3.7 / 3.7	0.0 / -0.0
JET_21NP_JET_EtaIntercalibration_NonClosure	-0.1 / 0.1	0.5 / -0.5	1.4 / -1.4	2.6 / -2.6	0.3 / -0.3	-0.3 / 0.3	-0.4 / 0.4	-1.2 / 1.2	-0.0 / 0.0
JET_21NP_JET_EtaIntercalibration_TotalStat	0.3 / -0.3	-1.8 / 1.8	1.2 / -1.2	-6.0 / 6.0	0.1 / -0.1	0.4 / -0.4	0.0 / -0.0	1.1 / -1.1	0.6 / -0.6
JET_21NP_JET_Flavor_Composition	1.1 / -1.1	0.6 / -0.6	1.8 / -1.8	13.3 / -13.3	1.9 / -1.9	1.0 / -1.0	0.1 / -0.1	8.1 / -8.1	0.1 / -0.1
JET_21NP_JET_Flavor_Response	-0.6 / 0.6	0.9 / -0.9	-0.5 / 0.5	7.2 / -5.9	-0.6 / 0.6	-0.4 / 0.4	0.4 / -0.4	-1.2 / 1.2	0.0 / -0.0
JET_21NP_JET_Pileup_OffsetNPV	0.4 / -0.4	-2.3 / 2.3	0.6 / -0.6	6.5 / -6.5	0.0 / -0.0	0.4 / -0.4	-0.2 / 0.2	1.2 / -1.2	0.4 / -0.4
JET_21NP_JET_Pileup_PtTerm	0.1 / -0.1	-0.4 / 0.4	-0.4 / 0.4	-8.5 / 8.5	-0.4 / 0.4	0.5 / -0.5	-0.5 / 0.5	0.2 / -0.2	-0.2 / 0.2
JET_21NP_JET_Pileup_RhoTopology	0.8 / -0.8	1.9 / -1.9	3.4 / -3.4	11.2 / -11.2	1.5 / -1.5	0.7 / -0.7	0.9 / -0.9	3.5 / -3.5	0.9 / -0.9
JET_JER_SINGLE_NP	-0.8 / 0.8	-0.5 / 0.5	6.0 / -6.0	-9.0 / 9.0	-0.3 / 0.3	-2.5 / 2.5	6.1 / -6.1	8.3 / -8.3	-1.7 / 1.7
MET_SoftTrk_ResoPara	0.2 / -0.2	0.1 / -0.1	3.7 / -3.7	21.2 / -21.2	0.3 / -0.3	-0.3 / 0.3	-0.2 / 0.2	-3.4 / 3.4	0.2 / -0.2
MET_SoftTrk_ResoPerp	0.2 / -0.2	-0.9 / 0.9	1.7 / -1.7	13.9 / -13.9	0.2 / -0.2	1.4 / -1.4	1.0 / -1.0	-5.2 / 5.2	0.3 / -0.3
MET_SoftTrk_Scale	0.3 / -0.3	0.4 / -0.4	-0.3 / 0.3	-6.3 / 6.3	0.1 / -0.1	0.9 / -0.9	0.3 / -0.3	-1.7 / 1.7	0.4 / -0.4
MUON_ID	0.0 / -0.0	-0.9 / 0.9	-1.0 / 1.0	-4.6 / 4.6	0.0 / -0.0	0.6 / -0.6	0.3 / -0.3	0.3 / -0.3	-0.1 / 0.1
MUON_MS	0.1 / -0.1	1.7 / -1.7	0.5 / -0.5	3.9 / -3.9	-0.2 / 0.2	-0.5 / 0.5	0.4 / -0.4	0.6 / -0.6	0.1 / -0.1
MUON_SCALE	0.2 / -0.2	-0.5 / 0.5	0.1 / -0.1	-3.2 / 3.2	-0.4 / 0.4	-0.2 / 0.2	0.0 / -0.0	-0.5 / 0.5	-0.1 / 0.1
Luminosity	2.1 / -2.1	2.1 / -2.1	2.1 / -2.1	2.1 / -2.1	2.1 / -2.1	2.1 / -2.1	2.1 / -2.1	0.0 / 0.0	2.1 / -2.1
$t\bar{t}Z$ normalization	10.1 / -10.1	0.0 / 0.0	0.0 / 0.0	0.0 / 0.0	0.0 / 0.0	0.0 / 0.0	0.0 / 0.0	0.0 / 0.0	0.0 / 0.0
$t\bar{t}Z$ modelling	4.2 / -4.2	0.0 / 0.0	0.0 / 0.0	0.0 / 0.0	0.0 / 0.0	0.0 / 0.0	0.0 / 0.0	0.0 / 0.0	0.0 / 0.0
$t\bar{t}W$ normalization	0.0 / 0.0	12.9 / -12.9	0.0 / 0.0	0.0 / 0.0	0.0 / 0.0	0.0 / 0.0	0.0 / 0.0	0.0 / 0.0	0.0 / 0.0
WZ b-tag norm.	0.0 / 0.0	0.0 / 0.0	12.0 / -12.0	0.0 / 0.0	0.0 / 0.0	0.0 / 0.0	0.0 / 0.0	0.0 / 0.0	0.0 / 0.0
WZ modelling	0.0 / 0.0	0.0 / 0.0	-31.1 / 31.1	0.0 / 0.0	0.0 / 0.0	0.0 / 0.0	0.0 / 0.0	0.0 / 0.0	0.0 / 0.0
WZ_2_Jet	0.0 / 0.0	0.0 / 0.0	14.0 / -14.0	0.0 / 0.0	0.0 / 0.0	0.0 / 0.0	0.0 / 0.0	0.0 / 0.0	0.0 / 0.0
WZ_3_Jet	0.0 / 0.0	0.0 / 0.0	12.2 / -12.2	0.0 / 0.0	0.0 / 0.0	0.0 / 0.0	0.0 / 0.0	0.0 / 0.0	0.0 / 0.0
WZ_4_Jet	0.0 / 0.0	0.0 / 0.0	6.3 / -6.3	0.0 / 0.0	0.0 / 0.0	0.0 / 0.0	0.0 / 0.0	0.0 / 0.0	0.0 / 0.0
WZ_5_Jet	0.0 / 0.0	0.0 / 0.0	3.8 / -3.8	0.0 / 0.0	0.0 / 0.0	0.0 / 0.0	0.0 / 0.0	0.0 / 0.0	0.0 / 0.0
ZZ normalization	0.0 / 0.0	0.0 / 0.0	0.0 / 0.0	10.5 / -10.5	0.0 / 0.0	0.0 / 0.0	0.0 / 0.0	0.0 / 0.0	0.0 / 0.0
tZ normalization	0.0 / 0.0	0.0 / 0.0	0.0 / 0.0	0.0 / 0.0	29.0 / -29.0	0.0 / 0.0	0.0 / 0.0	0.0 / 0.0	0.0 / 0.0
WtZ normalization	0.0 / 0.0	0.0 / 0.0	0.0 / 0.0	0.0 / 0.0	0.0 / 0.0	10.5 / -29.4	0.0 / 0.0	0.0 / 0.0	0.0 / 0.0
WtZ PS	0.0 / 0.0	0.0 / 0.0	0.0 / 0.0	0.0 / 0.0	0.0 / 0.0	5.7 / -5.7	0.0 / 0.0	0.0 / 0.0	0.0 / 0.0
Other bkg. normalization	0.0 / 0.0	0.0 / 0.0	0.0 / 0.0	0.0 / 0.0	0.0 / 0.0	0.0 / 0.0	47.5 / -47.5	0.0 / 0.0	0.0 / 0.0
EL_Fake_SF_ttbar_2j_b-tag	0.0 / 0.0	0.0 / 0.0	0.0 / 0.0	0.0 / 0.0	0.0 / 0.0	0.0 / 0.0	0.0 / 0.0	4.4 / -4.4	0.0 / 0.0
EL_Fake_SF_Zjets_2j_b-tag	0.0 / 0.0	0.0 / 0.0	0.0 / 0.0	0.0 / 0.0	0.0 / 0.0	0.0 / 0.0	0.0 / 0.0	2.2 / -2.2	0.0 / 0.0
MU_Fake_SF_ttbar_2j_b-tag	0.0 / 0.0	0.0 / 0.0	0.0 / 0.0	0.0 / 0.0	0.0 / 0.0	0.0 / 0.0	0.0 / 0.0	11.9 / -11.9	0.0 / 0.0
MU_Fake_SF_Zjets_2j_b-tag	0.0 / 0.0	0.0 / 0.0	0.0 / 0.0	0.0 / 0.0	0.0 / 0.0	0.0 / 0.0	0.0 / 0.0	6.0 / -6.0	0.0 / 0.0
EL_Fake_SF_ttbar_3j_b-tag	0.0 / 0.0	0.0 / 0.0	0.0 / 0.0	0.0 / 0.0	0.0 / 0.0	0.0 / 0.0	0.0 / 0.0	3.4 / -3.4	0.0 / 0.0
MU_Fake_SF_ttbar_3j_b-tag	0.0 / 0.0	0.0 / 0.0	0.0 / 0.0	0.0 / 0.0	0.0 / 0.0	0.0 / 0.0	0.0 / 0.0	4.8 / -4.8	0.0 / 0.0
MU_Fake_SF_Zjets_3j_b-tag	0.0 / 0.0	0.0 / 0.0	0.0 / 0.0	0.0 / 0.0	0.0 / 0.0	0.0 / 0.0	0.0 / 0.0	2.3 / -2.3	0.0 / 0.0
EL_Fake_SF_Zjets_MET20_b-tag	0.0 / 0.0	0.0 / 0.0	0.0 / 0.0	0.0 / 0.0	0.0 / 0.0	0.0 / 0.0	0.0 / 0.0	2.2 / -2.2	0.0 / 0.0
MU_Fake_SF_ttbar_MET20_b-tag	0.0 / 0.0	0.0 / 0.0	0.0 / 0.0	0.0 / 0.0	0.0 / 0.0	0.0 / 0.0	0.0 / 0.0	3.7 / -3.7	0.0 / 0.0
MU_Fake_SF_Zjets_MET20_b-tag	0.0 / 0.0	0.0 / 0.0	0.0 / 0.0	0.0 / 0.0	0.0 / 0.0	0.0 / 0.0	0.0 / 0.0	4.3 / -4.3	0.0 / 0.0
EL_Fake_SF_ttbar_MET40_b-tag	0.0 / 0.0	0.0 / 0.0	0.0 / 0.0	0.0 / 0.0	0.0 / 0.0	0.0 / 0.0	0.0 / 0.0	3.2 / -3.2	0.0 / 0.0
MU_Fake_SF_ttbar_MET40_b-tag	0.0 / 0.0	0.0 / 0.0	0.0 / 0.0	0.0 / 0.0	0.0 / 0.0	0.0 / 0.0	0.0 / 0.0	3.3 / -3.3	0.0 / 0.0
MU_Fake_SF_Zjets_MET40_b-tag	0.0 / 0.0	0.0 / 0.0	0.0 / 0.0	0.0 / 0.0	0.0 / 0.0	0.0 / 0.0	0.0 / 0.0	4.0 / -4.0	0.0 / 0.0
EL_Fake_SF_ttbar_MET60_b-tag	0.0 / 0.0	0.0 / 0.0	0.0 / 0.0	0.0 / 0.0	0.0 / 0.0	0.0 / 0.0	0.0 / 0.0	2.2 / -2.2	0.0 / 0.0
MU_Fake_SF_ttbar_MET60_b-tag	0.0 / 0.0	0.0 / 0.0	0.0 / 0.0	0.0 / 0.0	0.0 / 0.0	0.0 / 0.0	0.0 / 0.0	4.3 / -4.3	0.0 / 0.0
EL_Fake_SF_ttbar_MET80_b-tag	0.0 / 0.0	0.0 / 0.0	0.0 / 0.0	0.0 / 0.0	0.0 / 0.0	0.0 / 0.0	0.0 / 0.0	2.3 / -2.3	0.0 / 0.0
MU_Fake_SF_ttbar_MET80_b-tag	0.0 / 0.0	0.0 / 0.0	0.0 / 0.0	0.0 / 0.0	0.0 / 0.0	0.0 / 0.0	0.0 / 0.0	4.1 / -4.1	0.0 / 0.0
MU_Fake_SF_ttbar_MET100_b-tag	0.0 / 0.0	0.0 / 0.0	0.0 / 0.0	0.0 / 0.0	0.0 / 0.0	0.0 / 0.0	0.0 / 0.0	4.8 / -4.8	0.0 / 0.0
$t\bar{t}$ NLO generator	0.0 / 0.0	0.0 / 0.0	0.0 / 0.0	0.0 / 0.0	0.0 / 0.0	0.0 / 0.0	0.0 / 0.0	-14.2 / 14.2	0.0 / 0.0
$t\bar{t}$ QCD radiation	0.0 / 0.0	0.0 / 0.0	0.0 / 0.0	0.0 / 0.0	0.0 / 0.0	0.0 / 0.0	0.0 / 0.0	9.5 / -9.5	0.0 / 0.0
Signal normalization ($\sigma_{t\bar{t}}$(scale))	0.0 / 0.0	0.0 / 0.0	0.0 / 0.0	0.0 / 0.0	0.0 / 0.0	0.0 / 0.0	0.0 / 0.0	0.0 / 0.0	2.4 / -3.5
Signal normalization ($\sigma_{t\bar{t}}$(PDF+α_S))	0.0 / 0.0	0.0 / 0.0	0.0 / 0.0	0.0 / 0.0	0.0 / 0.0	0.0 / 0.0	0.0 / 0.0	0.0 / 0.0	4.2 / -4.2

Table 6.21.: Summary of the relative impact of each source of uncertainty on the event yields in the signal region for each individual sample (shown in percentage) after the combined fit under the background-only hypothesis, when in the signal region "Asimov data" is used, defined as the total expected pre-fit background. Only the systematic sources are shown which have the effect above 2% on at least one sample.

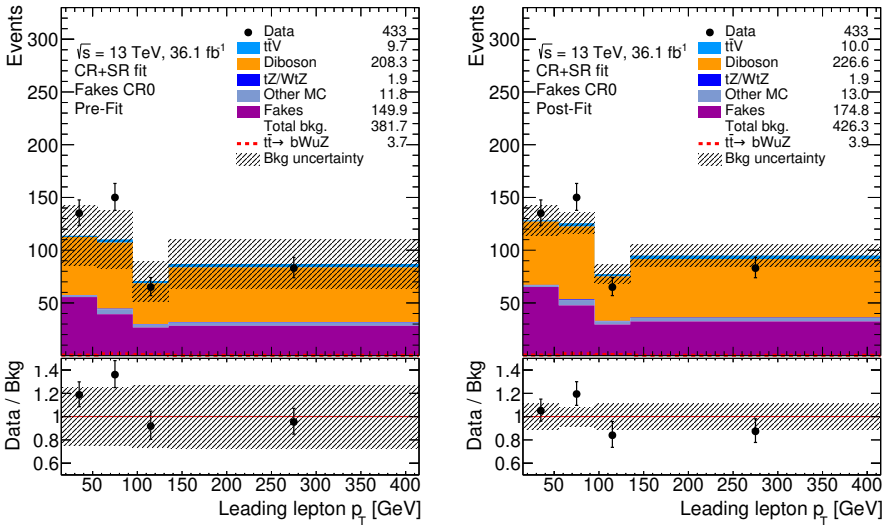

(a) (b)

Figure 6.36.: Comparison between data and prediction for the p_{T} of the leading lepton in the fake leptons background control region in b-veto events a) before and b) after the combined fit under the background-only hypothesis, when in the signal region "Asimov data" is used, defined as the total expected pre-fit background. The number of signal events is normalized to an arbitrary branching ratio of BR$(t \to qZ) = 0.1\%$. The dashed area represents total uncertainty on the background prediction.

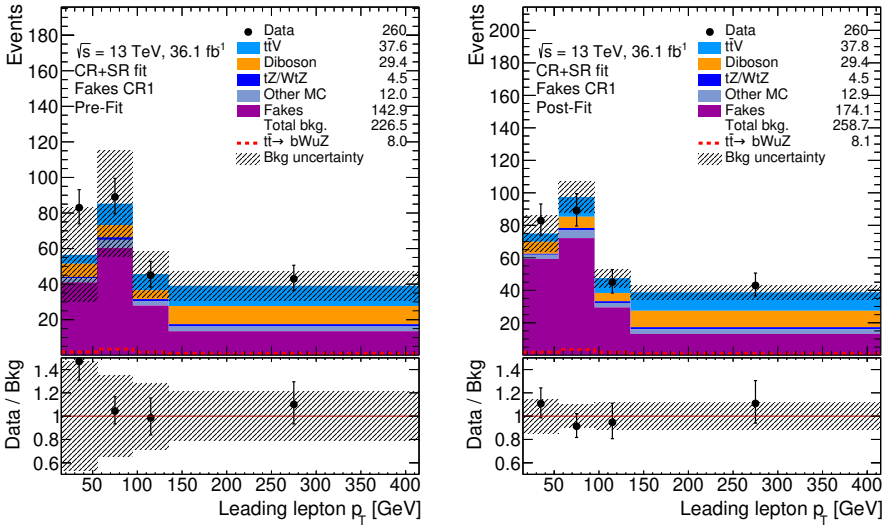

(a) (b)

Figure 6.37.: Comparison between data and prediction for the p_{T} of the leading lepton in the fake leptons background control region in one b-tag events a) before and b) after the combined fit under the background-only hypothesis, when in the signal region "Asimov data" is used, defined as the total expected pre-fit background. The number of signal events is normalized to an arbitrary branching ratio of BR$(t \to qZ) = 0.1\%$. The dashed area represents total uncertainty on the background prediction.

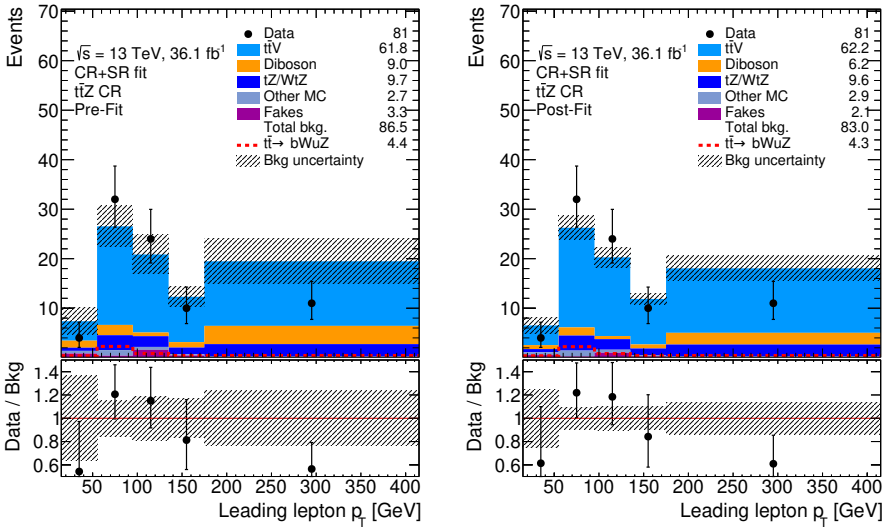

(a) (b)

Figure 6.38.: Comparison between data and prediction for the p_{T} of the leading lepton in the $t\bar{t}Z$ control region a) before and b) after the combined fit under the background-only hypothesis, when in the signal region "Asimov data" is used, defined as the total expected pre-fit background. The number of signal events is normalized to an arbitrary branching ratio of BR$(t \to qZ) = 0.1\%$. The dashed area represents total uncertainty on the background prediction.

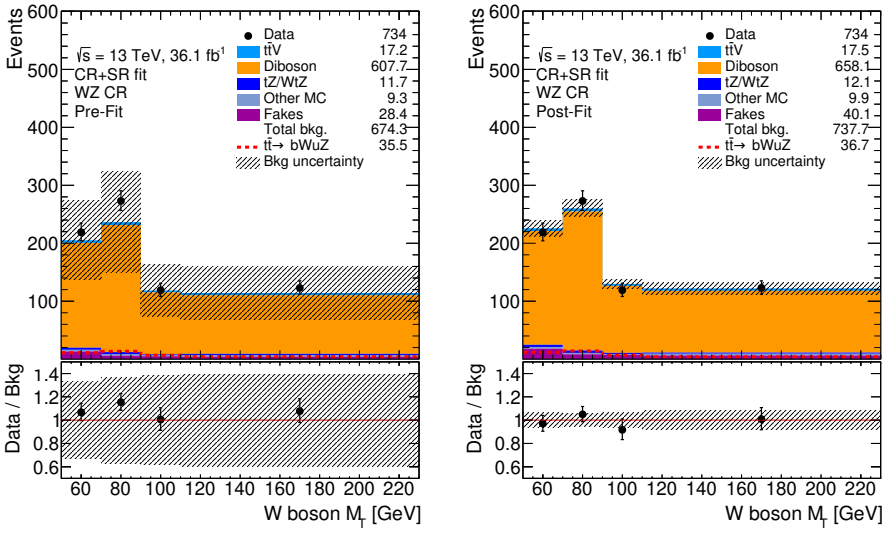

(a) (b)

Figure 6.39.: Comparison between data and prediction for the W boson transverse mass in the WZ control region a) before and b) after the combined fit under the background-only hypothesis, when in the signal region "Asimov data" is used, defined as the total expected pre-fit background. The number of signal events is normalized to an arbitrary branching ratio of BR$(t \to qZ) = 0.1\%$. The dashed area represents total uncertainty on the background prediction.

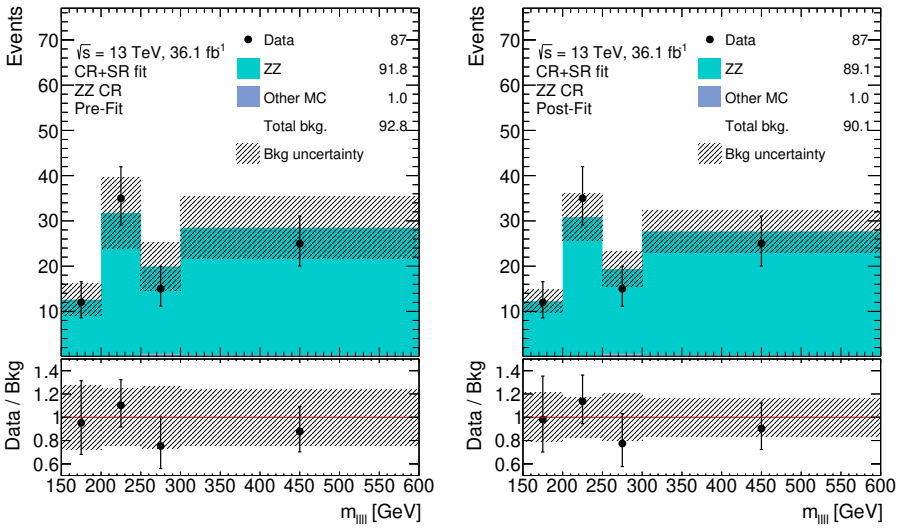

(a) (b)

Figure 6.40.: Comparison between data and prediction for the reconstructed ZZ system invariant mass in the ZZ control region a) before and b) after the combined fit under the background-only hypothesis, when in the signal region "Asimov data" is used, defined as the total expected pre-fit background. The dashed area represents total uncertainty on the background prediction.

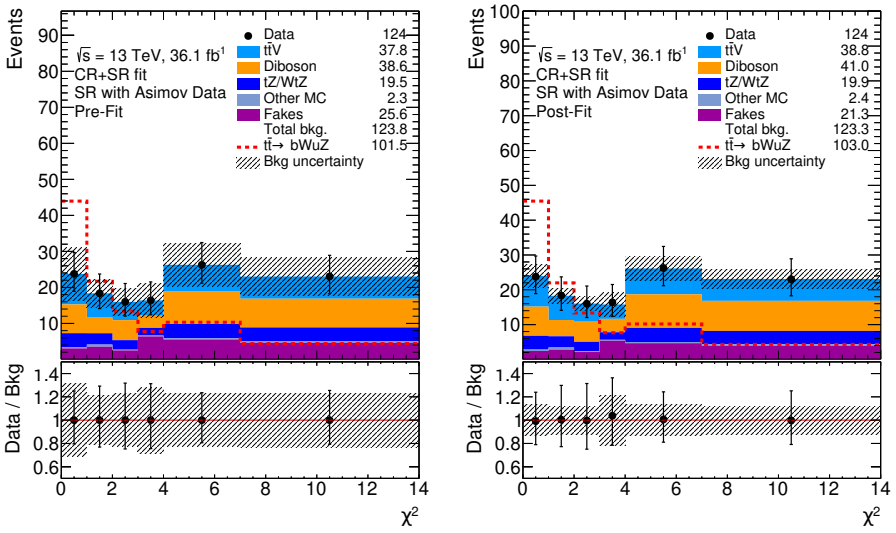

(a) (b)

Figure 6.41.: The distributions for the χ^2 after the event reconstruction in the signal region a) before and b) after the combined fit under the background-only hypothesis. The data points are from the "Asimov dataset", defined as a total expected pre-fit background. The number of signal events is normalized to an arbitrary branching ratio of BR$(t \to qZ) = 0.1\%$. The dashed area represents total uncertainty on the background prediction.

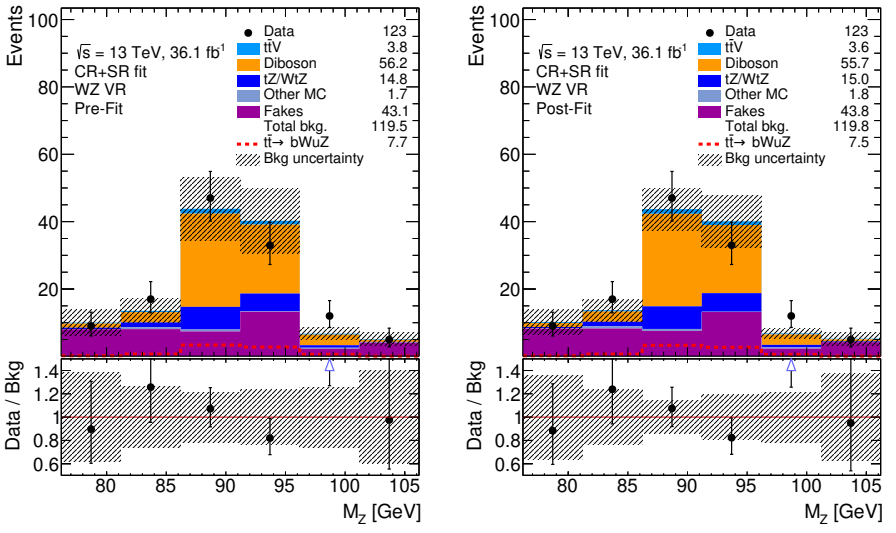

(a) (b)

Figure 6.42.: Comparison between data and prediction for the reconstructed Z boson mass in the WZ validation region a) before and b) after the combined fit under the background-only hypothesis, when in the signal region "Asimov data" is used, defined as the total expected pre-fit background. The number of signal events is normalized to an arbitrary branching ratio of BR$(t \to qZ) = 0.1\%$. The dashed area represents total uncertainty on the background prediction.

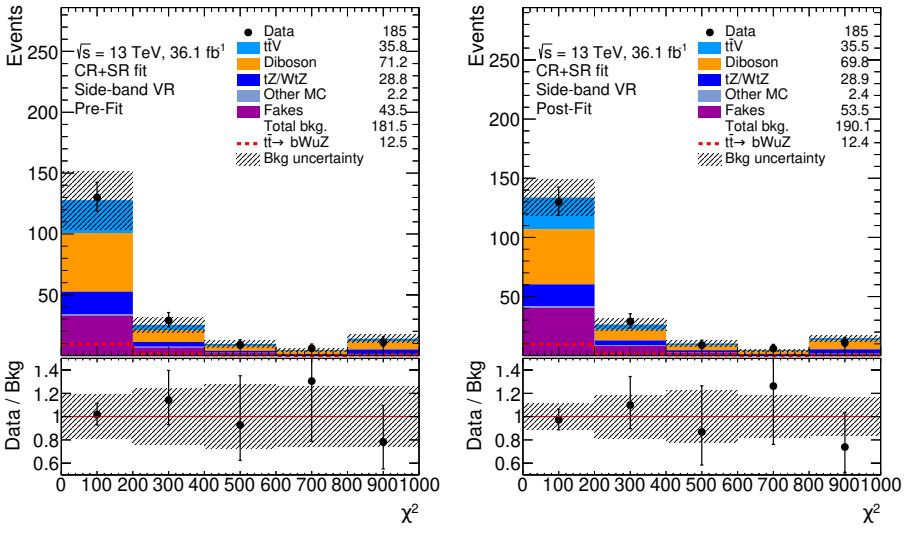

(a) (b)

Figure 6.43.: Comparison between data and prediction for the χ^2 after the event reconstruction in the side-band validation region a) before and b) after the combined fit under the background-only hypothesis, when in the signal region "Asimov data" is used, defined as the total expected pre-fit background. The number of signal events is normalized to an arbitrary branching ratio of BR$(t \to qZ) = 0.1\%$. The dashed area represents total uncertainty on the background prediction.

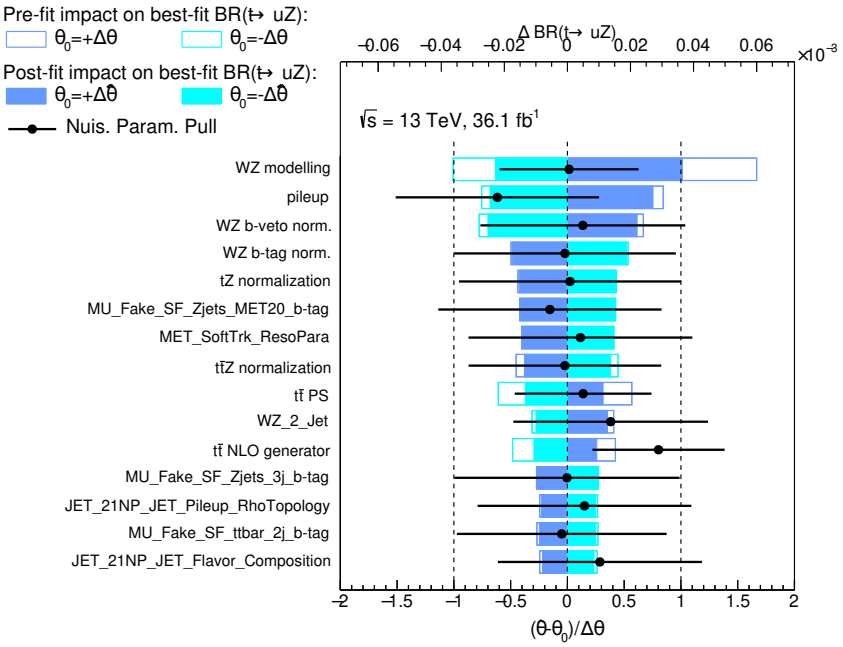

(a)

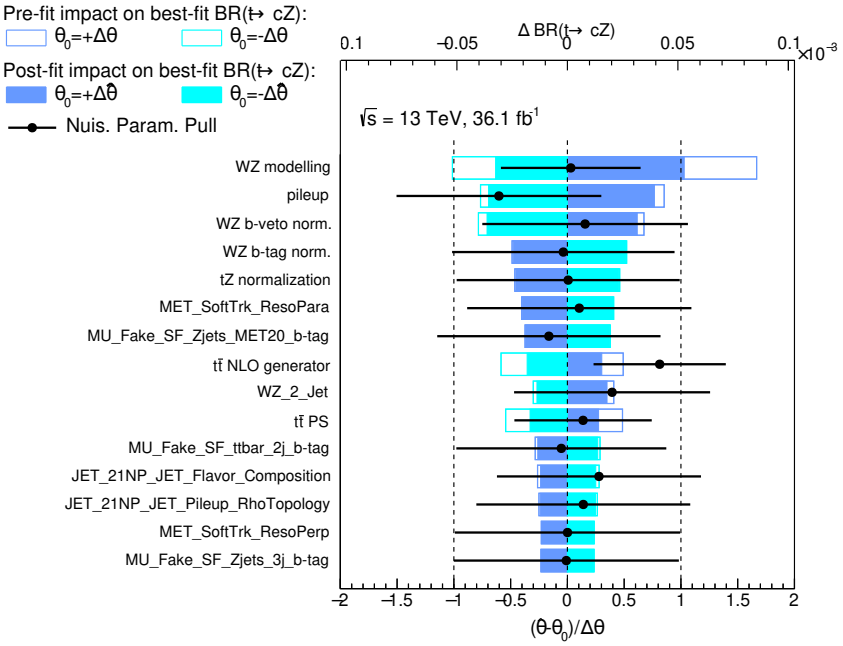

(b)

Figure 6.44.: The fitted values of the 15 most important nuisance parameters and their impact on the measured branching ratio of a) $t \to uZ$ and b) $t \to cZ$ are presented. The black points, which are plotted according to the bottom horizontal scale, show the deviation of each of the fitted nuisance parameters,$\hat{\theta}$, from θ_0, which is the nominal value of that nuisance parameter, in units of the pre-fit standard deviation $\Delta\theta$. This represents the preferred shift of the event yield with respect to the nominal prediction in units of its prior uncertainty. The black error bars show the post-fit errors, σ_θ, which represent the post-fit uncertainty on the event yield in units of the prior uncertainty. The nuisance parameters are sorted according to the post-fit effect of each on the best-fit branching ratio, with those with the largest impact at the top. The post-fit effect on the best-fit branching ratio, shown according to the top horizontal scale, is calculated by fixing the corresponding nuisance parameter at $\hat{\theta} \pm \sigma_\theta$ and redoing the fit.

6.10.2. Expected upper limit on BR($t \to qZ$) from Asimov data

The expected 95% confidence level (CL) upper limits on BR($t \to uZ$) and BR($t \to cZ$) are extracted from Asimov data in the signal region, defined as the total expected pre-fit background. Figure 6.45 shows the expected CL_s as a function of BR($t \to uZ$) and BR($t \to cZ$), while Table 6.22 shows the expected 95% CL upper limits together with the $\pm 1\sigma$ bands. Extracted expected limits are BR($t \to uZ$) < 0.024% and BR($t \to cZ$) < 0.032%. Due to the b-tagging mistag rate of c-jets, the signal efficiency is lower for the $t \to cZ$ channel and, as a result, the extracted limit is more conservative than the one obtained for the $t \to uZ$ channel.

To have an idea how much the extracted limits are influenced by the MC statistical and systematic uncertainties, limits are extracted using only the signal region without considering uncertainties. Results are shown in Table 6.23, concluding that the limit on BR($t \to uZ$) (BR($t \to cZ$)) is weakened by 26% (28%) due to the MC statistical and systematic uncertainties.

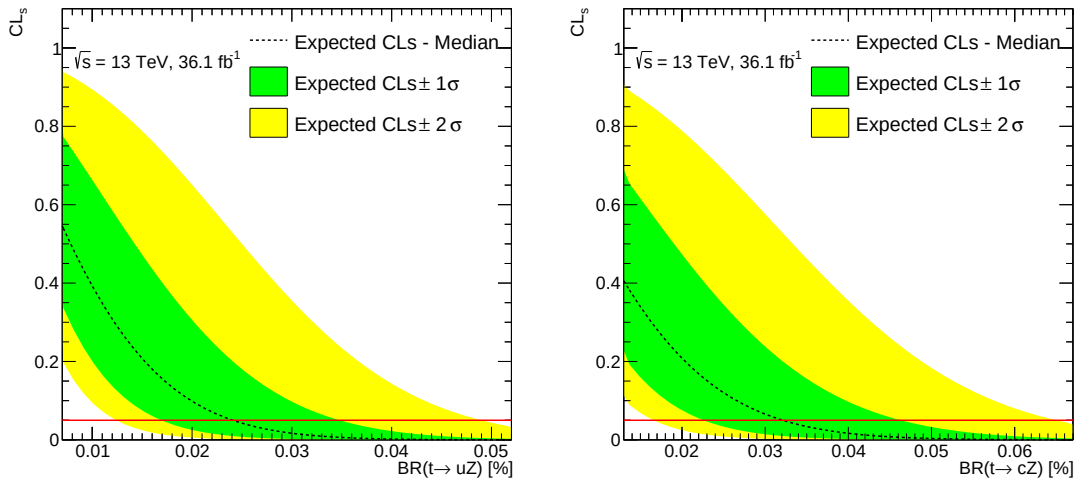

Figure 6.45.: CL_s vs BR($t \to uZ$) (a) and CL_s vs BR($t \to cZ$) (b) taking into account systematic and statistical uncertainties. The median expected CL_s under the background-only hypothesis (black dashed line) is displayed along with the ± 1 and ± 2 standard deviations bands (green and yellow, respectively). The solid red line at CL_s=0.05 denotes the threshold below which the hypothesis is excluded at 95% CL.

6.10.3. Unblinded data

The distributions from the signal region with unblinded data can be found in Figures 6.46-6.50. The expected and observed event yields in the signal region can be found in Table 6.24. A good agreement between data and the total expected pre-fit background is observed.

	-1σ	Expected	+1σ
BR($t \to uZ$) [%]	0.017	0.024	0.035
BR($t \to cZ$) [%]	0.023	0.032	0.046

Table 6.22.: The expected 95% confidence level upper limits on the top-quark FCNC decay branching ratios are shown together with the $\pm 1\sigma$ bands, which include the contribution from the statistical and systematic uncertainties. Presented limits are extracted from "Asimov data" in the signal region, defined as the total expected pre-fit background.

	-1σ	Expected	+1σ
BR($t \to uZ$) [%]	0.013	0.019	0.027
BR($t \to cZ$) [%]	0.017	0.024	0.034

Table 6.23.: The expected 95% confidence level upper limits on the top-quark FCNC decay branching ratios are shown together with the $\pm 1\sigma$ bands, without taking into account statistical and systematic uncertainties. Presented limits are extracted from "Asimov data" in the signal region, defined as the total expected pre-fit background.

The combined fit has been performed in the background control and signal regions with the real data under the background-only and signal-plus-background hypothesis. The fitted nuisance parameters are displayed in Figures 6.51 and 6.52. Fitted values are within their prior uncertainties, meaning that the data are well modeled with the MC within the uncertainties. The corresponding correlation matrices for the fitted nuisance parameters under the background-only and signal-plus-background hypothesis can be found in Figure 6.53 and 6.54, respectively. Figures 6.55-6.60 show the pre-fit and post-fit plots under the background-only hypothesis for the background control and signal regions respectively. Pre-fit and post-fit event yields under the background-only hypothesis in the signal and background control regions are presented in Table 6.24 and Table 6.25 respectively, while in Table 6.26 and Table 6.27 the pre-fit and post-fit yields in the validation regions are presented. Tables 6.28 and 6.29 show the ratio of the pre-fit and post-fit background yields under the background-only hypothesis with the unblinded data, for the background CRs, SR and VRs. Pre-fit and post-fit plots of the reconstructed Z boson in the WZ validation region are presented in Figure 6.61, while the pre-fit and post-fit plots of the χ^2 in the side-band VR are shown in Figure 6.62. Additional pre- and post-fit plots can be found in Appendix E. In the WZ validation region we observe that the agreement between data and background has slightly improved and stays within one sigma uncertainty after the fit under the background-only hypothesis in the background control and signal regions, while in the side-band VR total post-fit background has slightly increased, but stays in a good agreement with data.

Table 6.30 and Table 6.31 present the summary of the relative impact of each type of uncertainty on the total background yield in the background CRs and on the signal and background yields in the SR, before and after the fit under the background-only hypothesis, respectively.

Good agreement between observed data and background expectations is observed in background control and signal regions. No evidence for the $t \to qZ$ decay is found.

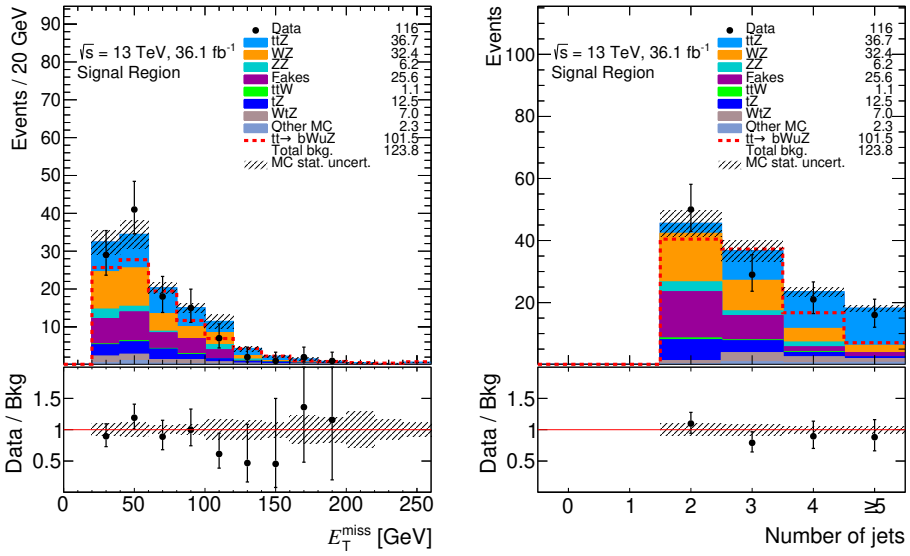

(a) (b)

Figure 6.46.: Expected and observed distributions in the signal region for the a) missing transverse momentum and b) the jet multiplicity. The number of signal events is normalized to an arbitrary branching ratio of BR$(t \to qZ) = 0.1\%$.

Sample	WZ CR	ZZ CR	$t\bar{t}Z$ CR	Fakes CR0	Fakes CR1	SR
$t\bar{t}Z$	16.3 ± 3.13	0 ± 0	60.8 ± 8.71	6.08 ± 1.24	22.1 ± 3.19	36.7 ± 5.02
$t\bar{t}W$	0.813 ± 0.177	0 ± 0	0.966 ± 0.232	3.65 ± 0.726	15.5 ± 2.17	1.12 ± 0.198
WZ	559 ± 238	0 ± 0	8.95 ± 8.75	150 ± 67.8	20.4 ± 9.24	32.4 ± 18.8
ZZ	48.3 ± 10.7	91.8 ± 20.4	0.0704 ± 0.0265	58.0 ± 15.6	9.02 ± 2.28	6.21 ± 3.18
tZ	6.25 ± 2.04	0 ± 0	3.61 ± 1.20	0.632 ± 0.220	1.98 ± 0.627	12.5 ± 3.80
WtZ	5.48 ± 1.28	0 ± 0	6.09 ± 1.99	1.28 ± 0.457	2.55 ± 0.575	7.03 ± 1.53
Other MC	9.26 ± 4.78	0.967 ± 0.602	2.73 ± 1.39	11.8 ± 6.11	12.0 ± 6.05	2.29 ± 1.24
Fakes	28.4 ± 16.1	0 ± 0	3.28 ± 5.54	150 ± 50.3	143 ± 68.5	25.6 ± 10.8
Total bkg.	674 ± 241	92.8 ± 20.4	86.5 ± 14.9	382 ± 91.7	226 ± 69.7	124 ± 25.7
Data	734	87	81	433	260	116
Data/Bkg	1.09 ± 0.392	0.938 ± 0.230	0.936 ± 0.191	1.13 ± 0.278	1.15 ± 0.360	0.937 ± 0.213

Table 6.24.: The expected and observed event yields in the WZ, ZZ, $t\bar{t}Z$, fakes control and signal regions before the fit under the background-only hypothesis. In the signal region data is unblinded. Shown uncertainties are total pre-fit uncertainties.

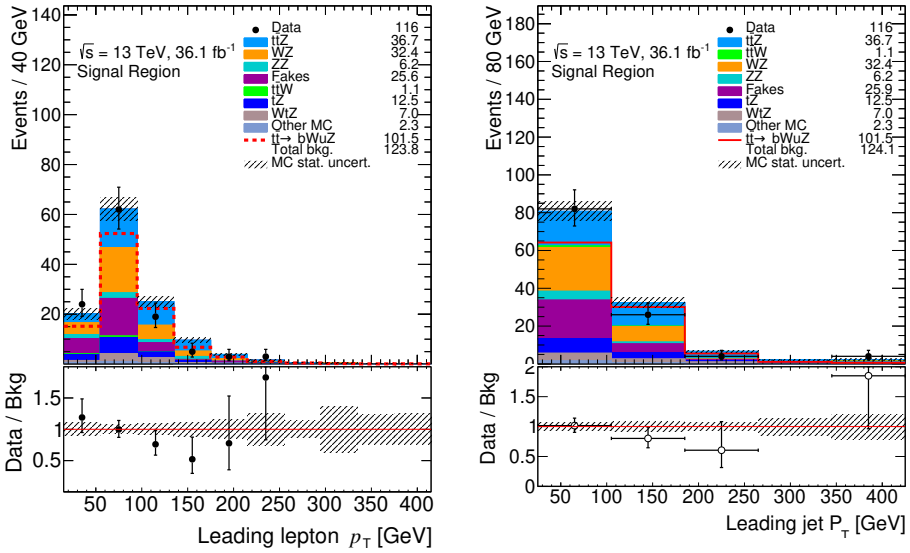

(a) (b)

Figure 6.47.: Expected and observed distributions in the signal region for the a) leading lepton p_{T} and b) the leading jet p_{T}. The number of signal events is normalized to an arbitrary branching ratio of $\mathrm{BR}(t \to qZ) = 0.1\%$.

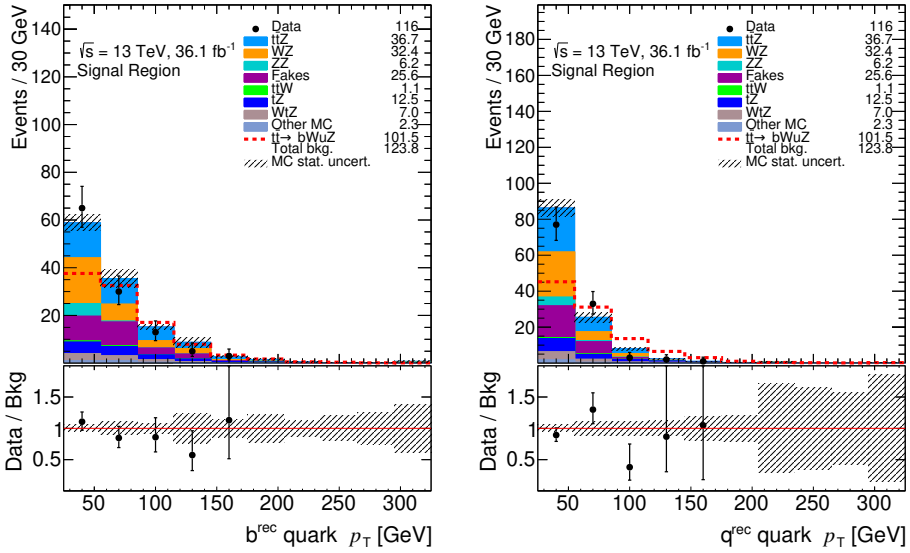

(a) (b)

Figure 6.48.: Expected and observed distributions in the signal region for the p_{T} of the a) b-quark and b) q-quark jets. The number of signal events is normalized to an arbitrary branching ratio of $\mathrm{BR}(t \to qZ) = 0.1\%$.

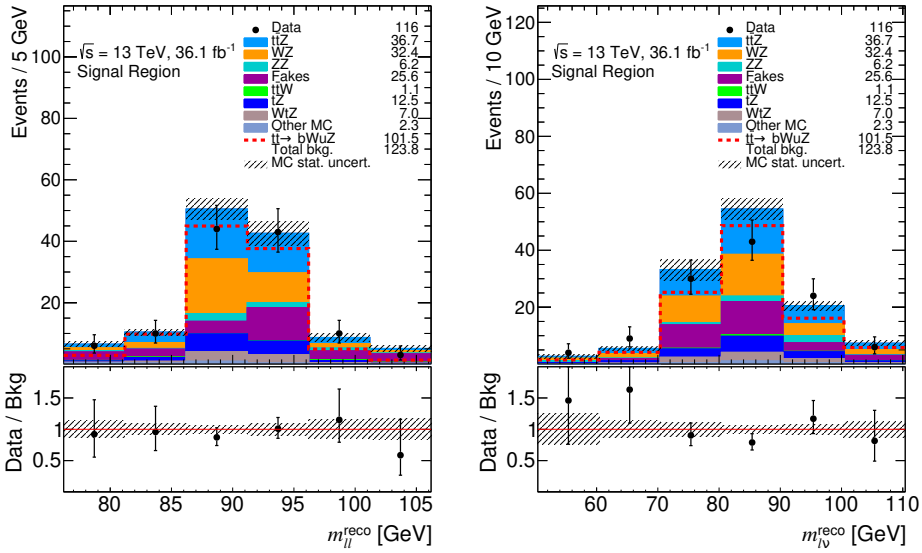

(a) (b)

Figure 6.49.: Expected and observed distributions in the signal region for the invariant masses of the a) Z boson and the b) W boson candidates. The number of signal events is normalized to an arbitrary branching ratio of BR$(t \to qZ) = 0.1\%$.

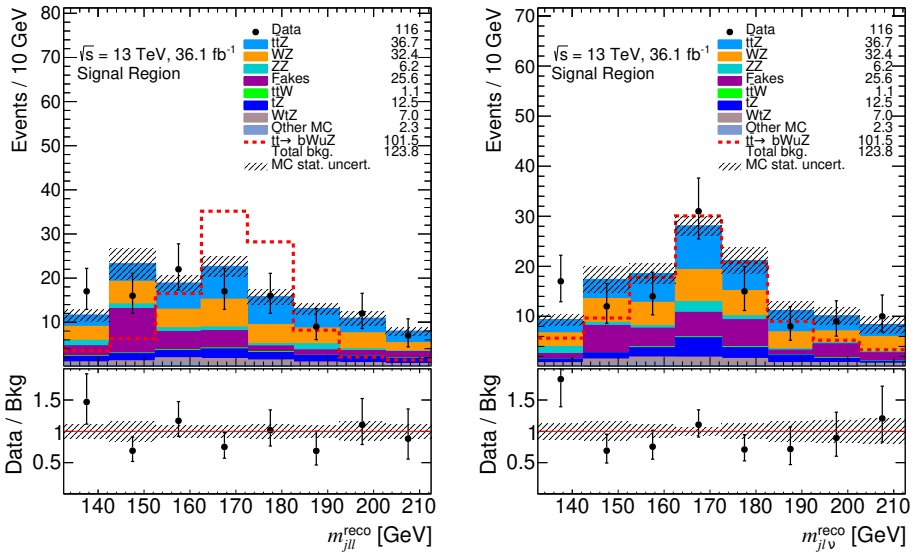

(a) (b)

Figure 6.50.: Expected and observed distributions in the signal region for the invariant masses of the a) FCNC top and the b) SM top candidates. The number of signal events is normalized to an arbitrary branching ratio of BR$(t \to qZ) = 0.1\%$.

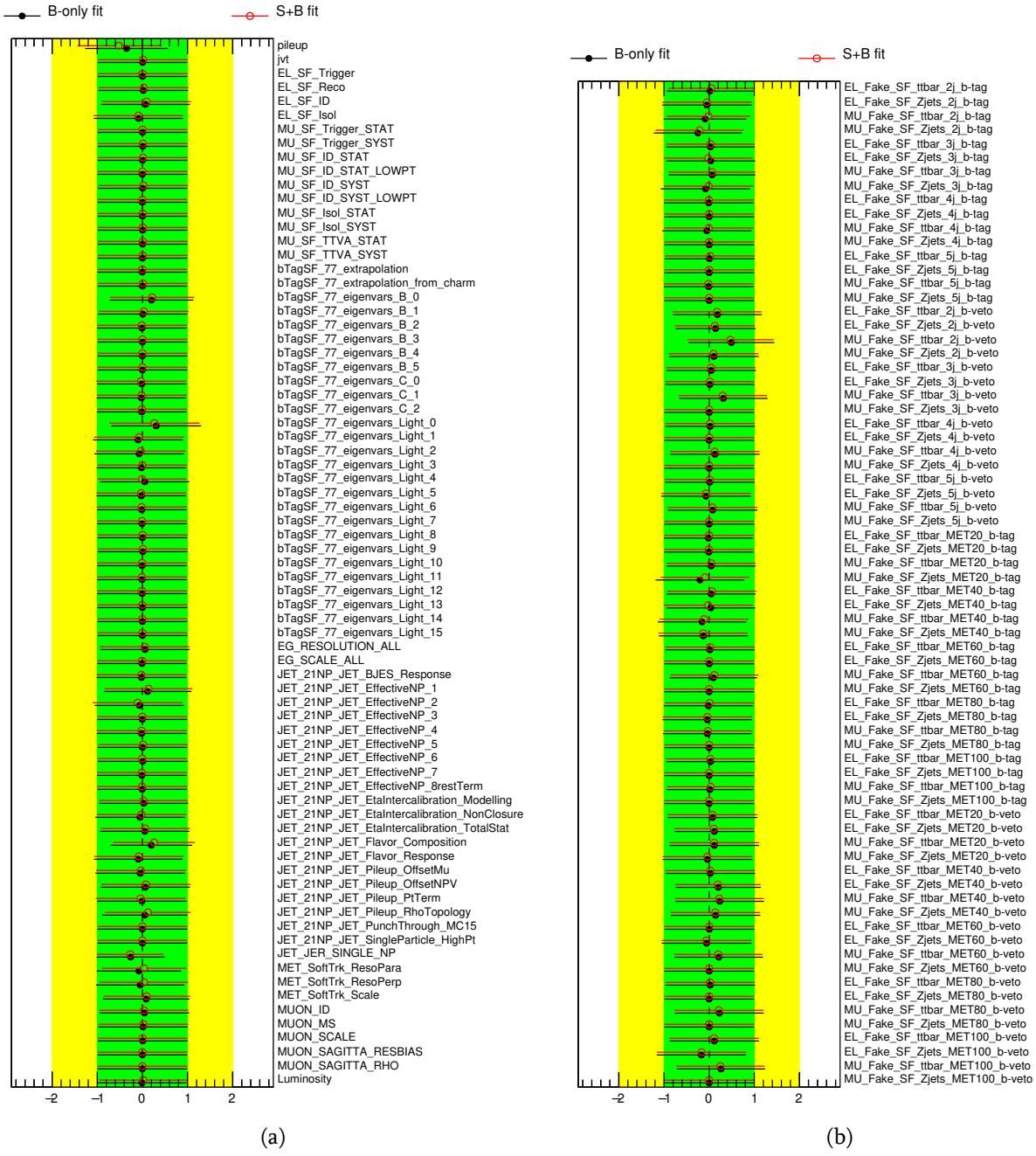

Figure 6.51.: Fitted nuisance parameters corresponding to a) instrumental and b) fakes scale factors uncertainties under the background-only hypothesis (black closed circles) and under the signal-plus-background hypothesis (red open circles) in the background control and signal regions with unblinded data.

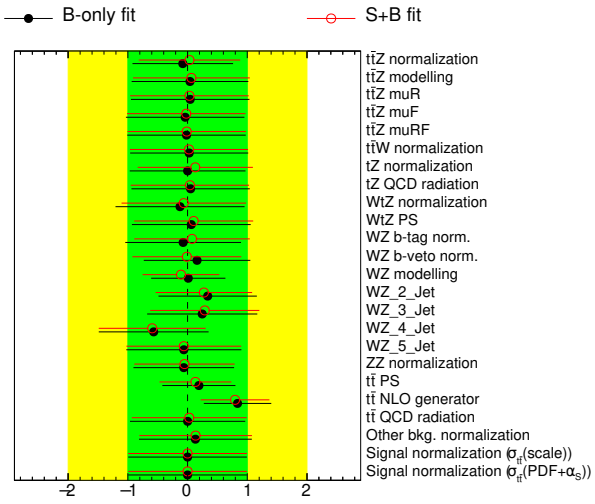

Figure 6.52.: Fitted nuisance parameters corresponding to the theoretical and modelling uncertainties under the background-only hypothesis (black closed circles) and under the signal-plus-background hypothesis (red open circles) in the background control and signal regions with unblinded data.

Sample	WZ CR	ZZ CR	$t\bar{t}Z$ CR	Fakes CR0	Fakes CR1	SR
$t\bar{t}Z$	16.5 ± 3.06	0 ± 0	60.5 ± 6.40	6.13 ± 1.21	21.9 ± 2.90	37.1 ± 4.29
$t\bar{t}W$	0.850 ± 0.177	0 ± 0	0.993 ± 0.219	3.76 ± 0.709	15.7 ± 2.16	1.15 ± 0.199
WZ	608 ± 38.8	0 ± 0	5.84 ± 3.97	166 ± 13.2	20.1 ± 5.02	32.5 ± 7.67
ZZ	48.6 ± 9.07	89.0 ± 11.6	0.0684 ± 0.0227	58.7 ± 10.2	8.96 ± 2.20	6.45 ± 2.97
tZ	6.45 ± 2.03	0 ± 0	3.70 ± 1.16	0.663 ± 0.222	1.97 ± 0.607	12.5 ± 3.68
WtZ	5.38 ± 1.32	0 ± 0	5.77 ± 1.89	1.23 ± 0.447	2.45 ± 0.580	7.04 ± 1.60
Other MC	10.0 ± 4.87	1.05 ± 0.612	2.91 ± 1.39	13.0 ± 6.31	13.0 ± 6.17	2.40 ± 1.22
Fakes	41.0 ± 14.8	0 ± 0	1.95 ± 2.32	177 ± 32.3	174 ± 21.0	19.8 ± 6.90
Total bkg.	737 ± 34.7	90.1 ± 11.6	81.7 ± 7.12	426 ± 30.1	258 ± 20.2	119 ± 9.94
Data	734	87	81	433	260	116
Data/Bkg	0.996 ± 0.0596	0.966 ± 0.161	0.991 ± 0.140	1.02 ± 0.0868	1.01 ± 0.100	0.975 ± 0.122

Table 6.25.: The expected and observed event yields in the signal region, WZ, ZZ, $t\bar{t}Z$ and fakes control regions after the combined fit under the background-only hypothesis with unblinded data. Shown uncertainties are total post-fit uncertainties.

Sample	Side-band VR	WZ VR
$t\bar{t}Z$	34.3 ± 4.67	2.77 ± 0.658
$t\bar{t}W$	1.54 ± 0.252	0.995 ± 0.197
WZ	59.9 ± 24.4	52.0 ± 17.1
ZZ	11.3 ± 9.91	4.16 ± 1.96
tZ	20.5 ± 6.25	13.8 ± 4.27
WtZ	8.30 ± 1.73	1.01 ± 0.471
Other MC	2.24 ± 1.44	1.66 ± 1.84
Fakes	43.5 ± 17.6	43.1 ± 12.7
Total bkg.	182 ± 33.7	120 ± 22.6
Data	185	123
Data/Bkg	1.02 ± 0.203	1.03 ± 0.215

Table 6.26.: The expected and observed yields in the side-band and WZ validation regions before the fit under the background-only hypothesis with unblinded data. Shown uncertainties are total pre-fit uncertainties.

Sample	Side-band VR	WZ VR
$t\bar{t}Z$	33.9 ± 4.12	2.68 ± 0.589
$t\bar{t}W$	1.54 ± 0.246	0.960 ± 0.186
WZ	60.9 ± 11.7	50.0 ± 8.83
ZZ	7.98 ± 5.31	4.45 ± 1.94
tZ	20.4 ± 6.01	13.8 ± 4.10
WtZ	8.02 ± 1.79	1.01 ± 0.476
Other MC	2.39 ± 1.40	1.79 ± 1.71
Fakes	51.0 ± 15.9	44.5 ± 11.5
Total bkg.	186 ± 19.9	119 ± 16.5
Data	185	123
Data/Bkg	0.994 ± 0.129	1.03 ± 0.171

Table 6.27.: The expected and observed yields in the side-band and WZ validation regions after the combined fit under the background-only hypothesis with unblinded data. Shown uncertainties are total post-fit uncertainties.

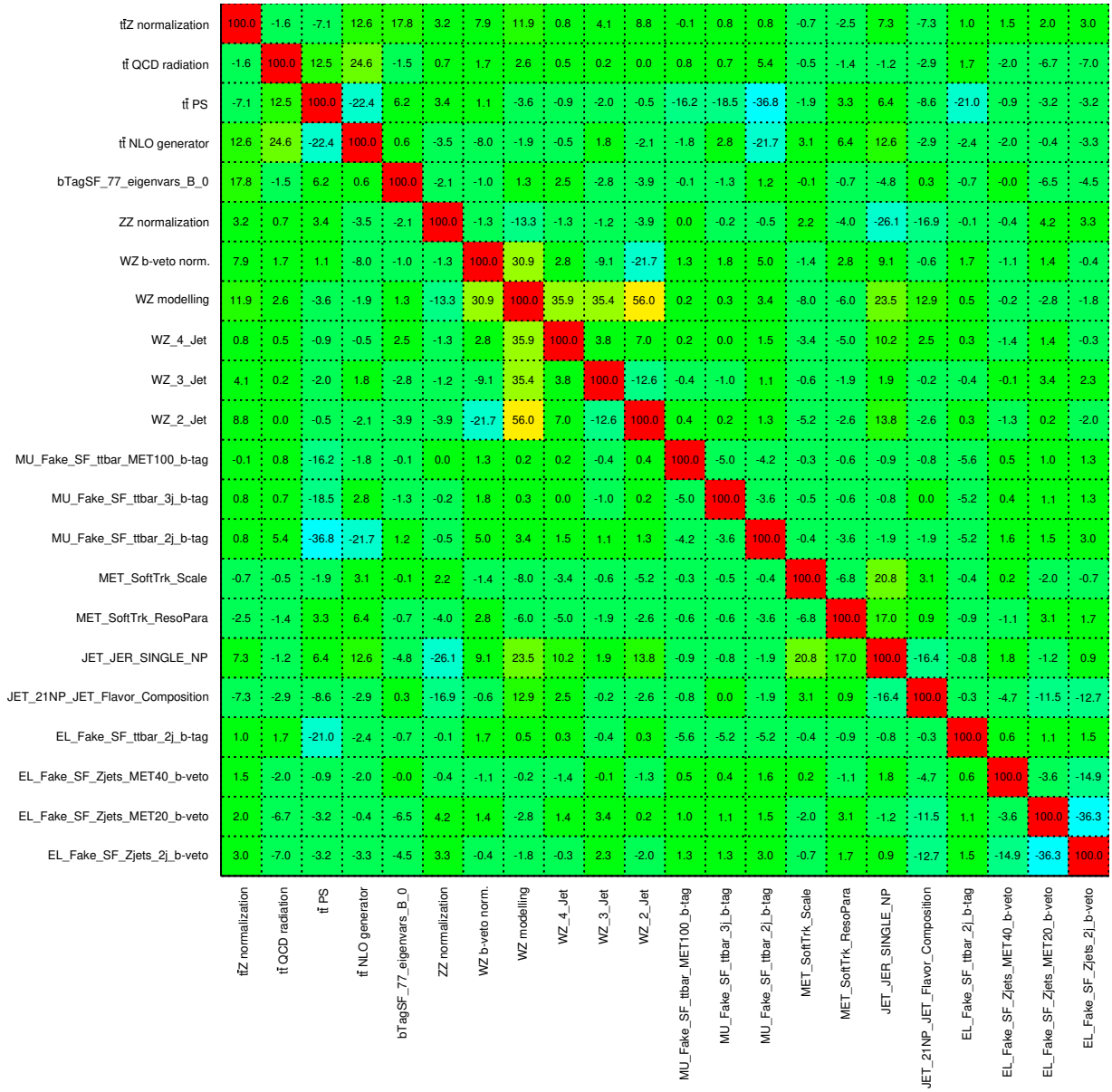

Figure 6.53.: Correlation matrix corresponding to the fit under the background-only hypothesis in the background control and signal regions after unblinding. Displayed values are in percentage. Only nuisance parameters with a correlation coefficient of at least 15% with any other parameter are displayed.

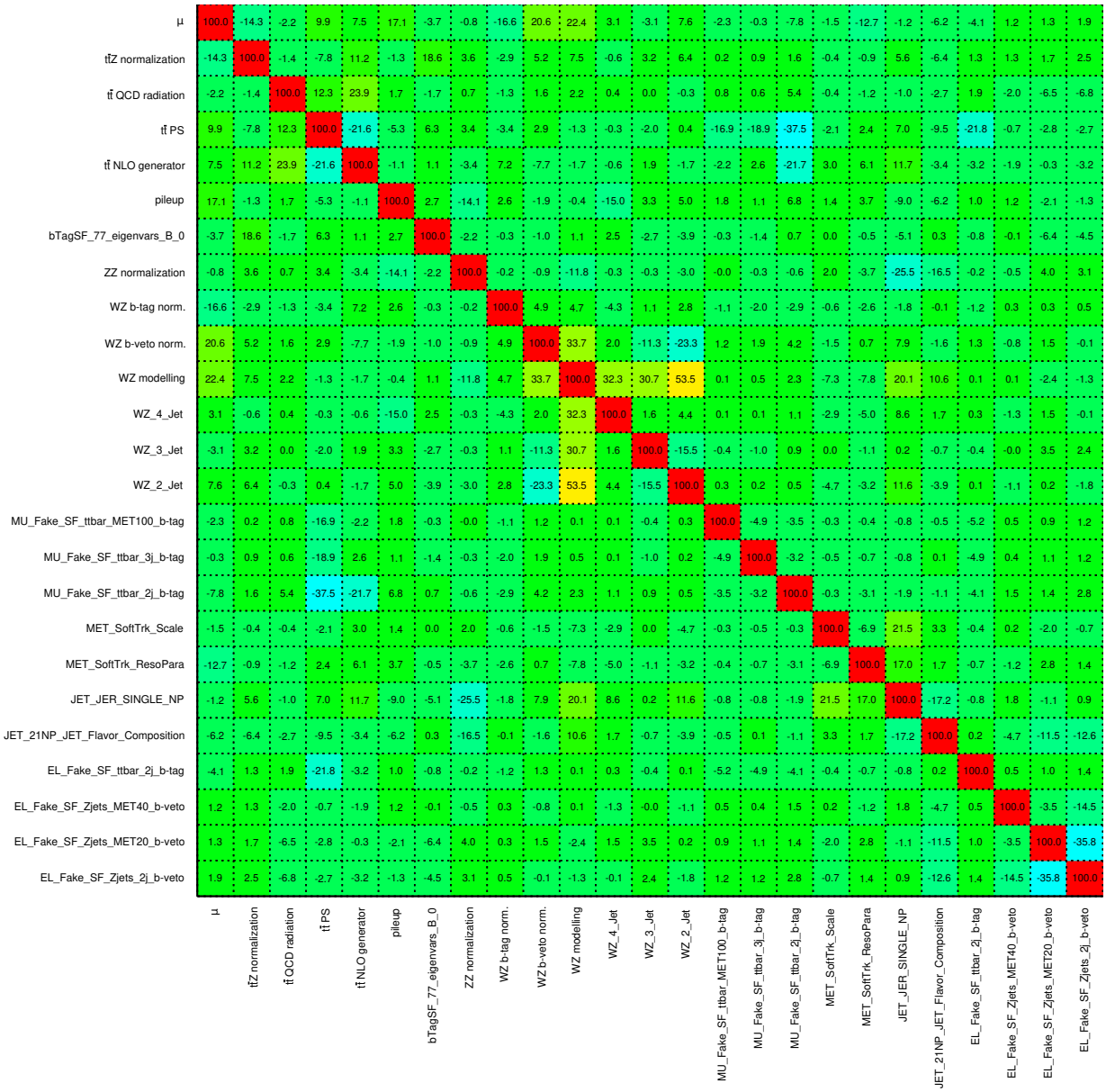

Figure 6.54.: Correlation matrix corresponding to the fit under the signal-plus-background hypothesis in the background control and signal regions after unblinding. Displayed values are in percentage. Only nuisance parameters with a correlation coefficient of at least 15% with any other parameter are displayed.

Sample	WZ CR	ZZ CR	$t\bar{t}Z$ CR	Fakes CR0	Fakes CR1	SR
$t\bar{t}Z$	1.01 ± 0.193	0 ± 0	0.995 ± 0.142	1.01 ± 0.205	0.992 ± 0.143	1.01 ± 0.138
$t\bar{t}W$	1.05 ± 0.228	0 ± 0	1.03 ± 0.247	1.03 ± 0.205	1.01 ± 0.142	1.03 ± 0.182
WZ	1.09 ± 0.462	0 ± 0	0.652 ± 0.638	1.10 ± 0.499	0.987 ± 0.448	1.00 ± 0.581
ZZ	1.01 ± 0.222	0.970 ± 0.216	0.971 ± 0.365	1.01 ± 0.273	0.993 ± 0.251	1.04 ± 0.532
tZ	1.03 ± 0.337	0 ± 0	1.02 ± 0.340	1.05 ± 0.366	0.995 ± 0.315	1.01 ± 0.307
WtZ	0.982 ± 0.229	0 ± 0	0.947 ± 0.310	0.960 ± 0.343	0.961 ± 0.217	1.00 ± 0.218
Other MC	1.08 ± 0.557	1.09 ± 0.676	1.06 ± 0.543	1.10 ± 0.567	1.08 ± 0.543	1.05 ± 0.565
Fakes	1.44 ± 0.814	0 ± 0	0.594 ± 1.00	1.18 ± 0.395	1.22 ± 0.584	0.774 ± 0.328
Total bkg.	1.09 ± 0.391	0.971 ± 0.214	0.945 ± 0.162	1.12 ± 0.268	1.14 ± 0.351	0.961 ± 0.199

Table 6.28.: Ratio of the pre-fit and post-fit background yields under the background-only hypothesis with unblinded data, for the background control and signal regions. Total pre-fit background uncertainties are presented.

Sample	Side-band VR	WZ VR
$t\bar{t}Z$	0.988 ± 0.134	0.970 ± 0.231
$t\bar{t}W$	0.998 ± 0.163	0.965 ± 0.192
WZ	1.02 ± 0.413	0.962 ± 0.316
ZZ	0.706 ± 0.619	1.07 ± 0.505
tZ	0.998 ± 0.305	0.998 ± 0.309
WtZ	0.966 ± 0.201	0.993 ± 0.461
Other MC	1.07 ± 0.691	1.07 ± 1.19
Fakes	1.17 ± 0.474	1.03 ± 0.304
Total bkg.	1.03 ± 0.190	0.997 ± 0.188

Table 6.29.: Ratio of the pre-fit and post-fit background yields under the background-only hypothesis with unblinded data, for the side-band and WZ validation regions. Total pre-fit background uncertainties are presented.

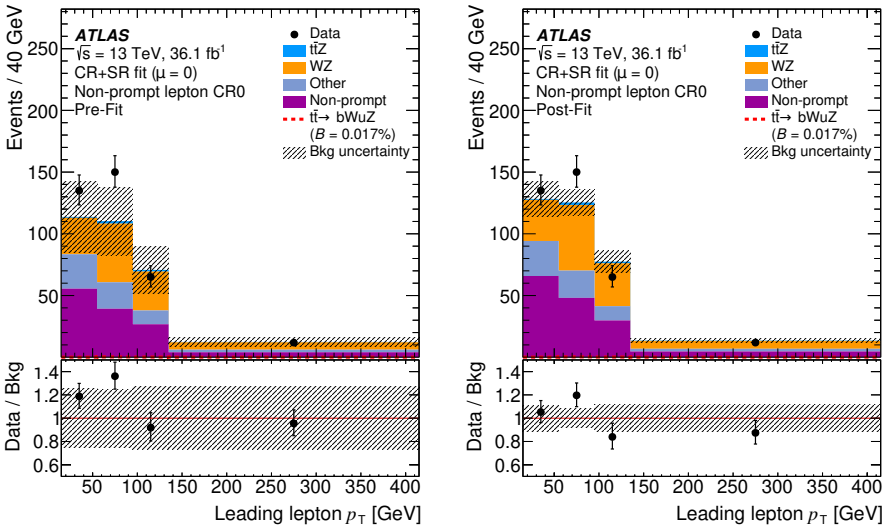

(a) (b)

Figure 6.55.: Comparison between data and prediction for the p_{T} of the leading lepton in the fake leptons background control region in b-veto events a) before and b) after the combined fit under the background-only hypothesis after unblinding. The number of signal events is normalized to the observed 95% CL limit. The dashed area represents total uncertainty on the background prediction.

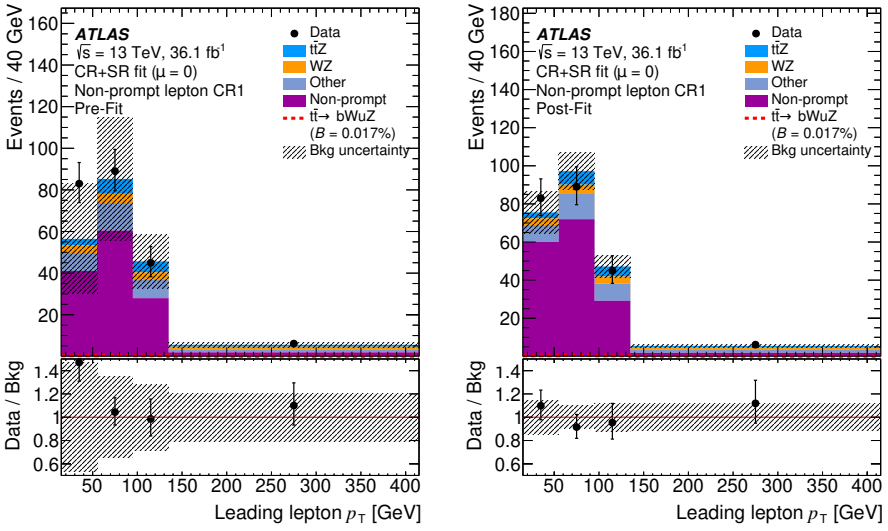

(a) (b)

Figure 6.56.: Comparison between data and prediction for the p_{T} of the leading lepton in the fake leptons background control region in one b-tag events a) before and b) after the combined fit under the background-only hypothesis after unblinding. The number of signal events is normalized to the observed 95% CL limit. The dashed area represents total uncertainty on the background prediction.

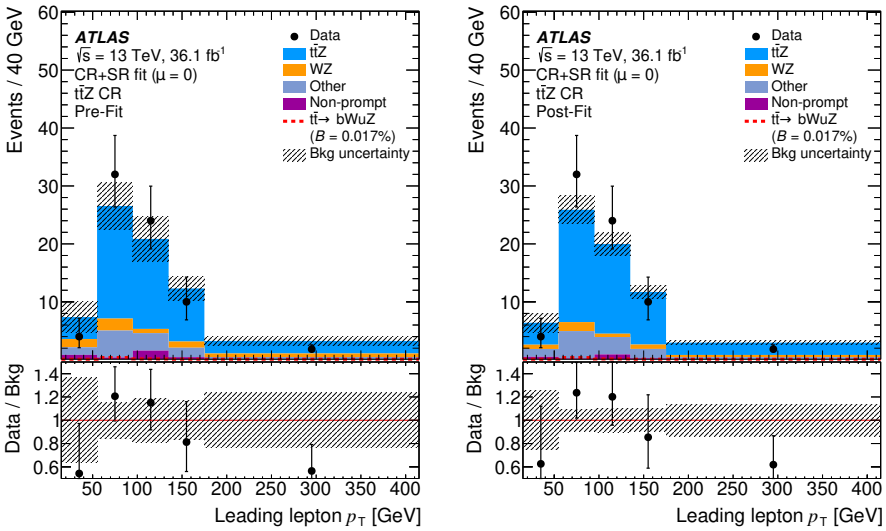

(a) (b)

Figure 6.57.: Comparison between data and prediction for the p_{T} of the leading lepton in the $t\bar{t}Z$ control region a) before and b) after the combined fit under the background-only hypothesis after unblinding. The number of signal events is normalized to the observed 95% CL limit. The dashed area represents total uncertainty on the background prediction.

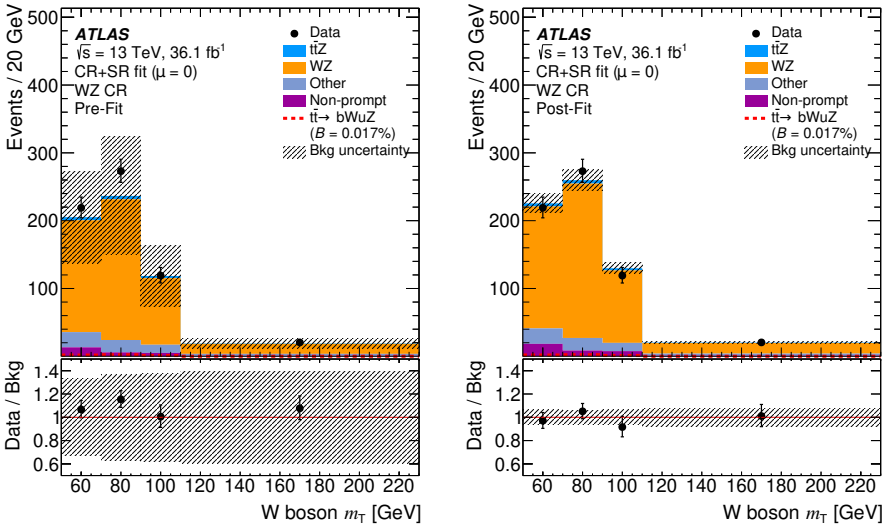

(a) (b)

Figure 6.58.: Comparison between data and prediction for the W boson transverse mass in the WZ control region a) before and b) after the combined fit under the background-only hypothesis after unblinding. The number of signal events is normalized to the observed 95% CL limit. The dashed area represents total uncertainty on the background prediction.

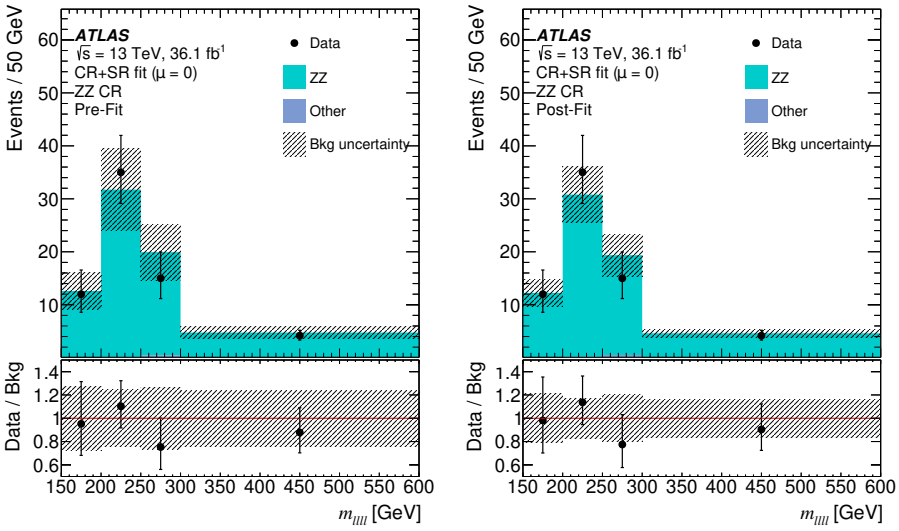

(a) (b)

Figure 6.59.: Comparison between data and prediction for the reconstructed ZZ system invariant mass in the ZZ control region a) before and b) after the combined fit under the background-only hypothesis after unblinding. The dashed area represents total uncertainty on the background prediction.

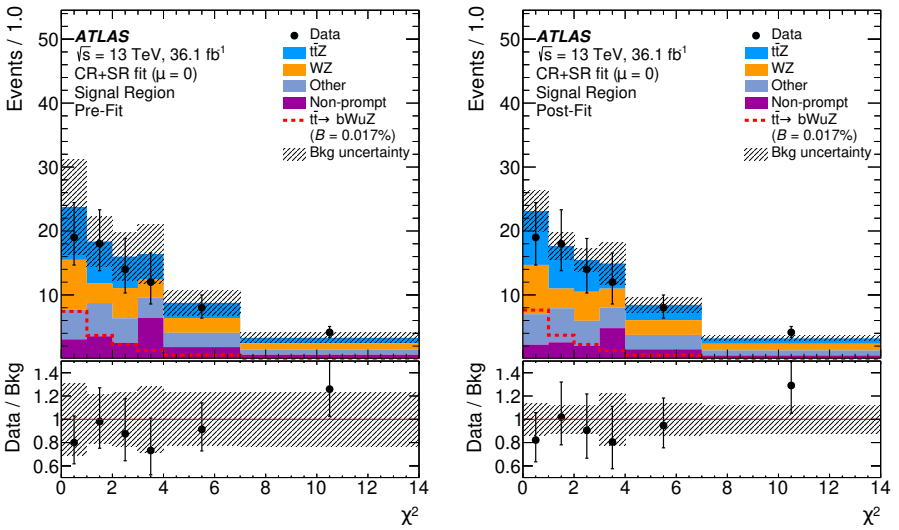

(a) (b)

Figure 6.60.: Comparison between data and prediction for the χ^2 after the event reconstruction in the signal region a) before and b) after the combined fit under the background-only hypothesis. The number of signal events is normalized to the observed 95% CL limit. The dashed area represents total uncertainty on the background prediction.

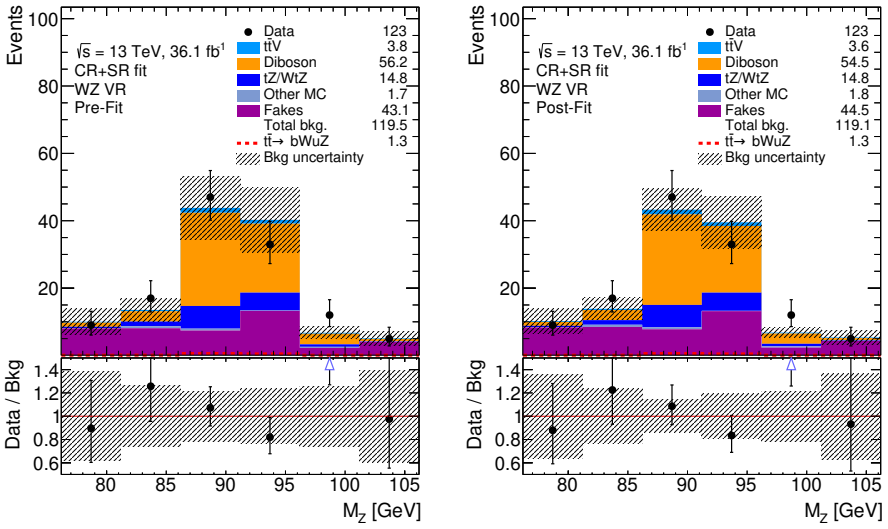

(a) (b)

Figure 6.61.: Comparison between data and prediction for the reconstructed Z boson mass in the WZ validation region a) before and b) after the combined fit under the background-only hypothesis after unblinding. The number of signal events is normalized to the observed 95% CL limit. The dashed area represents total uncertainty on the background prediction.

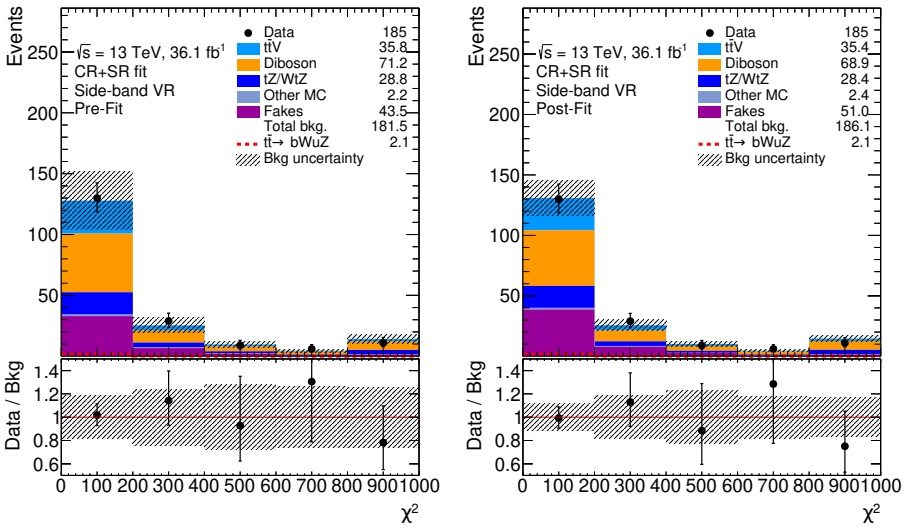

(a) (b)

Figure 6.62.: Comparison between data and prediction for the χ^2 after the event reconstruction in the side-band validation region a) before and b) after the combined fit under the background-only hypothesis after unblinding. The number of signal events is normalized to the observed 95% CL limit. The dashed area represents total uncertainty on the background prediction.

	WZ CR	ZZ CR	$t\bar{t}Z$ CR	Fakes CR0	Fakes CR1	SR	
Source	B [%]	B [%]	B [%]	B [%]	B [%]	B [%]	S [%]
Event modelling	40	13	29	24	40	30	5
Leptons	2.4	3.0	2.1	2.6	2.9	2.6	1.9
Jets	8	15	6	10	4	9	4
b-tagging	1.5	0.6	7	2.3	3.0	5	3.4
$E_{\mathrm{T}}^{\mathrm{miss}}$	4	2.6	0.4	3.0	0.8	5	1.4
Non-prompt leptons	1.3	—	1.1	12	15	6	—
Pile-up	1.3	5	5	3.5	1.8	4	2.3
Luminosity	2.0	2.1	2.0	1.3	0.8	1.7	2.1

Table 6.30.: Summary of the relative impact of each type of uncertainty on the total background yield in the background control regions and on the background and signal yields in the signal region before the combined fit under the background-only hypothesis. The values are shown in percentage.

	WZ CR	ZZ CR	$t\bar{t}Z$ CR	Fakes CR0	Fakes CR1	SR	
Source	B [%]	B [%]	B [%]	B [%]	B [%]	B [%]	S [%]
Event modelling	10	11	22	9	23	18	5
Leptons	2.4	2.9	2.0	2.6	2.9	2.6	1.8
Jets	6	11	5	8	4	8	4
b-tagging	1.4	0.6	7	2.1	2.8	4	3.1
$E_{\mathrm{T}}^{\mathrm{miss}}$	3.3	2.5	0.35	2.8	0.7	4	1.4
Non-prompt leptons	1.1	—	1.1	8	12	5	—
Pile-up	1.2	5	5	3.3	1.7	3.5	2.2
Luminosity	2.0	2.1	2.0	1.3	0.8	1.6	2.1

Table 6.31.: Summary of the relative impact of each type of uncertainty on the total background yield in the background control regions and on the background and signal yields in the signal region after the combined fit under the background-only hypothesis. The values are shown in percentage.

6.10.4. Upper limits on BR($t \to qZ$)

In the absence of signal, the 95% CL upper limits are set on BR($t \to uZ$) and BR($t \to cZ$). Figure 6.63 shows the observed and expected CL_s as a function of BR($t \to uZ$) and BR($t \to cZ$), while Table 6.32 shows the observed and expected 95% CL upper limits together with the $\pm 1\sigma$ bands. The observed limits are BR($t \to uZ$) < 0.017% and BR($t \to cZ$) < 0.024%, they are close to the -1σ bands of the expected limits: BR($t \to uZ$) < 0.024% and BR($t \to cZ$) < 0.032%. In Appendix F, the origin of the effect that the observed limits are close to the -1σ bands of the expected limits is investigated.

Using the effective field theory framework developed in the TopFCNC model [63, 64] and assuming a cut-off scale $\Lambda = 1$ TeV and that only one operator has a non-zero value, the upper limits on BR($t \to uZ$) and BR($t \to cZ$) are converted to 95% CL upper limits on the moduli of the operators contributing to the FCNC decay $t \to qZ$, which are presented in Table 6.33.

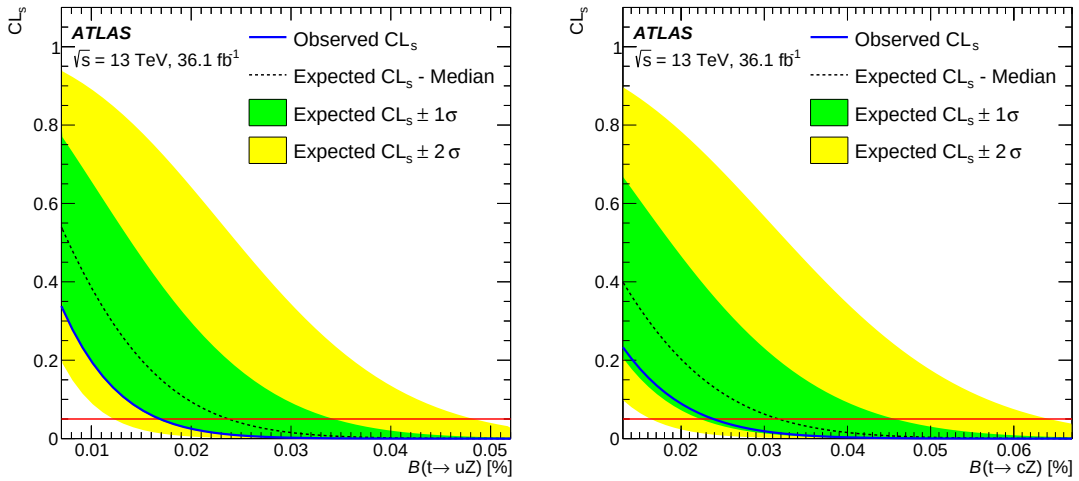

(a) (b)

Figure 6.63.: CL$_s$ vs BR($t \to uZ$) (a) and CL$_s$ vs BR($t \to cZ$) (b) taking into account systematic and statistical uncertainties. The median expected CL$_s$ under the background-only hypothesis (black dashed line) is displayed along with the ± 1 and ± 2 standard deviations bands (green and yellow, respectively). The solid red line at CL$_s$=0.05 denotes the threshold below which the hypothesis is excluded at 95% CL.

	Observed	-1σ	Expected	+1σ
BR($t \to uZ$) [%]	0.017	0.017	0.024	0.034
BR($t \to cZ$) [%]	0.024	0.022	0.032	0.046

Table 6.32.: Observed and expected 95% confidence level upper limits on the top-quark FCNC decay branching ratios. The expected central value are shown together with the $\pm 1\sigma$ bands, which include the contribution from the statistical and systematic uncertainties.

6.11. Conclusion

An analysis is performed to search for $t\bar{t}$ events with one top quark decaying through the FCNC $t \to qZ$ ($q = u, c$) channel and the other through the dominant Standard Model mode $t \to bW$, where only Z boson decays into charged leptons and leptonic W boson decays are considered as signal. The data were collected by the ATLAS experiment in pp collisions corresponding to

Operator	Observed	Expected
$\lvert C_{uB}^{(31)} \rvert$	0.25	0.30
$\lvert C_{uW}^{(31)} \rvert$	0.25	0.30
$\lvert C_{uB}^{(32)} \rvert$	0.30	0.34
$\lvert C_{uW}^{(32)} \rvert$	0.30	0.34

Table 6.33.: Observed and expected 95% CL upper limits on the moduli of the operators contributing to the FCNC decays $t \to uZ$ and $t \to cZ$ within the TopFCNC model for a new-physics energy scale $\Lambda = 1$ TeV.

an integrated luminosity of 36.1 fb^{-1} at the LHC at a centre-of-mass energy of $\sqrt{s} = 13$ TeV. There is good agreement between the data and Standard Model expectations, and no evidence of a signal is found. The 95% CL limits on the $t \to qZ$ branching ratio are BR$(t \to uZ) < 1.7 \times 10^{-4}$ and BR$(t \to cZ) < 2.4 \times 10^{-4}$, improving previous ATLAS results obtained at $\sqrt{s} = 8$ TeV by more than 60%. These limits constrain the values of effective field theory operators contributing to the $t \to uZ$ and $t \to cZ$ FCNC decays of the top quark.

Chapter 7.

The ATLAS experiment sensitivity to FCNC top-quark decays $t \to qZ$ at the High Luminosity LHC

The High Luminosity upgrade of the Large Hadron Collider (LHC) (HL-LHC) is currently expected to begin operations in the second half of 2026 [78, 79], to achieve an ultimate luminosity of 7.5×10^{34} cm^{-2}s^{-1}. The total integrated luminosity that is foreseen to be reached is 3000 fb^{-1}. This chapter presents a study of the sensitivity of the ATLAS experiment to top-quark decays via FCNC $t \to qZ$ ($q = u, c$ with $Z \to \ell^+\ell^-$). The top-quark–top-antiquark ($t\bar{t}$) events are studied, where one top quark decays through the FCNC mode and the other through the dominant SM mode ($t \to bW$). Only Z boson decays into charged leptons and leptonic W boson decays are considered. The final-state topology is thus characterized by the presence of three isolated charged leptons, at least two jets with exactly one being tagged as a jet containing a b-hadron, and missing transverse momentum from the undetected neutrino. The study is performed in the context of the LHC upgrade.

Based on the Run-1 search [2] (see Chapter 5), the ATLAS detector sensitivity to FCNC $t \to qZ$ decays for the HL-LHC was studied and reported in Ref. [190], predicting a sensitivity of $(2.4 - 5.8) \times 10^{-5}$, when considering statistical uncertainties only, depending on the exact FCNC $t \to qZ$ modeling and $(8.3 - 41) \times 10^{-5}$, depending on the detailed assumptions for the systematic uncertainties. In the present analysis, the description of the expected detector performance at the HL-LHC phase is improved and the analysis strategy closely follows the one of the Run-2 analysis [3] (see Chapter 6) rather than the Run-1 search.

Since it is difficult to accurately estimate the relevant systematic uncertainties that will impact the analysis in the high luminosity environment, several scenarios are studied and compared.

This study is released by the ATLAS Collaboration as a public document [4].

7.1. Signal and background simulation samples

Particle-level samples are generated at a center-of-mass energy of 14 TeV without detailed detector simulation. To emulate the HL-LHC run conditions and detector response, physics objects defined in Section 7.2 are smeared using performance functions derived from MC events passed through a full GEANT4 simulation of the upgraded ATLAS detector [89, 95, 96]. The effect of objects reconstruction and identification efficiencies as well as their momentum or energy resolutions are parameterized assuming an average number of additional pp collisions in the same or nearby bunch crossings (pile-up) of 200. In addition, pile-up jets are overlaid from a dedicated library.

In pp collisions at a centre-of-mass energy of $\sqrt{s} = 14$ TeV at the LHC, top quarks are produced according to the SM mainly in $t\bar{t}$ pairs with a predicted cross section of $\sigma_{t\bar{t}} = 0.98 \pm 0.06$ nb [39, 191–195]. The uncertainty includes contributions from uncertainties in the factorisation and renormalization scales, the parton distribution functions (PDF), the strong coupling α_S and the top-quark mass. The cross section is calculated at next-to-next-to-leading order (NNLO) in QCD including resummation of next-to-next-to-leading logarithmic soft gluon terms with Top++ 2.0. The effects of PDF and α_S uncertainties are calculated using the PDF4LHC prescription [40] with the MSTW 2008 68% CL NNLO [41, 98], CT10 NNLO [42, 127] and NNPDF 2.3 5f FFN [43] PDF sets and are added in quadrature to those from the renormalization and factorisation scale uncertainties. These calculations are done for the top-quark mass value of 172.5 GeV used to simulate events as described in the following paragraphs.

The next-to-leading-order (NLO) simulation of signal events was performed with the event generator MG5_aMC@NLO [159] interfaced to Pythia8 [160] with the A14 [94] set of tuned parameters and the NNPDF30ME PDF set [43]. Top quark FCNC decay is done using the TopFCNC model [63, 64]. The effects of new physics at an energy scale Λ were included by adding dimension-six effective terms to the SM Lagrangian. The Universal FeynRules Output (UFO) model [63, 64] is used for computation at NLO in QCD. No differences between the kinematical distributions from the $bWuZ$ and $bWcZ$ processes are observed. Due to the different b-tagging mistag rates for u- and c-quarks, the signal efficiencies differ after applying requirements on the b-tagged jet multiplicity. Hence limits on $\mathcal{B}(t \to qZ)$ are set separately for $q = u, c$. Only decays of the W and Z bosons with charged leptons were generated ($Z \to e^+e^-$, $\mu^+\mu^-$, or $\tau^+\tau^-$ and $W \to e\nu$, $\mu\nu$, or $\tau\nu$).

Several SM processes have final-state topologies similar to the signal, with at least three prompt[1] charged leptons, especially dibosons (WZ and ZZ), but also $t\bar{t}Z$, $t\bar{t}W$, $t\bar{t}WW$, tZ or $t\bar{t}t\bar{t}$ production. Events with non-prompt leptons, including the ones in which at least one jet is misidentified as a charged lepton, can also fulfil the event selection requirements. These events mainly consist of the $t\bar{t}$, Z+jets and tW processes. Such background processes cannot be realistically estimated by the transfer function approach used for the HL-LHC studies. There-

[1] Prompt leptons are electrons or muons from the decay of W or Z bosons, either directly or through an intermediate $\tau \to \ell\nu\nu$ decay.

Table 7.1.: Generators, parton shower simulation, parton distribution functions, and tune parameters used to produce particle-level samples without detailed detector simulation for this analysis. The acronyms ME and PS stand for matrix element and parton shower, respectively.

Sample	Generator	Parton shower	ME PDF	PS PDF	Tune parameters
$t\bar{t} \to bWqZ$	MG5_aMC@NLO [159]	Pythia8 [160]	NNPDF3.0NLO [161]	NNPDF2.3LO [43]	A14 [94]
$t\bar{t}Z$	MG5_aMC@NLO	Pythia8	NNPDF3.0NLO	NNPDF2.3LO	A14
ZZ, WZ	Sherpa v2 [130]	Sherpa v2	NNPDF3.0NNLO	NNPDF3.0NNLO	Sherpa default
tZ	MG5_aMC@NLO	Pythia8	NNPDF3.0NLO	NNPDF2.3LO	A14
$t\bar{t}WW$	MG5_aMC@NLO	Pythia8	NNPDF3.0NLO	NNPDF2.3LO	A14
Z+jets	Powheg-Box v1 [133]	Pythia8	CT10 [127]	CTEQ6L1 [119]	AZNLO [167]
$t\bar{t}$	Powheg-Box v2	Pythia8	NNPDF3.0NLO	NNPDF2.3LO	A14
tW	Powheg-Box v1	Pythia6 [120]	CT10f4	CTEQ6L1	Perugia2012 [121]
$t\bar{t}t\bar{t}$	MG5_aMC@NLO	Pythia8	NNPDF3.0NLO	NNPDF2.3LO	A14

fore, these backgrounds are scaled to the same fraction of the total event yield as observed in the Run-2 analysis [3] (see Chapter 6). All other background samples are normalized to their theory predictions.

Table 7.1 summarizes information about the generators, parton shower, and PDFs used to simulate the different event samples considered in this analysis.

7.2. Object reconstruction

Electrons and muons are required to have $p_{\mathrm{T}} > 25$ GeV. This threshold is increased in relation to the Run-2 analysis [3] (see Chapter 6) due to the expected higher yields of non-prompt lepton backgrounds. The single lepton trigger thresholds during the HL-LHC phase are expected to be 22 GeV for electrons and 20 GeV for muons [196], safely below the offline p_{T} requirement of 25 GeV considered in this analysis. Therefore no significant efficiency loss is expected from trigger threshold effects.

Electrons are required to be outside the transition region between the barrel and endcap calorimeters with $1.37 < |\eta_{\mathrm{cluster}}| < 1.52$. Electrons and muons with $|\eta| > 2.5$ are rejected. Reconstructed leptons within a cone of $\Delta R < 0.2$ of jets are removed. A truth-based isolation requirement is applied to the leptons, meaning that the sum of the transverse energies of stable[2] charged and neutral generator-level particles, with the exception of neutrinos, within a $\Delta R = 0.2$ cone around the lepton must be less than 23% (11%) of the electron (muon) candidate p_{T}. This requirement yields an efficiency of 95% for the prompt leptons and 37% (21%) efficiency for non-prompt electrons (muons) with $25 < p_{\mathrm{T}} < 50$ GeV in the $t\bar{t}$ events.

The missing transverse momentum (with the magnitude $E_{\mathrm{T}}^{\mathrm{miss}}$) is defined at particle level as the transverse component of the vector sum of the final-state neutrino momenta. The $E_{\mathrm{T}}^{\mathrm{miss}}$ resolution is parameterized as a function of the overall event activity.

Jets are reconstructed using the anti-k_t algorithm [99, 101] with a radius parameter $R = 0.4$.

[2] Particles in the MC event record with status code 1: a final-state particle, i.e. a particle that is not decayed further by the generator [197, 198].

They are required to have $p_{\mathrm{T}} > 30$ GeV and $|\eta| < 4.5$. Jets containing b-hadrons are randomly b-tagged to follow the 70% b-jet tagging efficiency working point of the MV2c10 algorithm [199]. The rejection rates for light-flavour jet and c-jet depend on the jet p_{T} and can be found in Ref. [199].

7.3. Event selection and reconstruction

The selection requirements follow the ones from the Run 2 analysis. Events are required to have exactly three leptons (any combination of electrons and muons), at least two jets, with exactly one of them b-tagged, one pair of opposite charge and same flavour leptons with $|m_{\ell^+\ell^-} - 91.2\ \mathrm{GeV}| < 15$ GeV and $E_{\mathrm{T}}^{\mathrm{miss}} > 20$ GeV. If more than one compatible lepton pair is found in the selection, the one with the reconstructed mass closest to 91.2 GeV is chosen as the Z boson candidate. The selection is finalized with the kinematical requirements explained next. For each possible jet combination, the following χ^2 function is minimized to derive the longitudinal momentum of the neutrino and, consequently, to reconstruct the top-quarks and the W boson. The solution (among all possible jet combinations) that yields the minimum χ^2 value is chosen.

$$\chi^2 = \frac{\left(m^{\mathrm{reco}}_{j_a\ell_a\ell_b} - m_{t_{\mathrm{FCNC}}}\right)^2}{\sigma^2_{t_{\mathrm{FCNC}}}} + \frac{\left(m^{\mathrm{reco}}_{j_b\ell_c\nu} - m_{t_{\mathrm{SM}}}\right)^2}{\sigma^2_{t_{\mathrm{SM}}}} + \frac{\left(m^{\mathrm{reco}}_{\ell_c\nu} - m_W\right)^2}{\sigma^2_W},$$

where $m^{\mathrm{reco}}_{j_a\ell_a\ell_b}$, $m^{\mathrm{reco}}_{j_b\ell_c\nu}$, and $m^{\mathrm{reco}}_{\ell_c\nu}$ are the reconstructed masses of the qZ, bW, and $\ell\nu$ systems, respectively, corresponding to the top-quarks and the W boson, respectively. For each jet combination, j_b corresponds to the b-tagged jet, while any non-b-tagged jet can be assigned to j_a. The central values of the masses and the widths of the top quarks and the W boson are taken from simulated signal events. This is done by matching the particles in the simulated events to the reconstructed ones, setting the longitudinal momentum of the neutrino to the p_z of the simulated neutrino, and then performing fitting to a Bukin function[3] [142] to the masses of the matched reconstructed top quarks and W boson. The obtained values are $m_{t_{\mathrm{FCNC}}} = 171.4$ GeV, $\sigma_{t_{\mathrm{FCNC}}} = 13.1$ GeV, $m_{t_{\mathrm{SM}}} = 177.1$ GeV, $\sigma_{t_{\mathrm{SM}}} = 38.1$ GeV, $m_W = 85.7$ GeV and $\sigma_W = 30.2$ GeV. Values for the $\sigma_{t_{\mathrm{SM}}}$ and σ_W are high due to the negative influence of the high pileup on the $E_{\mathrm{T}}^{\mathrm{miss}}$ resolution used to reconstruct the neutrino from the $t \to bW \to j\ell\nu$ decay. The events are then required to have $|m^{\mathrm{reco}}_{t_{\mathrm{FCNC}}} - 172.5\ \mathrm{GeV}| < 40$ GeV, $|m^{\mathrm{reco}}_{t_{\mathrm{SM}}} - 172.5\ \mathrm{GeV}| < 60$ GeV and $|m^{\mathrm{reco}}_W - 80.4\ \mathrm{GeV}| < 50$ GeV to remove outliers where the expected signal contribution is small. Note that the two last values were increased with respected to the Run-2 analysis due to the worse resolutions shown here. The fractions of correct assignments between the reconstructed top quarks and the true simulated top quarks at parton level (evaluated as a match within a

[3] These fits use a piecewise function with a Gaussian function in the centre and two asymmetric tails. Six parameters determine the overall normalization, the peak position, the width of the core, the asymmetry, the size of the lower tail, and the size of the higher tail. Of these, only the peak position and the width enter the χ^2.

Selection	Signal Region	$t\bar{t}Z$ CR	Non-prompt lepton CR
No. leptons	3	3	3
OSSF	Yes	Yes	Yes
$\lvert m_{\ell\ell}^{\text{reco}} - 91.2\text{ GeV}\rvert$	< 15 GeV	< 15 GeV	> 15 GeV
No. jets	≥ 2	≥ 4	≥ 2
No. b-tagged jets	1	2	1
$E_{\text{T}}^{\text{miss}}$	> 20 GeV	> 20 GeV	> 20 GeV
$\lvert m_{\ell\nu}^{\text{reco}} - 80.4\text{ GeV}\rvert$	< 50 GeV	-	-
$\lvert m_{j\ell\nu}^{\text{reco}} - 172.5\text{ GeV}\rvert$	< 60 GeV	-	-
$\lvert m_{j\ell\ell}^{\text{reco}} - 172.5\text{ GeV}\rvert$	< 40 GeV	-	-

Table 7.2.: The selection requirements applied for the signal and background control regions. OSSF refers to the presence of a pair of opposite-sign, same-flavour leptons.

cone of size $\Delta R = 0.4$) are $\epsilon_{t_{\text{FCNC}}} = 76\%$ and $\epsilon_{t_{\text{SM}}} = 40\%$, where the difference comes from the fact that for the SM top-quark decay the match of the $E_{\text{T}}^{\text{miss}}$ with the simulated neutrino is less efficient.

Following the strategy of the Run-2 analysis, dedicated control regions (CR) are defined for the main background contributions to help constrain systematic uncertainties. Here only CR for $t\bar{t}Z$ and non-prompt leptons were defined. The $t\bar{t}Z$ CR requires exactly three leptons, two of them with the same flavour, opposite charge and reconstructed mass within 15 GeV of the Z boson mass. Furthermore, the events are required to have at least four jets, two of which must be b-tagged, and $E_{\text{T}}^{\text{miss}} > 20$ GeV. The non-prompt lepton background CR requires three leptons with two of them having the same flavour, opposite charge and reconstructed mass outside 15 GeV of the Z boson mass, at least two jets with one being b-tagged and $E_{\text{T}}^{\text{miss}} > 20$ GeV.

Selection requirements applied in the signal and background control regions are summarized in Table 7.2. The expected distributions of relevant observables in the signal region are shown in Figure 7.1.

7.4. Systematic uncertainties

The background fit to the CRs, described in Section 7.5, reduces the systematic uncertainty from some sources, due to the constraints introduced by the Asimov simulated data. The main uncertainties, in both the background and signal estimations, are expected to come from theoretical normalization uncertainties and uncertainties in the modelling of background processes in the simulation. The effect of those uncertainties is estimated in the Run-2 analysis (see Chapter 6), and then reduced by a factor of two, as recommended in Ref. [200], to account for expected improvements in theoretical predictions. The reduced uncertainty is then applied in this analysis. The uncertainties obtained before the combined fit are discussed below and are

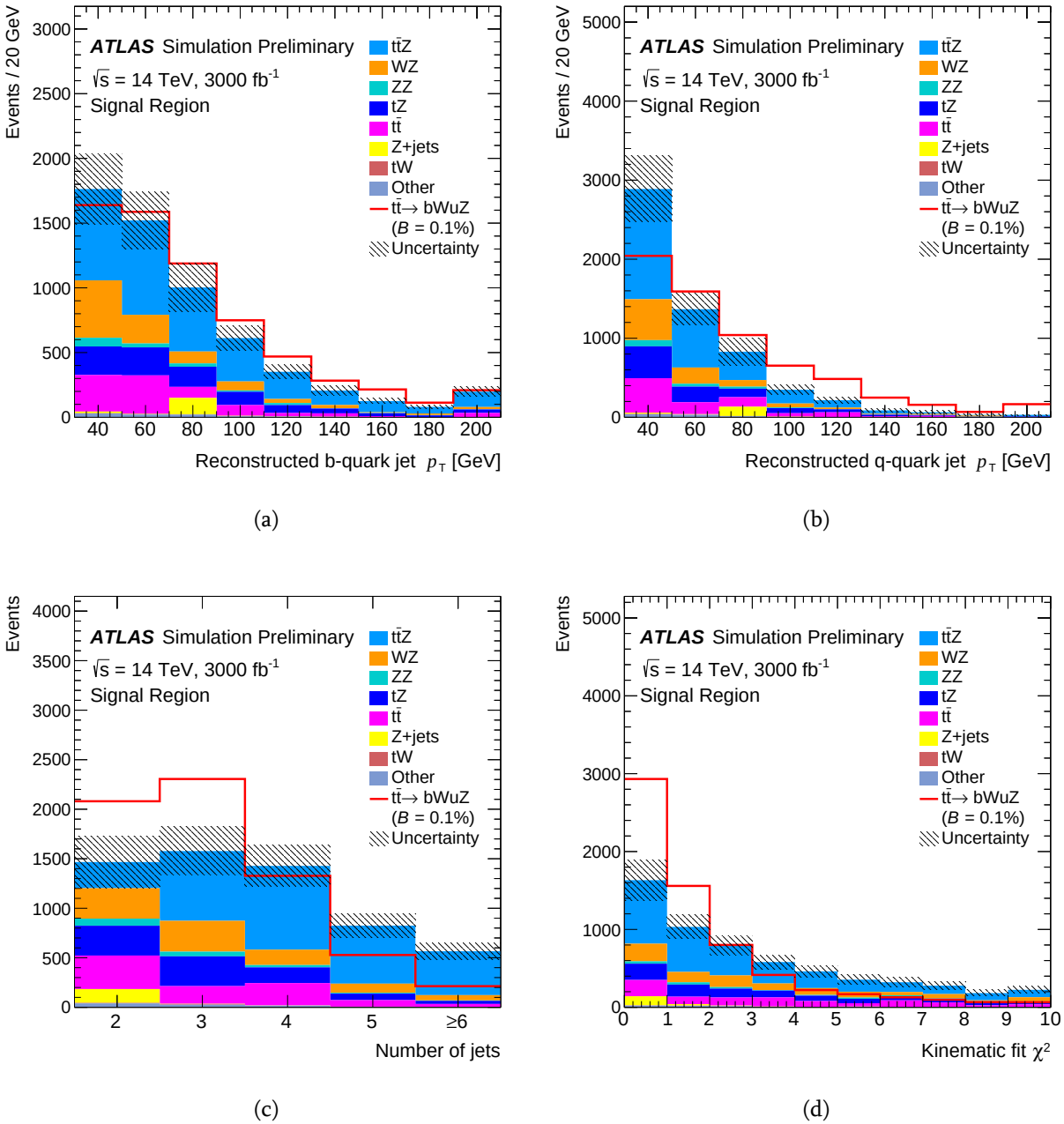

Figure 7.1.: Expected distributions in the signal region for p_{T} of the reconstructed a) b-quark jet from the $t \to bW$ decay and b) q-quark jet from the $t \to qZ$ decay, c) jet multiplicity and d) kinematic fit χ^2. The signal is not shown stacked on top of the backgrounds, but is normalized separately to an arbitrary branching ratio of $\mathrm{BR}(t \to qZ) = 0.1\%$. The dashed area represents the systematic uncertainty on the background prediction.

summarized in Table 7.3.

The cross section uncertainties of the $t\bar{t}Z$ and tZ background processes are taken to be 6% and 15%, respectively. For diboson production, a 6% theoretical normalization uncertainty is considered as well as 24% uncertainty on the WZ production in the SR due to the modelling in the simulation. In addition, a 12% uncertainty added in quadrature per jet is applied on the WZ yield in each jet multiplicity bin to account for the imperfect knowledge of the jet multiplicity distribution in WZ events. The $t\bar{t}$ production cross-section uncertainties from the independent variation of the factorisation and renormalization scales, the PDF choice, and α_S variations (see Refs. [39, 40] and references therein and Refs. [41–43]) give a 5% uncertainty in the signal normalization and 4% uncertainty on the total non-prompt leptons background in the SR. The 12% and 5% uncertainties due to the choice of NLO generator and amount of QCD radiation for the $t\bar{t}$ modelling are considered on the total non-prompt leptons background in the SR, while the uncertainty due to the choice of the parton shower algorithm is 1% in the SR and 19% in the non-prompt leptons CR. A 17% uncertainty is considered on the Z+jets normalization, which yields a 2.5% uncertainty on the total non-prompt leptons background in the SR. For the remaining small backgrounds, a 50% uncertainty is assumed.

For both the estimated signal and background event yields, experimental uncertainties resulting from detector effects are assumed to be same as in the Run-2 analysis. The uncertainties on the lepton reconstruction, identification and trigger efficiencies, as well as lepton momentum scales and resolutions, are added in quadrature resulting in a 2.6% (1.9%) uncertainty on the total background (signal) event yield in the SR. The uncertainty due to the jet-energy scale and resolution is 9% (4%) on the total background (signal) event yield in the SR, while total b-tagging uncertainty, which includes the uncertainty of the b-, c-, mistagged- and τ-jet scale factors, is 5% (3.4%). Uncertainties of the $E_{\mathrm{T}}^{\mathrm{miss}}$ scale and pile-up effects are 4% and 2.3% on the total background and signal yields in the SR, respectively.

The total uncertainties of the leptons, jets, b-tagging, $E_{\mathrm{T}}^{\mathrm{miss}}$ and pile-up uncertainties on the total background/signal event yields are considered on each background/signal process as an input normalization uncertainty for the combined fit.

The shape uncertainties are not considered, assuming that their effect on the final results is not significant, as it is found in the Run-2 analysis.

The MC statistical uncertainties are set to zero in the analysis, unless it is mentioned that they are considered, assuming that sufficiently large simulation samples will be available for the HL-LHC analysis.

7.5. Results

A simultaneous fit to the SR and the two CRs is used to search for a signal from FCNC decays of the top quark. A maximum-likelihood fit is performed to kinematic distributions in the signal and control regions to test for the presence of signal events. Contamination of the CRs by the

Source	Signal Region		$t\bar{t}Z$ CR	Non-prompt CR
	S [%]	B [%]	B [%]	B [%]
Event modelling	5	6	6	12
Leptons	1.9	2.6	2.1	2.9
Jets	4	9	6	4
b-tagging	3.4	5	7	3.0
$E_{\mathrm{T}}^{\mathrm{miss}}$	1.4	5	0.4	0.8
Pile-up	2.3	4	5	1.8

Table 7.3.: Summary of the relative impact of each type of uncertainty on the signal (S) and total background (B) yields in the signal region and on the total background yield in the background control regions before the combined fit.

signal is negligible. The kinematic distributions used in the fit are the χ^2 of the kinematical reconstruction for the SR and the leading lepton p_{T} for the $t\bar{t}Z$ and non-prompt leptons CRs. The expected number of events in each region are shown in Table 7.4 with the total systematic uncertainties before (after) the combined fit under the background-only hypothesis, while the expected distributions are presented in Figures 7.2-7.4.

Sample	Signal Region	$t\bar{t}Z$ CR	Non-prompt CR
$t\bar{t}Z$	2 840 $\pm$ 400 ($\pm$ 120)	3 330 $\pm$ 410 ($\pm$ 90)	1 500 $\pm$ 160 ($\pm$ 90)
WZ	920 $\pm$ 270 ($\pm$ 150)	210 $\pm$ 90 ($\pm$ 60)	660 $\pm$ 140 ($\pm$ 90)
ZZ	156 $\pm$ 22 ($\pm$ 12)	20.6 $\pm$ 2.6 ($\pm$ 1.6)	154 $\pm$ 13 ($\pm$ 11)
tZ	860 $\pm$ 170 ($\pm$ 110)	360 $\pm$ 70 ($\pm$ 50)	131 $\pm$ 21 ($\pm$ 18)
Non-prompt leptons	1 000 $\pm$ 190 ($\pm$ 90)	257 $\pm$ 93 ($\pm$ 25)	4 030 $\pm$ 900 ($\pm$ 110)
Other	90 $\pm$ 13 ($\pm$ 8)	70 $\pm$ 15 ($\pm$ 13)	1 290 $\pm$ 130 ($\pm$ 90)
Total bkg.	5 860 $\pm$ 810 ($\pm$ 70)	4 240 $\pm$ 520 ($\pm$ 60)	7 760 $\pm$ 1 020 ($\pm$ 90)
$t\bar{t} \to bWuZ$	299 $\pm$ 19 ($\pm$ 8)	6.77 $\pm$ 0.42 ($\pm$ 0.19)	17.7 $\pm$ 1.1 ($\pm$ 0.5)
$t\bar{t} \to bWcZ$	331 $\pm$ 20 ($\pm$ 9)	11.64 $\pm$ 0.72 ($\pm$ 0.32)	23.5 $\pm$ 1.5 ($\pm$ 0.7)

Table 7.4.: The expected event yields in the signal and background control regions. The number of signal events is normalized to the expected branching ratio limits of $\mathrm{BR}(t \to uZ) = 4.6 \times 10^{-5}$ and $\mathrm{BR}(t \to cZ) = 5.5 \times 10^{-5}$. Total systematic uncertainties are shown before (after) the combined fit under the background-only hypothesis. After the combined fit, the uncertainty on the total background is smaller than the uncertainty on some of the background contributions due to the negative correlations between some of the background sources.

The statistical analysis to extract the signal is based on a binned likelihood function $L(\mu, \theta)$ as for the Run-2 search [3] (see Chapter 6). The $L(\mu, \theta)$ is constructed as a product of Poisson probability terms over all bins in each considered distribution, and Gaussian constraint terms for θ, a set of nuisance parameters that parameterize effects of systematic uncertainties on the signal and background expectations. The parameter μ is a multiplicative factor for the number

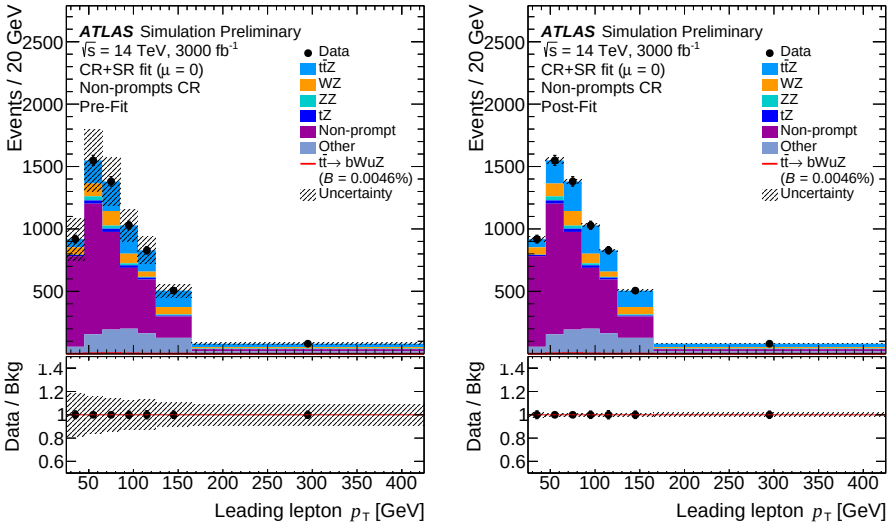

(a) (b)

Figure 7.2.: The distributions for the p_{T} of the leading lepton in the non-prompt leptons control region a) before and b) after the combined fit under the background-only hypothesis. The data points are from the "Asimov dataset", defined as a total expected pre-fit background. The number of signal events is normalized to the expected branching ratio limit of BR$(t \to uZ) = 4.6 \times 10^{-5}$. The dashed area represents the systematic uncertainty on the background prediction.

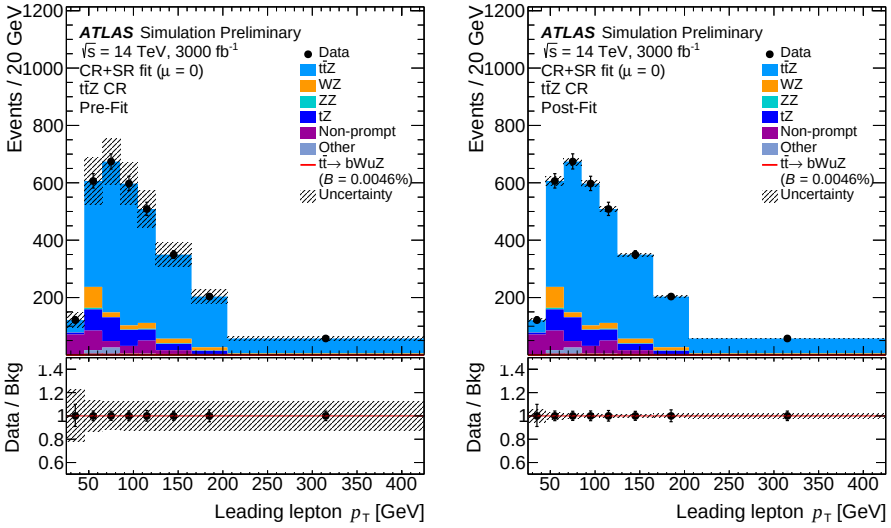

(a) (b)

Figure 7.3.: The distributions for the p_{T} of the leading lepton in the $t\bar{t}Z$ control region a) before and b) after the combined fit under the background-only hypothesis. The data points are from the "Asimov dataset", defined as a total expected pre-fit background. The number of signal events is normalized to the expected branching ratio limit of BR$(t \to uZ) = 4.6 \times 10^{-5}$. The dashed area represents the systematic uncertainty on the background prediction.

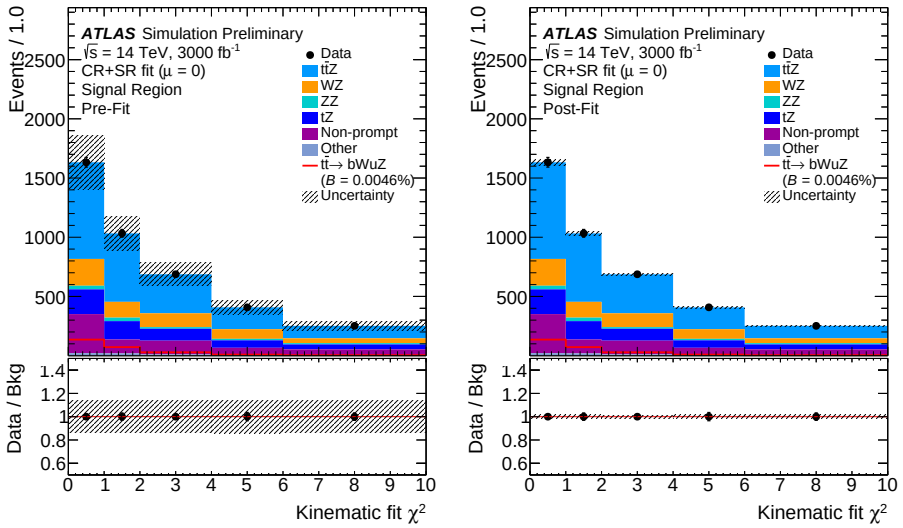

(a) (b)

Figure 7.4.: The distributions for the χ^2 after the event reconstruction in the signal region a) before and b) after the combined fit under the background-only hypothesis. The data points are from the "Asimov dataset", defined as a total expected pre-fit background. The number of signal events is normalized to the expected branching ratio limit of BR$(t \to uZ) = 4.6 \times 10^{-5}$. The dashed area represents the systematic uncertainty on the background prediction.

of signal events normalized to a branching ratio BR$_{\text{ref}}(t \to qZ) = 0.1\%$. In the absence of FCNC signal, upper limits on BR$(t \to qZ)$ can be computed with the CL$_s$ method [154, 155]. The expected 95% confidence level (CL) limit on BR$(t \to uZ)$ and on BR$(t \to cZ)$ are shown in Tables 7.5 and 7.6, which include the contribution from the statistical and systematic uncertainties. The latter one does not include contribution from the MC statistical uncertainty, which given the small size of some of the simulated event samples (Z+jets, for instance) is more realistic than the former one.

Inclusion of the CRs in the combined fit with the SR constrains backgrounds, reduces systematic uncertainties and thus improves the BR$(t \to qZ)$ limits. The limits obtained without inclusion of the CRs in the likelihood are about 13% worse compared to the results extracted from the CRs and SR combination. After the combined fit, the dominant contributions to systematic uncertainties come from $E_{\text{T}}^{\text{miss}}$ and jet reconstruction uncertainties. The effect of these uncertainties is estimated in the Run-2 analysis and the same uncertainties are applied in the HL-LHC studies. If the expected improvements for these sources of systematic uncertainties are taken into account by reducing their effect by a factor of two [200], a further improvement of about 15% on the BR$(t \to qZ)$ limits is to be expected.

The limits on the branching ratios can be interpreted in the framework of an Effective Field Theory (EFT) approach, see for example Refs. [63, 64]. In this context, limits can be set on the EFT coefficients. According to Ref. [64], the EFT operators to which the analysis is more sensitive are $C_{uB}^{(31)}$, $C_{uW}^{(31)}$, $C_{uB}^{(32)}$ and $C_{uW}^{(32)}$. Assuming a cut-off scale $\Lambda = 1$ TeV and that only one

FCNC mode contributes, the branching ratio limits presented in Table 7.6 are converted to 95% CL upper limits on the moduli of the EFT coefficients. These are shown in Table 7.7. The results of this analysis should not depend on the handedness of the EFT couplings [201].

	-1σ	Expected	+1σ
BR($t \to uZ$)	4.9 $\times 10^{-5}$	6.9 $\times 10^{-5}$	9.7 $\times 10^{-5}$
BR($t \to cZ$)	5.8 $\times 10^{-5}$	8.1 $\times 10^{-5}$	12 $\times 10^{-5}$

Table 7.5.: The expected 95% confidence level upper limits on the top-quark FCNC decay branching ratios are shown together with the $\pm 1\sigma$ bands, which include the contribution from the statistical and systematic uncertainties. Presented limits are extracted from "Asimov data" in the signal and background control regions, defined as the total expected pre-fit background. Systematic uncertainty from the MC statistical uncertainty is considered as well.

	-1σ	Expected	+1σ
BR($t \to uZ$)	3.3 $\times 10^{-5}$	4.6 $\times 10^{-5}$	6.5 $\times 10^{-5}$
BR($t \to cZ$)	3.9 $\times 10^{-5}$	5.5 $\times 10^{-5}$	7.7 $\times 10^{-5}$

Table 7.6.: The expected 95% confidence level upper limits on the top-quark FCNC decay branching ratios are shown together with the $\pm 1\sigma$ bands, which include the contribution from the statistical and systematic uncertainties. Presented limits are extracted from "Asimov data" in the signal and background control regions, defined as the total expected pre-fit backgrounds. Systematic uncertainty from the MC statistical uncertainty is not considered.

7.6. Conclusion

The sensitivity of the ATLAS experiment in the search for flavour-changing neutral-current top quark decays is presented. The study is performed in the context of the high luminosity phase of the Large Hadron Collider with a centre-of-mass energy of 14 TeV and an integrated

Operator	Expected limit
$\lvert C_{uB}^{(31)} \rvert$	0.13
$\lvert C_{uW}^{(31)} \rvert$	0.13
$\lvert C_{uB}^{(32)} \rvert$	0.14
$\lvert C_{uW}^{(32)} \rvert$	0.14

Table 7.7.: Expected 95% CL upper limits on the moduli of the operators contributing to the FCNC decays $t \to uZ$ and $t \to cZ$ within the TopFCNC model for a new-physics energy scale $\Lambda = 1$ TeV.

luminosity of 3000 fb^{-1}. The three charged lepton final state of $t\bar{t}$ events is considered, in which one of the top quarks decays through the $t \to qZ$ $(q = u, c)$ flavour-changing neutral-current channel and the other one decays to bW ($t\bar{t} \to bWqZ \to b\ell\nu q\ell\ell$). An improvement by a factor of four is expected over the current Run-2 analysis results of BR$(t \to uZ) < 1.7 \times 10^{-4}$ and BR$(t \to cZ) < 2.4 \times 10^{-4}$ with 36.1 fb^{-1} integrated luminosity. The branching ratio limits that are obtained are at the level of 4 to 5 $\times 10^{-5}$ depending on the considered scenarios for the systematic uncertainties.

Conclusions

Three topics of the doctorate work are presented in this thesis.

In the first topic, impact of the ATLAS Hadronic Tile Calorimeter granularity increase on the reconstruction of the jet mass and other jet properties variables is investigated in the context of High-Luminosity LHC upgrade. The study is based on the Monte Carlo simulated events with a high-mass new physics particles (W' and Z' bosons) and Standard Model events with high-p_{T} jets in the final-state. Improvements of the small-radius jet angular resolution in η and large-radius jet calorimeter-based mass resolution of approximately 20% is found using the possible modification of TileCal readout, increasing the granularity. In addition, a better measurements of the jet substructure variables is possible allowing for superior discrimination between QCD-jets and jets from boosted hadronically decaying heavy particles.

The electron energy calibration improvement in the ATLAS EM Calorimeter crack region is investigated in the second topic of the doctorate work. The ATLAS Tile Calorimeter E4 crack scintillators are used in the multivariate analysis based electron energy calibration procedure in order to correct energy losses in the passive material before and between Barrel and Endcape of the Electromagnetic Calorimeter. Improvements of about 10% to 50% are found in the energy resolution, depending on the electron pseudorapidity and transverse energy bins in the range $1.4 < |\eta| < 1.6$. In addition, possible improvement of the electron performance in the region $1.6 < |\eta| < 1.75$ is investigated using the simulated single electron sample with E4′ scinitllators implemented in the extension of E4 counters. The study shows that extending of TileCal gap/crack scintillators up to $|\eta| \sim 1.75$ would improve the electron energy resolution by about 30%, assuming that scintillators are radiation hard and well calibrated. These studies led to very important decisions in the Tile Calorimeter phase I upgrades of the tile crack counters as well as in the ATLAS e/γ performance group. In the long shutdown LS2, all the TileCal crack scintillators were replaced with new ones that have the extended pseudorapidity coverage up to $\eta \sim 1.72$, as motivated by the results obtained in this thesis. For the analysis with full LHC run 2 dataset, the ATLAS e/γ performance group used E4 crack scintillators as suggested in the thesis, leading to better electron/photon performance in the pseudorapidity region $1.4 < |\eta| < 1.6$ [1].

The last topic is devoted to the search for flavour-changing neutral-current (FCNC) top-quark decays $t \to qZ$ ($q = u, c$). The LHC proton–proton collisions data are used, collected by the ATLAS detector in 2012 at a center of mass energy of $\sqrt{s} = 8$ TeV and in 2015-2016 at $\sqrt{s} = 13$ TeV, corresponding to an integrated luminosity of 20.3 fb^{-1} and 36.1 fb^{-1}, respectively. The search is performed using the top-quark–top-antiquark pair production events, with one top

quark decaying through the $t \to qZ$ FCNC channel, and the other through the dominant Standard Model mode $t \to bW$. In the analysis with $\sqrt{s} = 8$ TeV data, the dilepton ($t\bar{t} \to bW(\to q\bar{q})qZ(\to \ell^+\ell^-)$) and trilepton ($t\bar{t} \to bW(\to \ell\nu)qZ(\to \ell^+\ell^-)$) channels are considered, resulting no evidence of $t \to qZ$ FCNC signal. A 95% CL upper limit on the $t \to qZ$ branching ratio is established at BR($t \to qZ$) $< 7 \times 10^{-4}$ using the trilepton channel, which is about 4 times stringent than the limit of BR($t \to qZ$) $< 2.9 \times 10^{-3}$ obtained in the dilepton channel.

The search using $\sqrt{s} = 13$ TeV data is performed in the trilepton ($t\bar{t} \to bW(\to \ell\nu)qZ(\to \ell^+\ell^-)$) channel. There is good agreement between the data and Standard Model expectations, and no evidence of a new physics signal is found. The 95% CL limits on the $t \to qZ$ branching ratio are set at BR($t \to uZ$) $< 1.7 \times 10^{-4}$ and BR($t \to cZ$) $< 2.4 \times 10^{-4}$, constituting the most stringent experimental limits to date of finishing of the dissertation work. These limits constrain the values of effective field theory operators contributing to the $t \to uZ$ and $t \to cZ$ FCNC decays of the top quark.

The sensitivity of the ATLAS experiment in the search for $t \to qZ$ FCNC decays is studied in the context of the high luminosity phase of the Large Hadron Collider with a center-of-mass energy of 14 TeV and an integrated luminosity of 3000 fb^{-1}. This study follows to the strategy of the analysis with $\sqrt{s} = 13$ TeV data and use particle-level simulated samples. Physics objects are smeared with the dedicated performance functions to emulate the HL-LHC run conditions and detector response. An improvement by a factor of four is expected over the current results with $\sqrt{s} = 13$ TeV data. The branching ratio limits that are obtained are at the level of 4 to 5 $\times 10^{-5}$ depending on the considered scenarios for the systematic uncertainties.

Bibliography

[1] ATLAS Collaboration, *Electron and photon energy calibration with the ATLAS detector using 2015–2016 LHC proton–proton collision data*, JINST **14** (2019) P03017, arXiv: 1812.03848 [hep-ex].

[2] ATLAS Collaboration, *Search for flavour-changing neutral current top-quark decays to qZ in pp collision data collected with the ATLAS detector at $\sqrt{s} = 8$ TeV*, Eur. Phys. J. C **76** (2016) p. 12, arXiv: 1508.05796 [hep-ex].

[3] ATLAS Collaboration, *Search for flavour-changing neutral current top-quark decays $t \to qZ$ in proton–proton collisions at $\sqrt{s} = 13$ TeV with the ATLAS detector*, JHEP **07** (2018) p. 176, arXiv: 1803.09923 [hep-ex].

[4] ATLAS Collaboration, *Sensitivity of searches for the flavour-changing neutral current decay $t \to qZ$ using the upgraded ATLAS experiment at the High Luminosity LHC*, ATL-PHYS-PUB-2019-001, 2019, url: https://cds.cern.ch/record/2653389.

[5] S. Glashow, *Partial Symmetries of Weak Interactions*, Nucl. Phys. **22** (1961) p. 579.

[6] A. Salam, *Weak and Electromagnetic Interactions*, Conf. Proc. **C680519** (1968) p. 367.

[7] A. Salam, *Gauge Unification of Fundamental Forces*, Rev. Mod. Phys. **52** (1980) p. 525.

[8] S. Weinberg, *A Model of Leptons*, Phys. Rev. Lett. **19** (1967) p. 1264.

[9] H. D. Politzer, *Reliable Perturbative Results for Strong Interactions?*, Rev. Lett. **30** (1973) p. 1346.

[10] ATLAS Collaboration, *Observation of a new particle in the search for the Standard Model Higgs boson with the ATLAS detector at the LHC*, Phys. Lett. B **716** (2012) p. 1, arXiv: 1207.7214 [hep-ex].

[11] CMS Collaboration, *Observation of a new boson at a mass of 125 GeV with the CMS experiment at the LHC*, Phys. Lett. B **716** (2012) p. 30, arXiv: 1207.7235 [hep-ex].

[12] G. Zweig, *An SU(3) model for strong interaction symmetry and its breaking. Version 2*, Developments in the Quark Theory of Hadrons, Volume 1. Edited by D. Lichtenberg and S. Rosen. (1964) p. 22.

[13] D. J. Gross and F. Wilczek, *Asymptotically Free Gauge Theories. I*, Phys. Rev. D **8** (1973) p. 3633.

[14] G. 't Hooft and M. J. G. Veltman, *Regularization and Renormalization of Gauge Fields*, Nucl. Phys. B **44** (1972) p. 189.

[15] P. W. Higgs, *Broken symmetries, massless particles and gauge fields*, Phys. Lett. **12** (1964) p. 132.

[16] P. W. Higgs, *Broken Symmetries and the Masses of Gauge Bosons*, Phys. Rev. Lett. **13** (1964) p. 508.

[17] G. S. Guralnik, C. R. Hagen, and T. W. B. Kibble, *Global Conservation Laws and Massless Particles*, Phys. Rev. Lett. **13** (1964) p. 585, [,162(1964)].

[18] F. Englert and R. Brout, *Broken Symmetry and the Mass of Gauge Vector Mesons*, Phys. Rev. Lett. **13** (1964) p. 321.

[19] N. Cabibbo, *Unitary Symmetry and Leptonic Decays*, Phys. Rev. Lett. **10** (1963) p. 531.

[20] M. Kobayashi and T. Maskawa, *CP Violation in the Renormalizable Theory of Weak Interaction*, Prog. Theor. Phys. **49** (1973) p. 652.

[21] M. Tanabashi et al., *Review of Particle Physics*, Phys. Rev. **D98** (2018) p. 030001.

[22] S. L. Glashow, J. Iliopoulos, and L. Maiani, *Weak Interactions with Lepton-Hadron Symmetry*, Phys. Rev. **D2** (1970) p. 1285.

[23] Super-Kamiokande Collaboration, *Determination of solar neutrino oscillation parameters using 1496 days of Super-Kamiokande I data*, Phys. Lett. B **539** (2002) p. 179, arXiv: hep-ex/0205075 [hep-ex].

[24] KamLAND Collaboration, *First results from KamLAND: Evidence for reactor anti-neutrino disappearance*, Phys. Rev. Lett. **90** (2003) p. 021802, arXiv: 0212021 [hep-ex].

[25] K2K Collaboration, *Indications of neutrino oscillation in a 250 km long baseline experiment*, Phys. Rev. Lett. **90** (2003) p. 041801, arXiv: 0212007 [hep-ex].

[26] SNO Collaboration, *Measurement of the total active B-8 solar neutrino flux at the Sudbury Neutrino Observatory with enhanced neutral current sensitivity*, Phys. Rev. Lett. **92** (2004) p. 181301, arXiv: nucl-ex/0309004 [nucl-ex].

[27] Planck Collaboration, *Planck 2015 results. I. Overview of products and scientific results*, Astron. Astrophys. **594** (2016) A1, arXiv: 1502.01582 [astro-ph.CO].

[28] J. Aguilar-Saavedra, *Effects of mixing with quark singlets*, Phys. Rev. D **67** (2003) p. 035003, arXiv: hep-ph/0210112 [hep-ph], Erratum: Phys. Rev. D **69** (2004) p. 099901.

[29] D. Atwood, L. Reina, and A. Soni,
Phenomenology of two Higgs doublet models with flavor changing neutral currents,
Phys. Rev. D **55** (1997) p. 3156, arXiv: hep-ph/9609279 [hep-ph].

[30] J. Cao et al., *SUSY-induced FCNC top-quark processes at the large hadron collider*,
Phys. Rev. D **75** (2007) p. 075021, arXiv: hep-ph/0702264 [hep-ph].

[31] J. M. Yang, B.-L. Young, and X. Zhang,
Flavor changing top quark decays in R-parity-violating SUSY,
Phys. Rev. D **58** (1998) p. 055001, arXiv: hep-ph/9705341 [hep-ph].

[32] K. Agashe, G. Perez, and A. Soni,
Collider Signals of Top Quark Flavor Violation from a Warped Extra Dimension,
Phys. Rev. D **75** (2007) p. 015002, arXiv: hep-ph/0606293 [hep-ph].

[33] P. Q. Hung et al., *Top Quark Rare Decays via Loop-Induced FCNC Interactions in Extended Mirror Fermion Model*, (2017), arXiv: 1709.01690 [hep-ph].

[34] CDF Collaboration, *Observation of top quark production in $p\bar{p}$ collisions*,
Rev. Lett. **74** (1995) p. 2626, arXiv: hep-ex/9503002 [hep-ex].

[35] D0 Collaboration, *Observation of top quark*, Rev. Lett. **74** (1995) p. 2632,
arXiv: hep-ex/9503003 [hep-ex].

[36] The ATLAS, CDF, CMS, D0 Collaborations,
First combination of Tevatron and LHC measurements of the top-quark mass, (2014),
arXiv: 1403.4427 [hep-ex].

[37] Top LHC WG, *Summary of the ATLAS and CMS direct m_{top} measurements*, 2019,
url: https://atlas.web.cern.ch/Atlas/GROUPS/PHYSICS/CombinedSummaryPlots/TOP/mtopSummary_TopLHC/mtopSummary_TopLHC.png.

[38] W. C. Carithers, *Top quark physics at hadron colliders*,
NATO Sci. Ser. B **351** (1995) p. 201.

[39] M. Czakon and A. Mitov,
Top++: a program for the calculation of the top-pair cross-section at hadron colliders,
Comput. Phys. Commun. **185** (2014) p. 2930, arXiv: 1112.5675 [hep-ph].

[40] M. Botje et al., *The PDF4LHC Working Group Interim Recommendations*, 2011,
arXiv: 1101.0538 [hep-ph].

[41] A. Martin et al., *Uncertainties on α_s in global PDF analyses and implications for predicted hadronic cross sections*, Eur. Phys. J. **C64** (2009) p. 653,
arXiv: 0905.3531 [hep-ph].

[42] J. Gao et al., *CT10 next-to-next-to-leading order global analysis of QCD*,
Phys. Rev. D **89** (2014) p. 033009, arXiv: 1302.6246 [hep-ph].

[43] R. D. Ball et al., *Parton distributions with LHC data*, Nucl. Phys. B **867** (2013) p. 244,
arXiv: 1207.1303 [hep-ph].

[44] Top LHC WG, *Summary of LHC and Tevatron measurements of the top-pair production cross-section as a function of the centre-of-mass energy*, 2018, url: https://atlas.web.cern.ch/Atlas/GROUPS/PHYSICS/CombinedSummaryPlots/TOP/tt_xsec_vsroots/tt_xsec_vsroots.png.

[45] Top LHC WG, *Summary of ATLAS and CMS measurements of the single top production cross-sections in various channels as a function of the center of mass energy*, 2018, url: https://atlas.web.cern.ch/Atlas/GROUPS/PHYSICS/CombinedSummaryPlots/TOP/singletop_allchanvsroots/singletop_allchanvsroots.png.

[46] J. Aguilar-Saavedra, *Top flavor-changing neutral interactions: Theoretical expectations and experimental detection*, Acta Phys. Polon. B **35** (2004) p. 2695, arXiv: hep-ph/0409342 [hep-ph].

[47] Snowmass Top Quark Working Group, K. Agashe, et al., *Working Group Report: Top Quark*, 2013, arXiv: 1311.2028 [hep-ph].

[48] ALEPH Collaboration, *Search for single top production in e^+e^- collisions at $\sqrt{s}$ up to 209 GeV*, Phys. Lett. B **543** (2002) p. 173, arXiv: hep-ex/0206070 [hep-ex].

[49] DELPHI Collaboration, *Search for single top production via FCNC at LEP at $\sqrt{s}$ = 189–208 GeV*, Phys. Lett. B **590** (2004) p. 21, arXiv: hep-ex/0404014 [hep-ex].

[50] OPAL Collaboration, *Search for single top quark production at LEP-2*, Phys. Lett. B **521** (2001) p. 181, arXiv: hep-ex/0110009 [hep-ex].

[51] L3 Collaboration, *Search for single top production at LEP*, Phys. Lett. B **549** (2002) p. 290, arXiv: hep-ex/0210041 [hep-ex].

[52] The LEP Exotica WG, *Search for single top production via flavour changing neutral currents: preliminary combined results of the LEP experiments*, LEP-Exotica-WG-2001-01, 2001, url: https://cds.cern.ch/record/1006392.

[53] ZEUS Collaboration, *Search for single-top production in ep collisions at HERA*, Phys. Lett. B **708** (2012) p. 27, arXiv: 1111.3901 [hep-ex].

[54] CDF Collaboration, *Search for the Flavor Changing Neutral Current Decay $t \to Zq$ in $p\bar{p}$ Collisions at $\sqrt{s} = 1.96$ TeV*, Phys. Rev. Lett. **101** (2008) p. 192002, arXiv: 0805.2109 [hep-ex].

[55] DØ Collaboration, *Search for flavor changing neutral currents in decays of top quarks*, Phys. Lett. B **701** (2011) p. 313, arXiv: 1103.4574 [hep-ex].

[56] ATLAS Collaboration, *A search for flavour changing neutral currents in top-quark decays in pp collision data collected with the ATLAS detector at $\sqrt{s} = 7$ TeV*, JHEP **09** (2012) p. 139, arXiv: 1206.0257 [hep-ex].

[57] CMS Collaboration, *Search for flavor-changing neutral currents in top-quark decays $t \to Zq$ in pp collisions at $\sqrt{s} = 8$ TeV*, Phys. Rev. Lett. **112** (2014) p. 171802, arXiv: 1312.4194 [hep-ex].

[58] CMS Collaboration, *Search for associated production of a Z boson with a single top quark and for tZ flavour-changing interactions in pp collisions at $\sqrt{s} = 8$ TeV*, JHEP **07** (2017) p. 003, arXiv: 1702.01404 [hep-ex].

[59] CMS Collaboration,
Search for flavour changing neutral currents in top quark production and decays with three-lepton final state using the data collected at $\sqrt{s} = 13$ TeV,
CMS-PAS-TOP-17-017 (2017).

[60] C. Zhang and S. Willenbrock,
Effective-field-theory approach to top-quark production and decay,
Phys. Rev. D **83** (3 2011) p. 034006,
url: https://link.aps.org/doi/10.1103/PhysRevD.83.034006.

[61] J. Aguilar-Saavedra, *A minimal set of top anomalous couplings*,
Nuclear Physics B **812** (2009) p. 181, issn: 0550-3213,
url: http://www.sciencedirect.com/science/article/pii/S0550321308007062.

[62] B. Galhardo, *Measurement of rare top quark decays in ATLAS/LHC*,
CERN-THESIS-2016-338 (2016).

[63] C. Degrande et al., *Automatic computations at next-to-leading order in QCD for top-quark flavor-changing neutral processes*, Phys. Rev. D **91** (2015) p. 034024,
arXiv: 1412.5594 [hep-ph].

[64] G. Durieux, F. Maltoni, and C. Zhang,
A global approach to top-quark flavor-changing interactions,
Phys. Rev. D **91** (2015) p. 074017, arXiv: 1412.7166 [hep-ph].

[65] L. Evans and P. Bryant, *LHC Machine*, JINST **3** (2008) S08001.

[66] *LEP design report*, Copies shelved as reports in LEP, PS and SPS libraries, CERN, 1984,
url: https://cds.cern.ch/record/102083.

[67] ATLAS Collaboration, *The ATLAS Experiment at the CERN Large Hadron Collider*,
JINST **3** (2008) S08003.

[68] CMS Collaboration, *The CMS experiment at the CERN LHC*, JINST **3** (2008) S08004.

[69] ALICE Collaboration, *The ALICE experiment at the CERN LHC*,
JINST **3** (2008) S08002.

[70] LHCb Collaboration, *The LHCb Detector at the LHC*, JINST **3** (2008) S08005.

[71] J. Haffner, *The CERN accelerator complex. Complexe des accélérateurs du CERN*,
(2013), General Photo, url: https://cds.cern.ch/record/1621894.

[72] ATLAS Collaboration, *ATLAS Luminosity Public Results*, 2019, url: https://twiki.cern.ch/twiki/bin/view/AtlasPublic/LuminosityPublicResults.

[73] ATLAS Collaboration, *ATLAS Luminosity Public Results Run2*, 2019, url: https://twiki.cern.ch/twiki/bin/view/AtlasPublic/LuminosityPublicResultsRun2.

[74] R. Bruce et al., *Reaching record-low β^* at the CERN Large Hadron Collider using a novel scheme of collimator settings and optics*, Nuclear Instruments and Methods in Physics Research Section A: Accelerators, Spectrometers, Detectors and Associated Equipment **848** (2017) p. 19, issn: 0168-9002, url: http://www.sciencedirect.com/science/article/pii/S0168900216313092.

[75] ATLAS Collaboration, *ATLAS Insertable B-Layer Technical Design Report*, ATLAS-TDR-19, 2010, url: https://cds.cern.ch/record/1291633, Addendum: ATLAS-TDR-19-ADD-1, 2012, url: https://cds.cern.ch/record/1451888.

[76] B. Abbott et al., *Production and integration of the ATLAS Insertable B-Layer*, JINST **13** (2018) T05008, arXiv: 1803.00844 [physics.ins-det].

[77] ATLAS Collaboration, *Performance of the ATLAS trigger system in 2015*, Eur. Phys. J. C **77** (2017) p. 317, arXiv: 1611.09661 [hep-ex].

[78] ATLAS Collaboration, "Letter of Intent for the Phase-II Upgrade of the ATLAS Experiment", tech. rep. CERN-LHCC-2012-022. LHCC-I-023, CERN, 2012, url: https://cds.cern.ch/record/1502664.

[79] ATLAS Collaboration, "ATLAS Phase-II Upgrade Scoping Document", tech. rep. CERN-LHCC-2015-020. LHCC-G-166, CERN, 2015, url: https://cds.cern.ch/record/2055248.

[80] D. London and J. L. Rosner, *Extra gauge bosons in E_6*, Phys. Rev. D **34** (5 1986) p. 1530, url: https://link.aps.org/doi/10.1103/PhysRevD.34.1530.

[81] A. Datta et al., *Effects of Kaluza-Klein excited W on single top quark production at the Tevatron*, Physics Letters B **483** (2000) p. 203, issn: 0370-2693, url: http://www.sciencedirect.com/science/article/pii/S0370269300005542.

[82] D. E. Kaplan and M. Schmaltz, *The Little Higgs from a simple group*, JHEP **10** (2003) p. 039, arXiv: hep-ph/0302049 [hep-ph].

[83] P. Langacker, *The physics of heavy Z' gauge bosons*, Rev. Mod. Phys. **81** (3 2009) p. 1199, url: https://link.aps.org/doi/10.1103/RevModPhys.81.1199.

[84] ATLAS Collaboration, *Performance of jet substructure techniques for large-R jets in proton-proton collisions at $\sqrt{s} = 7$ TeV using the ATLAS detector*, JHEP **2013** (2013) p. 76, issn: 1029-8479, url: https://doi.org/10.1007/JHEP09(2013)076.

[85] ATLAS Collaboration, *ATLAS tile calorimeter: Technical Design Report*, Technical Design Report ATLAS, CERN, 1996, url: https://cds.cern.ch/record/331062.

[86] ATLAS Collaboration, *Approved Tile Calorimeter Plots (Cosmics/Single beam, Calibrations, Testbeam, Upgrades)*, 2019, url: https://twiki.cern.ch/twiki/bin/view/AtlasPublic/ApprovedPlotsTile.

[87] ATLAS Collaboration, "Technical Design Report for the Phase-II Upgrade of the ATLAS Tile Calorimeter", tech. rep. CERN-LHCC-2017-019. ATLAS-TDR-028, CERN, 2017, url: https://cds.cern.ch/record/2285583.

[88] ATLAS Tile Collaboration, "Initial Design for the Phase-II Upgrade of the ATLAS Tile Calorimeter System", tech. rep. ATL-COM-TILECAL-2016-054, CERN, 2016, url: https://cds.cern.ch/record/2237711.

[89] ATLAS Collaboration, *The ATLAS Simulation Infrastructure*, Eur. Phys. J. C **70** (2010) p. 823, arXiv: 1005.4568 [physics.ins-det].

[90] W. Cleland and E. Stern, *Signal processing considerations for liquid ionization calorimeters in a high rate environment*, Nuclear Instruments and Methods in Physics Research Section A: Accelerators, Spectrometers, Detectors and Associated Equipment **338** (1994) p. 467, issn: 0168-9002, url: http://www.sciencedirect.com/science/article/pii/0168900294913323.

[91] ATLAS Collaboration, *Readiness of the ATLAS Tile Calorimeter for LHC collisions*, Eur. Phys. J. C **70** (2010) p. 1193, arXiv: 1007.5423 [hep-ex].

[92] ATLAS Collaboration, *Topological cell clustering in the ATLAS calorimeters and its performance in LHC Run 1*, Eur. Phys. J. C **77** (2017) p. 490, arXiv: 1603.02934 [hep-ex].

[93] T. Sjostrand, S. Mrenna, and P. Z. Skands, *A Brief Introduction to PYTHIA 8.1*, Comput. Phys. Commun. **178** (2008) p. 852, arXiv: 0710.3820 [hep-ph].

[94] ATLAS Collaboration, *ATLAS Pythia 8 tunes to 7 TeV data*, ATL-PHYS-PUB-2014-021, 2014, url: https://cds.cern.ch/record/1966419.

[95] S. Agostinelli et al., *GEANT4: A Simulation toolkit*, Nucl. Instrum. Meth. **A506** (2003) p. 250.

[96] ATLAS Collaboration,
Expected performance for an upgraded ATLAS detector at High-Luminosity LHC,
ATL-PHYS-PUB-2016-026, 2016, url: https://cds.cern.ch/record/2223839.

[97] ATLAS Collaboration, *Summary of ATLAS Pythia 8 tunes*, ATL-PHYS-PUB-2012-003, 2012, url: https://cds.cern.ch/record/1474107.

[98] A. D. Martin et al., *Parton distributions for the LHC*, Eur. Phys. J. **C63** (2009) p. 189, arXiv: 0901.0002 [hep-ph].

[99] M. Cacciari, G. P. Salam, and G. Soyez, *The anti-k_t jet clustering algorithm*, JHEP **04** (2008) p. 063, arXiv: 0802.1189 [hep-ph].

[100] ATLAS Collaboration, *Search for new phenomena in dijet mass and angular distributions from pp collisions at $\sqrt{s} = 13$ TeV with the ATLAS detector*, Phys. Lett. **B754** (2016) p. 302, arXiv: 1512.01530 [hep-ex].

[101] M. Cacciari, G. P. Salam, and G. Soyez, *FastJet user manual*, Eur. Phys. J. C **72** (2012) p. 1896, arXiv: 1111.6097 [hep-ph].

[102] D. Krohn, J. Thaler, and L.-T. Wang, *Jet Trimming*, JHEP **02** (2010) p. 084, arXiv: 0912.1342 [hep-ph].

[103] M. Cacciari and G. P. Salam, *Pileup subtraction using jet areas*, Phys. Lett. **B659** (2008) p. 119, arXiv: 0707.1378 [hep-ph].

[104] J. Thaler and K. Van Tilburg, *Identifying Boosted Objects with N-subjettiness*, JHEP **03** (2011) p. 015, arXiv: 1011.2268 [hep-ph].

[105] J. Thaler and K. Van Tilburg,
Maximizing Boosted Top Identification by Minimizing N-subjettiness,
JHEP **02** (2012) p. 093, arXiv: 1108.2701 [hep-ph].

[106] A. J. Larkoski, G. P. Salam, and J. Thaler,
Energy Correlation Functions for Jet Substructure, JHEP **06** (2013) p. 108,
arXiv: 1305.0007 [hep-ph].

[107] ATLAS Collaboration, *In situ calibration of large-radius jet energy and mass in 13 TeV proton–proton collisions with the ATLAS detector*, Eur. Phys. J. **C79** (2019) p. 135, arXiv: 1807.09477 [hep-ex].

[108] F. Zimmermann et al.,
"Future Circular Collider - European Strategy Update Documents",
tech. rep. CERN-ACC-2019-0006, CERN, 2019,
url: https://cds.cern.ch/record/2653676.

[109] ATLAS Collaboration, *Electron performance measurements with the ATLAS detector using the 2010 LHC proton-proton collision data*, Eur. Phys. J. **C72** (2012) p. 1909, arXiv: 1110.3174 [hep-ex].

[110] ATLAS Collaboration,
Expected Performance of the ATLAS Experiment - Detector, Trigger and Physics, (2009), arXiv: 0901.0512 [hep-ex].

[111] ATLAS Collaboration, *Electron and photon energy calibration with the ATLAS detector using LHC Run 1 data*, Eur. Phys. J. C **74** (2014) p. 3071, arXiv: 1407.5063 [hep-ex].

[112] ATLAS Collaboration,
Measurement of inclusive and differential cross sections in the $H \to ZZ^* \to 4l$ decay channel in pp collisions at $\sqrt{s} = 13$ TeV with the ATLAS detector,
JHEP **2017** (2017) p. 132, issn: 1029-8479,
url: https://doi.org/10.1007/JHEP10(2017)132.

[113] ATLAS Collaboration, *ATLAS liquid-argon calorimeter: Technical Design Report*, Technical Design Report ATLAS, CERN, 1996,
url: https://cds.cern.ch/record/331061.

[114] ATLAS Collaboration,
Readiness of the ATLAS liquid argon calorimeter for LHC collisions,
Eur. Phys. J. C **70** (2010) p. 723, arXiv: 0912.2642 [hep-ex].

[115] A. Hocker et al., *TMVA - Toolkit for Multivariate Data Analysis*, (2007), arXiv: physics/0703039 [physics.data-an].

[116] ATLAS Collaboration, *The ATLAS Simulation Infrastructure*, Eur. Phys. J. **C70** (2010) p. 823, issn: 1434-6052,
url: https://doi.org/10.1140/epjc/s10052-010-1429-9.

[117] J. A. Aguilar-Saavedra, *Protos - PROgram for TOp Simulations.*,
url: https://jaguilar.web.cern.ch/jaguilar/protos/.

[118] J. Aguilar-Saavedra, *Zt, γt and t production at hadron colliders via strong flavour-changing neutral couplings*, Nuclear Physics B **837** (2010) p. 122, issn: 0550-3213,
url: http://www.sciencedirect.com/science/article/pii/S0550321310002737.

[119] J. Pumplin et al.,
New generation of parton distributions with uncertainties from global QCD analysis,
JHEP **07** (2002) p. 012, arXiv: hep-ph/0201195 [hep-ph].

[120] S. M. T. Sjöstrand and P. Z. Skand, *PYTHIA 6.4 physics and manual*, JHEP **05** (2006) p. 026, arXiv: hep-ph/0603175 [hep-ph].

[121] P. Z. Skands, *Tuning Monte Carlo generators: The Perugia tunes*, Phys. Rev. D **82** (2010) p. 074018, arXiv: 1005.3457 [hep-ph].

[122] S. Jadach, J. H. Kuhn and Z. Was, *TAUOLA - a library of Monte Carlo programs to simulate decays of polarized τ leptons*,
Computer Physics Communications **64** (1991) p. 275, issn: 0010-4655,
url: http://www.sciencedirect.com/science/article/pii/001046559190038M.

[123] K. Nakamura and Particle Data Group 2010, *Review of Particle Physics*,
J. Phys. G: Nucl. Part. Phys. **37** (2010) p. 075021.

[124] M. L. Mangano et al.,
ALPGEN, a generator for hard multiparton processes in hadronic collisions,
JHEP **2003** (2003) p. 001,
url: https://doi.org/10.1088%2F1126-6708%2F2003%2F07%2F001.

[125] M. L. Mangano et al., *Multijet matrix elements and shower evolution in hadronic collisions: $Wb\bar{b}$+n-jets as a case study*, Nuclear Physics B **632** (2002) p. 343,
issn: 0550-3213,
url: http://www.sciencedirect.com/science/article/pii/S0550321302002493.

[126] S. Frixione and B. R. Webber,
Matching NLO QCD computations and parton shower simulations,
JHEP **0206** (2002) p. 029, arXiv: hep-ph/0204244 [hep-ph].

[127] H.-L. Lai et al., *New parton distributions for collider physics*,
Phys. Rev. D **82** (2010) p. 074024, arXiv: 1007.2241 [hep-ph].

[128] G. Corcella et al., *HERWIG 6.5 release note*, 2002, arXiv: hep-ph/0210213 [hep-ph].

[129] ATLAS collaboration, *New ATLAS event generator tunes to 2010 data*, (2011).

[130] T. G. et al., *Event generation with SHERPA 1.1*, JHEP **02** (2009) p. 007,
arXiv: 0811.4622 [hep-ph].

[131] J. Alwall et al., *MadGraph 5 : Going Beyond*, JHEP **1106** (2011) p. 128,
arXiv: 1106.0522 [hep-ph].

[132] S. Frixione, P. Nason, and C. Oleari, *Matching NLO QCD computations with Parton Shower simulations: the POWHEG method*, JHEP **0711** (2007) p. 070,
arXiv: 0709.2092 [hep-ph].

[133] S. Alioli et al., *A general framework for implementing NLO calculations in shower Monte Carlo programs: the POWHEG BOX*, JHEP **06** (2010) p. 043,
arXiv: 1002.2581 [hep-ph].

[134] ATLAS Collaboration, *Muon reconstruction efficiency and momentum resolution of the ATLAS experiment in proton–proton collisions at $\sqrt{s} = 7$ TeV in 2010*,
Eur. Phys. J. C **74** (2014) p. 3034, arXiv: 1404.4562 [hep-ex].

[135] K. Rehermann and B. Tweedie,
Efficient identification of boosted semileptonic top quarks at the LHC,
JHEP **2011** (2011) p. 59, issn: 1029-8479,
url: https://doi.org/10.1007/JHEP03(2011)059.

[136] ATLAS Collaboration, *Jet energy measurement and its systematic uncertainty in proton–proton collisions at $\sqrt{s} = 7$ TeV with the ATLAS detector*, Eur. Phys. J. C **75** (2015) p. 17, arXiv: 1406.0076 [hep-ex].

[137] ATLAS Collaboration, *Jet energy measurement with the ATLAS detector in proton–proton collisions at $\sqrt{s} = 7$ TeV*, Eur. Phys. J. C **73** (2013) p. 2304, arXiv: 1112.6426 [hep-ex].

[138] ATLAS Collaboration, *Commissioning of the ATLAS high performance b-tagging algorithms in the 7 TeV collision data*, ATLAS-CONF-2011-102, 2011, url: https://cds.cern.ch/record/1369219.

[139] ATLAS Collaboration, *Performance of missing transverse momentum reconstruction in proton–proton collisions at $\sqrt{s} = 7$ TeV with ATLAS*, Eur. Phys. J. C **72** (2012) p. 1844, arXiv: 1108.5602 [hep-ex].

[140] ATLAS Collaboration, *Performance of the ATLAS Electron and Photon Trigger in pp Collisions at $\sqrt{s} = 7$ TeV in 2011*, ATLAS-CONF-2012-048, 2012, url: https://cds.cern.ch/record/1450089.

[141] ATLAS Collaboration, *Performance of the ATLAS muon trigger in pp collisions at $\sqrt{s} = 8$ TeV*, Eur. Phys. J. C **75** (2015) p. 120, arXiv: 1408.3179 [hep-ex].

[142] A. D. Bukin, *Fitting function for asymmetric peaks*, 2007, arXiv: 0711.4449 [physics.data-an].

[143] ATLAS Collaboration, *Summary plots from the ATLAS Standard Model physics group*, 2018, url: https://atlas.web.cern.ch/Atlas/GROUPS/PHYSICS/CombinedSummaryPlots/SM/.

[144] ATLAS Collaboration, *Measurement of the top quark pair production cross-section with ATLAS in the single lepton channel*, Phys. Lett. B **711** (2012) p. 244, arXiv: 1201.1889 [hep-ex].

[145] J. M. Campbell and R. K. Ellis, *Update on vector boson pair production at hadron colliders*, Phys. Rev. D **60** (11 1999) p. 113006, url: https://link.aps.org/doi/10.1103/PhysRevD.60.113006.

[146] J. M. Campbell and R. K. Ellis, *$t\bar{t}W^{\pm}$ production and decay at NLO*, Journal of High Energy Physics **2012** (2012) p. 52, url: https://doi.org/10.1007/JHEP07(2012)052.

[147] M. V. Garzelli et al., *$t\bar{t}W^{\pm}$+$t\bar{t}Z$ hadroproduction at NLO accuracy in QCD with Parton Shower and Hadronization effects*, Journal of High Energy Physics **2012** (2012) p. 56, issn: 1029-8479, url: https://doi.org/10.1007/JHEP11(2012)056.

[148] J. Campbell, R. K. Ellis, and R. Röntsch,
Single top production in association with a Z boson at the LHC,
Phys. Rev. D **87** (11 2013) p. 114006,
url: https://link.aps.org/doi/10.1103/PhysRevD.87.114006.

[149] S. Heinemeyer et al., *Handbook of LHC Higgs Cross Sections: 3. Higgs Properties: Report of the LHC Higgs Cross Section Working Group*, ed. by S. Heinemeyer,
CERN Yellow Reports: Monographs,
Comments: 404 pages, 139 figures, to be submitted to CERN Report. Working Group web page: https://twiki.cern.ch/twiki/bin/view/LHCPhysics/CrossSections, 2013,
url: https://cds.cern.ch/record/1559921.

[150] ATLAS Collaboration,
Electron reconstruction and identification efficiency measurements with the ATLAS detector using the 2011 LHC proton–proton collision data,
Eur. Phys. J. C **74** (2014) p. 2941, arXiv: 1404.2240 [hep-ex].

[151] ATLAS Collaboration, *Measurement of the muon reconstruction performance of the ATLAS detector using 2011 and 2012 LHC proton–proton collision data*,
Eur. Phys. J. C **74** (2014) p. 3130, arXiv: 1407.3935 [hep-ex].

[152] ATLAS Collaboration, *Jet energy resolution in proton–proton collisions at $\sqrt{s} = 7$ TeV recorded in 2010 with the ATLAS detector*,
Eur. Phys. J. C **73** (2013) p. 2306, arXiv: 1210.6210 [hep-ex].

[153] ATLAS Collaboration, *Luminosity determination in pp collisions at $\sqrt{s} = 7$ TeV using the ATLAS detector at the LHC*, Eur. Phys. J. C **71** (2011) p. 1630,
arXiv: 1101.2185 [hep-ex].

[154] A. L. Read, *Presentation of search results: The CL_s technique*,
J. Phys. G **28** (2002) p. 2693.

[155] T. Junk, *Confidence level computation for combining searches with small statistics*,
Nucl. Instrum. Meth. A **434** (1999) p. 435, arXiv: hep-ex/9902006 [hep-ex].

[156] G. Cowan et al., *Asymptotic formulae for likelihood-based tests of new physics*,
Eur. Phys. J. C **71** (2011) p. 1554, arXiv: 1007.1727 [physics.data-an],
Erratum: Eur. Phys. J. C **73** (2013) p. 2501.

[157] L. Moneta et al., *The RooStats Project*, PoS **ACAT2010** (2010) p. 057,
arXiv: 1009.1003 [physics.data-an].

[158] D. J. Lange, *The EvtGen particle decay simulation package*,
Nucl. Instrum. Meth. **A462** (2001) p. 152.

[159] J. Alwall et al., *The automated computation of tree-level and next-to-leading order differential cross sections, and their matching to parton shower simulations*,
JHEP **07** (2014) p. 079, arXiv: 1405.0301 [hep-ph].

[160] T. Sjöstrand et al., *An Introduction to PYTHIA 8.2*, Comput. Phys. Commun. **191** (2015) p. 159, arXiv: 1410.3012 [hep-ph].

[161] R. D. Ball et al., *Parton distributions for the LHC Run II*, JHEP **04** (2015) p. 040, arXiv: 1410.8849 [hep-ph].

[162] D. de Florian et al., *Handbook of LHC Higgs Cross Sections: 4. Deciphering the Nature of the Higgs Sector*, (2016), arXiv: 1610.07922 [hep-ph].

[163] S. Höche et al., *QCD matrix elements + parton showers: The NLO case*, JHEP **04** (2013) p. 027, arXiv: 1207.5030 [hep-ph].

[164] S. Frixione et al., *Single-top hadroproduction in association with a W boson*, JHEP **07** (2008) p. 029, arXiv: 0805.3067 [hep-ph].

[165] T. Gleisberg and S. Hoeche, *Comix, a new matrix element generator*, JHEP **12** (2008) p. 039, arXiv: 0808.3674 [hep-ph].

[166] F. Cascioli, P. Maierhofer, and S. Pozzorini, *Scattering Amplitudes with Open Loops*, Phys. Rev. Lett. **108** (2012) p. 111601, arXiv: 1111.5206 [hep-ph].

[167] ATLAS Collaboration, *Measurement of the Z/γ^* boson transverse momentum distribution in pp collisions at $\sqrt{s} = 7$ TeV with the ATLAS detector*, JHEP **09** (2014) p. 145, arXiv: 1406.3660 [hep-ex].

[168] N. Davidson, T. Przedzinski, and Z. Was, *PHOTOS interface in C++: Technical and physics documentation*, Comput. Phys. Commun. **199** (2016) p. 86, arXiv: 1011.0937 [hep-ph].

[169] M. Bahr et al., *Herwig++ Physics and Manual*, Eur. Phys. J. **C58** (2008) p. 639, arXiv: 0803.0883 [hep-ph].

[170] J. Bellm et al., *Herwig 7.0/Herwig++ 3.0 release note*, Eur. Phys. J. **C76** (2016) p. 196, arXiv: 1512.01178 [hep-ph].

[171] S. Gieseke, C. Rohr, and A. Siodmok, *Colour reconnections in Herwig++*, Eur. Phys. J. **C72** (2012) p. 2225, arXiv: 1206.0041 [hep-ph].

[172] L. A. Harland-Lang et al., *Parton distributions in the LHC era: MMHT 2014 PDFs*, Eur. Phys. J. C **75** (2015) p. 204, arXiv: 1412.3989 [hep-ph].

[173] ATLAS Collaboration, *Electron reconstruction and identification in the ATLAS experiment using the 2015 and 2016 LHC proton–proton collision data at $\sqrt{s} = 13$ TeV*, Eur. Phys. J. (2019), arXiv: 1902.04655 [hep-ex].

[174] ATLAS Collaboration, *Muon reconstruction performance of the ATLAS detector in proton–proton collision data at $\sqrt{s} = 13$ TeV*, Eur. Phys. J. C **76** (2016) p. 292, arXiv: 1603.05598 [hep-ex].

[175] ATLAS Collaboration, *Jet energy scale measurements and their systematic uncertainties in proton–proton collisions at $\sqrt{s} = 13$ TeV with the ATLAS detector*, Phys. Rev. D **96** (2017) p. 072002, arXiv: 1703.09665 [hep-ex].

[176] ATLAS Collaboration, *Performance of pile-up mitigation techniques for jets in pp collisions at $\sqrt{s} = 8$ TeV using the ATLAS detector*, Eur. Phys. J. C **76** (2016) p. 581, arXiv: 1510.03823 [hep-ex].

[177] ATLAS Collaboration, *Performance of b-jet identification in the ATLAS experiment*, JINST **11** (2016) P04008, arXiv: 1512.01094 [hep-ex].

[178] ATLAS Collaboration, *Optimisation of the ATLAS b-tagging performance for the 2016 LHC Run*, ATL-PHYS-PUB-2016-012, 2016, url: https://cds.cern.ch/record/2160731.

[179] ATLAS Collaboration, *Performance of missing transverse momentum reconstruction with the ATLAS detector using proton–proton collisions at $\sqrt{s} = 13$ TeV*, Eur. Phys. J. C **78** (2018) p. 903, arXiv: 1802.08168 [hep-ex].

[180] ATLAS Collaboration, *Performance of the ATLAS Trigger System in 2015*, Eur. Phys. J. **C77** (2017) p. 317, arXiv: 1611.09661 [hep-ex].

[181] ATLAS Collaboration, *Trigger Menu in 2016*, ATL-DAQ-PUB-2017-001, 2017, url: https://cds.cern.ch/record/2242069.

[182] ATLAS Collaboration, *Luminosity determination in pp collisions at $\sqrt{s} = 8$ TeV using the ATLAS detector at the LHC*, Eur. Phys. J. C **76** (2016) p. 653, arXiv: 1608.03953 [hep-ex].

[183] ATLAS Collaboration, *Expected performance of the ATLAS b-tagging algorithms in Run-2*, ATL-PHYS-PUB-2015-022, 2015, url: https://cds.cern.ch/record/2037697.

[184] ATLAS Collaboration, *Measurement of the $W^{\pm}Z$ boson pair-production cross section in pp collisions at $\sqrt{s} = 13$ TeV with the ATLAS Detector*, Phys. Lett. B **762** (2016) p. 1, arXiv: 1606.04017 [hep-ex].

[185] S. Hoche et al., *NLO matrix elements and truncated showers*, JHEP **08** (2011) p. 123, arXiv: 1009.1127 [hep-ph].

[186] S. D. Ellis, R. Kleiss, and W. J. Stirling, *W's, Z's and Jets*, Phys. Lett. **154B** (1985) p. 435.

[187] F. A. Berends et al., *On the production of a W and jets at hadron colliders*, Nucl. Phys. **B357** (1991) p. 32.

[188] ATLAS Collaboration, *Measurement of the production cross-section of a single top quark in association with a Z boson in proton–proton collisions at 13 TeV with the ATLAS detector*, Phys. Lett. B **780** (2018) p. 557, arXiv: 1710.03659 [hep-ex].

[189] ATLAS Collaboration,
Measurement of the $t\bar{t}Z$ and $t\bar{t}W$ production cross sections in multilepton final states using $3.2\ fb^{-1}$ of pp collisions at $\sqrt{s} = 13$ TeV with the ATLAS detector,
Eur. Phys. J. C **77** (2017) p. 40, arXiv: 1609.01599 [hep-ex].

[190] ATLAS Collaboration, *Expected sensitivity of ATLAS to FCNC top quark decays $t \to Zq$ and $t \to Hq$ at the High Luminosity LHC*, ATL-PHYS-PUB-2016-019, 2016, url: https://cds.cern.ch/record/2209126.

[191] M. Cacciari et al., *Top-pair production at hadron colliders with next-to-next-to-leading logarithmic soft-gluon resummation*,
Phys. Lett. B **710** (2012) p. 612, arXiv: 1111.5869 [hep-ph].

[192] P. Baernreuther, M. Czakon, and A. Mitov, *Percent Level Precision Physics at the Tevatron: First Genuine NNLO QCD Corrections to $q\bar{q} \to t\bar{t} + X$*,
Phys. Rev. Lett. **109** (2012) p. 132001, arXiv: 1204.5201 [hep-ph].

[193] M. Czakon and A. Mitov, *NNLO corrections to top-pair production at hadron colliders: the all-fermionic scattering channels*, JHEP **12** (2012) p. 054,
arXiv: 1207.0236 [hep-ph].

[194] M. Czakon and A. Mitov, *NNLO corrections to top pair production at hadron colliders: the quark-gluon reaction*, JHEP **01** (2013) p. 080, arXiv: 1210.6832 [hep-ph].

[195] M. Czakon, P. Fiedler, and A. Mitov,
Total Top-Quark Pair-Production Cross Section at Hadron Colliders Through $O(\alpha_S^4)$,
Phys. Rev. Lett. **110** (2013) p. 252004, arXiv: 1303.6254 [hep-ph].

[196] ATLAS Collaboration,
Technical Design Report for the Phase-II Upgrade of the ATLAS TDAQ System,
ATLAS-TDR-029, url: https://cds.cern.ch/record/2285584.

[197] M. Dobbs and J. B. Hanse,
The HepMC C++ Monte Carlo event record for High Energy Physics,
Comput. Phys. Commun. **134** (2001) p. 41.

[198] M. Dobbs et al., *HepMC 2 a C++ Event Record for Monte Carlo Generators*,
User Manual Version 2.06, 2010, url:
http://lcgapp.cern.ch/project/simu/HepMC/206/HepMC2_user_manual.pdf.

[199] ATLAS Collaboration, *Measurements of b-jet tagging efficiency with the ATLAS detector using $t\bar{t}$ events at $\sqrt{s} = 13$ TeV*, JHEP **08** (2018) p. 089,
arXiv: 1805.01845 [hep-ex].

[200] M. N. Simone Pagan Griso,
Perspectives on the determination of systematic uncertainties at HL-LHC,
Workshop on the physics of HL-LHC, and perspectives at HE-LHC, 2018,
url: https://indico.cern.ch/event/686494/contributions/2984660/attachments/1670486/2679630/HLLHC-Systematics.pdf.

[201] A. Amorim et al., *Production of $t\gamma$, tZ and tH via Flavour Changing Neutral Currents*, 2015, arXiv: 1511.09432v1 [hep-ph].

Appendix A.

Modified topo-cluster splitting scheme in the nominal TileCal geometry

In the simulation setup with modified TileCal geometry A-layer cells are allowed to split a cluster if the local maxima is found in these cells. The same cluster splitting algorithm is implemented in the nominal geometry and the effect of this modification is studied. The calibration at hadronic scale using the local cell signal weighting (LCW) method [92], derived for the nominal geometry, might not be optimal for the modified cluster splitting algorithm, so that the results for the large-radius jets are obtained at both EM- and LCW-scales. No further calibration is applied on the jets.

The comparison of the number of jet constituents between nominal and modified clustering algorithms, presented in Figures A.1 and A.2, shows similar shapes in both cases with a slight shift towards higher number of jet constituents for the modified clustering, since it allows for more topo-clusters to be reconstructed. The average number of jet constituents as a function of the truth jet p_{T} depicted in Figure A.3, displays about 5% higher average number of jet constituents for the jet p_{T} smaller that around 1.5 TeVand the same average number of jet constituents for the higher p_{T} values.

The distributions of the calorimeter jet mass response are presented in Figures A.4 and A.5. The study of the average calorimeter jet mass response as a function of the truth jet mass in bins of the truth p_{T} is presented in Figures A.6 and A.7 for the W/Z-jets at the LCW- and EM-scale, respectively. The average jet mass response is not at one, since the jet mass is not calibrated in this study. As expected, the EM-scale jets demonstrate lower jet mass response compared to the LCW-jets.

The average jet mass responses are nearly equal for both cluster splitting configurations in the $p_{\mathrm{T}} < 800$ GeV range. With increasing p_{T} the modified cluster splitting scheme provides a somewhat lower jet mass response in the low jet mass region. This difference increases up to 30% as p_{T} grows. The dependence of the average jet mass response on the truth p_{T} is depicted in Figure A.8.

The fractional mass resolution as a function of the truth jet transverse momentum is presented in Figure A.9. Both cluster splitting schemes show similar performance, although the modified splitting algorithm has somewhat worse resolution in the $0.8 < p_{\mathrm{T}} < 1.8$ TeV range.

In conclusion, modification of the topo-cluster splitting scheme in the TileCal first layer for the nominal TileCal geometry leads to a larger number of jet constituents and slightly narrows the large-radius jet mass resolution in the low-p_{T} range. This suggests that modified cluster splitting might improve jet performance even in the nominal TileCal geometry. The LCW-calibration for topo-clusters as well as dedicated jet energy scale and jet mass scale calibrations for all four possible configuration would be required to fully separate and quantify the impact of the higher TileCal granularity and the topo-cluster splitting scheme modification on the jet performance. However, studies of this kind go beyond the scope of the current note.

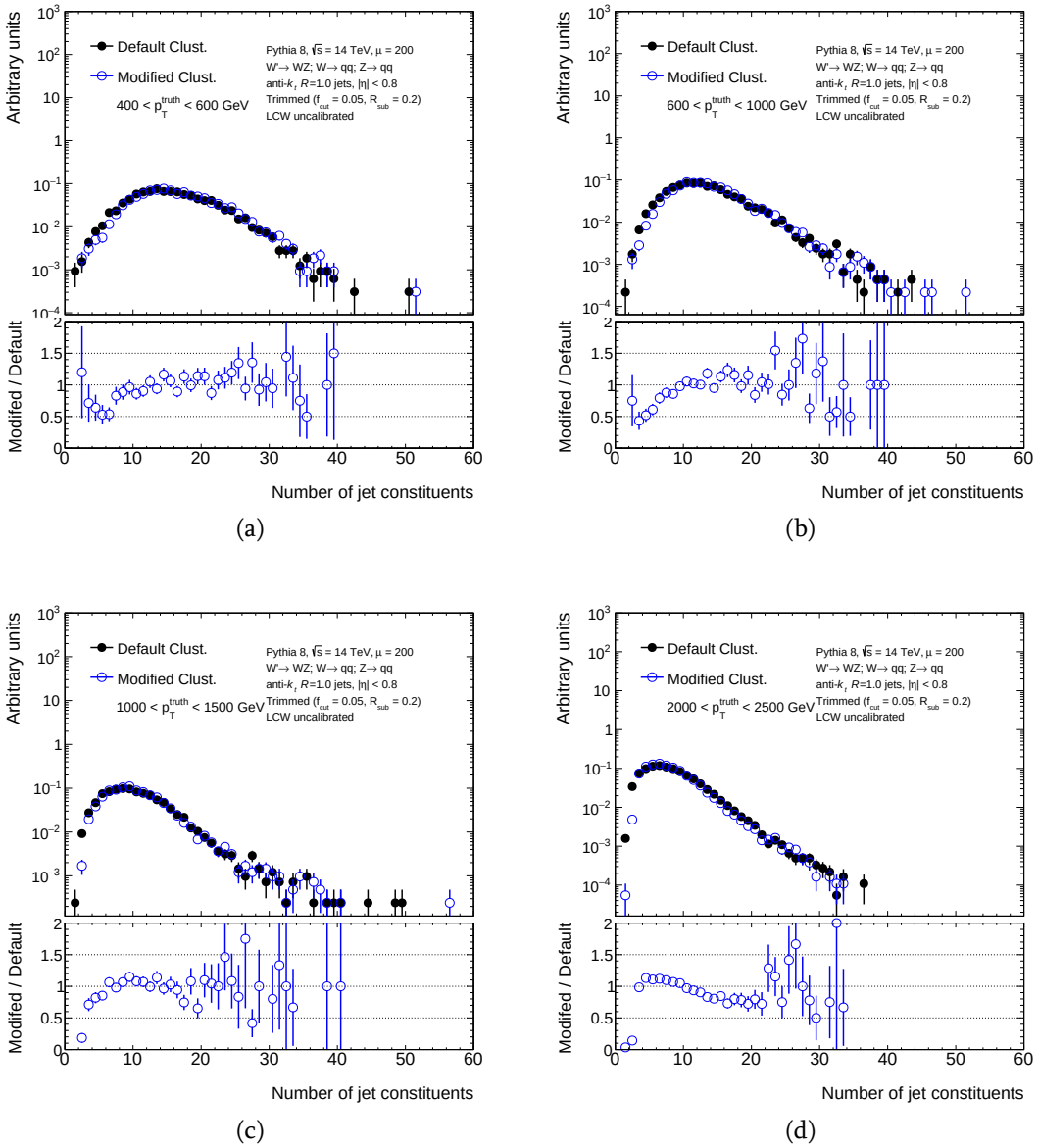

Figure A.1.: Distribution of the number of W/Z-jets constituents in the nominal TileCal geometry with default (black closed circles) and modified (blue open circles) cluster splitting algorithms. Jets are in the $|\eta| < 0.8$ region, with the truth-level p_{T} in the (a) [400,600] GeV, (b) [600, 1000] GeV, (c) [1000, 1500] GeVand (d) [2000, 2500] GeVrange. Jets are at LCW scale.

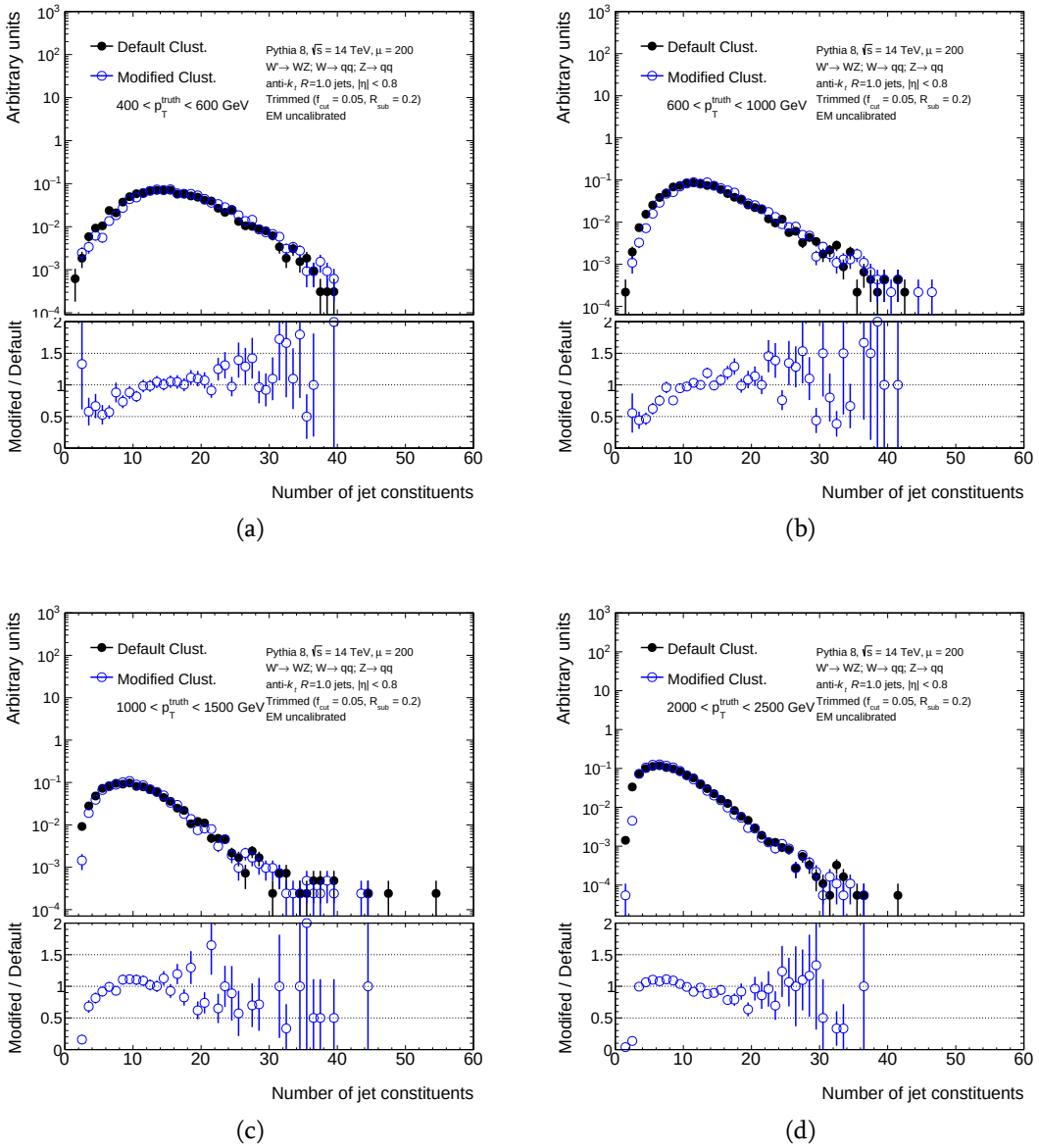

Figure A.2.: Distribution of the number of W/Z-jets constituents in the nominal TileCal geometry with default (black closed circles) and modified (blue open circles) cluster splitting algorithms. Jets are in the $|\eta| < 0.8$ region, with the truth-level p_{T} in the (a) [400,600] GeV, (b) [600, 1000] GeV, (c) [1000, 1500] GeVand (d) [2000, 2500] GeVrange. Jets are at EM scale.

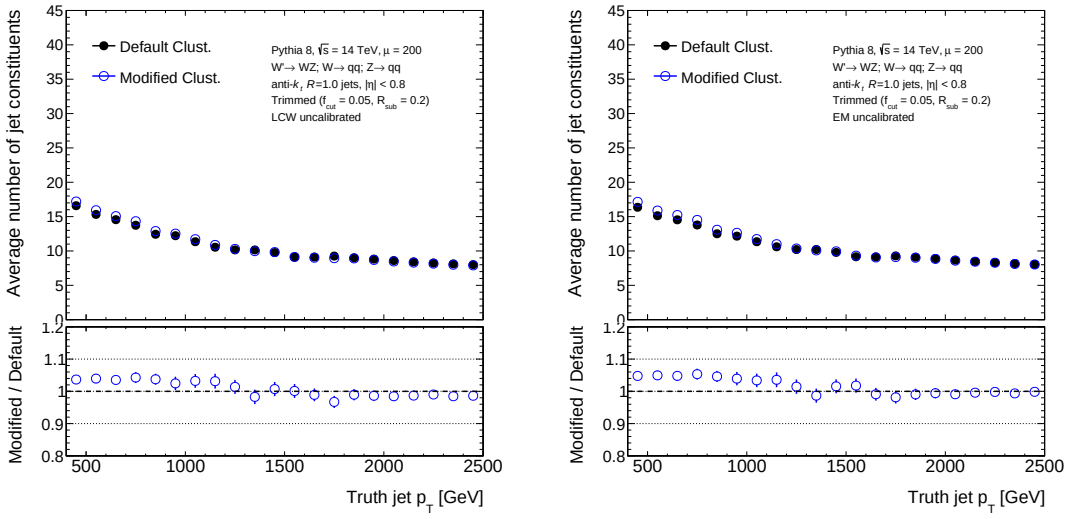

Figure A.3.: Average number of W/Z-jet constituents as a function of the truth-level jet p_{T} in the nominal TileCal geometry with default (black closed circles) and modified (blue open circles) cluster splitting algorithms. Jets are in the $|\eta| < 0.8$ region. Jets are at (a) LCW and (b) EM scale.

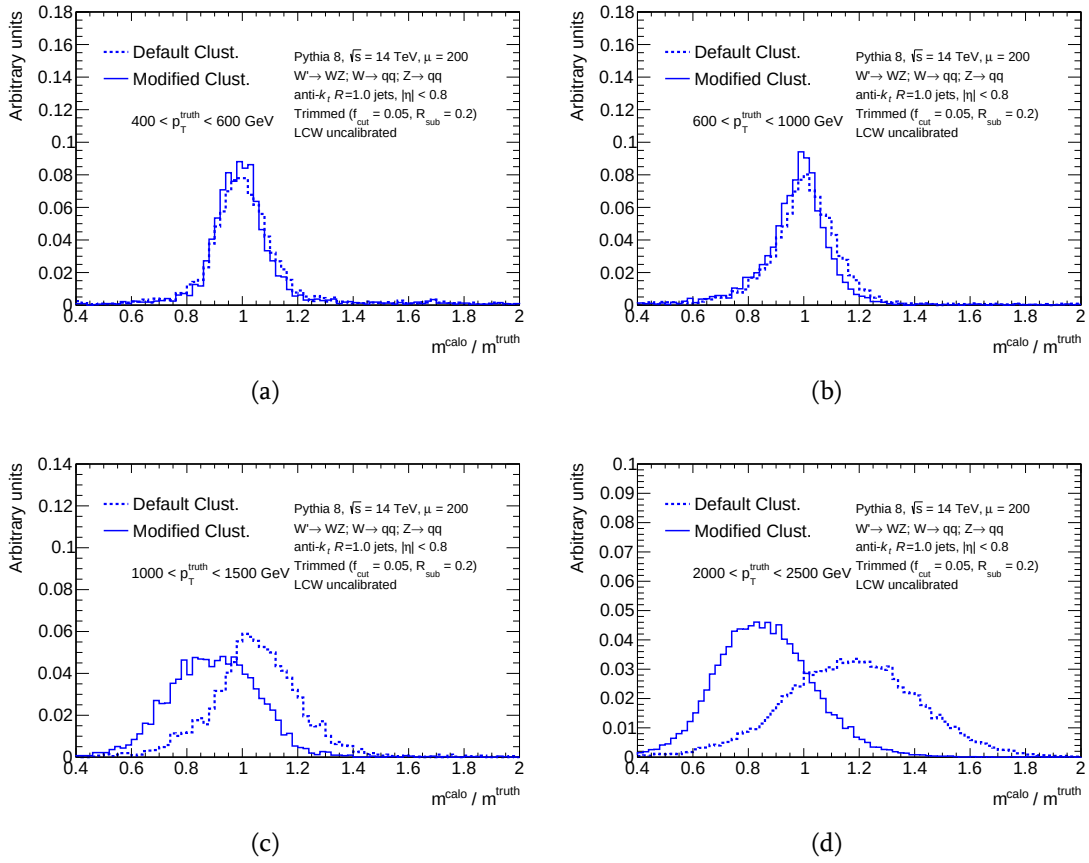

Figure A.4.: Distributions of the calorimeter W/Z- jet mass response in the nominal TileCal geometry with default (dashed line) and modified (solid line) cluster splitting algorithms. Jets are in the $|\eta| < 0.8$ region, with the truth-level p_{T} in the (a) [400,600] GeV, (b) [600, 1000] GeV, (c) [1000, 1500] GeV and (d) [2000, 2500] GeV range. Jets are at LCW scale.

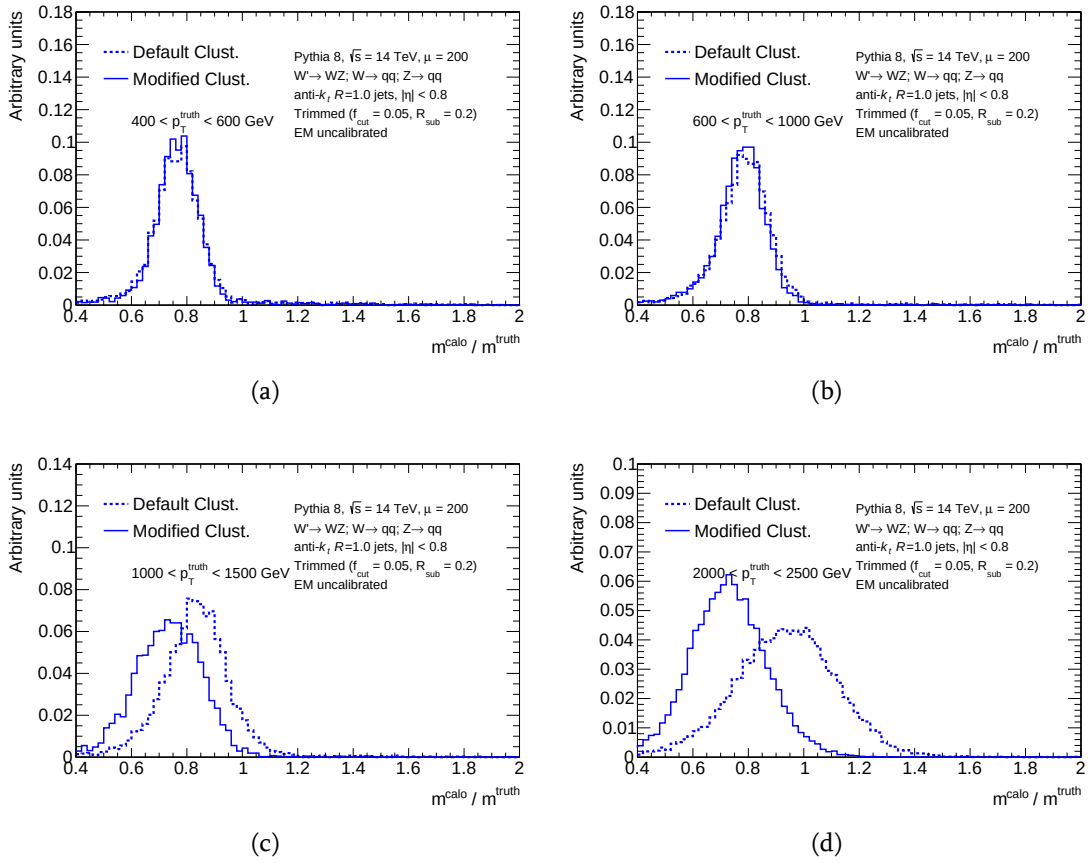

Figure A.5.: Distributions of the calorimeter W/Z-jet mass response in the nominal TileCal geometry with default (dashed line) and modified (solid line) cluster splitting algorithms. Jets are in the $|\eta| < 0.8$ region, with the truth-level p_{T} in the (a) [400,600] GeV, (b) [600, 1000] GeV, (c) [1000, 1500] GeV and (d) [2000, 2500] GeV range. Jets are at EM scale.

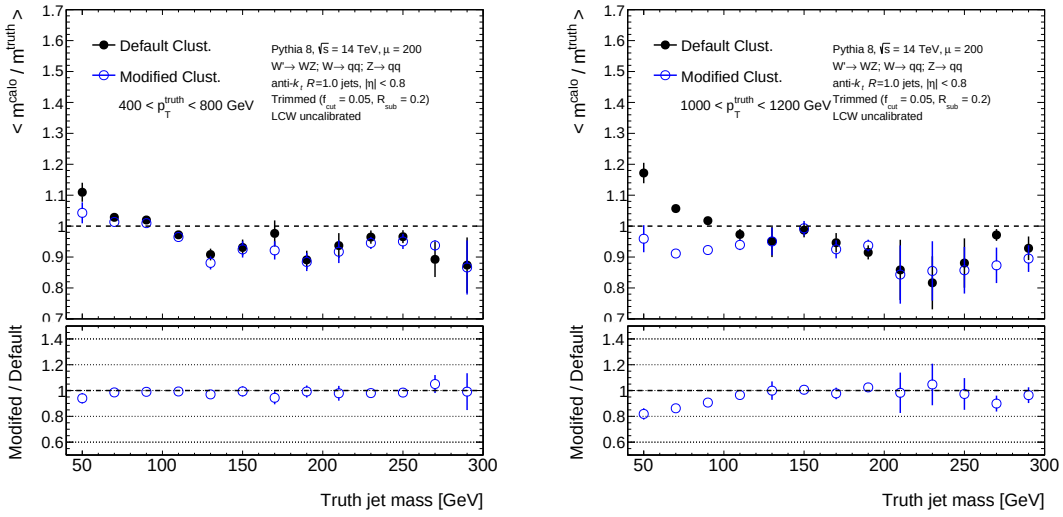

Figure A.6.: Average calorimeter W/Z-jet mass response (m^{calo}/m^{truth}) as a function of the truth jet mass in the nominal TileCal geometry with default (black closed circles) and modified (blue open circles) cluster splitting algorithms. Jets are in the $|\eta| < 0.8$ region, with the truth-level p_{T} in the (a) [400,600] GeV, (b) [600, 1000] GeV, (c) [1000, 1500] GeV and (d) [2000, 2500] GeV range. Jets are at LCW scale.

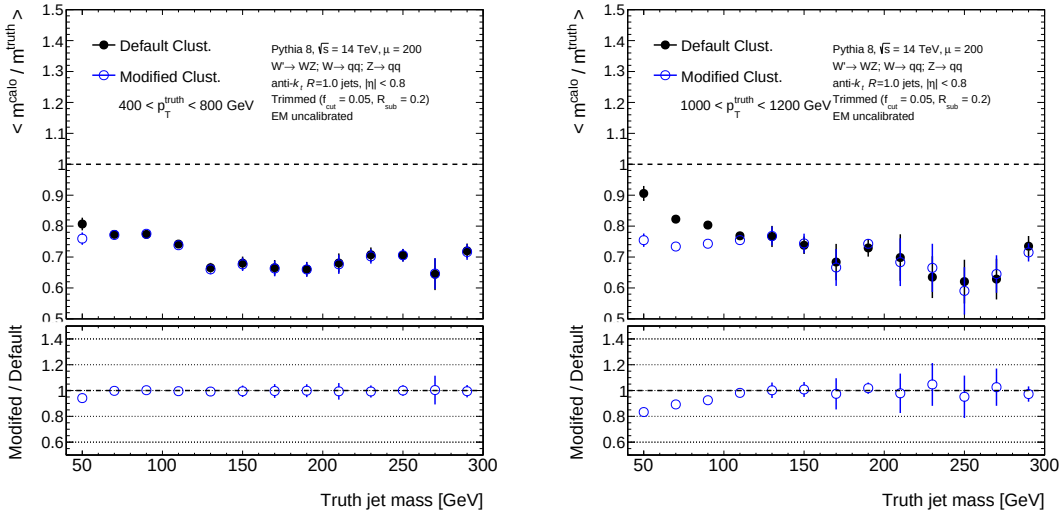

Figure A.7.: Average calorimeter W/Z-jet mass response (m^{calo}/m^{truth}) as a function of the truth jet mass in the nominal TileCal geometry with default (black closed circles) and modified (blue open circles) cluster splitting algorithms. Jets are in the $|\eta| < 0.8$ region, with the truth-level p_{T} in the (a) [400,600] GeV, (b) [600, 1000] GeV, (c) [1000, 1500] GeV and (d) [2000, 2500] GeV range. Jets are at EM scale.

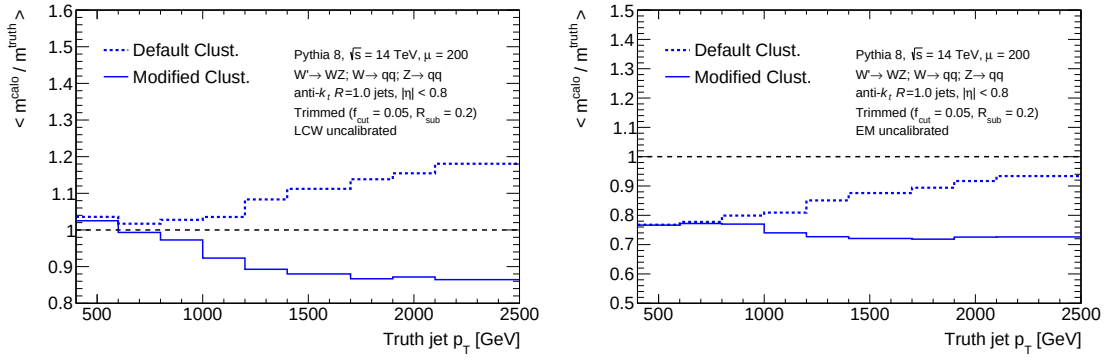

(a) (b)

Figure A.8.: Average calorimeter W/Z-jet mass response (m^{calo}/m^{truth}) as a function of the truth-jet p_{T} in the nominal TileCal geometry with default (dashed line) and modified (solid line) cluster splitting algorithms. Jets are in the $|\eta| < 0.8$ region. Jets are at (a) LCW and (b) EM scale.

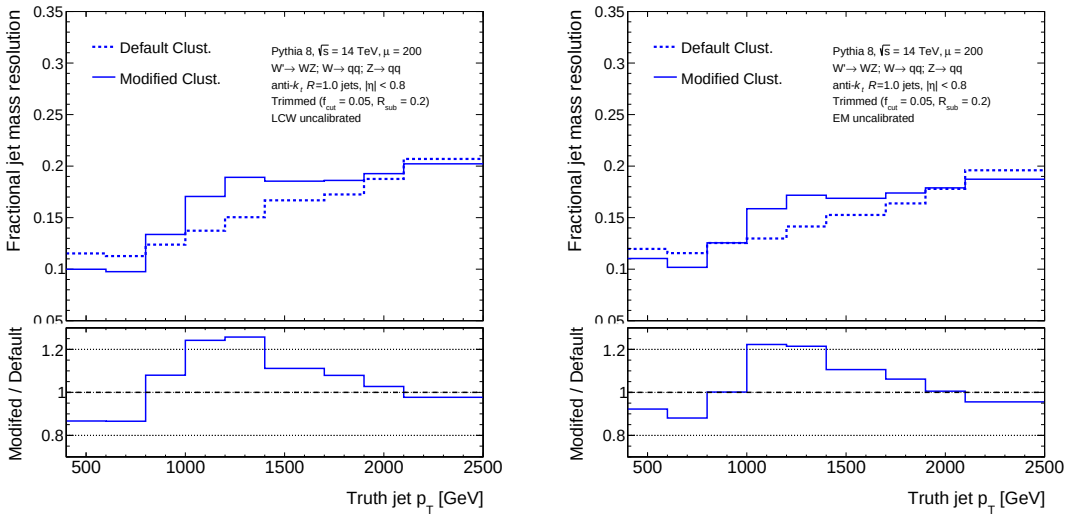

(a) (b)

Figure A.9.: The fractional calorimeter W/Z-jet mass resolution as a function of the truth jet p_{T} in the nominal TileCal geometry with default (dashed line) and modified (solid line) cluster splitting algorithms. Jets are in the $|\eta| < 0.8$ region. The half of the 68% interquantile range divided by the median of the jet mass response is used as an outlier insensitive measure of the resolution. Jets are at (a) LCW and (b) EM scale.

Appendix B.

Mass resolution

The signal events are reconstructed using a χ^2 minimization as it is described in Section 6.3.2. The central value for the masses and the widths in the χ^2 expression are taken from a Bukin fit[1] [142] to the reconstructed masses from the objects with the minimum ΔR in relation to the actual particles generated by MG5 in the signal samples. The missing transverse momentum is assumed to be the neutrino transverse momentum, while the longitudinal momentum of the neutrino is set to the p_z of the true generated particle. These represent the optimal resolution of the reconstructed top-quarks and W boson masses. These fits are shown in Figure B.1 along with the mean values and standard deviations.

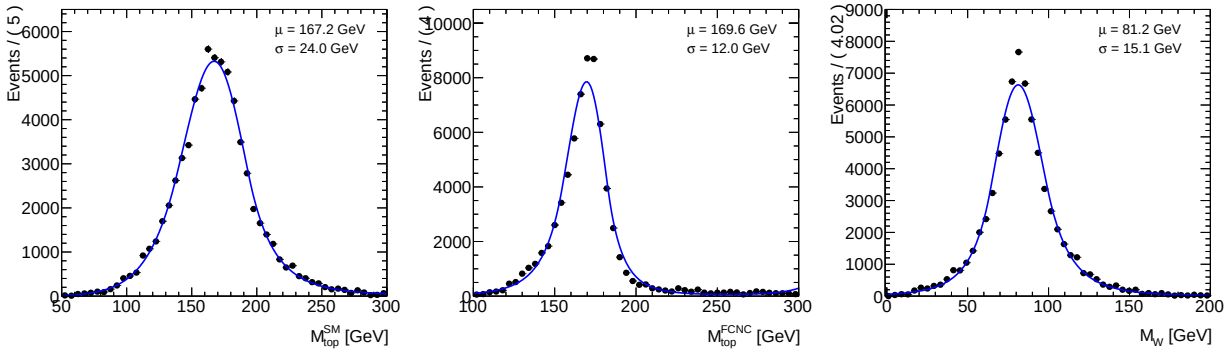

(a) (b) (c)

Figure B.1.: Reconstructed masses of the a) top-quark coming from the SM decay, b) the top-quark coming from the FCNC decay and c) the W boson from the object with the minimum ΔR in relation to the true particle generated by MG5.

In order to investigate why the fitted mean value of the SM top-quark is shifted from the reference value, the following selection is applied: to improve the truth matching efficiency of the jets events are required to have exactly 2 jets and truth light quark $p_{\mathrm{T}} > 50$ GeV. Then SM

[1] This is a piecewise function with a gaussian function in the center and two asymmetric tails.

top-quark mass is reconstructed using the object that are closest to the corresponding truth particles, except neutrino. Transverse component of neutrino momentum is reconstructed from $E_{\mathrm{T}}^{\mathrm{miss}}$, while longitudinal component is set to the p_z of the truth neutrino. The result is presented in Figure B.2(a) and shows that the mean value is still shifted from the reference value, while Figure B.2(b) shows the option when both components of the neutrino momentum are taken from the truth neutrino. In this option fitted mean value is closer to the reference values. These results allow us to conclude that the shift of the fitted mean value of the SM top-quark is due to the neutrino, which is reconstructed using the $E_{\mathrm{T}}^{\mathrm{miss}}$.

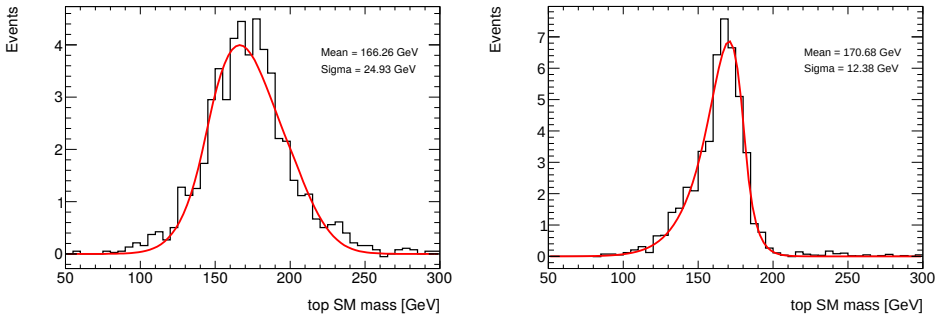

(a) (b)

Figure B.2.: Reconstructed masses of the top-quark coming from the SM decay, from the object with the minimum ΔR in relation to the true particle generated by MG5. Exactly 2 jets are required, truth light quark is required to have $p_{\mathrm{T}} > 50$ GeV, a) transverse component of neutrino momentum is reconstructed from $E_{\mathrm{T}}^{\mathrm{miss}}$, while longitudinal component is set to the p_z of the truth neutrino; b) both components of the neutrino momentum are taken from the truth neutrino.

Appendix C.

Z+jets and $t\bar{t}$ MC events categorization

For the determination of the Fake Scale Factors (see Section 6.6), the Z+jets and $t\bar{t}$ MC events with three reconstructed leptons are categorized into the following four categories:

- Electron fakes in $t\bar{t}$ events — e-fakes ($t\bar{t}$)
- Electron fakes in Z+jets events — e-fakes (Zjets)
- Muon fakes in $t\bar{t}$ events — μ-fakes ($t\bar{t}$)
- Muon fakes in Z+jets events — μ-fakes (Zjets)

The categorization is done based on the lepton truth information. A scale factor is extracted for each of these categories from the corresponding four control regions (see Section 6.6). The Figure C.1 shows the number of fake-leptons in the Z+jets and $t\bar{t}$ MC events in each FSF control region determined based on the lepton truth information. During the categorization, if the event contains both, electron and muon fake, then this event is assigned to the category which is under consideration in the given control region.

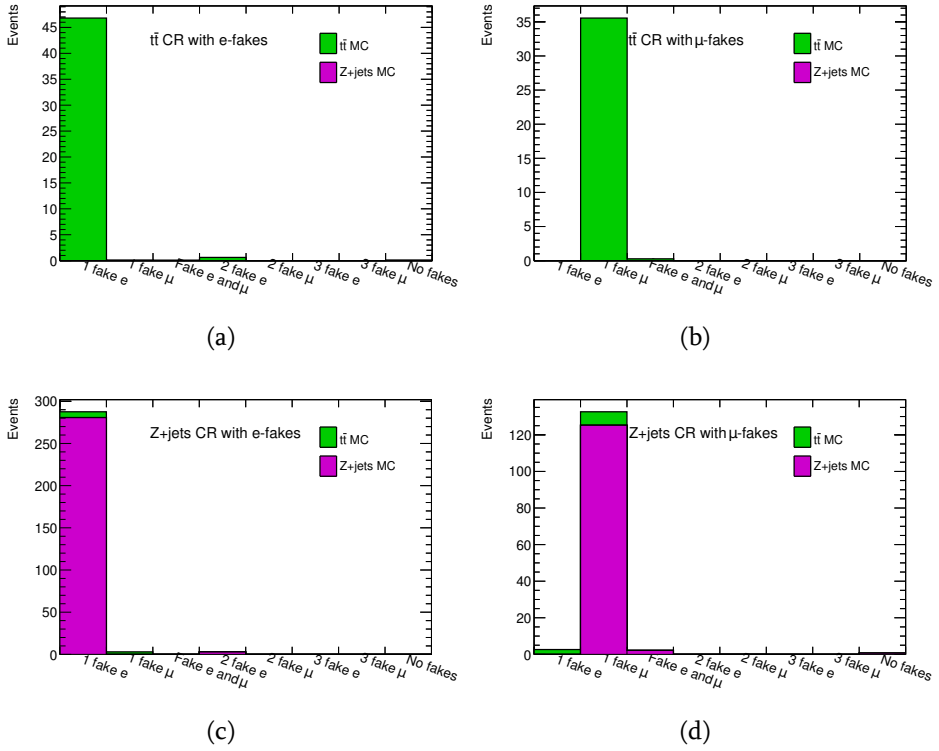

Figure C.1.: The number of fake-leptons in the Z+jets and $t\bar{t}$ MC events in the a) $t\bar{t}$ CR with e-fakes, b) $t\bar{t}$ CR with μ-fakes, c) Z+jets CR with e-fakes and d) Z+jets CR with μ-fakes.

Appendix D.

Systematics plots

D.0.1. Uncertainties with large pull/constrain

In Figures D.1 and D.2 the nominal background and the background obtained with the $t\bar{t}$ NLO generator and $t\bar{t}$ Parton Showering variation are compared to the data for the fakes control regions and signal region. The shape smoothing is not applied on the background variation histograms. In the fakes control region with one b-tag events we see that the background with $t\bar{t}$ NLO generator variation gives better agreement with the data in the first bin, while the nominal background shows a large discrepancy. Since in the other bins the nominal background and $t\bar{t}$ NLO generator variation show small difference, the fit is able to introduce a large pull on the $t\bar{t}$ NLO generator NP to improve Data/Bkg agreement in the first bin of the histogram in the fakes control region with one b-tag events. This is what we observe in Figures 6.33 and 6.37. In case of the $t\bar{t}$ Parton Showering variation we see that the background shape does not change significantly, but it has a significant effect on the normalization in the fakes control region with one b-tag events. Due to this normalization effect, fit introduces a large constrain on the corresponding NP. In Figure D.3 the nominal background and the background obtained with the alternative generator for WZ are compared to the data for WZ control and signal regions. We can see that the alternative generator for WZ does not change the background shape significantly, though it has a significant effect on the normalization. Since the nominal background yield is closer to the data in the WZ control region, which is high statistics region, data has enough statistical power to constrain this uncertainty by the fit. This is what we observe in Figure 6.33. In Figures D.4 and D.5 the nominal background and the background obtained with the pileup up and down variation are compared to the data for the background control and signal regions. Since the pileup uncertainty is applied on each background sample the data can easily introduce the pull on the corresponding NP by the fit.

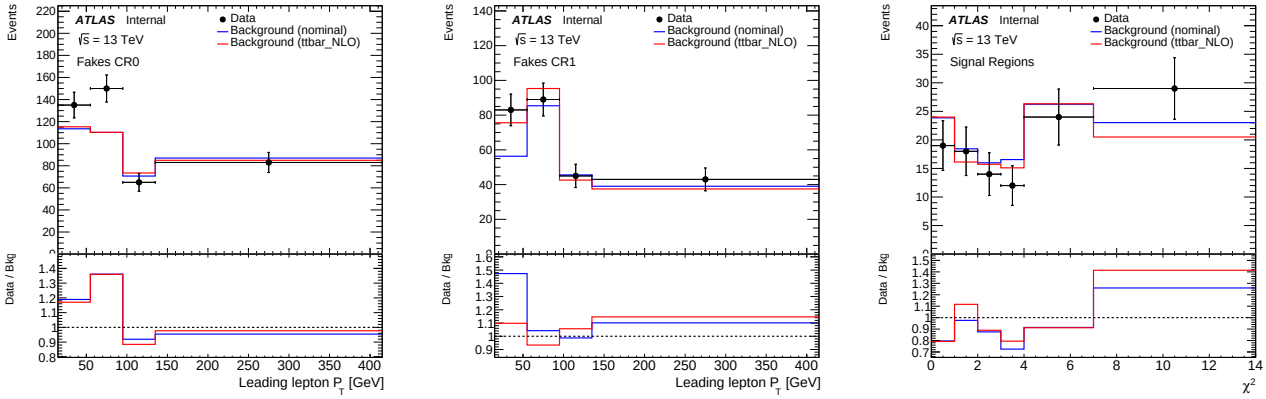

(a) (b) (c)

Figure D.1.: The expected and observed distributions of the leading lepton p_{T} in the a) fakes CR with b-veto events, b) fakes CR with one b-tag events and c) χ^2 variable in the signal region. The blue line is the nominal background and red line is the background with the $t\bar{t}$ Parton Showering variation, while black dots are data.

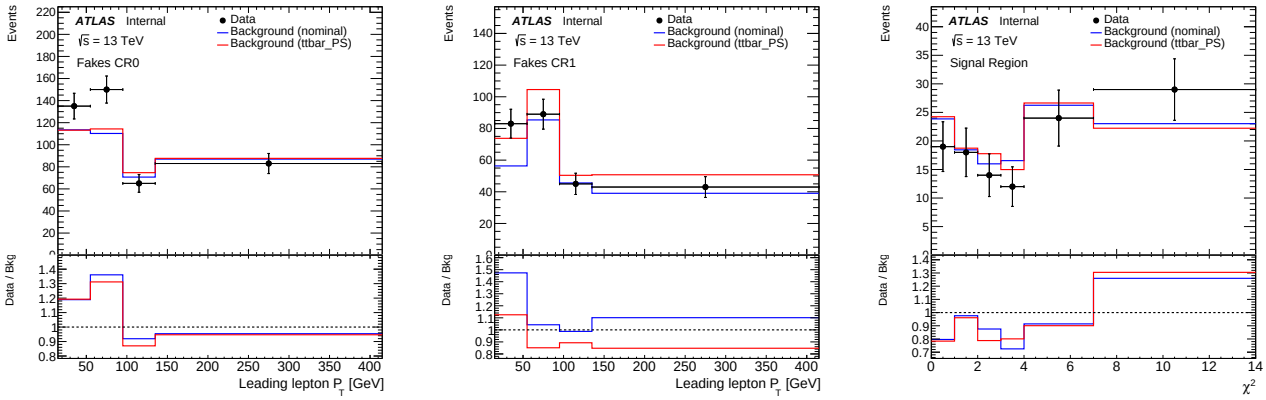

(a) (b) (c)

Figure D.2.: The expected and observed distributions of the leading lepton p_{T} in the a) fakes CR with b-veto events, b) fakes CR with one b-tag events and c) χ^2 variable in the signal region. The blue line is the nominal background and red line is the background with the $t\bar{t}$ NLO generator variation, while black dots are data.

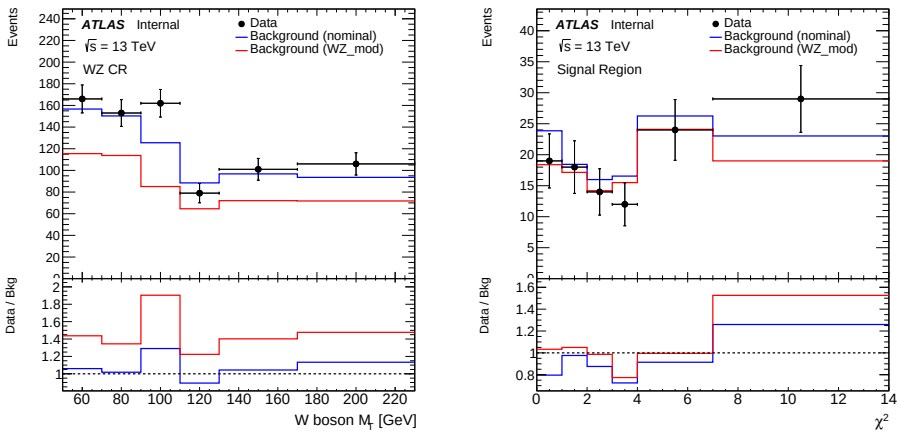

(a) (b)

Figure D.3.: The expected and observed distributions of a) the W boson transverse mass in the WZ CR and b) the χ^2 variable in the signal region. The blue line is the nominal background and red line is the background with the alternative generator for WZ background, while black dots are data.

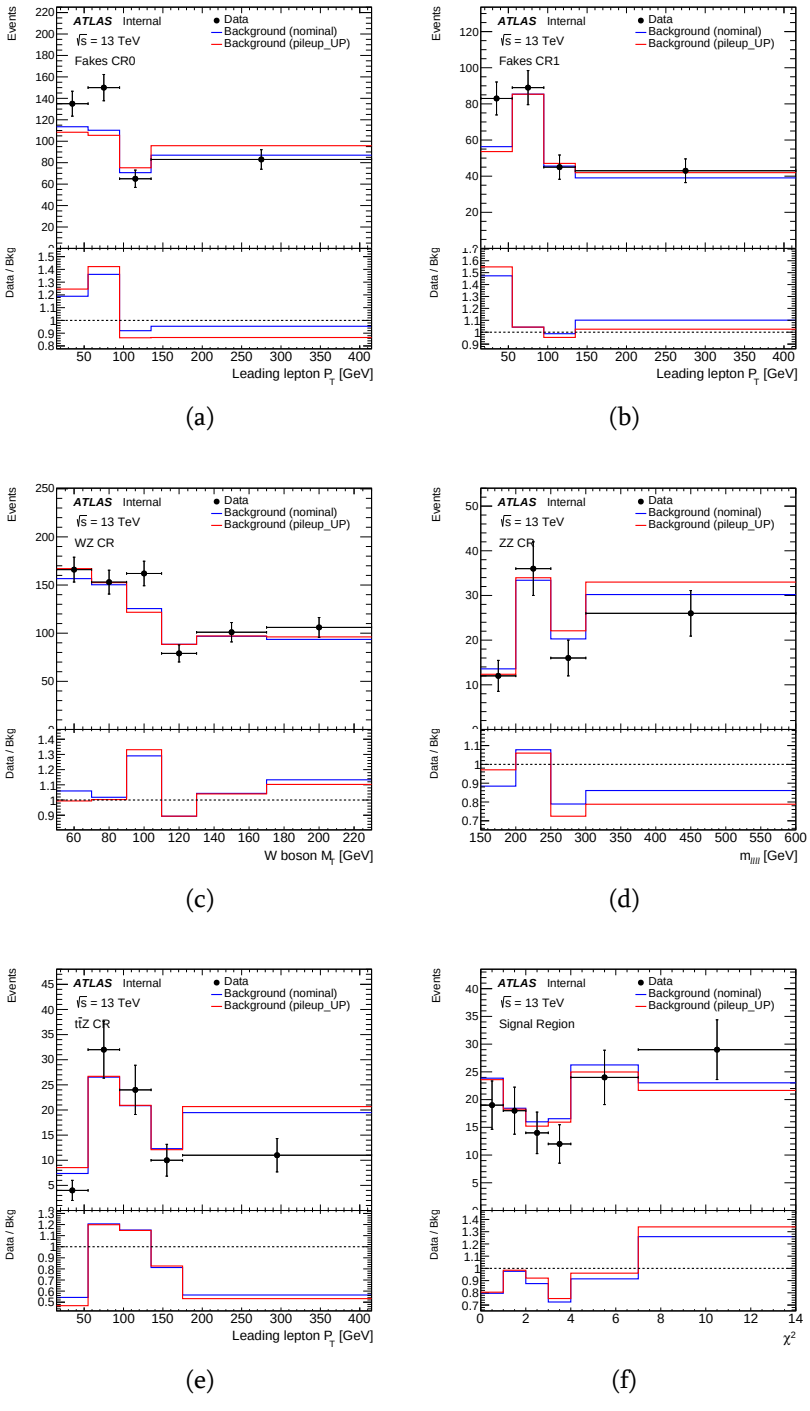

Figure D.4.: The expected and observed distributions of the leading lepton p_{T} in the a) fakes CR with b-veto events, b) fakes CR with one b-tag events; c) the W boson transverse mass in the WZ CR; d) four lepton system mass in the ZZ CR; e) leading lepton p_{T} in the $t\bar{t}Z$ CR and f) χ^2 variable in the signal region. The blue line is the nominal background and red line is the background with up variation of pileup uncertainty, while black dots are data.

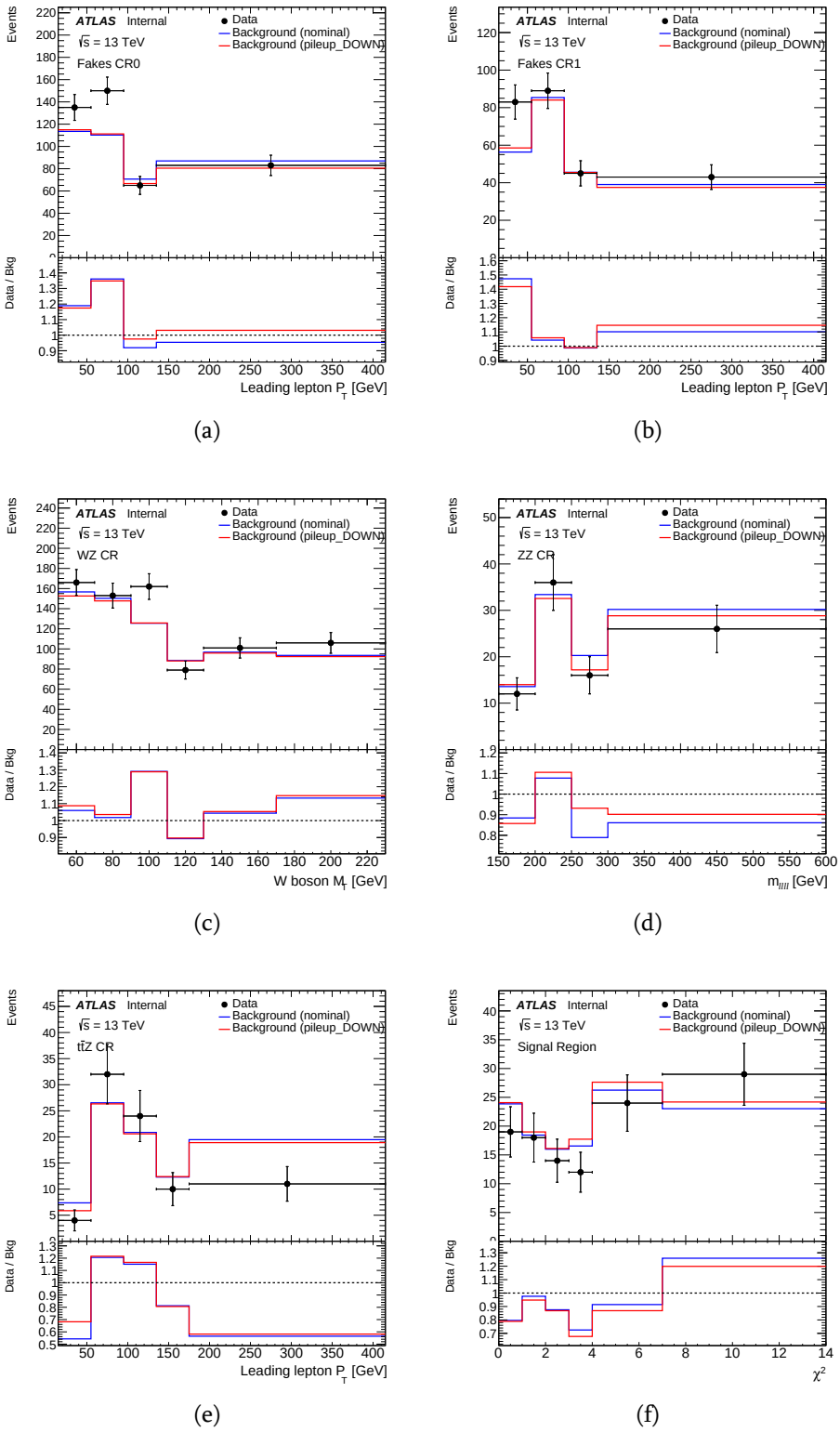

Figure D.5.: The expected and observed distributions of the leading lepton p_{T} in the a) fakes CR with b-veto events, b) fakes CR with one b-tag events; c) the W boson transverse mass in the WZ CR; d) four lepton system mass in the ZZ CR; e) leading lepton p_{T} in the $t\bar{t}Z$ CR and f) χ^2 variable in the signal region. The blue line is the nominal background and red line is the background with down variation of pileup uncertainty, while black dots are data.

D.0.2. Systematics plots from TRExFitter

The Figures D.6-D.19 show the systematic variation plots for the systematic sources that appeared in the ranking plots (see Figure 6.44), while Figures D.12-D.18 show the modelling uncertainties plots. Figure D.19 shows the systematic variation plots due to the fake scale factors variation that appeared in the ranking plot. The effect of the smoothing on the pileup uncertainty can be seen in Figures D.6-D.8. For most of the samples the effect of the pileup uncertainty is within the statistical uncertainty thus the shape variation is vanished after the smoothing.

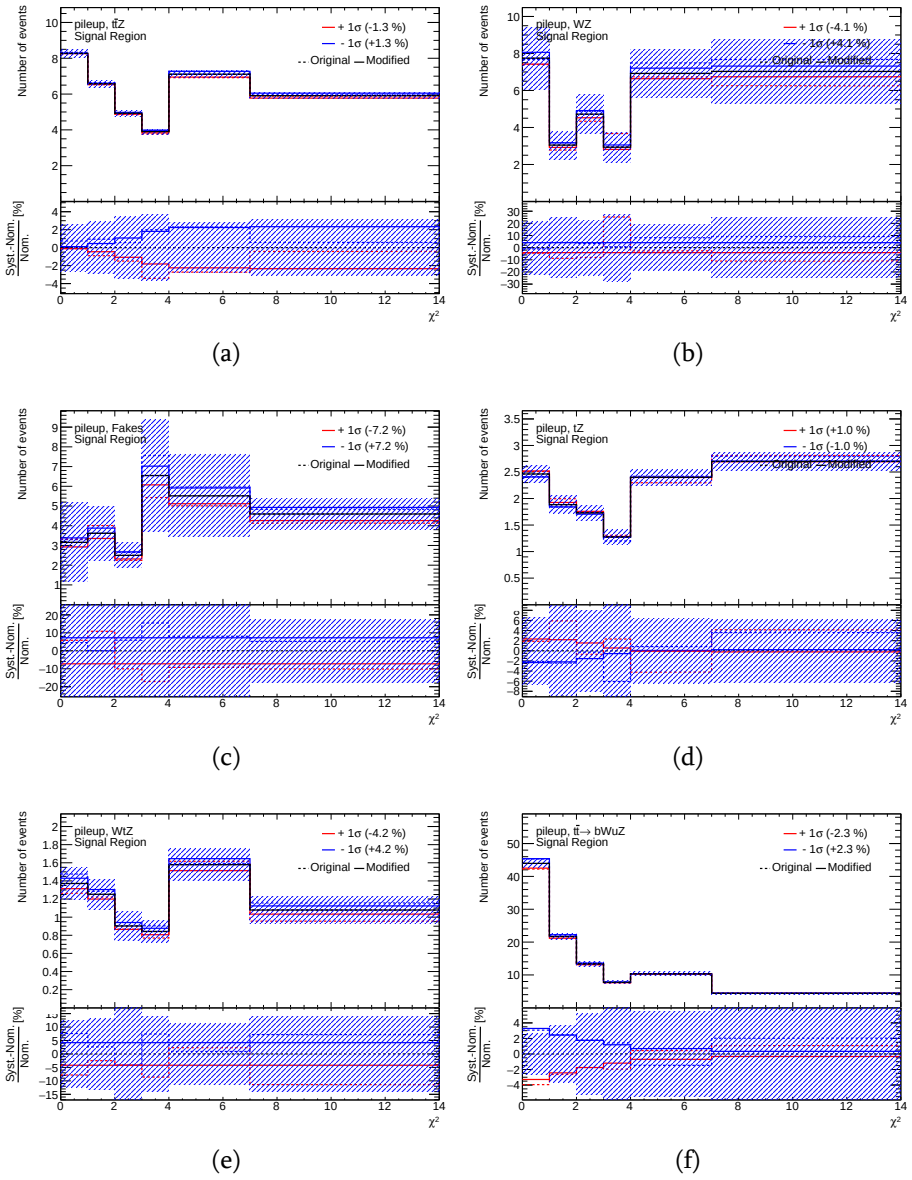

Figure D.6.: The expected distributions (black solid line) of the χ^2 variable in the signal region for a) $t\bar{t}Z$, b) WZ, c) Fakes, d) tZ, e) WtZ and d) signal sample. The dashed red and blue lines represent the $\pm 1\sigma$ variation of `pileup` systematic uncertainty, while solid red and blue lines show corresponding distributions after applying smoothing algorithm as implemented in the TRExFitter package. The dashed area represents the statistical uncertainty.

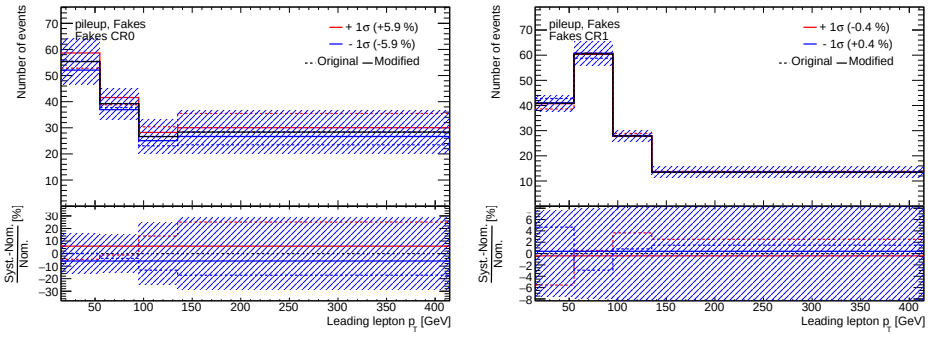

(a) (b)

Figure D.7.: The expected distributions (black solid line) of the leading lepton p_{T} in the fakes control region with a) b-veto events and with b) one b-tag events for the fake-lepton background contribution. The dashed red and blue lines represent the $\pm 1\sigma$ variation of `pileup` systematic uncertainty, while solid red and blue lines show corresponding distributions after applying smoothing algorithm as implemented in the TRExFitter package. The dashed area represents the statistical uncertainty.

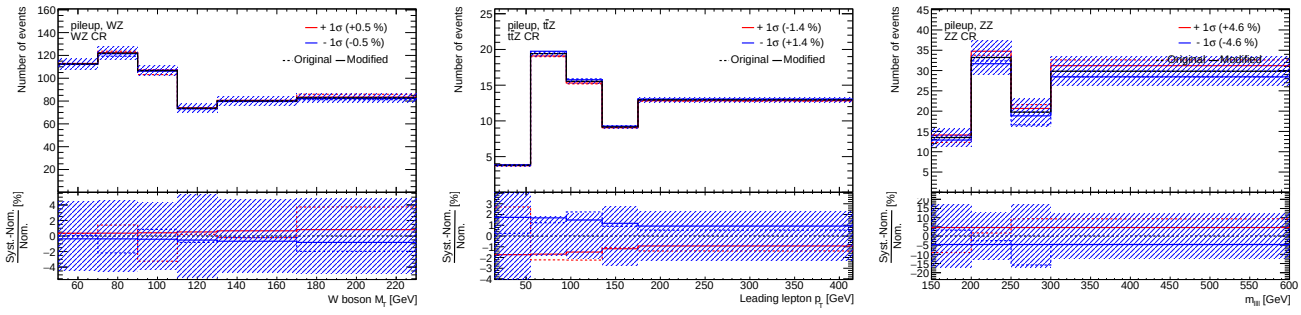

(a) (b) (c)

Figure D.8.: The expected distributions (black solid line) of the a) W boson transverse mass in the WZ CR, b) leading lepton p_{T} in the $t\bar{t}$ CR and c) four leptons system mass in the ZZ CR for the WZ, $t\bar{t}Z$ and ZZ background contributions respectively. The dashed red and blue lines represent the $\pm 1\sigma$ variation of `pileup` systematic uncertainty, while solid red and blue lines show corresponding distributions after applying smoothing algorithm as implemented in the TRExFitter package. The dashed area represents the statistical uncertainty.

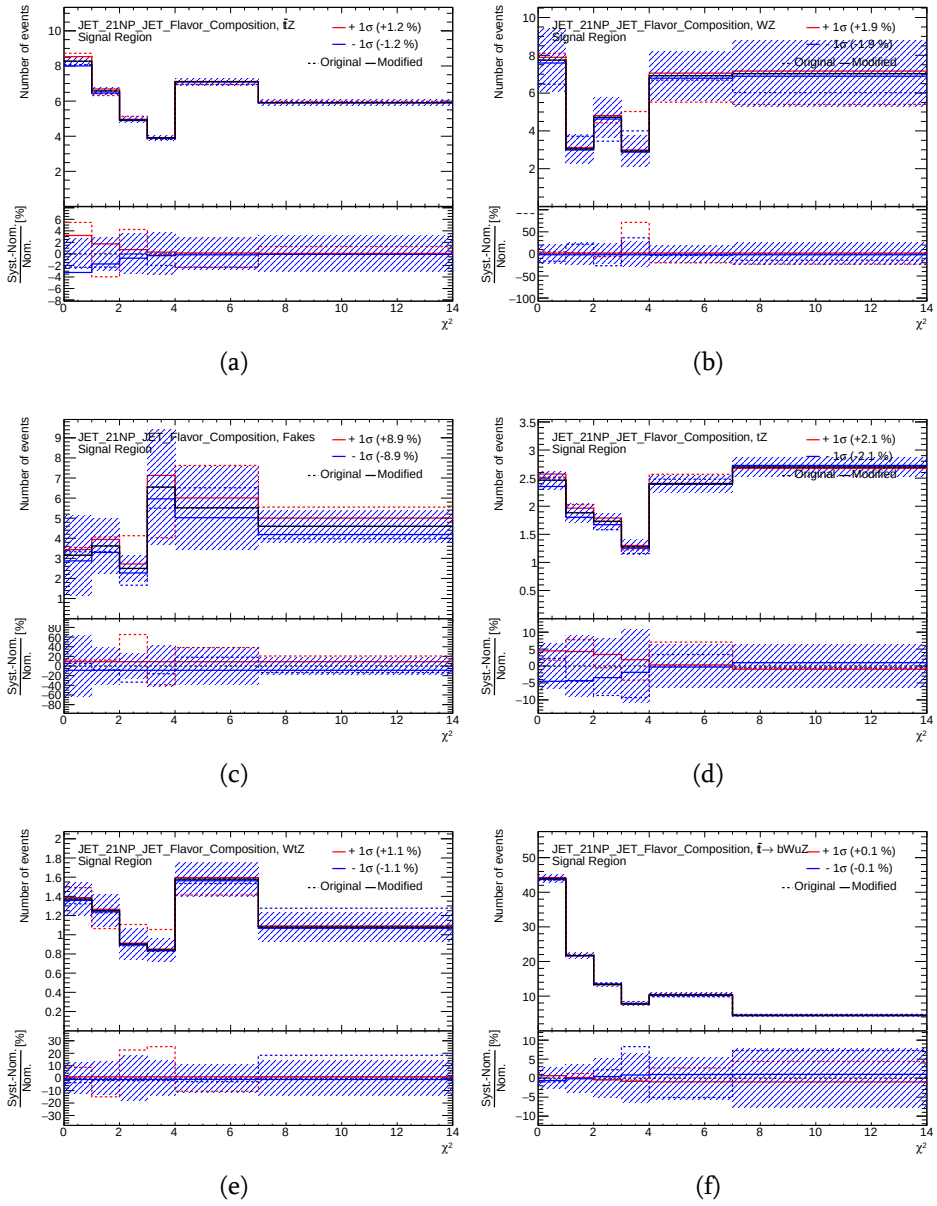

Figure D.9.: The expected distributions (black solid line) of the χ^2 variable in the signal region for a) $t\bar{t}Z$, b) WZ, c) Fakes, d) tZ, e) WtZ and d) signal sample. The dashed red and blue lines represent the $\pm 1\sigma$ variation of `JET_21NP_JET_Flavor_Composition` systematic uncertainty, while solid red and blue lines show corresponding distributions after applying smoothing algorithm as implemented in the TRExFitter package. The dashed area represents the statistical uncertainty.

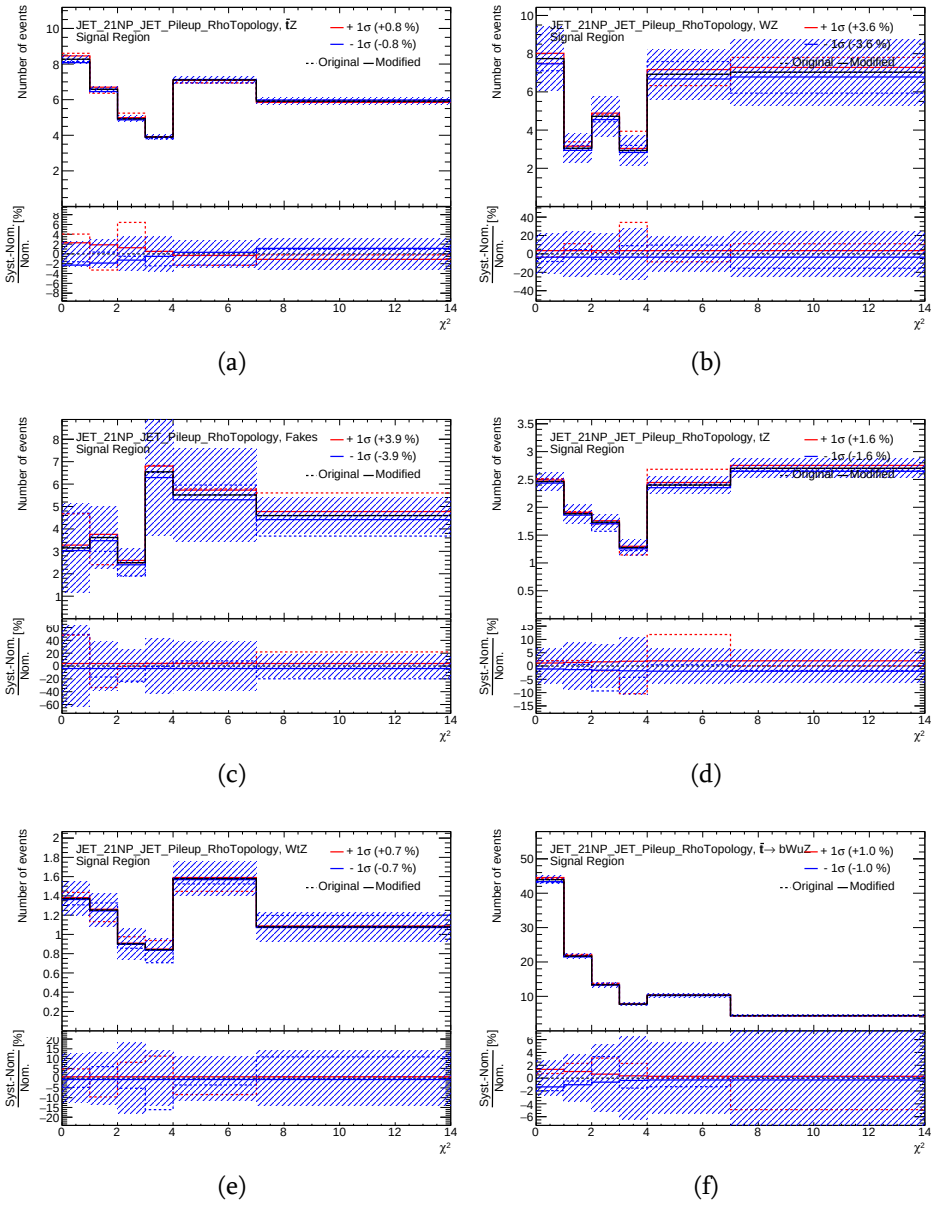

Figure D.10.: The expected distributions (black solid line) of the χ^2 variable in the signal region for a) $t\bar{t}Z$, b) WZ, c) Fakes, d) tZ, e) WtZ and d) signal sample. The dashed red and blue lines represent the $\pm 1\sigma$ variation of `JET_21NP_JET_Pileup_RhoTopology` systematic uncertainty, while solid red and blue lines show corresponding distributions after applying smoothing algorithm as implemented in the TRExFitter package. The dashed area represents the statistical uncertainty.

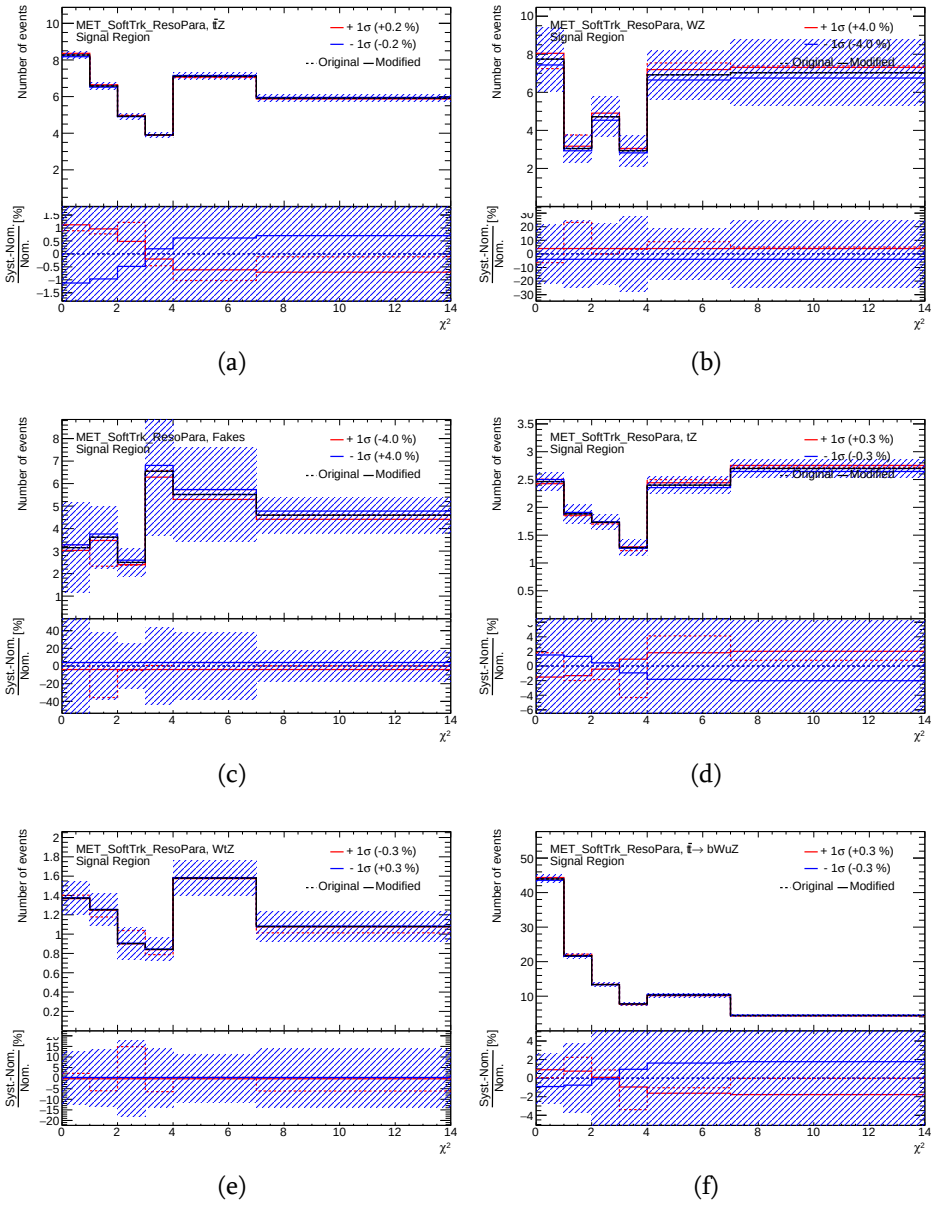

Figure D.11.: The expected distributions (black solid line) of the χ^2 variable in the signal region for a) $t\bar{t}Z$, b) WZ, c) Fakes, d) tZ, e) WtZ and d) signal sample. The dashed red and blue lines represent the $\pm 1\sigma$ variation of `MET_SoftTrk_ResoPara` systematic uncertainty, while solid red and blue lines show corresponding distributions after applying smoothing algorithm as implemented in the TRExFitter package. The dashed area represents the statistical uncertainty.

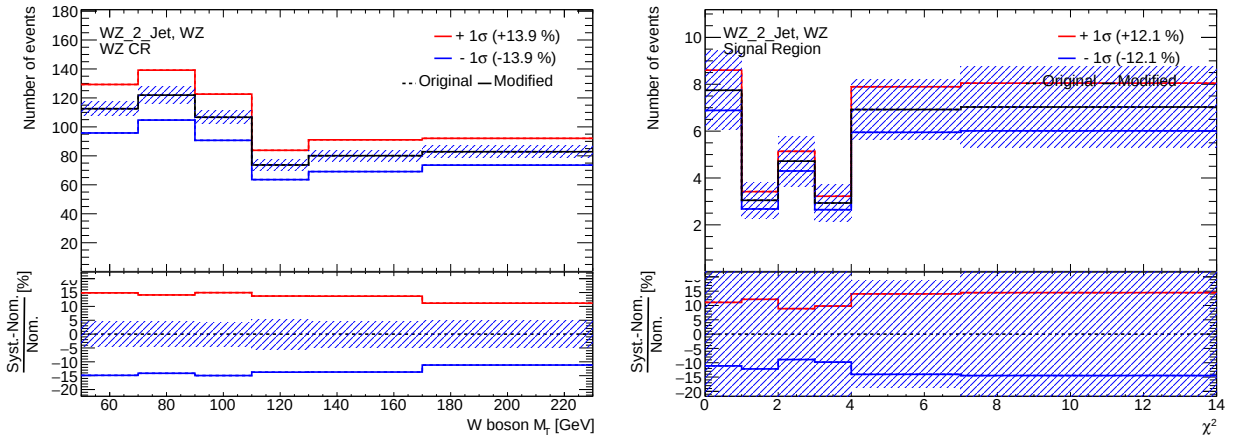

(a) (b)

Figure D.12.: The expected distributions (black solid line) of the a) W boson transverse mass in the WZ control region and b) the χ^2 variable in the signal region for WZ sample. The red and blue lines represent the variations of WZ yield in 2 jet bin by $\pm 25\%$ (see Section 6.8). The dashed area represents the statistical uncertainty.

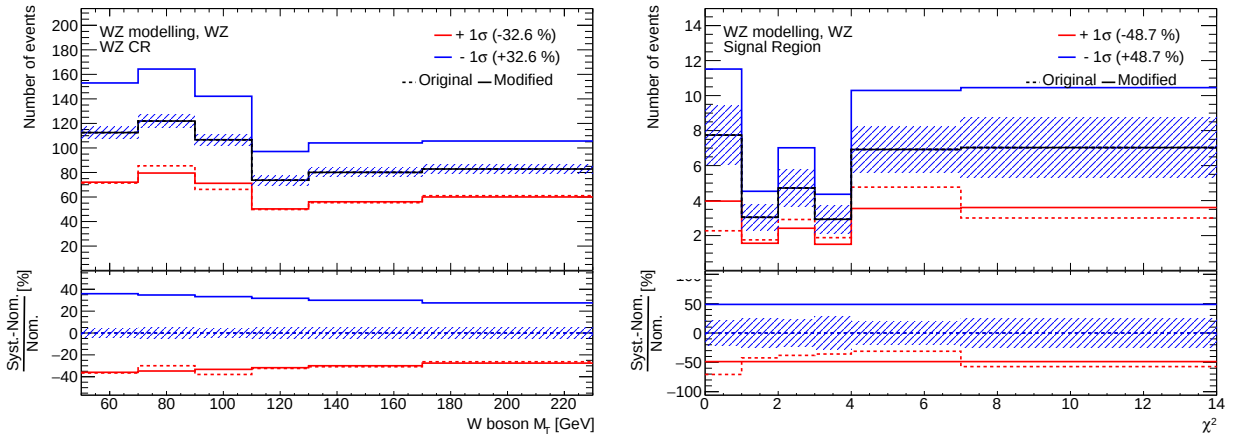

(a) (b)

Figure D.13.: The expected distributions (black solid line) of the a) W boson transverse mass in the WZ control region and b) the χ^2 variable in the signal region for WZ sample. The dashed red and blue lines represent the variations obtained by considering alternative event generator for WZ sample (see Section 6.8). The solid red and blue lines show corresponding distributions after applying smoothing algorithm as implemented in the TRExFitter package. The dashed area represents the statistical uncertainty.

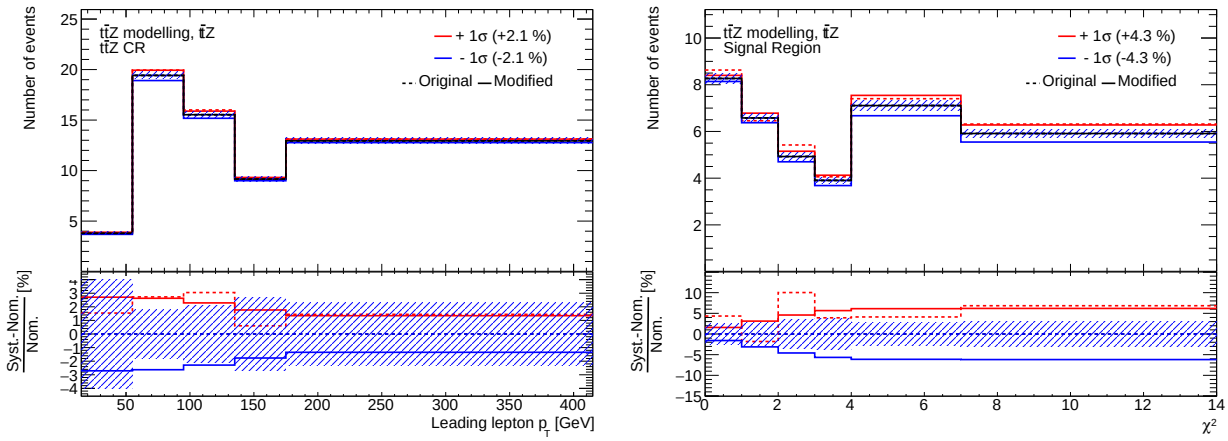

(a) (b)

Figure D.14.: The expected distributions (black solid line) of the a) leading lepton p_{T} in the $t\bar{t}Z$ control region and b) the χ^2 variable in the signal region for $t\bar{t}Z$ sample. The dashed red and blue lines represent the variations obtained by considering alternative event generator for $t\bar{t}Z$ sample (see Section 6.8). The solid red and blue lines show corresponding distributions after applying smoothing algorithm as implemented in the TRExFitter package. The dashed area represents the statistical uncertainty.

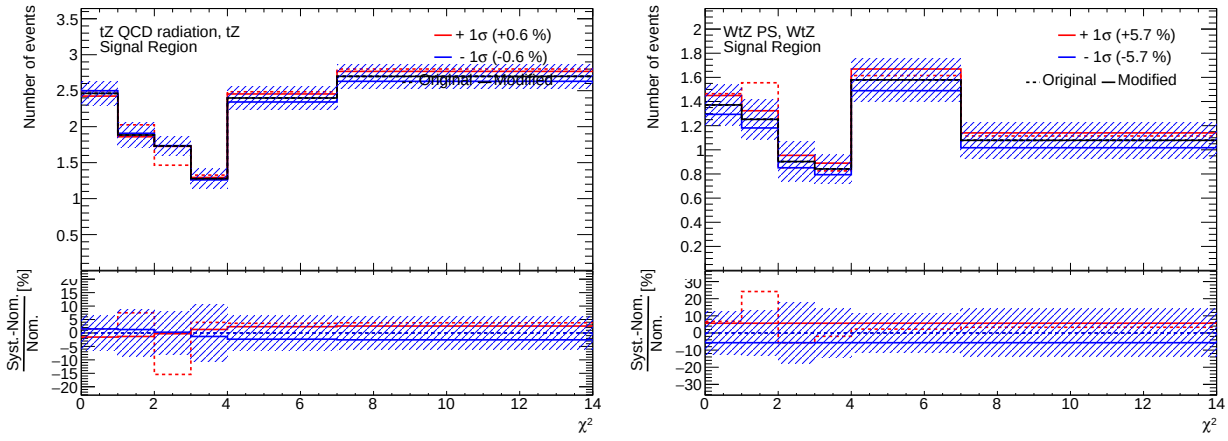

(a) (b)

Figure D.15.: The expected distributions (black solid line) of the χ^2 variable in the signal region for the a) tZ and b) WtZ samples. The dashed red and blue lines represent the variations obtained by considering alternative sample with additional QCD radiation for tZ sample and alternative samples with different parton shower algorithm for WtZ sample (see Section 6.8). The solid red and blue lines show corresponding distributions after applying smoothing algorithm as implemented in the TRExFitter package. The dashed area represents the statistical uncertainty.

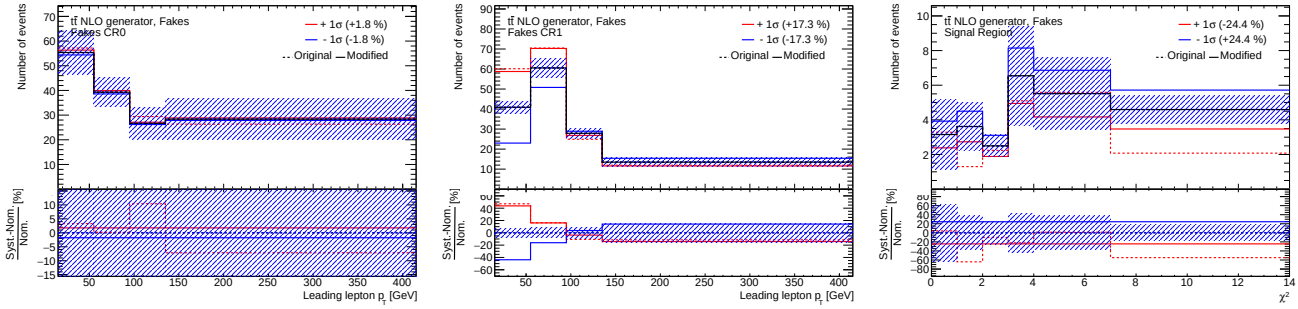

(a) (b) (c)

Figure D.16.: The expected distributions (black solid line) of the leading lepton p_{T} in the fakes control region with a) b-veto events and with b) one b-tag events, and c) the χ^2 variable in the signal region for the fake-lepton background contribution. The dashed red and blue lines represent the variations obtained by considering alternative event generator for the $t\bar{t}$ sample (see Section 6.8). The solid red and blue lines show corresponding distributions after applying smoothing algorithm as implemented in the TRExFitter package. The dashed area represents the statistical uncertainty.

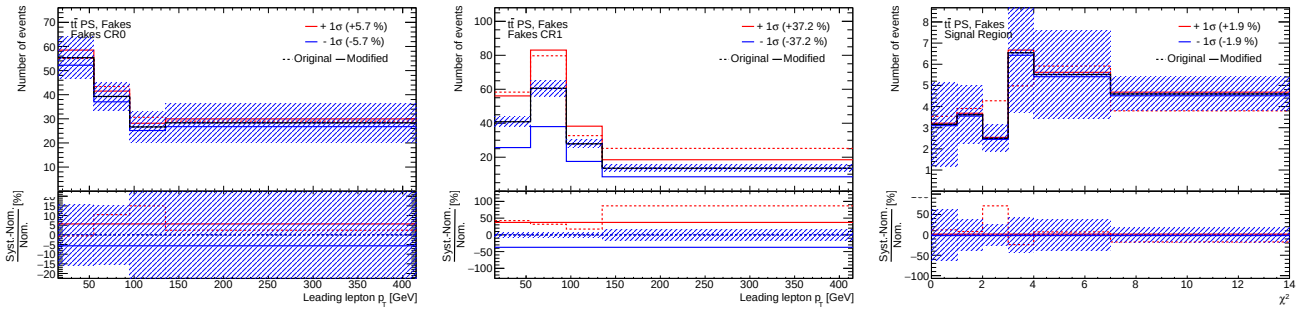

(a) (b) (c)

Figure D.17.: The expected distributions (black solid line) of the leading lepton p_{T} in the fakes control region with a) b-veto events and with b) one b-tag events, and c) the χ^2 variable in the signal region for the fake-lepton background contribution. The dashed red and blue lines represent the variations obtained by considering alternative parton showering algorithm for the $t\bar{t}$ sample (see Section 6.8). The solid red and blue lines show corresponding distributions after applying smoothing algorithm as implemented in the TRExFitter package. The dashed area represents the statistical uncertainty.

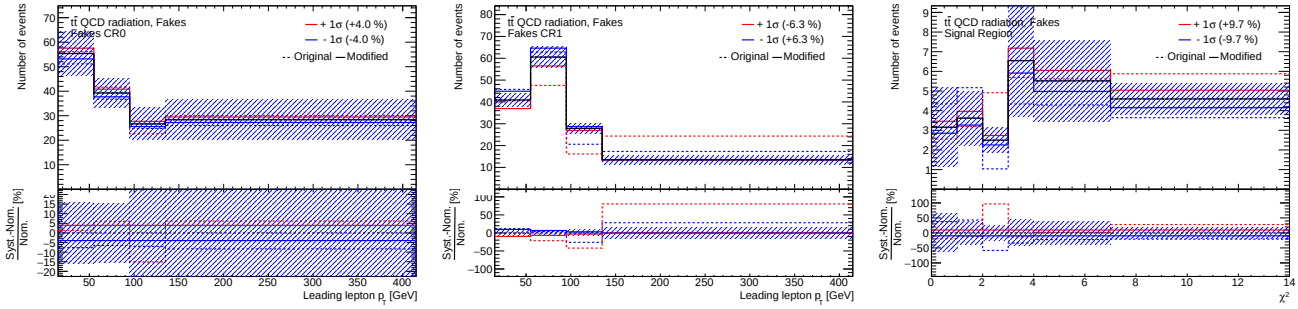

(a) (b) (c)

Figure D.18.: The expected distributions (black solid line) of the leading lepton p_{T} in the fakes control region with a) b-veto events and with b) one b-tag events, and c) the χ^2 variable in the signal region for the fake-lepton background contribution. The dashed red and blue lines represent the variations obtained by considering alternative sample with additional QCD radiation for the $t\bar{t}$ sample (see Section 6.8). The solid red and blue lines show corresponding distributions after applying smoothing algorithm as implemented in the TRExFitter package. The dashed area represents the statistical uncertainty.

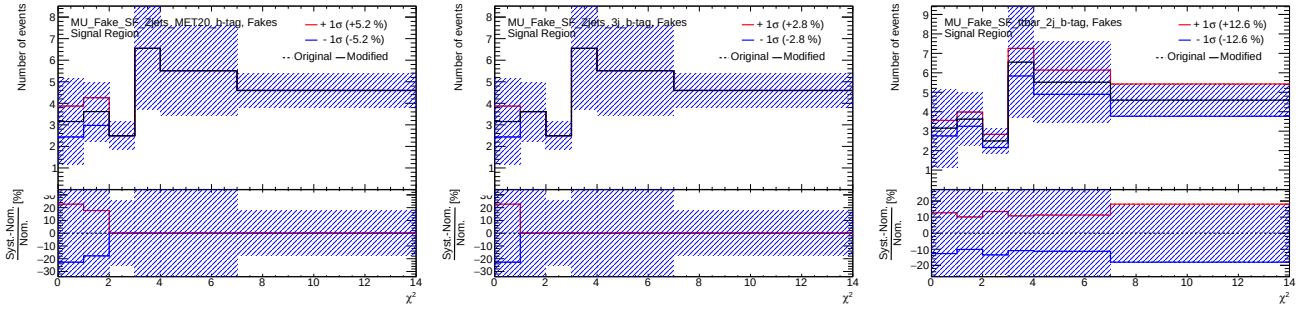

(a) (b) (c)

Figure D.19.: The expected distributions (black solid line) of the χ^2 variable in the signal region for the fake-lepton background contribution. The blue and red lines represent the $\pm 1\sigma$ variation of a) $\lambda^{\mu}_{\mathrm{Zjets}}$ in the $E^{\mathrm{miss}}_{\mathrm{T}}$ bin of [20,40] GeV, b) $\lambda^{\mu}_{\mathrm{Zjets}}$ in 3 jet bins, c) $\lambda^{\mu}_{t\bar{t}}$ in 2 jet bin. The dashed area represents the statistical uncertainty.

Appendix E.

Additional pre- and post-fit plots

The Figures E.2 and E.3 show the jet multiplicity distributions in the fakes control regions with b-veto and with one b-tag events, while the Figure E.1 presents the jet multiplicity distributions in the WZ CR before and after the combined fit under the background-only hypothesis. The data does not have enough statistical power to correct the shape agreement between data and background in the fakes CRs, while in the WZ CR it is improved after the fit. The Figures E.4-E.6 present the plots from the side-band and WZ validation regions before and after the combined fit under the background-only hypothesis. Observe that the agreement between data and background is slightly improved and stays within one sigma of uncertainty after the fit.

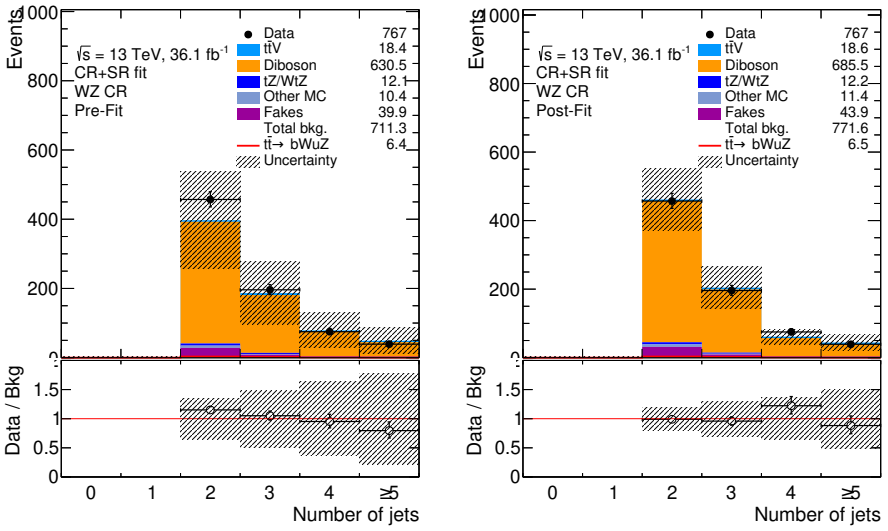

(a) (b)

Figure E.1.: Comparison between data and prediction for the jet multiplicity distributions in the WZ control region a) before and b) after the combined fit under the background-only hypothesis after unblinding. The number of signal events is normalized to the observed 95% CL limit. The dashed area represents total uncertainty on the background prediction.

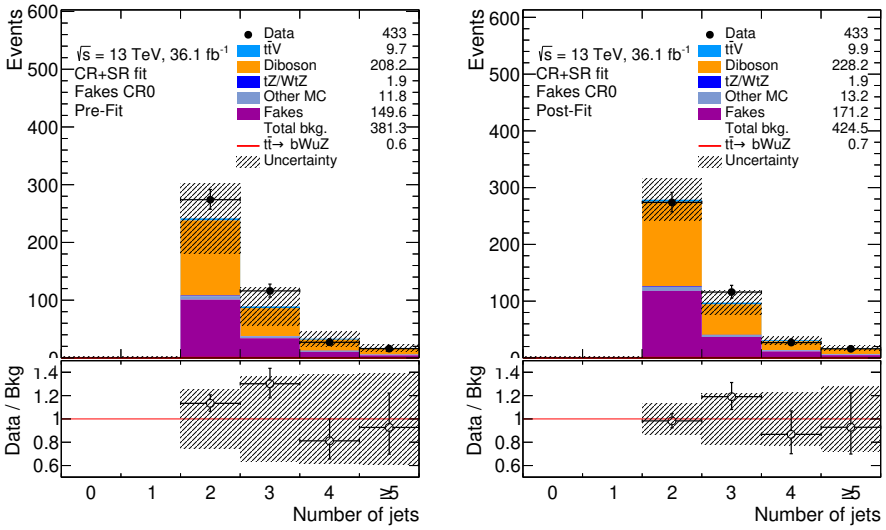

(a) (b)

Figure E.2.: Comparison between data and prediction for the jet multiplicity distributions in the fake leptons background control region in b-veto events a) before and b) after the combined fit under the background-only hypothesis after unblinding. The number of signal events is normalized to the observed 95% CL limit. The dashed area represents total uncertainty on the background prediction.

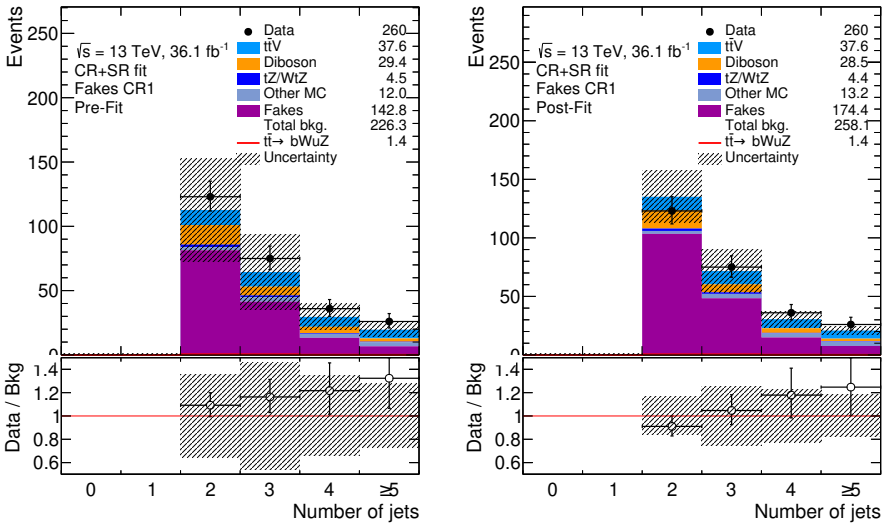

(a) (b)

Figure E.3.: Comparison between data and prediction for the jet multiplicity distributions in the fake leptons background control region in one b-tag events a) before and b) after the combined fit under the background-only hypothesis after unblinding. The number of signal events is normalized to the observed 95% CL limit. The dashed area represents total uncertainty on the background prediction.

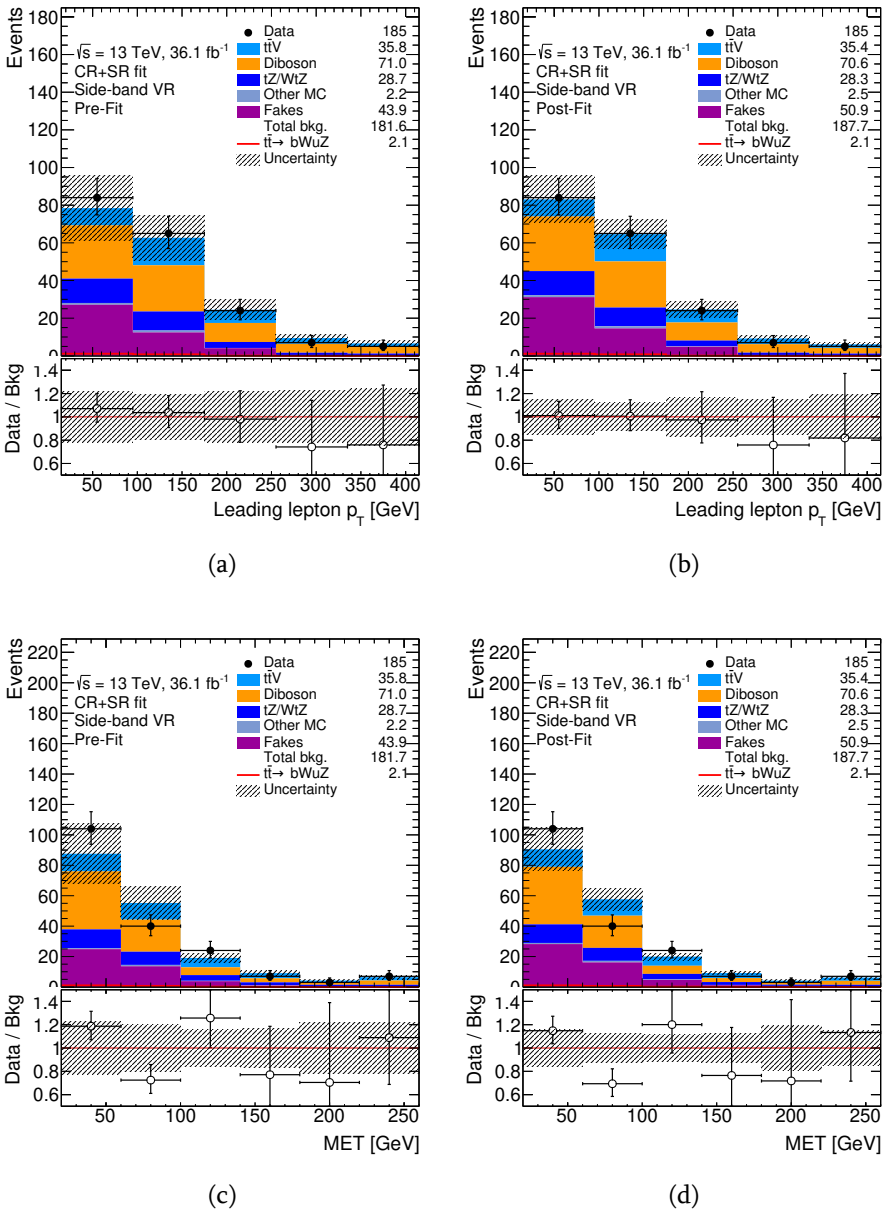

Figure E.4.: Comparison between data and prediction for the leading lepton p_{T} (a,b) and missing transverse momentum (c,d) in the side-band validation region before (left) and after (right) the combined fit under the background-only hypothesis after unblinding. The number of signal events is normalized to the observed 95% CL limit. The dashed area represents total uncertainty on the background prediction.

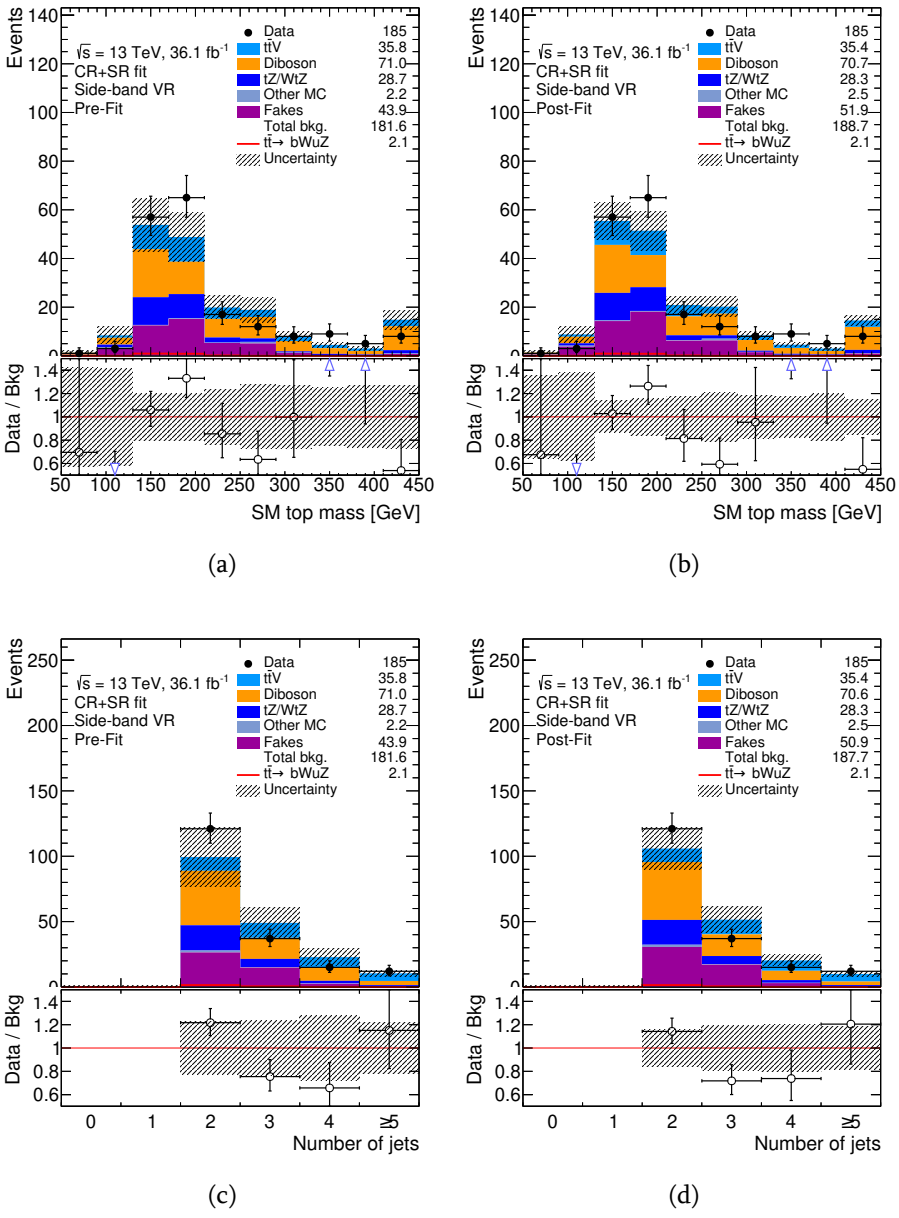

Figure E.5.: Comparison between data and prediction for the SM top-quark mass (a,b) and jet multiplicity (c,d) in the side-band validation region before (left) and after (right) the combined fit under the background-only hypothesis after unblinding. The number of signal events is normalized to the observed 95% CL limit. The dashed area represents total uncertainty on the background prediction.

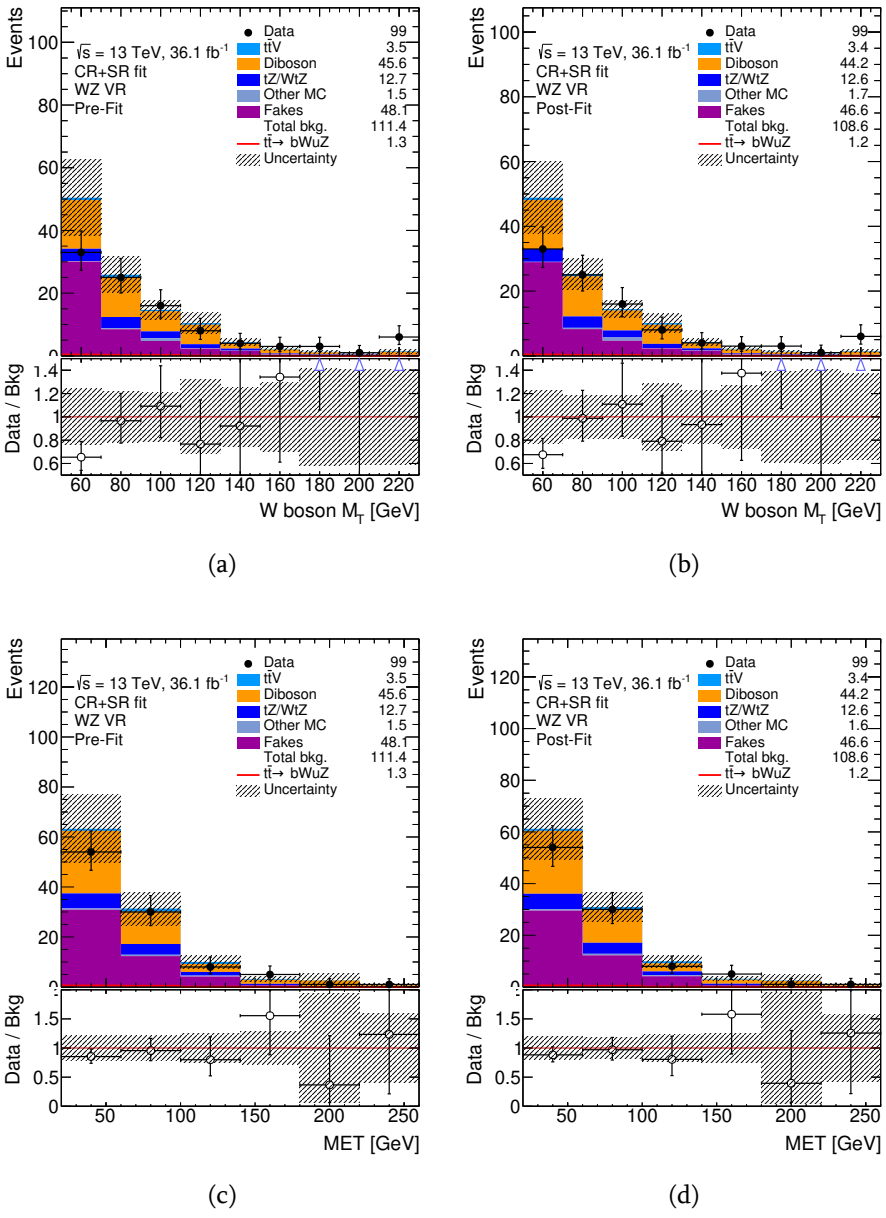

Figure E.6.: Comparison between data and prediction for the W boson transverse mass (a,b) and missing transverse momentum (c,d) in the WZ validation region before (left) and after (right) the combined fit under the background-only hypothesis after unblinding. The number of signal events is normalized to the observed 95% CL limit. The dashed area represents total uncertainty on the background prediction.

Appendix F.

Investigation of the observed limit

We find that the observed limit matches to the -1σ band of the expected limit (see Section 6.10.4). In order to understand the origin of this effect the following checks have been performed.

We expect that the first bin of the χ^2 distribution in the SR (see Figure 6.60) has a driving force in the observed limit calculation. In order to confirm that the first bin is the most important one, we considered the following two scenarios:

1. The data value in the first bin of the χ^2 distribution is replaced with the yield of the pre-fit background in the same bin.

2. In the first bin of the χ^2 distribution the real data is used, while in other bins the "Asimov data" is used, defined as the total expected pre-fit background.

The results of the combined fit under background-only hypothesis for the χ^2 distribution in the first and second scenario are presented in Figures F.1 and F.2, respectively. Figure F.3 shows the observed and expected CL_s as a function of $BR(t \to uZ)$ for the first (left) and second (right) scenario, while the extracted observed and expected limits are presented in Tables F.1 and F.2, respectively. Changing the first bin with the Asimov data (first scenario) significantly affects the observed limit, while using the real data in the first bin and the Asimov data in the next bins (second scenario), slightly affects the observed limit. This result confirms that the first bin of the χ^2 distribution has a driving force in the observed limit calculation, and since the data value in this bin is close to the -1σ variation of the post-fit background, the resulting observed limit is close to the -1σ band of the expected limit.

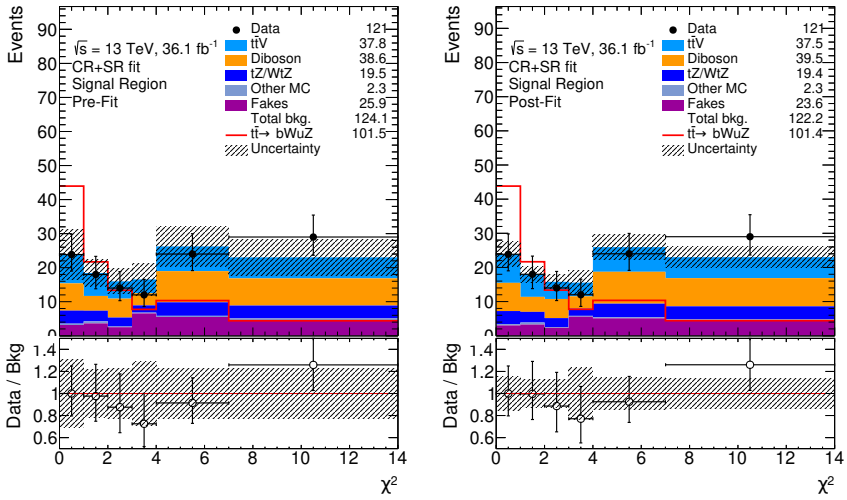

(a) (b)

Figure F.1.: The distributions for the χ^2 after the event reconstruction in the signal region a) before and b) after the combined fit under the background-only hypothesis. The data value in the first bin is replaced with the yield of the pre-fit background in the same bin. The dashed area represents total uncertainty on the background prediction.

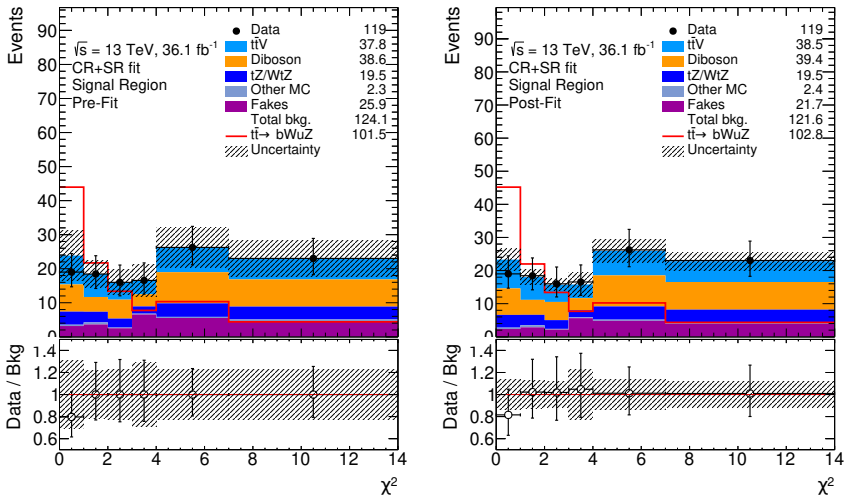

(a) (b)

Figure F.2.: The distributions for the χ^2 after the event reconstruction in the signal region a) before and b) after the combined fit under the background-only hypothesis. In the first bin the real data is presented, while in all others the "Asimov data" is used, defined as the total expected pre-fit background. The dashed area represents total uncertainty on the background prediction.

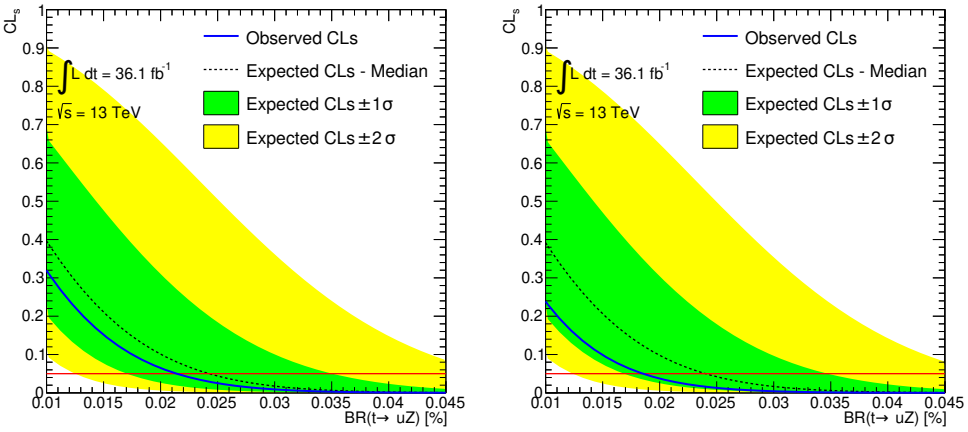

Figure F.3.: CL_s vs $BR(t \to uZ)$ taking into account systematic and statistical uncertainties, a) when the data value in the first bin of the χ^2 distribution is replaced with the yield of the pre-fit background in the same bin, b) when in the χ^2 distribution the "Asimov data" is used, defined as the total expected pre-fit background, except the first bin where the real data is used.

	Observed	-1σ	Expected	+1σ
$BR(t \to uZ)$ [%]	0.021	0.017	0.024	0.035

Table F.1.: Observed and expected 95% confidence level upper limit on the $t \to uZ$ branching ratio. The expected central value are shown together with the $\pm 1\sigma$ bands, which include the contribution from the statistical and systematic uncertainties. Limits are obtained when the data value in the first bin of the χ^2 distribution is replaced with the yield of the pre-fit background in the same bin.

	Observed	-1σ	Expected	+1σ
$BR(t \to uZ)$ [%]	0.019	0.017	0.024	0.035

Table F.2.: Observed and expected 95% confidence level upper limit on the $t \to uZ$ branching ratio. The expected central value are shown together with the $\pm 1\sigma$ bands, which include the contribution from the statistical and systematic uncertainties. Limits are obtained when in the first bin of the χ^2 histogram the real data is used, while in all other bins of the same histogram the "Asimov data" is used, defined as the total expected pre-fit background.